UNIVERSIDADE FEDERAL DE SANTA CATARINA
CENTRO TECNOLÓGICO
PROGRAMA DE PÓS-GRADUAÇÃO EM ENGENHARIA MECÂNICA

GUILHERME CARTAGENA MIRON

DEVELOPMENT OF PIEZOELECTRIC ENERGY HARVESTER FOR WIRELESS VIBRATION SENSORS

FLORIANÓPOLIS - SC
Monday 27th February, 2023

Guilherme Cartagena Miron

DEVELOPMENT OF PIEZOELECTRIC ENERGY HARVESTER FOR WIRELESS VIBRATION SENSORS

Dissertação submetida ao Programa de Pós-Graduação em Engenharia Mecânica da Universidade Federal de Santa Catarina para a obtenção do Grau de Mestre em Engenharia Mecânica.
Orientador: Júlio A. Cordioli, Dr. Eng.
Co-orientador: Olavo M. Silva, Dr. Eng.

Florianópolis - SC

Monday 27th February, 2023

Ficha de identificação da obra elaborada pelo autor,
através do Programa de Geração Automática da Biblioteca Universitária da UFSC.

Miron, Guilherme
Development of piezoelectric MEMS energy harvester for wireless sensors / Guilherme Miron ; orientador, Júlio A. Cordioli, coorientador, Olavo M. Silva, 2023.
151 p.

Dissertação (mestrado) - Universidade Federal de Santa Catarina, Centro Tecnológico, Programa de Pós-Graduação em Engenharia Mecânica, Florianópolis, 2023.

Inclui referências.

1. Engenharia Mecânica. 2. Manutenção. 3. Micro usinagem. 4. Otimização. 5. Elementos finitos. I. A. Cordioli, Júlio. II. M. Silva, Olavo. III. Universidade Federal de Santa Catarina. Programa de Pós-Graduação em Engenharia Mecânica. IV. Título.

Guilherme Cartagena Miron

Development of piezoelectric energy harvester for wireless vibration sensors

O presente trabalho em nível de mestrado foi avaliado e aprovado por banca examinadora composta pelos seguintes membros:

Prof. Emílio Carlos Nelli Silva, Dr. Eng.
Universidade de São Paulo

Prof. Fábio Durante Pereira Alves, Dr. Eng.
Naval Postgraduate School

Certificamos que esta é a **versão original e final** do trabalho de conclusão que foi julgado adequado para obtenção do título de Mestre em Engenharia Mecânica.

Prof. Henrique Simas, Dr. Eng.
Coordenador do Programa

Júlio A. Cordioli, Dr. Eng.
Orientador

Florianópolis - SC, Monday 27th February, 2023.

This work is dedicated to wife.
It was an insane couple of years,
thank god you were there!

ACKNOWLEDGEMENTS

First of all, my family. I thank my wife for every moment of our lives together, in happiness and sickness, but hopefully not so much sickness anymore. Thanks to my mother and father every step of the way, I am who I am because of everything you did. My brother, there is no person I trust more in my life. My aunt, surely could not have done this text without you. Thank you to all my family for being there for me during all my life; this support is what lead me to all my accomplishments and where I am today.

I would like to acknowledge my supervisor Julio Cordioli for the guidance and opportunities given to me. My thanks to my advisors and colleagues Olavo, Braga, Racquel, Maria, and Airton; every input was important to building this work. In addition, to all my colleagues from the Laboratory of Vibration and Acoustics, sharing experiences with my colleagues is a big part of how I learned what I needed for this work.

I would also like to take this opportunity to thank the Federal University of Santa Catarina for the 7 years of education. Finally, I would like to acknowledge Dynamox for all the financial and technical support in this work.

"They are ill discoverers who think there is no land, when they can see nothing but sea."
Sir Francis Bacon

RESUMO

O Monitoramento Baseado em Condição via análise de vibração é um dos principais métodos preditivos utilizados na manutenção industrial ao longo das últimas décadas. Atualmente, o sensoriamento utilizado neste tipo de análise tem evoluído para os sensores sem fio, os quais permitem medições continuas e de equipamentos que antes eram considerados inacessíveis para sensores cabeados. Contudo, uma grande limitação para estas tecnologias é a vida útil da bateria que é reduzida sobre condições de temperaturas extrema, volume de dados monitorados e processados e frequência de uso. Este trabalho apresenta o desenvolvimento de um *energy harvester* piezoelétrico adaptado para sensores de monitoramento de vibração. Uma revisão da literatura é realizada para entender as tecnologias em *energy harvesting* e otimização disponiveis para execução do projeto. Em seguida a metodologia escolhida é apresentada, detalhando os modelos numéricos criados, as variaveis parametricas que serão otimizadas dos modelos e os algoritimos que serão utilizados assim como suas configurações. Diferentes designs de *vibrational energy harvester* são testados tomando duas frentes de projeto. Uma utilizando tecnologia de fabricação MEMS e outra utilizando micro usinagem. Primeiramente é realizado o projeto com o dispositivo MEMS identificando a cada passo formas de melhorar a função objetivo da otimização assim como definindo em que cenários cada uma se encaixam melhor. O dispositivo a partir de micro usinagem fazem uso do conhecimento obtido durante o projeto do MEMS para selecionar a função objetivo. São selecionados dois modelos para prototipação e destacado um modelo que não foi prototipado mas possui uma ótima performance prevista pelo modelo numérico. Após prototipação e realização de experimentos, os modelos numéricos são validados. Onde o modelo numérico MEMS apresentou uma ótima precisão, enquanto o micro usinado demonstrou alguns desvios. Contudo, em termos de performance o dispositivo micro usinado foi significativamente superior ao MEMS, inclusive se posicionando entre os melhores da literatura, em especial para dispositivos de baixa frequência natural e pequeno volume.

Palavras-chaves: Micro usinado; MEMS; Piezoelétrico; Vibração; Baixa frequência; Otimização; Modelo numérico; Pequena escala; Manutenção.

Resumo expandido

Introdução

Na indústria de manutenção de máquinas, em geral, existem três abordagens principais para a manutenção de equipamentos: corretiva, preventiva e preditiva. Embora cada abordagem tenha suas vantagens e desvantagens, a manutenção preditiva tornou-se a estratégia de manutenção mais eficaz devido aos avanços nas técnicas de monitoramento (RANDALL, 2010). Isso é especialmente importante para indústrias com máquinas de alto custo ou críticas que devem operar por períodos prolongados sem tempo de inatividade. O monitoramento de vibração é o método mais comumente usado para manutenção preditiva, e os acelerômetros piezoelétricos são os sensores mais amplamente utilizados para medir dados de vibração (RANDALL, 2010). Atualmente, existem soluções com e sem fio para monitoramento de condições. O uso de sensores sem fio fornece maior autonomia e flexibilidade, aumentando a segurança dos trabalhadores e permitindo o monitoramento de espaços inacessíveis. No entanto, a alimentação por bateria limita a vida útil dos sensores sem fio em comparação com os sensores com fio.

A longevidade de dispositivos eletrônicos, especialmente sensores sem fio, está diretamente relacionada ao consumo de energia de seus componentes. Nos últimos anos, microdispositivos passaram por avanços tecnológicos significativos que levaram a uma rápida redução no consumo de energia, aumentando assim a vida útil de dispositivos a bateria. Essa redução abriu caminho para investigar novas alternativas para estender a vida útil do equipamento eletrônico, incluindo a possibilidade de substituir ou complementar baterias tradicionais que alimentam dispositivos como sensores de vibração por sistemas de captura de energia do ambiente (GAMMAITONI, 2012). Esses dispositivos, coletivamente conhecidos como *Energy Harvesters* (EH), dependem da disponibilidade de energia no ambiente, como energia solar, térmica, química e mecânica (SELVAN; MOHAMED ALI, 2016). Entre os EHs, aquelas que trabalham com energia de vibrações oferecem as vantagens de serem sustentáveis, estáveis e pequenos (KHALIGH; PENG ZENG; CONG ZHENG, 2010). Além disso, a energia vibracional pode ser coletada de diversas fontes, como máquinas e equipamentos industriais, veículos, movimento humano e fluidos (ZOU et al., 2019).

Objetivos

O desenvolvimento de *Vibration Energy Harvester* (VEH) para aplicações de sensores sem fio requer que o VEH seja pequeno o suficiente para não aumentar significativamente o tamanho do dispositivo (sensor sem fio). Nesse contexto, destaca-se que a densidade de potência do VEH teoricamente não dependa do volume do dispositivo, mas, na prática, ela diminui com o volume para todos os tipos de transdução (BRIAND et al., 2015). Além disso, as frequências fundamentais adequadas para aplicações de VEHs são comumente encontradas nas faixas de 30Hz a 60Hz e 100Hz a 125Hz (AKTAKKA; PETERSON; NAJAFI, 2012). Portanto, o VEH deve operar em uma frequência baixa, que muitas vezes está associada a estruturas maiores e mais pesadas.

Os métodos mais comuns de transdução para VEH são Piezoelétrico (PZ), Eletromagnético (EM) ou Eletrostático (ES) (DHADWAL; RASTEGAR, 2017). A piezeletricidade, em particular, se destaca por sua estrutura simples, compatibilidade com a tecnologia de sistemas micro-eletromecânicos (MEMS) Dhadwal and Rastegar (2017), e alta densidade de armazenamento de energia (ROUNDY; LELAND, et al., 2005; ROUNDY; WRIGHT, 2004). MEMS, bem como a micro-usinagem (MM), são alternativas atraentes para a fabricação de dispositivos em pequena escala. Neste contexto, este estudo busca utilizar ambos processos de fabricação para o desenvolvimento de dois *Piezoelectric Vibration Energy Harvester* (PVEH) que possam atender aos requisitos demandados por um sensor wireless para monitoramento de ativos industriais.

Metodologia

A metodologia utilizada no presente trabalho para desenvolver o PVEH pode ser dividida em duas etapas: (i) o processo de construção do modelo numérico e (ii) o procedimento de otimização. Este trabalho propõe o uso de duas estratégias de fabricação, portanto, os modelos numéricos são construídos usando as especificações de cada técnica de fabricação como base para construir a geometria, selecionar os materiais e os parâmetros de otimização. Os projetos são simulados usando COMSOL multiphysics (COMSOL MUL-

TIPHYSICS® V. 5.6, n.d.) e utilizam um *design* do tipo viga, comumente utilizado na literatura. Todos os modelos tem sua malha refinada de forma a aumentar a discretizarão dos elementos nas regiões em que se espera ter maior deformação, sendo nesse caso as vigas que seguram a massa sísmica.

O projeto do PVEH é otimizado usando um algoritmo de Evolução Diferencial (DE). Esse algoritmo foi escolhido como procedimento de otimização porque já foi utilizado em estudos similares pelo nosso grupo de pesquisa (MIRON; PAUL; CORDIOLI, 2022). O DE implementado no MATLAB (BUEHREN, 2014) é integrado ao COMSOL, sendo diversas funções objetivas testadas para identificar quais obtém o melhor resultado. Os modelos MEMS e MM foram pré-validados antes da fabricação de qualquer protótipo. O modelo numérico MEMS foi pré-validado usando um projeto semelhante previamente desenvolvido (MIRON; PAUL; CORDIOLI, 2022), enquanto o MM foi testado com o bimorfo piezoelétrico sem quaisquer alterações geométricas, com e sem o uso de uma massa sísmica (SM) de 5,1 g posicionada na ponta do bimorfo.

Resultados e Discussão

Ambos os dispositivos MEMS e MM foram prototipados. O dispositivo MEMS foi fabricado usando o processo PiezoMUMPs (COWEN et al., 2014). Já o protótipo MM foi feito com o bimorfo SMBA4510T05M da STEMINC e cortado usando uma serra de fio de diamante contínuo (COSTA; SANTOS, et al., 2022; COSTA; WEINGAERTNER; XAVIER, 2022) com um dispositivo feito sob medida para segurar o bimorfo. Duas massas sísmicas de aço foram usinadas para coincidir com a frequência natural do protótipo que usava uma massa de tungstênio porque nenhum outro material mais denso estava disponível durante o período de fabricação. As massas foram posicionadas manualmente e coladas ao bimorfo usando cianoacrilato.

Após os experimentos os modelos numéricos foram ajustados para melhor descrever o protótipo fabricado e validados contra esses dados experimentais. Assim, a potência normalizada máxima obtida pelo protótipo MEMS foi de 177 nW/m/s^2, enquanto o modelo obteve 224 nW/m/s^2. Isso resulta em um NPD de 1,3 mW/cm^3/g^2 para o protótipo e 1,6 mW/cm^3/g^2 para o modelo. Já em termos de F.o.M., obteve-se 0,9 mW Hz/cm^3/g^2 e 1,1 mW Hz/cm^3/g^2, para o protótipo e o modelo, respectivamente. O protótipo MM tem um volume ativo de 4,5 cm^3, mas poderia ser tão baixo quanto 1,8 cm^3 se uma massa de tungstênio fosse usada. A máxima potência normalizada do dispositivo é de 433 µW/m/s^2, resultando em um NPD de aproximadamente 9,2 mW/cm^3/g^2, mas poderia ser tão alto quanto 23,4 mW/cm^3/g^2 com uma massa de tungstênio. A largura de banda do dispositivo é de 1,45 Hz, resultando em uma F.o.M. de 13,4 mW/cm^3/g^2 para a massa sísmica de aço e 34,0 mW/cm^3/g^2 se a massa de tungstênio for usada.

A comparação do desempenho dos protótipos MM e MEMS revelou a superioridade do primeiro em termos de NPD e F.o.M. Embora o uso de um material com um coeficiente piezoelétrico mais alto possa aumentar o desempenho do dispositivo MEMS, o material piezoelétrico em de grande espessura tende a ter um coeficiente piezoelétrico mais alto (SONG et al., 2017), o que implica que processos comuns de deposição de filmes finos de PZT resultaria em uma pequena melhoria no NPD do dispositivo. Uma alternativa para melhorar o protótipo MEMS seria a introdução de não-linearidades, como um limitador mecânico, para mitigar os excessivos estresses gerados na ressonância e aumentar a largura de banda.

O protótipo MM, por outro lado, demonstrou maior robustez devido à sua estrutura maior facilitando a ressonância em frequências mais baixas. Além disso, o acoplamento eletromecânico maior permitiu uma largura de banda maior, favorecendo o F.o.M. do dispositivo. O NPD também foi significativamente melhorado pelo processo de fabricação de microusinagem, e o uso de filmes piezoelétricas disponíveis comercialmente proporcionou uma solução fácil para a fabricação de PVEHs bimorfos. Em comparação, os processos MEMS exigiam maior complexidade para fabricar tais dispositivos.

Considerações Finais

Esta dissertação apresenta um processo detalhado de projeto, otimização, prototipagem e validação de dois PVEHs, utilizando duas técnicas de fabricação diferentes. Apesar das limitações impostas por cada abordagem, a metodologia levou ao desenvolvimento de dois dispositivos com métricas competitivas, indicando que o processo de otimização pode levar a um desempenho excepcional apesar das limitações dos modelos numéricos. O PVEH MEMS obteve bom desempenho em termos de NPD, mas fica aquém em termos de F.o.M., enquanto o PVEH MM apresentou bom desempenho em ambas as métricas.

O trabalho destaca a importância de especificar corretamente a função objetivo ao otimizar PVEH em termos de NPD, enfatizando a necessidade de considerar fatores como tensão máxima e aceleração ótima. A função objetivo deve ser projetada para diminuir a tensão o máximo possível, uma vez que a tensão no material piezoelétrico é uma restrição significativa para o processo de otimização. Além disso, técnicas para mitigação de tensão, como aumentar o amortecimento amortecimento ou introduzir batentes mecânicos,

podem ser implementadas para melhorar o desempenho de tais dispositivos.

Palavras-chaves: Micro usinado; MEMS; Piezoelétrico; Vibração; Baixa frequência; Otimização; Modelo numérico; Pequena escala; Manutenção.

Abstract

Condition Based Monitoring via vibration analysis is one of the main predictive methods used in industrial maintenance over the last few decades. Currently, the sensing used in this type of analysis has evolved to wireless sensors, which allow continuous measurements of equipment that were previously considered inaccessible to wired sensors. However, a major limitation for these technologies is the battery life which is reduced under conditions of extreme temperatures, volume of monitored and processed data and frequency of use. This work presents the development of a piezoelectric energy harvester adapted for vibration monitoring sensors. A literature review is carried out to understand the technologies in energy harvesting and the optimization techniques available for the project execution. Then, the chosen methodology is presented, detailing the numerical models created, the parametric variables that will be optimized from the models and the algorithms that will be used as well as their settings. Different vibrational energy harvesters designs are tested taking two design fronts. One using MEMS manufacturing technology and the other using micro-machining fabrication techniques. Firstly, the project is carried out with the MEMS device, identifying at each step ways to improve the objective function of the optimization in addition to defining in which scenarios each one fits best. The micro-machining device makes use of the knowledge gained during the MEMS design to select the objective function. Two models are selected for prototyping and a model, that was not prototyped, were highlighted for its optimal performance predicted by the numerical model. The two selected models, are then fabricated following the previously chosen manufacturing method. After carrying out experiments, numerical models were validated, where the MEMS numerical model showed greater accuracy while the micro-machined one showed some deviations. However, in terms of performance, the micro-machined device was significantly superior to the MEMS device, even positioning itself among the best in the literature, especially for devices with low natural frequency and small volume.

Keywords: Micromachined; MEMS; Piezoelectric; Vibration; Low frequency; Optimization; Numerical model; Small-scale; Maintenance.

List of Figures

List of Tables

LIST OF ABBREVIATIONS AND ACRONYMS

EH	Energy Harvester
VEH	Vibrational Energy Harvester
MEMS	Microelectromechanical Systems
MM	Micro-Machining
PVEH	Piezoelectric Vibrational Energy Harvesters
IC	Integrated Circuits
PZ	Piezoelectric
EM	Electromagnetic
ES	Electrostatic
EMVEH	Electromagnetic Vibrational Energy Harvesters
NP	Normalized Power
DoF	Degree of Freedom
NPD	Normalized Power Density
F.o.M.	Figure of Merit
NdFeB	Neodymium Iron Boron
EVEH	Electrostatic Vibrational Energy Harvesters
SS430	Ferritic Stainless Steel
KNN	$(K,Na)NbO_3$
PZT	Lead Zirconate Titanate
AlN	Aluminum Nitride
PTFE	Polytetrafluoroethylene
DE	Differential Evolution
NM	Nelder-Mead
SO	Surrogate Optimization
FEM	Finite Element Method
RBF	Radial Basis Function
BC	Boundary Conditions
LDV	Laser Dopler Vibrometer

DAQ	Data Acquisition
RIE	Reactive Ion Etching
DRIE	Deep Reactive Ion Etching
FRF	Frequency Response Function

LIST OF SYMBOLS

$f_{\mathrm{n},1}$	First natural frequency
NP	Normalized power
P	Power
$\ddot{x}_{\mathrm{b}}$	Acceleration of the base
ξ_{e}	Electrical damping
ξ_{m}	Mechanical damping
$\omega_{\mathrm{n},1}$	First natural angular frequency
m_{eq}	Equivalent mass
V_{work}	Working volume
V_{active}	Active volume
V_{gap}	Gap volume
$\mathrm{NPD}_{\mathrm{a}}$	Area normalized power density
A_{active}	Active area
NPD	Normalized power density
B	Half-power bandwidth
e_{31}	Transverse piezoelectric coefficient in the stress-charge form
d_{33}	Longitudinal piezoelectric coefficient in the strain-charge form
Q	Quality factor
ξ	Total damping ratio
$\boldsymbol{D}$	Vector of electric displacement
$\boldsymbol{\delta}$	Strain vector
$\boldsymbol{E}$	Electric field
$\boldsymbol{\sigma}$	Stress vector
$\boldsymbol{\varepsilon}^{\boldsymbol{\sigma}}$	Matrix of dielectric permittivity at constant stress
$\boldsymbol{d}$	Matrix of piezoelectric coefficients
$\boldsymbol{s}^{\mathbf{E}}$	Elastic compliance matrix at constant electric field
d_{31}	Transverse piezoelectric coefficient in the strain-charge form
k_{31}	Transverse electromechanical coupling coefficient

k_{33}	Longitudinal electromechanical coupling coefficient
ε_r	Relative permittivity
s_{33}^E	Longitudinal compliance coefficient
f_obj	Objective function
l_i	Lower boundary
u_i	Upper boundary
$X_\mathrm{i,G}$	Representation of a member from DE optimization
$V_\mathrm{i,G}$	Representation of a mutant vector from DE optimization
PN	Population number
F	Scale factor
CR	Mutation factor
ρ_NM	Reflection coefficient
X_NM	Expansion coefficient
λ_NM	Contraction coefficient
σ_NM	Shrinkage coefficient
f_merit	Merit function
$\mathrm{NPD}_\mathrm{goal}$	NPD goal
B_req	Bandwidth requirement
P_req	Power requirement
V_req	Volume requirement
$\ddot{x}_\mathrm{opt}$	Optimum acceleration
ρ	Material density
V_t	Voltage in terminal
R_l	Resistive load
η	Structural damping
Z_l	Impedance load
C_p	Capacitance of piezoelectric
I_p	Current generated by piezoelectric material
W_sm	Seismic mass width
W_b	beam width
W_pz	Width of piezoelectric material
E_el	Electrode width
$W_\mathrm{b+}$	Increment to base width

L_{sm}	Length of seismic mass
L_{b}	Length of beam
L_{pz}	Length of piezoelectric material
L_{el}	Length of electrode
T_{sm}	Thickness of seismic mass
T_{b}	Thickness of beam
T_{pz}	Thickness of piezoelectric material
T_{el}	Thickness of electrode
$L_{\mathrm{b,i}}$	Length of the i^{th} beam
$L_{\mathrm{sm,i}}$	Length of the i^{th} seismic mass
r_{c}	Radius of the central seismic mass
$\theta_{\mathrm{b,i}}$	Angle of the i^{th} beam + seismic mass
$\boldsymbol{\varepsilon_r^{\sigma}}$	Matrix of relative permittivity at constant stress
$\boldsymbol{e}$	Matrix of piezoelectric coefficients in stress-charge
$\boldsymbol{c}^{\mathbf{E}}$	Elasticity matrix
$\boldsymbol{\varepsilon}_{\mathbf{r}}^{\boldsymbol{\delta}}$	Matrix of relative permittivity at constant strain
$\boldsymbol{\varepsilon}^{\boldsymbol{\delta}}$	Matrix of permittivity at constant strain
ε_0	Vacuum permittivity
$\mathscr{V}_{\mathrm{f}}$	Volume fraction of fibers
$f_{\mathrm{obj,pen}}$	Penalized objective function
$L_{\max}$	Maximum allowed length
$\sigma_{\mathrm{max,pz}}$	Maximum Von-mises stress in the piezoelectric film
σ_{limit}	Maximum allowed stress
R_{eq}	Equivalent resistance
m_{eq}	Equivalent mass
b_{m}	Mechanical damping coefficient
k_{sp}	Equivalent spring constant
d_i	Mechanical stopper position
z_1	Ratio of vertical force to stress
z_2	Ratio of stress to vertical displacement
φ_i	Angle of contact between seismic mass and stopper

CONTENTS

CHAPTER 1

INTRODUCTION

1.1 CONDITION-BASED MAINTENANCE

The machinery maintenance sector broadly presents, three approaches on how to and when to carry out the maintenance of specific equipment. These approaches are corrective, preventive, and predictive maintenance. Although each alternative can bring advantages and disadvantages, with the improvements in monitoring techniques, predictive maintenance has become the best maintenance strategy in most cases (RANDALL, 2010). Industries with high-cost machines or machines that must run for long periods without downtime are examples of sectors in which predictive maintenance is essential.

The predictive maintenance technique can predict the condition of a machine from several indicators, and can analyze vibrations, particles in the lubricant, temperature, or even machine efficiency. Vibration monitoring is the most prevalent method for condition monitoring (RANDALL, 2010). Vibration data from machinery are measured and analyzed to make predictions about their health, and for that, vibration sensors such as accelerometers, speed transducers, and proximity sensors are used. The most common for condition monitoring are piezoelectric accelerometers, as they have a broad working range in terms of vibration amplitude and frequency (RANDALL, 2010). These can be used in continuous measurements with systems permanently fixed to one place, where long cables must be carefully positioned to avoid interfering with the operation of the machines. Likewise, they can be used in routine intermittent measurements performed with a single accelerometer and vibration collector, where the inspector must go by each machine at once.

Continuous measurements used to be applied only to high-cost machines or those critical for factory operation, whereas intermittent measurements had a much lower cost and allowed for a detailed analysis of vibration signals. However, it was not recommended to identify sudden breaks. In both cases, some disadvantages can be mitigated using wireless sensors such as Dynamox's Dynalogger®. The Dynalogger is a wireless triaxial vibration and temperature sensor, approximately 53 cm^3, with a battery life of 3 to 5 years, depending on the usage (DYNAMOX®, 2021). Compact and wireless devices with greater autonomy, such as this one, allow great versatility in use, as they eliminate connection problems between accelerometers and vibration collectors caused by defects or cable misuse. It removes the need for people to carry out field inspections, which increases worker safety, allows the monitoring of machines in spaces inaccessible to humans or where the use of cables is not feasible, and data collection continues instead of en route and periodic measurements. However, the absence of wires requires the sensor to be powered by a battery which limits the sensor's lifespan compared to wired sensors.

The longevity of electronic devices such as wireless sensors is directly linked to the electrical consumption of their components. Microdevices have recently experienced a major technological breakthrough that has caused a rapid reduction in electrical consumption, thus increasing the lifespan of such devices. In addition, this reduction allows new alternatives to extend the life of electronic equipment to be investigated. This makes it possible to replace or complement traditional batteries that power devices such as vibration sensors with various methods of capturing energy from the environment (GAMMAITONI, 2012). This compilation of devices called Energy Harvesters (EH) rely on the availability of different forms of energy in the environment, such as solar, thermal, chemical, and mechanical energy (SELVAN; MOHAMED ALI, 2016). EHs that harvest vibrational energy have the advantage of being sustainable, stable, and small (KHALIGH; PENG ZENG; CONG ZHENG, 2010). Mechanical energy can be scavenged from various sources, such as industrial machinery and equipment, vehicles, human movement, and fluids (ZOU et al., 2019).

In this work, the vibration of the machines was the energy source of interest. Therefore, EH alternatives are proposed to capture energy from vibrations or the so-called Vibration Energy Harvester (VEH) to increase the useful life of sensors for vibration monitoring used in predictive maintenance. Wireless sensors for vibration monitoring usually have compact dimensions and an average power consumption of around 100 µW (GAMMAITONI, 2012). On the other hand, even under good conditions, industrial machinery has most of its vibrational energy on the range of approximately 40 Hz to 200 Hz (AKTAKKA; PETERSON; NAJAFI, 2012). Thus, developing a compact energy harvesting system capable of delivering energies on the order of 100 µW or more and working at low frequencies is a technological challenge and an alternative of great interest to the monitoring industry. Thus, this work demonstrates the development of a VEH using piezoelectricity as a form of transduction (to achieve small sizes efficiently) using two different fabrication technologies. Microelectromechanical Systems (MEMS) technology and Micro-Machining (MM). These devices should operate at approximately 60 Hz. Thus, it can operate at the same frequency as the power grid. In addition, it should have an optimized power-to-volume ratio and be capable of supplying 160 µW to match the consumption of a wireless sensor and fit within the limits of a standard 7.7 mm x 25.5 ⌀ mm battery. For this purpose, the merits of each transduction principle used in VEHs are reviewed to determine the advantages and disadvantages of each type. A three-dimensional numerical model in COMSOL (COMSOL MULTIPHYSICS® V. 5.6, n.d.) was proposed and coupled to an optimization algorithm implemented in MATLAB by Mathworks™ (BUEHREN, 2014). This work offers two distinct approaches to developing Piezoelectric Vibrational Energy Harvesters (PVEH), presents strengths and weaknesses during the process, and offers viable design options that meet the requirements shown in Table 1.1. The requirements are a set of goals that should allow the PVEH full autonomy to a device, such as wireless sensors for vibration monitoring.

Table 1.1 – Project requirements.

Project requirements	Numeric goal
Low frequency	60 Hz
High power	160 µW
Small volume	7.7 mm x 25.5 ⌀ mm or 3.93 cm^3
Large bandwidth	20 Hz

1.2 OBJECTIVES

The global objective of this work is to execute two complete cycles of design, optimization, prototyping, and validation using two different fabrication technologies (MEMS and MM) to comply with the requirements of a PVEH for wireless sensors for vibration monitoring.

1.3 SPECIFIC OBJECTIVES

The specific goals are:

- Develop PVEHs numerical models using available information from the literature;
- Optimize the PVEH's designs using COMSOL with a MATLAB integrated algorithm;
- Prototype a device capable of validating the numerical designs developed in this work;

- Conduct an experimental analysis of the fabricated devices to determine their performance and validate the numerical model;
- Compare the different methods highlighting each approach's merits and compare them with other devices from the literature.

1.4 DOCUMENT OUTLINES

The document is divided into 6 chapters titled:

1. Introduction;
2. Literature review;
3. Methodology;
4. Optimization results;
5. Experimental analysis;
6. Final remarks.

In the first chapter, the problem tackled by this study is contextualized, and the requirements and objectives are presented. The second chapter reviews the literature and presents similar devices developed by other authors using different technologies and techniques. In addition, it describes the theoretical background in terms of the physical behavior, available technologies, and optimization techniques needed for this project. It displays a quick overview of commercially available devices to understand where the market stands today. The chapter concludes with a summary of the vital information gathered from the review. Chapter three displays the methodology used to develop the PVEHs. The numerical modeling, optimization setup, and experimental procedure are described. Chapter four shows the results of the optimizations and discusses the adjustments necessary to improve the devices until designs feasible for fabrication and validation are obtained. The next chapter (five) overviews the fabrication process executed with a foundry and partner laboratory, following up on the experimental results compared with the numerical models and highlighting the appropriate adjustments. Finally, the sixth and the last chapters discuss the results of this work.

Chapter 2

Literature Review

This chapter explores the relevant literature in the Energy Harvesting (EH) field and the tools that can aid the development and optimization of EH devices. The review begins with a discussion of the various EH transduction types and the merits of each, followed by a description of some relevant devices in the literature and available on the market. The review ends with an overview of some of the optimization tools used in this work and the metrics used to classify each design.

2.1 ENERGY HARVESTERS IN LITERATURE

The most common devices in the literature utilize Piezoelectric (PZ), Electromagnetic (EM), or Electrostatic (ES) transduction(DHADWAL; RASTEGAR, 2017). Nevertheless, there are other forms of transduction, such as magnetostriction (YANG; TAN; ZU, 2017) and triboelectricity (YANG; CHEN, et al., 2014). Dhadwal and Rastegar (2017) gathered four of these transduction principles and qualitatively highlighted the advantages and disadvantages of each for energy harvesting. Table 2.1 summarizes his review. According to him, piezoelectric EHs have advantages over electromagnetic regarding of its simple structure and capability for MEMS technology. Micro Electromechanical Systems or MEMS is a process used to create tiny integrated devices or systems that combine mechanical and electrical components using the fabrication processing techniques of Integrated Circuits (IC) and can range in size from a few micrometers to millimeters (PRIME FARADAY PARTNERSHIP, 2002). Electromagnetic transduction for VEH is a well-established technology as described in Section 2.4, where the available commercial devices are reviewed. Nevertheless, Electromagnetic Vibrational Energy Harvesters (EMVEH) are difficulty to integrate with MEMS because of their permanent magnets and pick-up coils, which are difficult to fabricate using current manufacturing techniques. Moreover, when miniaturizing EMVEHs, their efficiency tend to decrease compared to other transductions (DHADWAL; RASTEGAR, 2017).

Roundy, Leland, et al. (2005) and Roundy and Wright (2004) made a quantitative comparison in terms of energy storage density for each of the main transduction. The analysis presented two calculation approaches: aggressive and practical. The aggressive approach considers what is theoretically possible, whereas the practical approach represents what is possible using the technology available at the time of the article's publication (2005). At the time of the study, piezoelectric transduction presented the most promising form of transduction in the practical scenario shown in Table 2.2, whereas electromagnetic transduction theoreticcally showed the best potential. However, it should be noted, that it is impossible to establish a clear and definitive comparison between the different types of transducers (BRIAND et al., 2015). Briand et al. (2015) point out that, theoretically, the power density of the EH does not depend on the volume of the device, but in practice, it reduces with the volume for all types of transductions. Thus, the author proposed a "rule of thumb" based on the desired device size. Electrostatic transducers are the most recommended for micrometer to millimeter scales. Piezoelectrics are suitable for millimeter to centimeter scales and small strain applications, and electromagnetic are better for large displacements at centimeter to decimeter scales.

Table 2.1 – Qualitative strengths and weaknesses of the four different types of EH transduction (Obtained from Dhadwal and Rastegar (2017))

Type	Advantages	Disadvantages
Piezoelectric	• No external voltage source • High output voltage • Compatible with MEMS • Simple structure	• Low output current • Low toughness • Low tensile strength * • Charge leakage ** • Depolarization and aging ***
Electrostatic	• Easy to integrate with MEMS • High output voltage • Function well at slow and fast displacement rates • High degree of miniaturization possible	• External voltage source needed (iv) • Low output current • Difficult to fabricate large capacitor surfaces
Electromagnetic	• No external voltage source • High output current • Well-established technology	• Difficult to integrate with MEMS - requires permanent magnet and pick-up coil • Low output voltage • Low output energy at slow speeds • Low output energy in small size
Magnetostrictive	• No external voltage source • No depolarization problem • Highly flexible films available (v)	• Difficult to integrate with MEMS - requires pick-up coil • Low output energy at slow speeds • Low output energy in small size • May needs biasing magnets

*It may need to be preloaded in compression if subjected to equal compressive and tensile loading.
**Makes it not suitable for applications with slow stain rates.
***Mainly for polymer and polycrystalline ceramic types at high temperature.
(iv)Unless a charged electret is used.
(v)Particularly, the amorphous metallic glass type (Metglas).

PVEH and EMVEH are the most noticeable types of transduction for energy storage, but this is one of the numerous metrics used to compare energy harvesting devices. To determine which of the two transduction principles (PZ or EM) is the most effective, Marin (2013) and Priya et al. (2019) plotted the Normalized Power (NP), which is given by Equation 2.1. Figure 2.1 illustrates this analysis. In this graph, EM devices show a meaningful advantage over PZ for volumes over ≈ 0.5 cm^3, whereas PZ dominates at smaller volumes. Marin (2013) and Priya et al. (2019) highlighted the ≈ 0.5 cm^3 region as a “transition zone” where there is no clear advantage between PZ and EM transduction. It is important to note that Marin (2013) and Priya et al. (2019) use NP $\cdot\, f_{\mathrm{n},1}$ as a metric because, generally, the available ambient energy is inversely proportional to the first natural frequency as demonstrated by (XU, 2012),

$$\mathrm{NP} = \frac{P}{\ddot{x}_{\mathrm{b}}^2} = \frac{\xi_{\mathrm{e}}}{4\omega_{\mathrm{n},1}\left(\xi_{\mathrm{e}}+\xi_{\mathrm{m}}\right)^2} m_{\mathrm{eq}}, \tag{2.1}$$

where P is the power harvested, $\ddot{x}_{\mathrm{b}}$ is the acceleration of the base to where the VEH is fixed, ξ_{e} is the electrical damping, ξ_{m} is the mechanical damping, $\omega_{\mathrm{n},1}$ is the first natural angular frequency, and m_{eq} is the one Degree of Freedom (DoF) equivalent mass of the system.

Other metrics can be used to compare and measure the performance of VEHs. These metrics can reference the geometrical aspects, power, and bandwidth. The geometrical metrics important to this work are the working volume V_{work}, active volume V_{active}, and gap volume V_{gap}. V_{work} is defined as $V_{\mathrm{active}} + V_{\mathrm{gap}}$, where V_{active} is equal to the volume of a hexahedron that encompasses all components of the EH and V_{gap} is the volume of a hexahedron of the same length and width as of V_{active} but a height equal to the maximum displacement of the device, as illustrated in Figure 2.2.

Table 2.2 – Comparison of performances of VEHs in terms of energy storage (Obtained from Roundy, Leland, et al. (2005) and Roundy and Wright (2004))

Type	Practical maximum (mJ/cm^3)	Aggressive maximum (mJ/cm^3)	Equation
Piezoelectric	35.4	335	$(1/2)\sigma_y^2 k^2/2c$
Electrostatic	4	44	$(1/2)\varepsilon E^2$
Electromagnetic	24.8	400	$(1/2)B^2/\mu_0$

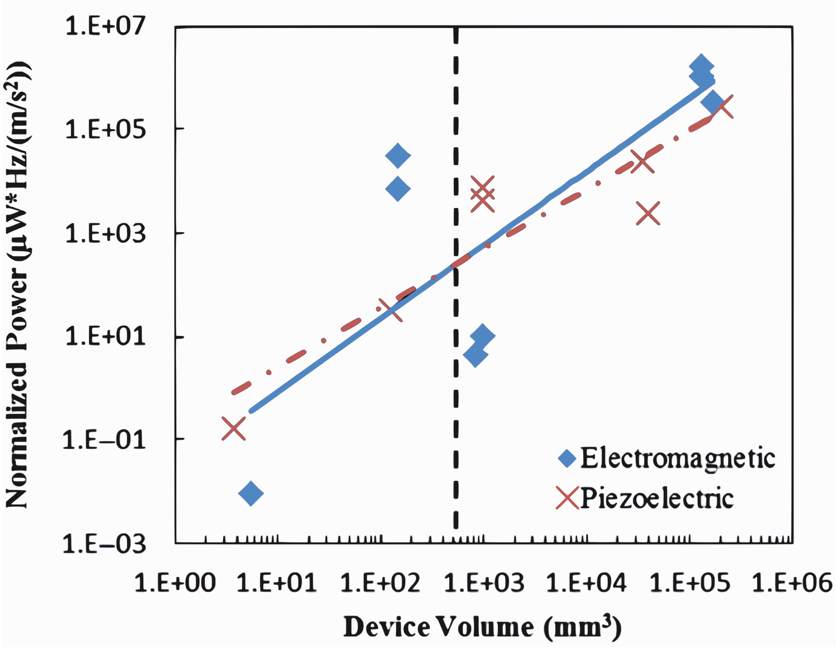

Figure 2.1 – Performance comparison of EMVEHs and PVEHs in terms of $\mathrm{NP} \cdot f_{\mathrm{n},1}$ (Obtained from Marin (2013))

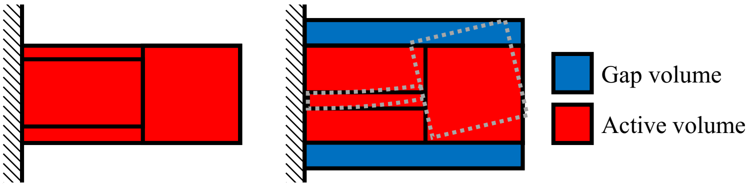

(a) Top view. (b) Side view.

Figure 2.2 – Illustration of how active and gap volume are calculated.

In terms of power, there are four important metrics to highlight. The Normalized Power is given by Equation 2.1. The Normalized Power Density (NPD) based on the area, which is given by

$$\mathrm{NPD_a} = \frac{P}{A_{\mathrm{active}}\ \ddot{x}_{\mathrm{b}}^2}, \tag{2.2}$$

where A_{active} is an area analogous to the volume V_{active}. The volumetric NPD referred to in the entirety of this text as just NPD is given by

$$\mathrm{NPD} = \frac{P}{V_{\mathrm{active}}\ \ddot{x}_{\mathrm{b}}^2}. \tag{2.3}$$

Finally, the Figure of Merit (F.o.M.) can be defined as

$$\mathrm{F.o.M.} = \mathrm{NPD} \cdot B, \tag{2.4}$$

where B denotes the half-power bandwidth of the device. Finally, it is also essential to target the optimal acceleration of the device, e.g., the acceleration amplitude on which it will be developed to work or the amplitude of which it best performs. Above its optimal excitation point, the device may lose efficiency due to nonlinear behavior. In addition, every device has an acceleration limit due to electromagnetic, electrical, mechanical limitations, etc. These restrictions establish another important metric, denoted as the device's dynamic range.

2.1.1 Electromagnetic Energy Harvesters

The first set of VEHs from the literature reviewed here are the Electromagnetic EHs. An EMVEH converts mechanical energy into electricity by creating a relative motion between a permanent magnet and coil. The magnetic field of the magnet cuts through the coil, and the relative movement causes the magnetic field to change over time, creating a magnetic flux that introduces voltage into the coil, according to Faraday's law of electromagnetic induction (BATRA; ALOMARI, 2017). Beeby et al. (2007) and Torah et al. (2007) developed the devices Mk2 and Mk3 presented in Figure 2.3, respectively. These devices are based on a cantilever structure with a Neodymium Iron Boron (NdFeB) magnet bonded to the beam's free end and a stationary coil positioned between the magnets. These devices have outstanding NPDs of 85 mW/cm^{3}g^2 and 103 mW/cm^{3}g^2, respectively. Both have an active volume of 0.15 cm^3, an optimal acceleration of 0.6 m/s^2, and a first natural frequency of 52 Hz. Mk3 can deliver 120 µW$_{\mathrm{rms}}$ at its maximum deflection. A small bandwidth of 0.26 Hz is one of the main drawbacks of MK2 (AYALA-GARCIA et al., 2010). A narrow bandwidth can become a problem because the available vibrational energy might vary in its frequency from source to source and in time. This problem can be addressed with the broadband techniques discussed in Section 2.3, however, depending on the technique, there can be drawbacks. Here, the F.o.M. is used to measure the device's performance by considering the bandwidth. For Mk2, the F.o.M. was 22 mW Hz/cm^{3}g^2.

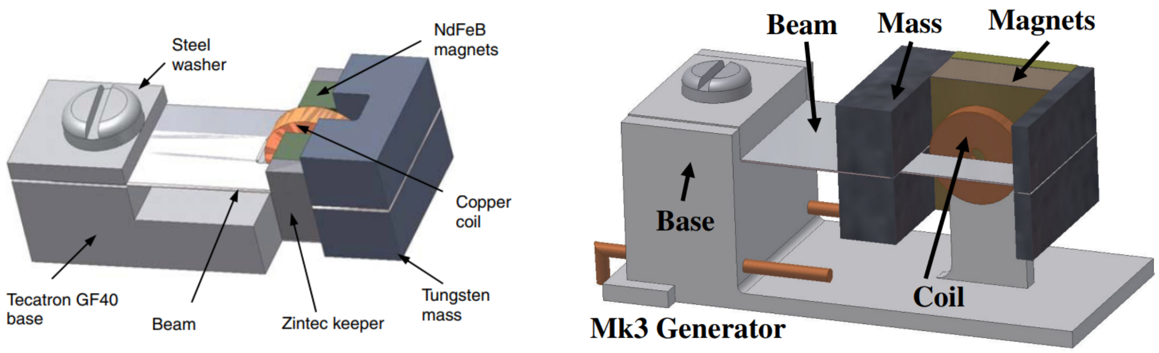

(a) Mk2 Generator. (b) Mk3 Generator.

Figure 2.3 – Drawing of EMVEHs Mk2 and Mk3 (Obtained from Torah et al. (2007)).

Perpetuum is a manufacturer that produced the PMG energy harvester (Figure 2.4). According to the company, the harvester could produce 1.2 mW at an acceleration of 0.025 g with a half-current bandwidth of 1.6 Hz (PERPETUUM LTD., 2013). The volume, considering a cylinder surrounding the case but ignoring the connector, was 253 cm^3. The device has two nominal voltages (5V and 8 V) with six different $f_{\mathrm{n},1}$ (25 Hz, 30 Hz, 50 Hz, 60 Hz, 100 Hz, and 120 Hz). With these metrics, the NPD is 7.6 mW/cm^{3}g^2 (considering the volume of the case that is the working volume) and F.o.M. of 12 mW Hz/cm^{3}g^2 (considering the half current bandwidth). Beeby et al. (2007) provide data from a different Perpetuum model, the PMG7. This model has an $f_{n,1}$ = 100Hz power output of 4 mW at a 0.4 m/s^2 acceleration with a volume of 30 cm^3. Therefore, this model has a total NPD of 80 mW/cm^{3}g^2.

Figure 2.4 – Perpetuum's PMG (Obtained from Perpetuum Ltd. (2013)).

As previously discussed, the miniaturization of EMVEHs is complex, and MEMS technology is unsuitable for this type of transduction. In response to this challenge, Ching et al. (2002) proposed the use of micromachining techniques to manufacture an EMVEH at MEMS scales. A copper spring laser-cut in a spiral configuration, and a rare-earth magnet NdFeB was later attached to the center. The stationary coil is fixed to the rigid housing of the device. Figure 2.5 shows pictures of the vibration modes of the VEH. The 1 cm^3 device can generate up to 830 µW at 100 Hz under 200 µm amplitude vibration. In most cases, multimodal EHs are built to cover the highest frequency band, possibly to the detriment of maximum power. Therefore, it is unreasonable to compare the device with other single-resonance devices in terms of the NPD. All things considered, vibration of 200 µm at 100 Hz renders an acceleration of approximately 8.1 g, providing an NPD of 0.01 mW/cm^3g^2.

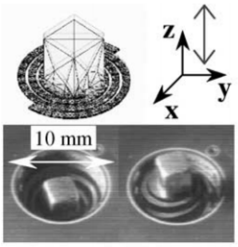

Figure 2.5 – Modes of vibration of Ching's device (Obtained from Ching et al. (2002)).

Yuen et al. (2007) used MEMS electroplating techniques to build a spiral copper spring with an N45-grading magnet attached to the middle of the spring and a stationary coil fixed to the housing (Figure 2.6). For low-frequency, small-size, vibration-based EMVEHs, mechanical design based on a spiral spring, a magnet in the middle, and a coil at the housing is regularly used (CEPNIK; LAUSECKER; WALLRABE, 2013). His device has a volume of 2.262 cm^3, an output power of 120 µW at 4.63 m/s^2 of acceleration at resonance (80 Hz), giving an NPD of 0.2 mW/cm^3g^2.

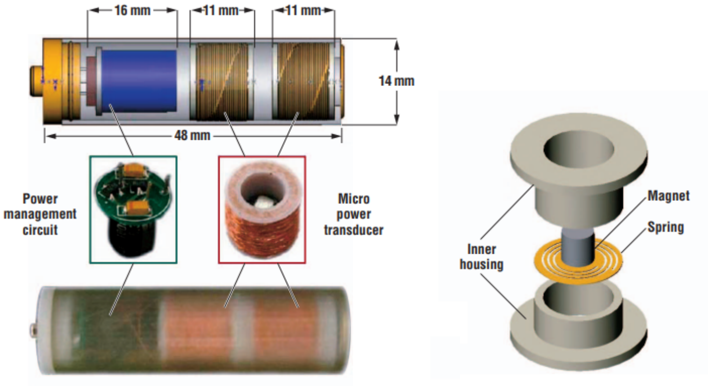

Figure 2.6 – Illustration of Yuen's device (Obtained from Yuen et al. (2007)).

Although challenging, some authors have developed EMVEHs using MEMS technology to fabricate an entire device. Peihong Wang et al. (2009) developed the EH in Figure 2.7 by separately processing the spring and the coil. The magnet was then attached to a spring that was stacked over the coil. Because MEMS technology was used for most of the fabrication, the final device's volume was small (0.13 cm^3), generating 0.7 µW at 4.94 m/s^2 at resonance (94.5 Hz). Finally, its NPD was 0.02 mW/cm^3g^2. It is essential to note that the device was not optimized; however, the final NPD illustrates the challenges in using MEMS technology to build EMVEHs.

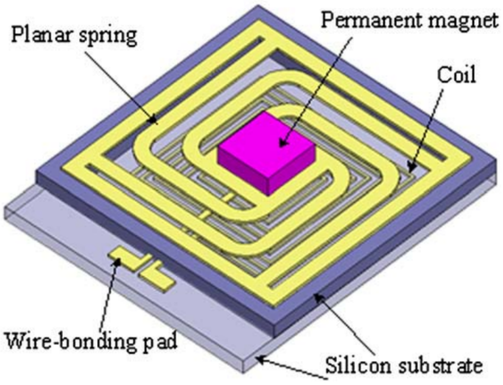

Figure 2.7 – Illustration of Wang's device (Obtained from Peihong Wang et al. (2009)).

2.1.2 Electrostatic Energy Harvesters

Electrostatic Vibrational Energy Harvesters (EVEHs) are structures with variable capacitance. A relative motion between the two plates creates a varying capacitance that causes surface charges from the plates to move to a storage device as the capacitance decreases. In this way, the mechanical energy from the moving plates is converted into electrical energy (BATRA; ALOMARI, 2017). Despesse et al. (2005) chose an in-plane gap closing electrode design of macro-scale, fabricated by electrical discharge matching of tungsten (Figure 2.8). The tungsten device has a volume of 18 cm^3, a resonant frequency of 50 Hz, and is capable of delivering 1.052 mW of power with 90 µm of amplitude vibration at resonance, rendering an acceleration of 0.9 g. The NPD of this device was 0.07 mW/cm^3g^2.

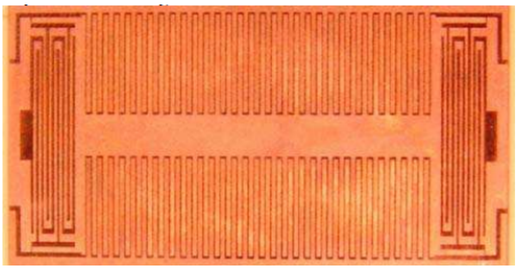

Figure 2.8 – Despesse tungsten electrostatic device (Obtained from Despesse et al. (2005)).

Altena et al. (2013) used MEMS technology to develop a micro-scale 3-terminal transducer built from a stack of 3 wafers. Figure 2.9 shows, from left to right, a simplified lumped parameter diagram of the device, the components of the EVEH, and a picture of the finished prototype. His work generated a device capable of generating 495 µW with 2.5 g of acceleration at a resonance of 1187 Hz. The overall volume of the device was not supplied; however, the footprint was 1 cm^2. Rendering an area NPD of approximately 0.08 mW/cm^2g^2, MEMS devices tend to have small thicknesses, usually submillimeters, putting this device on the order of ≈ 1 mW/cm^3g^2 NPD. These EVEHs exemplify the advantage of electrostatic devices have in terms of miniaturization capabilities when compared to other transductions. Nevertheless, the NPD shown by these devices is significantly smaller than EMVEHs and PVEHs.

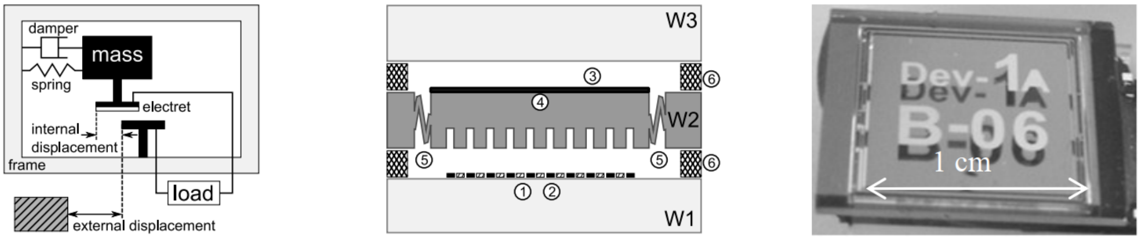

Figure 2.9 – MEMS EVEH of Altena et al. (Obteined from Altena et al. (2013)).

2.1.3 Piezoelectric Energy Harvesters

Piezoelectric energy harvesters utilize a class of material that can accumulate electrical charges in response to applied mechanical stress (TIAN et al., 2018). Therefore, electrical energy is transformed from mechanical energy used to deform the piezoelectric material. Mitcheson et al. (2007) have shown that at milliliter scales, piezoelectric transduction provides the best output power density at low frequencies as compared to the other most common transduction. The first PVEH detailed in this study was developed by Tsujiura et al. (2013). They fabricated a cantilever-type harvester from Pt-coated ferritic stainless steel (SS430) and (K,Na)NbO_3 (KNN) using MEMS technology (Figure 2.10). The measured piezoelectric coefficient e_{31} was -3.8 C/m^2. The geometry is a simple rectangular beam with a seismic mass on the tip (both made from SS430), with KNN deposited on one side of the beam. The prototype is 7.5 mm x 5 mm x 0.3 mm, resulting in an active volume of 0.01125 cm^3. The maximum output power was 1.6 µW with 10 m/s^2 of acceleration and a resonance of 393 Hz. The NPD of this device was 0.14 mW/cm^3g^2. The half-power bandwidth of the device is 4.3 Hz rendering an F.o.M. of 0.6 mW Hz/cm^3g^2. It is important to note that this device presented a nonlinear resonant frequency attributed to the softening stiffness effect, which can increase the bandwidth of the device without compromising the maximum power (RAMLAN et al., 2010).

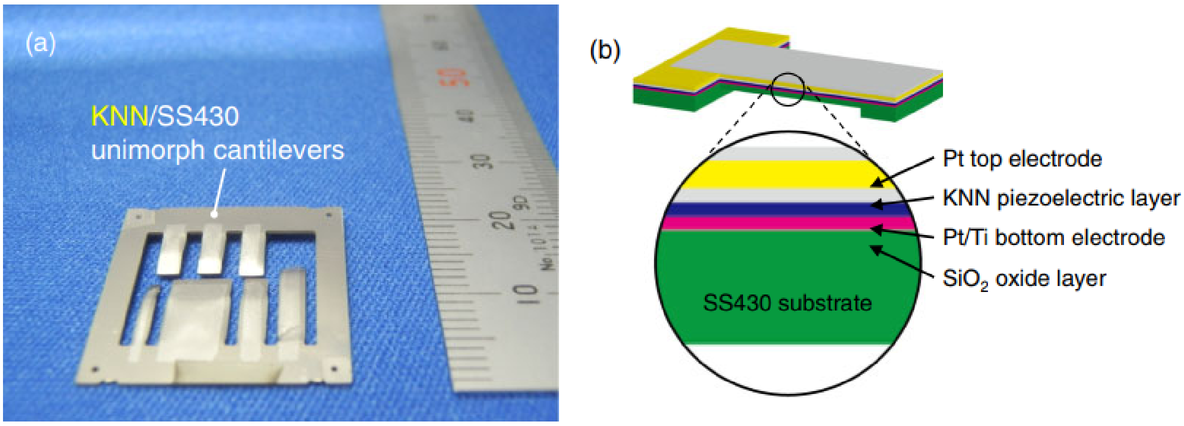

Figure 2.10 – Device of Tsujiura et al. (a) Picture of the unimorph cantilever devices and (b) diagram of the construction of the device (Obtained from Tsujiura et al. (2013)).

Song et al. (2017) used a spiral design (Figure 2.11) to reduce the natural frequency of the device. The authors used COMSOL to model a Lead Zirconate Titanate (PZT) based device and studied its behavior. The spiral design concentrated most of its stress on the merging curvature rather than the center of the spiral. Hence, the stress distribution on the inside edge is much larger than that on the outside edge. The power output of a PVEH is proportional to the square of stress (Described in Appendix A). Thus, the poor distribution of the stress field compromises the PVEH efficiency. Song et al. (2017) investigated the effects of the number of spiral turns on the natural frequency, and the best power output was formed from the five-turn spiral with resonance at 68 Hz. The piezoelectric coefficient d_{33} was measured to be 155 pC/N, and the power was 23.3 nW at 0.25 g with an active volume of 0.11 mm^3. Therefore, the NPD was 3.39 mW/cm^3g^2.

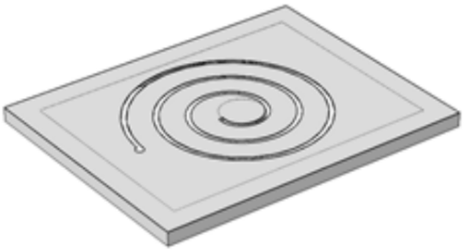

Figure 2.11 – Spiral MEMS PVEH by Song et al. (Obtained from Song et al. (2017)).

Sharpes, Abdelkefi, and Priya (2015) took a different approach to achieve a low-frequency PVEH. The author investigated three different hand-assembled designs (Figure 2.12) denominated as Zigzag shown in Subfigures (a,b,c,d), Flex (e,f,g,h), and Elephant (i,j,k,l). All the structures were made of mild steel and a piezoelectric layer from the American Piezoceramics APC850 PZT. The optimized devices were confined to an area of 25.4 mm x 25.4 mm, and the neodymium magnets were 6.35 mm x 3.175 mm x 3.175 mm. Assuming that the thickness of the beam was negligible, the active size of all three devices was 2 cm^3. Under 0.1 g of acceleration, the zigzag, flex, and elephant showed a maximum power output of 2.93 µW, 32.2 µW, and 81.3 µW, respectively. Which makes an NPD of 0.14 mW/cm^{3}g^2, 1.58 mW/cm^{3}g^2, and 3.97 mW/cm^{3}g^2, respectively. The bandwidth can be calculated from the available damping ratio using,

$$Q = \frac{f_{\mathrm{n},1}}{B} \tag{2.5}$$

and

$$Q = \frac{1}{2\,\xi} \tag{2.6}$$

where Q is the quality factor and ξ is the viscous damping loss factor. Zigzag, flex, and elephant have damping ratios equal to 0.00611, 0.00365, and 0.00374, and natural frequencies at 65.6 Hz, 62.0 Hz, and 68.125 Hz, respectively. Therefore, the bandwidths are approximately 0.80 Hz, 0.45, and 0.51 Hz, for an F.o.M. of 0.1 mW Hz/cm^{3}g^2, 0.7 mW Hz/cm^{3}g^2, and 2.0 mW Hz/cm^{3}g^2, respectively.

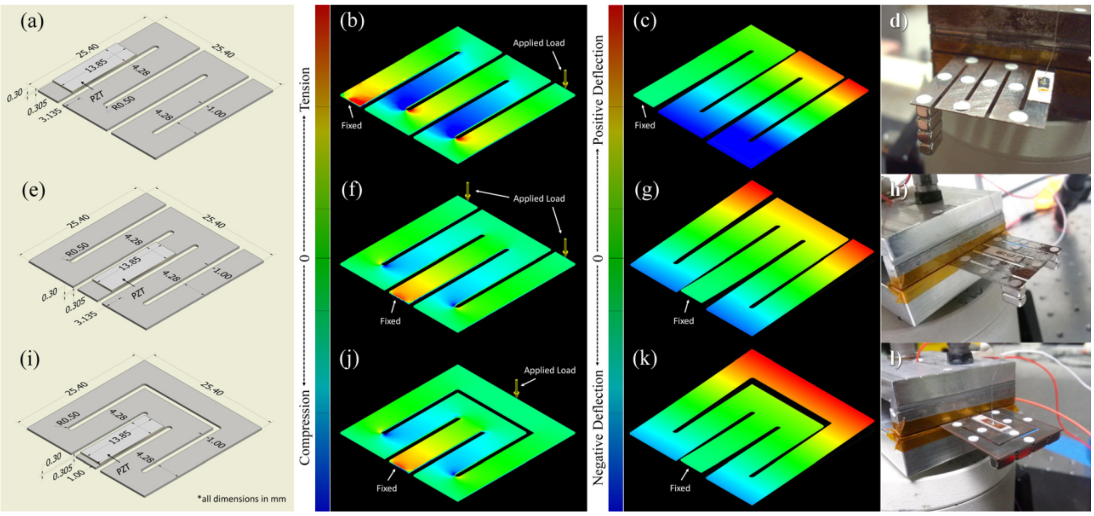

Figure 2.12 – Dimensioned drawing (a), (e) and (i), finite element stress analysis for first bending mode (b), (f) and (j), first mode shape (c), (g) and (k), and picture of the fabricated device in test setup (d), (h) and (l) for zigzag (a)–(d), Flex (e)–(h), and Elephant (i)–(l), respectively (Obtained from Sharpes, Abdelkefi, and Priya (2015)).

Elfrink et al. (2010) worked on a low-frequency unimorph cantilever-type energy harvester with Aluminum Nitride (AlN) as the piezoelectric material and used a vacuum-packaged encapsulation to reduce mechanical loss to the air. The active volume of the device was 0.015 cm^3 (AKTAKKA; PETERSON; NAJAFI, 2012). Output power at resonance with an acceleration of 0.2 g is 1.46 µW under atmospheric pressure and 6.9 µW under a vacuum of 1 mbar. The quality factor from an unpackaged device under atmospheric pressure and vacuum level was measured as 256 and 560, whereas the natural frequency shifted from 596.8 Hz to 598.7 Hz, respectively. Using Equation 2.5, the bandwidths were 2.3 Hz (at atmospheric pressure) and 1.0 Hz (under vacuum). Therefore, under atmospheric pressure, the device has a 2.4 mW/cm^{3}g^2 NPD and F.o.M. 5.7 mW Hz/cm^{3}g^2, whereas under vacuum the NPD is 11.5 mW/cm^{3}g^2 and F.o.M. is 11.5 mW Hz/cm^{3}g^2. Interestingly, although an increase in the output power is desired, it comes at the cost of the device's bandwidth. This work is an excellent example of how it is essential to include the bandwidth in the metrics to evaluate performance, i.e., from atmospheric pressure to vacuum, the performance in terms of NPD increased approximately 479%. However, in terms of F.o.M., the increase was only 216%.

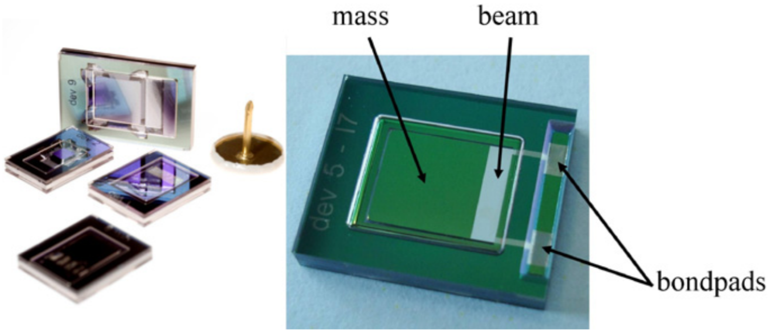

Figure 2.13 – Encapsulated vacuum-packaged device by Elfink et al. (Obtained from Elfrink et al. (2010)).

Roundy (2003) chose a hand assembly device using bulk off-the-shelf piezoelectric material PSI-5H4E from Piezo Systems Inc. Figure 2.14 shows the author's prototypes denominated as Design 1 and Design 2. Design 1 is a 6.5 mm x 3 mm x 0.381 mm beam with an 8.5 mm x 6.7 mm x 7.7 mm seismic mass of a tungsten alloy. Design 2 is a 10.7 mm x 3.2 mm x 0.381 mm beam with 17.3 mm x 3.6 mm x 7.7 mm seismic mass. The active volume of these devices was approximately 0.81 cm^3. The measured output power at 2.25 m/s^2 of acceleration for devices 1 and 2 were 207 µW and 335 µW, respectively. The final NPD was then 4.84 mW/cm^{3}g^2 and 7.81 mW/cm^{3}g^2. The estimated bandwidth of design 2 is 7 Hz. Thus, its F.o.M. was 54.7 mW Hz/cm^{3}g^2.

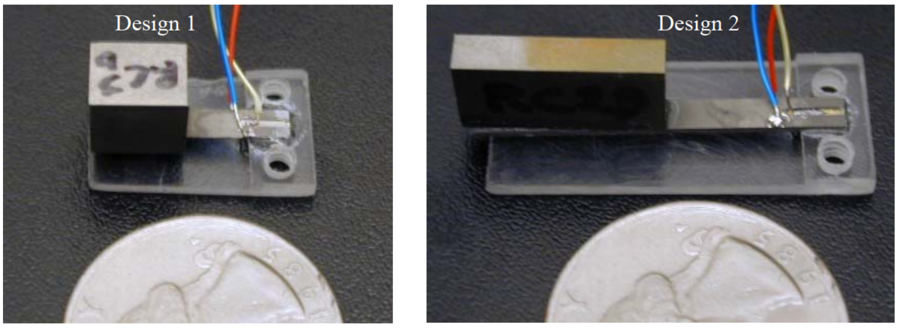

Figure 2.14 – Design 1 (left) and design 2 (right) from Roundy (Obtained from Roundy (2003)).

As seen by Roundy (2003), the use of bulk piezoelectric materials can significantly increase the performance of the device because their piezoelectric constants are larger than those of thin films (SONG et al., 2017). Durou et al. (2010) developed a PVEH using a 200 µm thick PZT-5H sheet bonded to silicon with epoxy using bulk piezoelectric materials with MEMS process combined with conventional packaging process and laser etching technologies. The device consists of four cantilevers sharing the same tungsten proof mass (Figure 2.15). The active volume of this device was 0.464 cm^3, an output power of 13.9 µW under 0.2 g of an acceleration at resonance of 76 Hz. The NPD of this device is 0.75 mW/cm^{3}g^2 with a bandwidth of 4.7 Hz (AKTAKKA; PETERSON; NAJAFI, 2012), rendering an F.o.M. of 3.5 mW Hz/cm^{3}g^2. The works of Roundy (2003) and Durou et al. (2010) highlight the use of off-the-shelf bulk piezoelectric materials with tools such as conventional packaging processes or micromachining techniques to fabricate

VEHs at the mesoscale. Although MEMS technology is a good option for miniaturization at the micrometer scale, micromachining and packaging processes may be advantageous at the milliliter scale. This is because of the higher piezoelectric constants of off-the-shelf materials and the manufacturability of larger structures.

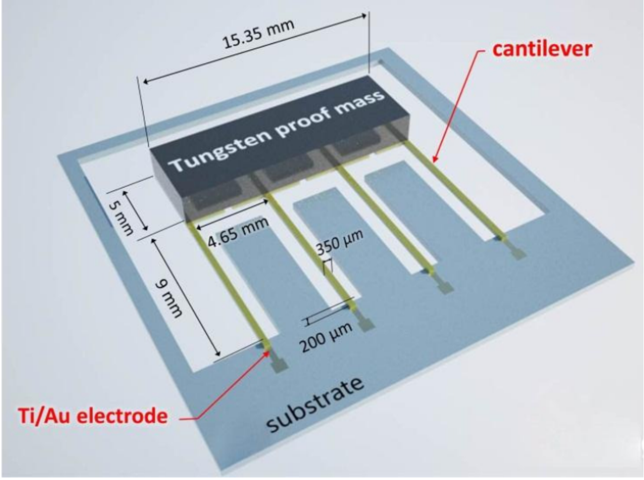

Figure 2.15 – Four beams, 200 µm bulk PZT of Durou et al. (Obtained from Durou et al. (2010)).

Finally, Aktakka, Peterson, and Najafi (2012) adopted an approach similar to that of Durou et al. (2010) utilizing bulk PZT, MEMS, and packaging processes but added a thinning step to the PZT, where the highly thick piezoelectric layer would be thinned down to an optimum designed thickness. The author devised five designs using three beam structures and two seismic mass materials. The beam structures were a bimorph of PZT/AuIn/PZT, a unimorph of PZT/Si, and another unimorph of PZT/AuIn. For all structures, the piezoelectric material was PZT-5A. The bimorph used a seismic mass of tungsten, whereas both unimorphs had designs with tungsten and silicon seismic masses. Figure 2.16 shows a picture of the PZT/Si design, which exhibited the best F.o.M. performance.

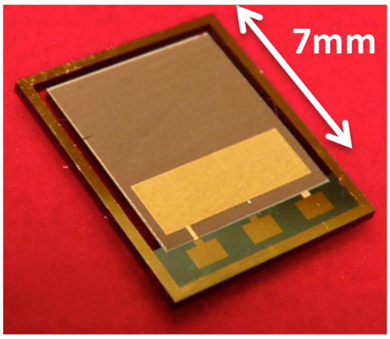

Figure 2.16 – Picture of unimorph PZT/Si design from Aktakka (Obtained from Aktakka, Peterson, and Najafi (2012)).

The unimorph PZT/AuIn is the first design of Aktakka, Peterson, and Najafi (2012), which has 12.1 mm^3 of the active volume. This beam structure has two different designs using a tungsten seismic mass or silicon. The power output at the resonance of 80.1 Hz and 263 Hz an under acceleration of 0.1 g produced a 6.31 mW/cm^{3}g^2 and 1.22 mW/cm^{3}g^2 NPD for the tungsten and silicon mass, respectively. The bandwidth is 2.5 Hz and 4.2 Hz forming F.o.M. of 15.8 mW Hz/cm^{3}g^2 and 5.1 mW Hz/cm^{3}g^2, respectively. The unimorph PZT/Si was larger than the first design (27 mm^3). The beam structure also has tungsten and silicon masses variations, where the power is 2.74 µW and 1.78 µW at a resonance of 167 Hz and 427 Hz under 0.1 g of acceleration, rendering 10.02 mW/cm^{3}g^2 and 6.74 mW/cm^{3}g^2 NPD, respectively. The bandwidth is 6.1 Hz and 16 Hz for an F.o.M. of 61.4 mW Hz/cm^{3}g^2 and 107.8 mW Hz/cm^{3}g^2, for W and Si masses, respectively. The final bimorph was 27 mm^3 in volume. It used only a tungsten mass, and was tested in parallel and series connections. The series connection was superior in terms of NPD and the parallel connection in terms of F.o.M. The output power was 2.36 µW and 1.58 µW, excited at a resonance of 163 Hz and 158 Hz with 0.1 g of acceleration, respectively. Thus, the NPD is 8.74 mW/cm^{3}g^2 and 5.86

mW/cm^{3}g^2. Whereas the bandwidth is 7 Hz and 12.5 Hz forming an F.o.M. of 73.2 mW Hz/cm^{3}g^2 and 61.2 mW Hz/cm^{3}g^2 for the series and parallel connection, respectively.

2.1.4 Other transductions

Magnetostrictive materials can also be used to harvest energy. These materials have specific properties that exhibit a coupling relationship between strain and stress, mechanical quantities, and magnetic and induction field strengths. A magnetostrictive EH requires a coil warped around the magnetostrictive material and a magnetic circuit to convey and close the magnetic flux lines. Thus, when stress is induced in the magnetostrictive material, a time-variable magnetization is created, which leads to the voltage induced in the coils (BATRA; ALOMARI, 2017). Yang, Tan, and Zu (2017) developed a finger-tapping-based magnetostrictive energy harvester. The design is illustrated in Figure 2.17. An iron-gallium alloy (Galfenol, a magnetostrictive material) was bonded to an L-shaped stainless steel beam, an 820-turn coil is wrapped around the alloy with the beam, and an NdFeB grade N42 magnet was placed at the end of the Galfenol. Finally, a sawtooth was bonded to the free end of the beam and activated by a tapping pad. It is not a vibration-based harvester, but it can be analyzed as one by removing the tapping pad excitation and adding acceleration to the base of the cantilever. The L-shaped beam is 0.5 mm x 5 mm x 35 mm, and the magnet is 3.175 mm x 12.7 mm x 12.7 mm. Therefore, the active volume is 35 mm x 12.7 mm x 12.7 mm or 5.65 mm^3. The output power under 4 g acceleration at a resonance of 238 Hz is 0.25 mW, giving an NPD of 0.003 mW/cm^{3}g^2. Since this device was developed to work with an up-frequency technique (discussed in Section 2.3), it is unreasonable to compare this prototype with the VEHs described here. Nevertheless, the device is a reliable example of magnetostrictive EH design.

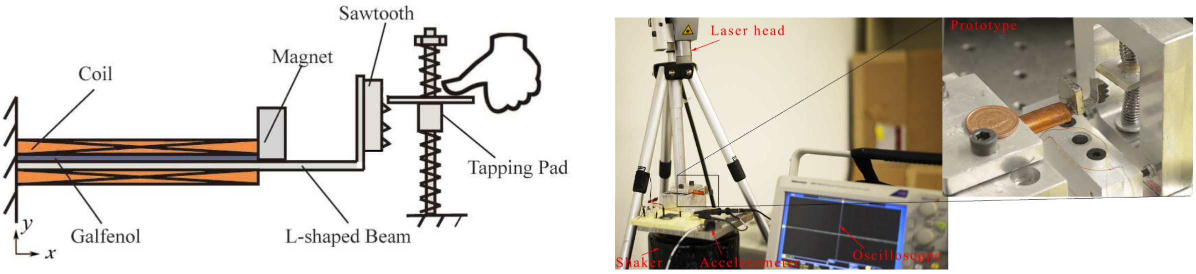

(a) Diagram.

(b) Picture.

Figure 2.17 – Diagram and picture of the magnetostrictive harvesting system based on finger tapping (Obtained form Yang, Tan, and Zu (2017)).

Another form of transduction can convert mechanical energy from vibrations into electrical based on the coupling between triboelectrification and electrostatic induction. The triboelectrically charged planes of the triboelectric VEH change the electric polarization and field across two electrodes by either periodic vertical contact separation or in-plane sliding, leading to an alternating flow of electrons through an external load (YANG; CHEN, et al., 2014). Yang, Chen, et al. (2014) designed the triboelectric VEH shown in Figure 2.18. An aluminum thin film with nanopores was deposited on an acrylic substrate (shown in Figure 2.18 (b)), which works as another contact surface and contact electrode. On the moving part, there is a polytetrafluoroethylene (PTFE) film as one contact surface bonded to a copper thin film working as a back electrode sub-sequentially coupled to an iron seismic mass. The mass was fixed by three springs with a 120° angle between them to ensure a constant resonant frequency in arbitrary in-plane directions. The acrylic substrate had a thickness of 3 mm x 100 $\varnothing$ mm, and the iron mass was 5 mm thick. Therefore, the cylindroid core has an active volume of 8 mm x 30 $\varnothing$ mm or 5.7 cm^3.

Under an acceleration of 6 m/s^2, the author measured an area power density of 1.35 W/m^2 and 1.45 W/m^2 (considering the cylindrical core area) for the out-of-plane and in-plane excitations, respectively. The NPD can then be calculated as 0.45 mW/cm^{3}g^2 and 0.48 mW/cm^{3}g^2. Nevertheless, the relatively low NPD of these devices can be counterbalanced by the large bandwidths of 75 Hz and 14.4 Hz, for out-of-plane and in-plane excitation, for F.o.M. of 33.8 mW Hz/cm^{3}g^2 and 7 mW Hz/cm^{3}g^2, respectively. One important note is that the area power density described by the author used the cylindroid core of the device. Although, an argument can be made to compare with other devices properly, the spring elements must be considered, resulting in an overall active volume of 8 mm x 100 $\varnothing$ mm or 62.8 cm^3. This way, the NPD and F.o.M. decrease significantly to 0.041 $\mathrm{mW/cm^3g^2}$ NPD, 0.044 $\mathrm{mW/cm^3g^2}$ NPD, 3.0 $\mathrm{mW\ Hz/cm^3g^2}$ F.o.M., 0.6 $\mathrm{mW\ Hz/cm^3g^2}$ F.o.M., for out-of-plane and in-plane excitation, respectively.

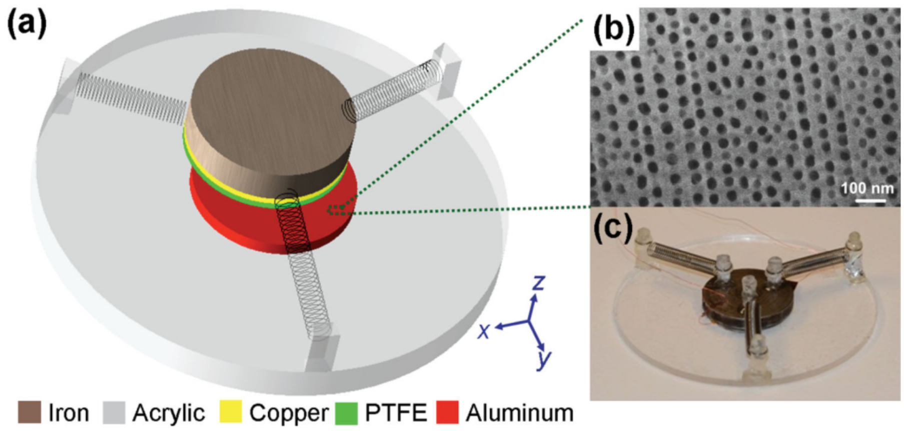

Figure 2.18 – Yang's triboelectric VEH (Obtained from Yang, Chen, et al. (2014)).

2.2 PIEZOELECTRICITY IN VEH

PVEHs use the variation in the electric charge polarization of piezoelectric materials to harvest power. The mathematical principles that describe this phenomenon can be written as (MAITZLER et al., 1988),

$$D_i = \varepsilon^{\sigma}_{ij} E_j + d^{d}_{im} \sigma_m, \tag{2.7}$$

and

$$\delta_k = d^{c}_{jk} E_j + s^{E}_{sk} \sigma_m, \tag{2.8}$$

which can be rewritten as

$$\begin{bmatrix} \boldsymbol{D} \\ \boldsymbol{\delta} \end{bmatrix} = \begin{bmatrix} \boldsymbol{\varepsilon}^{\boldsymbol{\sigma}} & \boldsymbol{d} \\ \boldsymbol{d}^{T} & \boldsymbol{s}^{\mathbf{E}} \end{bmatrix} \begin{bmatrix} \boldsymbol{E} \\ \boldsymbol{\sigma} \end{bmatrix} \tag{2.9}$$

where $\boldsymbol{D}$ is a 3 by 1 vector of electric displacement, $\boldsymbol{\delta}$ is a 6 by 1 strain vector, E is the applied electric field (3 by 1), $\boldsymbol{\sigma}$ is the 6 by 1 stress vector, $\boldsymbol{\varepsilon}^{\boldsymbol{\sigma}}$ is the 3 by 3 matrix of dielectric permittivity at constant stress, $\boldsymbol{d}$ is the 3 by 6 matrix of piezoelectric coefficients, and $\boldsymbol{s}^{\mathbf{E}}$ is the elastic compliance at constant electric field matrix (6 by 6). In the absence of an applied electric field the expanded equation can be written as (SIROHI; CHOPRA, 2000),

$$\begin{bmatrix} D_1 \\ D_2 \\ D_3 \end{bmatrix} = \begin{bmatrix} 0 & 0 & 0 & 0 & d_{15} & 0 \\ 0 & 0 & 0 & d_{24} & 0 & 0 \\ d_{31} & d_{32} & d_{33} & 0 & 0 & 0 \end{bmatrix} \begin{bmatrix} \sigma_1 \\ \sigma_2 \\ \sigma_3 \\ \sigma_4 \\ \sigma_5 \\ \sigma_6 \end{bmatrix}, \tag{2.10}$$

where D_1, D_2, and D_3 represent the electrical displacements in directions 1, 2, and 3, respectively. σ_1, σ_2, and σ_3 are the normal stresses in directions 1, 2, and 3, respectively. σ_4, σ_5, and σ_6 are the shear stresses referring to planes 1-3, 2-3, and 1-2, respectively. d_{31}, d_{32}, and d_{33} are the piezoelectric coefficients that relate the normal voltages applied in directions 1, 2, and 3, respectively, to an electrical displacement in the polarization direction, D_3. The piezoelectric coefficients d_{24} and d_{15} relate shear stresses in the 1-3 plane to the electrical displacement in direction 2 and shear stresses in the 2-3 plane to the electrical displacement in direction 1, respectively.

We consider the stress field of a cantilever beam under vibration. Figure 2.19a shows a cantilever PVEH polarized in the direction normal to the beam surface Z, which is numbered 3 by convention, and the axial direction of beam X becomes 1. In this case, the most relevant piezoelectric coefficient is d_{31} for a cantilever beam where the most significant stress direction is X. For the cantilever in Figure 2.19b, the polarization direction is in the axial direction of the beam X, thus defined as direction 3. In this case, the coefficient d_{33} is the most relevant. These are the so-called d_{31} and d_{33} working modes of piezoelectric devices.

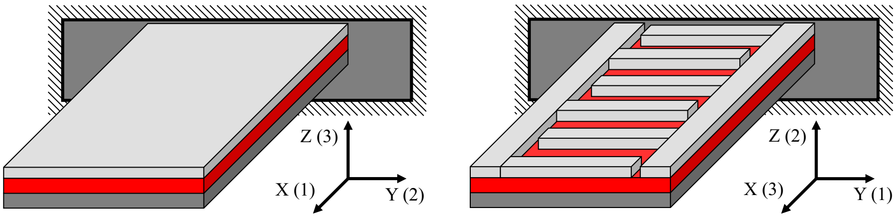

(a) d_{31} mode cantilever design. (b) d_{33} mode cantilever design.

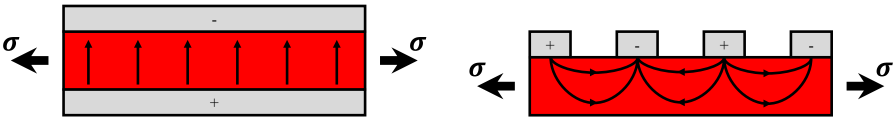

(c) d_{31} mode polarization. (d) d_{33} mode polarization.

Figure 2.19 – Schematic of piezoelectric cantilever working modes.

It is critical to properly polarize the device to ensure that it functions in the desired mode. To do so, it is necessary to impose a strong electric field on the piezoelectric material along the desired polarization direction. To impose the desired polarization onto the piezoelectric material, the constructions represented in Figures 2.19c and 2.19d are utilized. Both beams working in the d_{31} mode (Figure 2.19c) and the one working in d_{33} mode (Figure 2.19d) have their merits. The main points to be raised regarding this comparison are as follows: the coefficient d_{33} is usually approximately ≈ 2.4 times greater than that of the d_{31} (DUTOIT; WARDLE; KIM, 2005); PVEHs working in d_{33} mode tend to have a higher voltage, whereas d_{31} has a higher current (KIM et al., 2013); and d_{31} usually has a higher power because they have a higher capacitance (SODANO; LLOYD; INMAN, 2006). By contrast, d_{33} usually performs better as an actuator (BILGEN; WANG; INMAN, 2012). In addition, it is important to highlight factors such as the difficulty of polarizing or manufacturing. It can be complex to polarize a piezoelectric film in the d_{33} mode because of the inactive zone (the area below the electrodes where the electric field in the direction of mechanical stress is low) (BECKERT; KREHER, 2003; BOWEN et al., 2006). In contrast, the device in the d_{31} mode may require an extra layer of material to form the bottom electrode, making the fabrication more complicated.

It is also possible to separate these EHs into unimorphic and bimorphic beams (Figure 2.20), where the unimorphs have piezoelectric material on only one face of the beam and the bimorphic beams have piezoelectric materials on the two opposite faces of the beam. Thus, the energy produced doubles without significant changes in the total volume of the piezoelectric material (LI; TIAN; DENG, 2014). Although bimorphs have an advantage in power generation, owing to manufacturing limitations, it is not

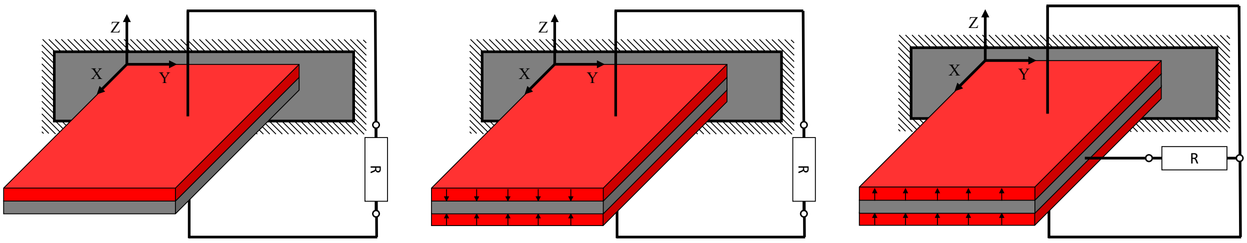

(a) Unimorph. (b) Bimorph connected in series. (c) Bimorph connected in parallel.

Figure 2.20 – Piezoelectric types of electrical connection.

always possible to obtain designs of this type. When choosing to work with bimorphs, the alternatives of connecting the bottom and upper films in parallel or series must be addressed. Aktakka, Peterson, and Najafi (2012) experimented both electrical connections with their device, and the performances obtained are discussed in Subsection 2.1.3.

Table 2.3 shows the typical values of some of the most commonly used piezoelectric materials. AlN has piezoelectric and electromechanical coupling coefficients that are considerably lower than those of other materials presented in the table. However, it is a simple binary compound that can be deposited via sputtering[1] on a wide variety of surfaces (UCHINO, 2017). It is difficult to determine the best alternative for the other materials. However, single crystals have a piezoelectric coefficient one order of magnitude higher than that of PZTs and a considerably higher electromechanical coupling coefficient. There are scenarios in which PZT stands out, such as in PVEHs where the layer of piezoelectric material is much thinner than the elastic layer because, in this case, the Young's modulus of the piezoelectric material can be neglected (XU; KIM, 2012).

Table 2.3 – Typical values of the main piezoelectric materials (Adapted from Briand et al. (2015))

Material	Type	d_{33} (pm/V)	d_{31} (pm/V)	k_{33}	k_{31}	ε_r	$1/s_{33}^E$ (Gpa)
PZT 5H	Ceramic	650	-320	0,75	0,44	3800	50
PZT	Composite	400	-170	-	-	-	15-30
PMN-32PT	Single cristal	2000	-920	0,95	0,78	4950	20
PZN-8PT	Single cristal	2500	-	0,94	-	5000	7,7
AlN	Poly-film	5	-2,5	0,07	-	10	300

2.3 BROADBAND TECHNIQUES

As resonant systems, VEHs are generally structures whose natural frequency has been carefully tuned to the external excitation since a slight deviation between the excitation frequency and the device's resonance results in a drastic drop in performance (TANG; YANG; SOH, 2010). As machines in the industry have different vibration spectra, it is interesting to investigate band-widening techniques to make the PVEH work in a broader range of frequencies. Table 2.4 presents the available techniques and their merits, weaknesses, and applicability. Among the four methods, tuning the resonance frequency is usually more complex than the other methods (TANG; YANG; SOH, 2010). This method can be subdivided into two categories: passive and active tuning. Active tuning requires a power supply, whereas passive tuning does not (ROUNDY; ZHANG, 2005). There are several tuning mechanisms such as magnetic force-based, piezoelectric actuator-based, axial loads, clamp position, variable reluctance, and variable center of gravity (COSTANZO; VITELLI, 2020). A device developed by Roundy and Zhang (2005) is an example of active piezoelectric actuator-based tuning. This self-tuning device (with the diagram shown in Figure 2.21) utilizes the converse piezoelectric effect to control the stiffness of the beam by introducing an electric field in the tuning electrode. In particular, a signal 180° out of phase with the scavenging electrode "softens" the beam and reduces its equivalent stiffness. The unchanged natural frequency of 67 Hz can be tuned down to approximately 60 Hz. Nevertheless, the power used for actuation significantly outweighed the harvested power, yielding a net power of -358 µW.

---

[1] The phenomenon that removes atoms from the surface of a material after bombarding with energetic particles. This process can be used to deposit thin films from bombarded materials onto the substrate underneath (BEHRISCH, 1981).

Table 2.4 – Qualitative comparison of band widening methods for VEHs (Obtained from Tang, Yang, and Soh (2010)).

Methods		Merits, weakness and applicability
Resonance frequency tuning	Active tuning	• Mostly piezoelectric methods • Limited tunability • Cost of tuning mostly outweighs the power harvested • Continuously achievable during operation by automatic controller • Applicable for excitation with fast-varying frequency or random excitation, given affordable power consumption for tuning
	Passive tuning	• Mostly by mechanical and magnetic methods • Difficult to achieve automatically and during operation • Magnetic methods require power to perturb the harvester into high amplitude branch • Relatively large tunability • Applicable for excitation with slow-varying frequency
Multimodal energy harvester		• Much easier to implement than resonance tuning techniques • Should be designed with proper parameters to cover the targeted frequency range with the least sacrifice of energy density • Require complex energy storage circuit
Frequency up-conversion		• Preferable if drastic difference exists between low excitation frequency and high natural frequency of the harvester, e.g., MEMS harvester
Nonlinear Techniques	Monostable*	• Applicable for excitations with slow and proper frequency sweep • Require perturbation if the harvester enters low-energy branch
	Bistable**	• Applicable for high-level periodic excitation • Applicable for low-level periodic excitation but with perturbation mechanism to drive the harvester into high-energy branch • Applicable for stochastic excitation and can further improve the performance by proper periodic change of potential barrier (stochastic resonance)

*System with a single minimum potential energy state.
**System with two minimum potential energy states.

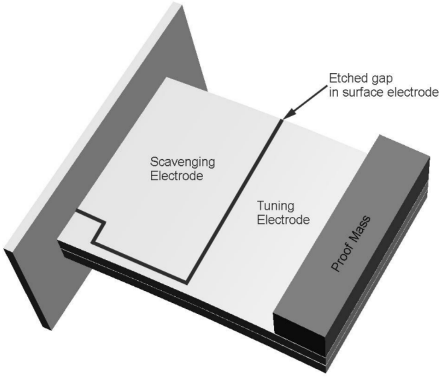

Figure 2.21 – Roundy's piezoelectric actuator based active tuning device (Obtained from Roundy and Zhang (2005)).

Alternatively, Ayala-Garcia et al. (2010) used a magnetic-force-based active tuning approach to extend the narrow bandwidth of the EMVEH from Beeby et al. (2007) (Figure 2.22). The device with originally 0.26 Hz of bandwidth was extended to 14 Hz. This was achieved by fixing one tuning magnet at the free end of the cantilever and another magnet at the end of the actuator (Hydon LC1574 actuator). Nevertheless, the recovery time between tuning procedures depends on the amount of actuation required to reposition the natural frequency. The recovery time is equal to the time required for the harvesting to replenish the supercapacitor that supplies energy to the actuator. A frequency variation of 0.5 Hz leads to a recovery time of 4.16 min, whereas a maximum variation of 14 Hz requires a recovery time of 126.6 minutes. Owing to the long recovery time, this type of system can only be used when small and infrequent changes in frequency occur. Moreover, the device occupies a much larger volume to give space for the actuator of approximately 55.6 mm x 14 ⌀ mm or 8.6 cm^3, which is 57 times bigger than the EMVEH itself. Passive tuning is the best alternative of the two tuning techniques (ROUNDY; ZHANG, 2005).

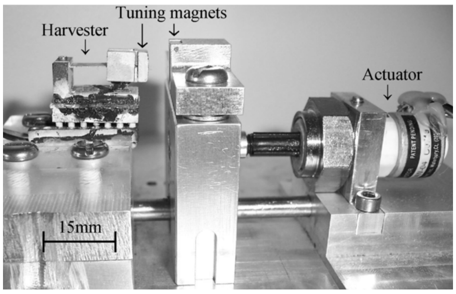

Figure 2.22 – Ayala-Garcia's magnetic force based active tuning device (Obtained from Ayala-Garcia et al. (2010)).

Huan Xue, Yuantai Hu, and Qing-ming Wang (2008) mathematically demonstrated the power response of several bi-morphic beams with different natural frequencies working simultaneously to compose a broadband PVEH device. Figure 2.23a illustrates the power spectrum of a system composed of 10 beams in series compared with a single beam. However, it is essential to note that for the effective application of these devices, it is necessary to rectify the output voltage of the PVEH individually because of the phase difference between the beams. Figure 2.23b illustrates the problem of not using rectifiers before merging the voltage signals using the sum of the voltages of the three beams without rectification. Jing-Quan Liu et al. (2008) developed the three PVEH with different natural frequencies from Figure 2.23b. This graph shows the output voltage of an EH composed of three beams covering a band of 226 - 234 Hz, under an excitation of 229 Hz. The peak voltages were 2.01 V (C1), 1.664 V (C2), and 1.606 (C3). The sum of the results is 3.06 V, which is considerably lower than the 5.256 V expected by the sum of the values of all peaks. After passing the 3.06 V wave through a rectifier, the DC voltage value was 2.51 V, and the power was 3.15 µW. However, if a rectifier is used for each beam before adding them up, in that case, it is possible to obtain a continuous voltage of 3.93 V and a power of 3.98 µW. We can observe that despite the losses generated by the use of three rectifiers, the power obtained is even greater than that obtained by the rectification performed only at the end. Therefore, is is important to develop an appropriate rectification

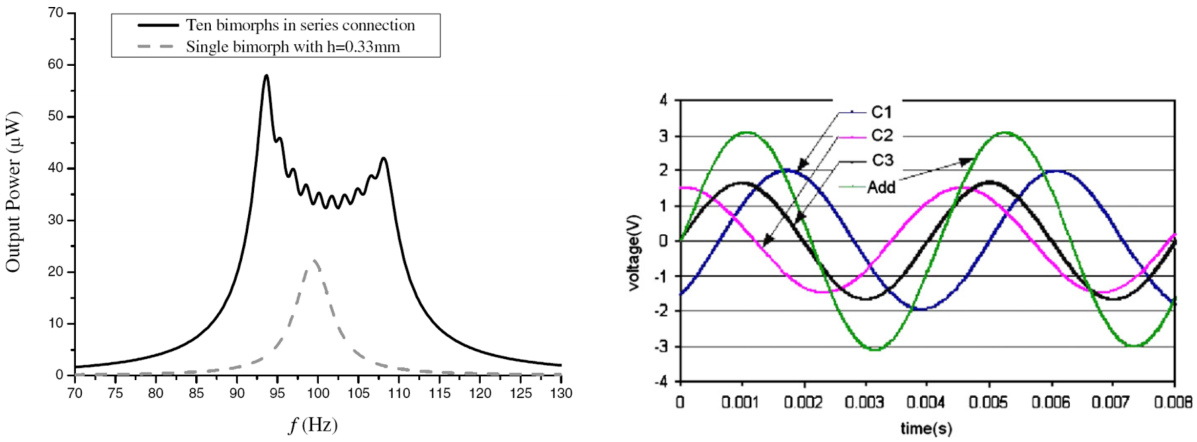

(a) Analytical power from one cantilever and the sum of ten cantilevers with shifted natural frequencies.

(b) Measured voltage of 3 different cantilevers and the sum of all three before rectification.

Figure 2.23 – Power and voltage output of multimodal devices (Obtained form (a) Huan Xue, Yuantai Hu, and Qing-ming Wang (2008) and (b) Jing-Quan Liu et al. (2008)).

circuit for multimodal devices.

It should be noted that adding several cantilever beams with different natural frequencies can increase the bandwidth and power of the device but compromise the NPD. This is especially important when discussing small-scale devices such as MEMS. In these small-scale situations, it is interesting to consider using the Frequency Up-Conversion (FUC) method. Most of the vibration sources available in the environment are in the range of 30 - 200 Hz, while most PVEHs are above this range (HUANG et al., 2019). Therefore, the FUC technique is used, as this method allows the conversion of low-frequency vibrations present in the environment into high-frequency excitations applied to the power generation devices. Gu (2011) propose a PVEH device with a FUC system illustrated in Figure 2.24 that demonstrates a way of applying the method. In the proposed design, electricity is generated by the oxide/nitride and PZT beams (blue and purple, respectively). The FUC is performed by the impact between the low natural frequency system formed by the Parylene and Si substrate beams (in orange and gray, respectively) that vibrate in resonance with the medium and the high natural frequency beams that make the transduction of mechanical energy into electrical energy. Another example of FUC already discussed is the magnetostrictive device of Yang, Tan, and Zu (2017).

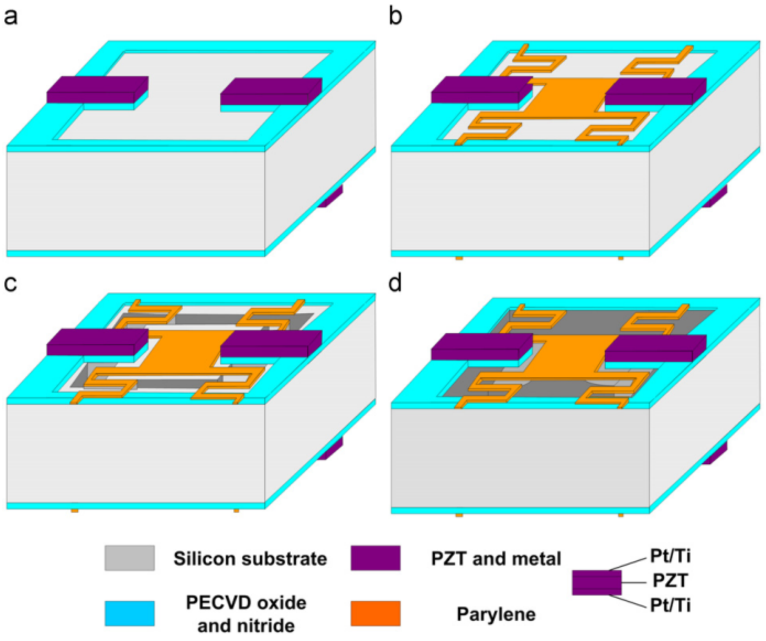

Figure 2.24 – Diagram of the proposed FUC device from Gu (2011) (Obtained from Gu (2011)).

As seen in the device of Tsujiura et al. (2013), non-linear techniques can be implemented to increase the bandwidth of a device without compromising the maximum power (RAMLAN et al., 2010). Stanton, McGehee, and Mann (2009) created a cantilever-based PVEH bimorph with a Neodymium magnet as seismic mass. Monostable nonlinearity was introduced to the system by adding two magnets (one above and another below the cantilever) with vertical distance h and horizontal distance d to the seismic mass (Figure 2.25a). A negative value of d (towards the base of the cantilever) creates a hardening response, whereas positive values create a softening response. Figure 2.25b displays the measured power outputs of the prototypes. It is essential to highlight that the advantages of this technique depend upon maintaining the excitation in the high-energy branch. A momentary short circuit or mechanical perturbation may be required if the device falls into a low-energy branch.

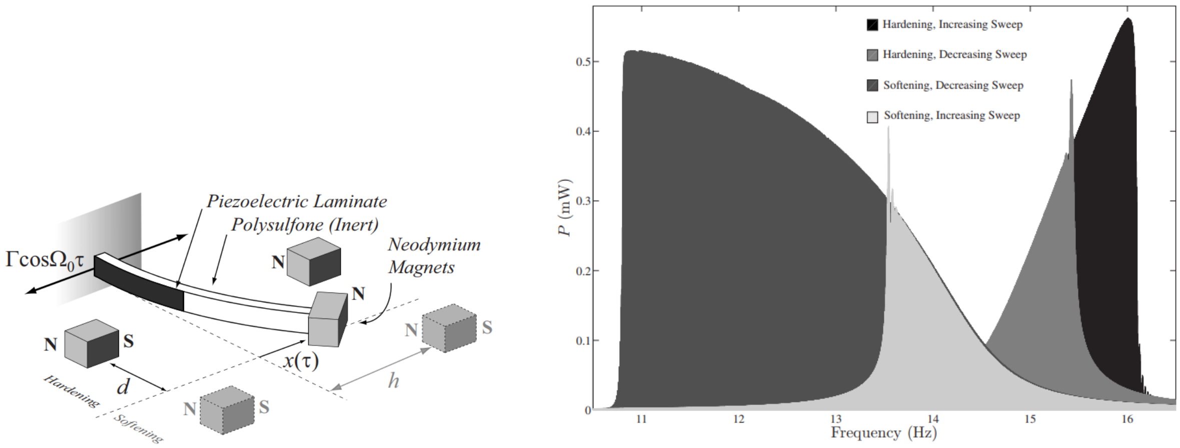

(a) Diagram of the monostable PVEH.

(b) Measured power of the devices under hardening and softening with an increasing and decreasing excitation sweep.

Figure 2.25 – Device developed by Stanton et al. (Obtained form Stanton, McGehee, and Mann (2009)).

Zhou et al. (2014) adopted a similar approach to Stanton et al. but oriented the two magnets with different angles to achieve a bistable (Figure 2.26a) and tristable (Figure 2.26b) VEH. These devices harvest energy by high-energy interwell motion, e.g., the movement between different regions of low potential energy is best demonstrated by Figure 2.27. Maintaining the high-energy interwell motion of the bistables technique can be challenging (HARNE; WANG, 2013). This work shows that the use of the tristable technique can reduce the magnitude of the wells making the device better adapted to lower accelerations. Nevertheless, bistable and tristable techniques are designed to operate under a known excitation intensity

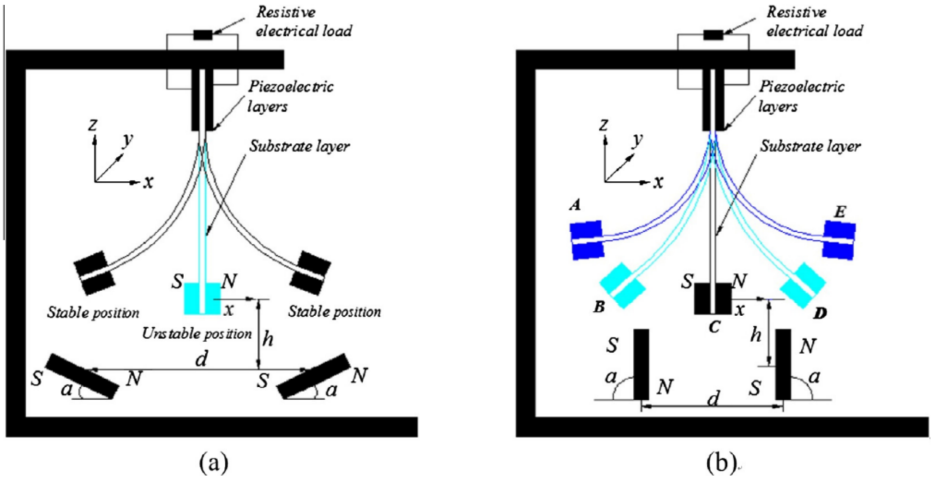

(a) Diagram of the bistable PVEH.

(b) Diagram of tristable PVEH.

Figure 2.26 – Device developed by Zhou et al. (Obtained form Zhou et al. (2014)).

and are preferred under stochastic excitation. Otherwise, monostable approches might be more robust and practical (ZHOU et al., 2014).

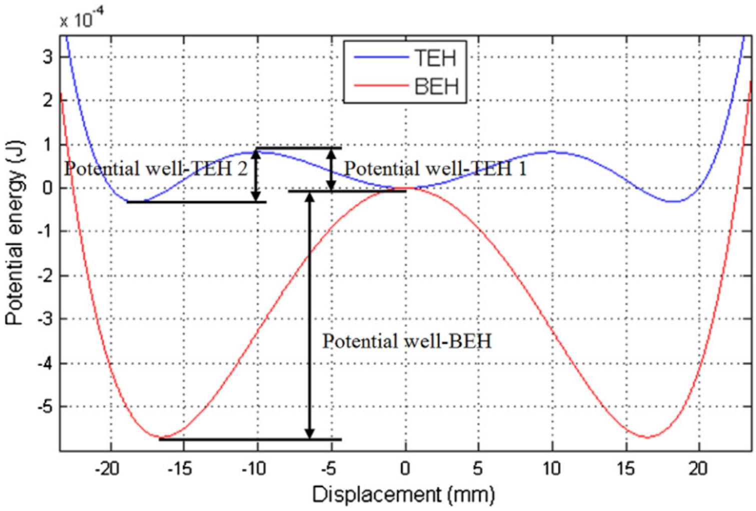

Figure 2.27 – Potential energy versus mass displacement (Obtained from Zhou et al. (2014)).

As stated before, nonlinear techniques can increase the bandwidth of a device without compromising the maximum power, and Figure 2.25b exemplifies this. Nevertheless, the nonlinear method used by Huicong Liu et al. (2012b,a) comes at the expense of reducing the maximum power. A mechanical stopper is used to limit the movement of the seismic mass. A broadband effect occurs when the mass impacts the stopper, creating a hardening response. The closer this stopper is to the seismic mass, the wider the bandwidth gets, however the maximum power decreases. This technique is interesting for its simplicity and is explored more in-depth in Appendix E.

2.4 COMMERCIAL ENERGY HARVESTERS

In addition to the literature, some commercially available devices are worth mentioning because of their excellent performance. Although they have positive power output, they all fall in the realm of large VEH, whereas this work is primarily interested in the 1 cm^3 region. The VEG from Xidas IOT (XIDAS IOT, n.d.) is a 52 $\varnothing$ mm x 24 mm or 50.97 cm^3 electromagnetic device, with five choices of natural frequency (20 Hz, 30 Hz, 50 Hz, 60 Hz, and 70 Hz). The 60 Hz device outputs a power of approximately 45 mW at 0.7 g of acceleration, rendering an NPD of 1.8 mW/cm^{3}g^2. The estimated bandwidth is 2.5 Hz at 0.7 g, resulting in an F.o.M. of 4.5 mW Hz/cm^{3}g^2. Model Q of Revibe Energy (REVIBE ENERGY, 2021) is an EMVEH and one of the smallest devices found on the market with dimensions of 25 mm x 25 mm x 25 mm (Figure 2.28b) or 15.6 cm^3. Its power output is 35 mW at 1 g of acceleration for the 60 Hz model, which

(a) Xidas. (b) Revibe.

Figure 2.28 – XIdas model VP3 and Revibe model Q (Obtained from XIDAS IOT (n.d.) and Revibe Energy (2021)).

gives an NPD of 2.24 mW/cm^{3}g^2. The model of 80 Hz is the same size but outputs approximately 35.5 mW at 0.8 g, and the estimated bandwidth is 2.5 Hz, giving an NPD of 3.55 mW/cm^{3}g^2 and an F.o.M. of 8.9 mW Hz/cm^{3}g^2.

Most of the devices settled in the market work on electromagnetic transduction, but Viezo's powerail employ a piezoelectric cantilever made from PVDF polymer, as shown in Figure 2.29. Further information was not obtained from the device. However, it is crucial to acknowledge the existence of a PVEH in the market and highlight the use of a cantilever-based design. The Figures 2.30 and 2.31 show the values of NPD and F.o.M., respectively, for the devices presented in this chapter and other relevant designs.

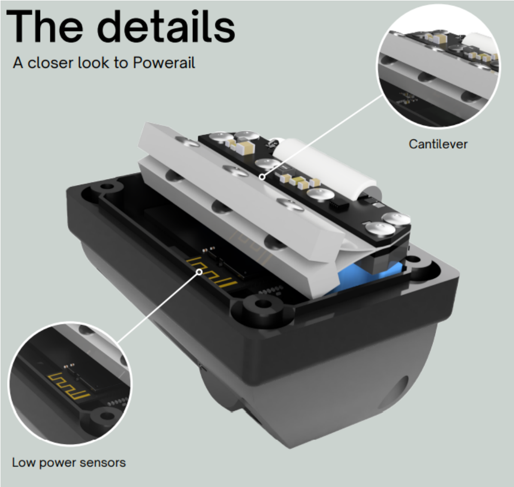

Figure 2.29 – Viezo powerail (Obtained from Viezo (2022)).

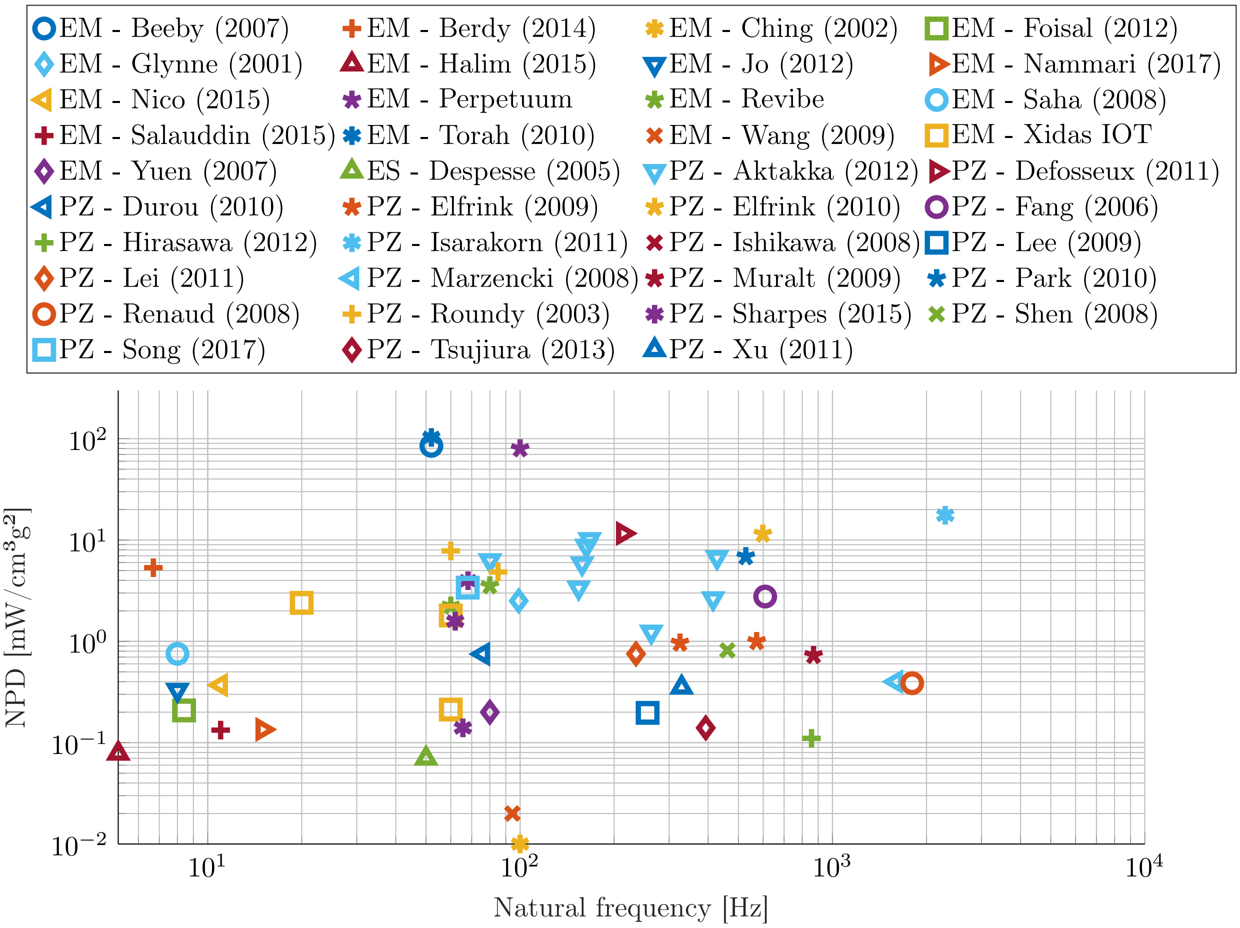

Figure 2.30 – Scatter graph of devices from literature in terms of NPD as a function of natural frequency.

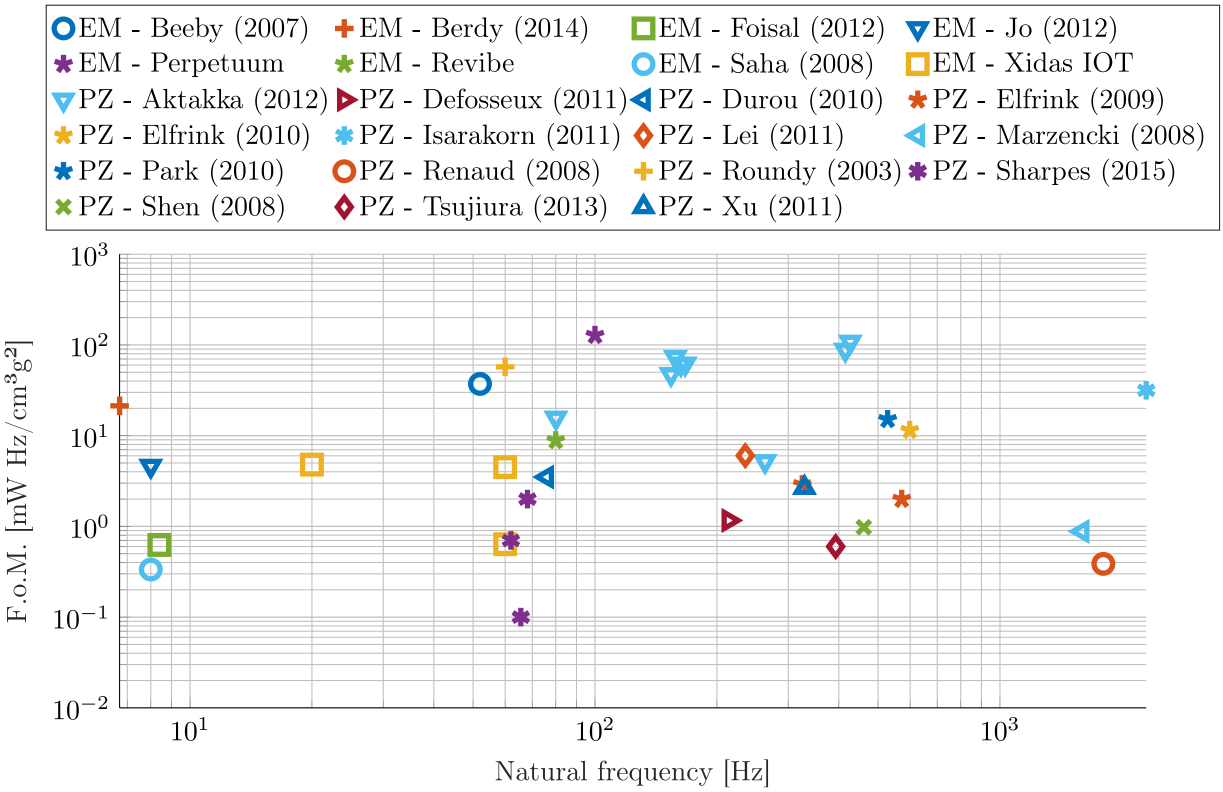

Figure 2.31 – Scatter graph of devices from literature in terms of F.o.M. as a function of natural frequency.

2.5 OPTIMIZATION

The designs of systems such as the PVEH proposed in this work can be challenging. Defining the best solution can be performed via a conventional or an optimum design method. Figure 2.32 illustrates the process flow for each method. Both have blocks that require similar calculations and others that require different calculations. These differences are as follows (ARORA, 2017):

0. The optimum design method has block 0, where the problem is formulated as one of optimization. An objective function is defined that measures the merits of different designs.

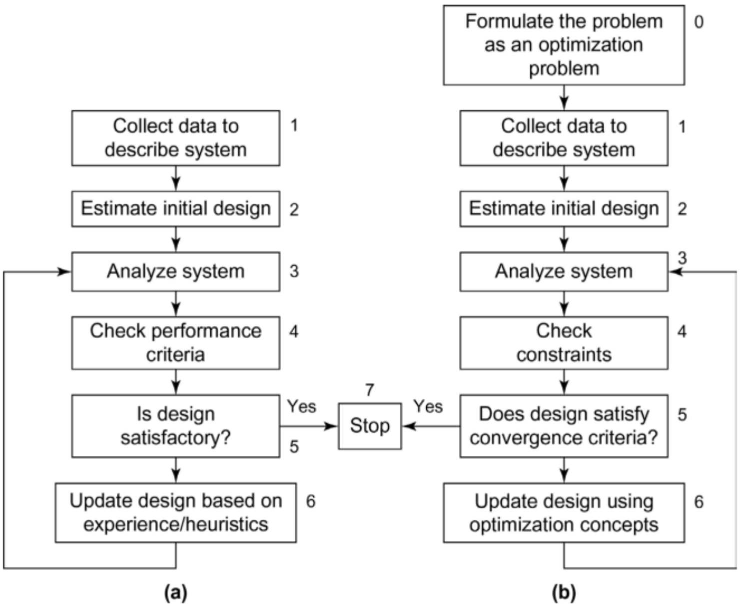

Figure 2.32 – Conventional design method (a) and optimum design method (b) (Obtained from Arora (2017)).

1. Both methods require data to describe the system in block 1.
2. Both methods require an initial design estimate in block 2.
3. Both methods require analysis of the system in block 3.
4. In block 4, the conventional design method checks to ensure that the performance criteria are met, whereas the optimum design method checks for the satisfaction of all of the constraints for the problem formulated in block 0.
5. In block 5, stopping criteria for the two methods are checked, and the iteration is stopped if the specified stopping criteria are satisfied.
6. In block 6, the conventional design method updates the design based on the designer's experience, intuition, and other information gathered from one or more trial designs; the optimum design method uses optimization concepts and procedures to update the current design.

The main difference between the methods is the existence of an objective function that can quantify the performance of each design. The traditional method does not establish this objective function. Thus, it usually does not calculate trend information or make decisions from that on block six for system improvement. In both cases, particularly when using an optimum design method, it is crucial to classify the optimization algorithm used. Table 2.5 highlights some forms of categorizing these algorithms (HAUPT; HAUPT, 2004). Following Haupt's classification, the conventional method described by Arora (2017) could be classified as a trial-and-error algorithm, where the opposing classification would be a function-based algorithm.

Table 2.5 – Classification of optimization algorithms (Adapted from Haupt and Haupt (2004)).

Function or trial and error	Trial-and-error optimization refers to the process of adjusting variables that affect the output without much knowledge of the process that produces the output. In contrast, a mathematical formula describes the objective function in the function optimization. Various mathematical manipulations of the function lead to the optimal solution.
Single or multiple variable	If there is only one variable, the optimization is one-dimensional. A problem with more than one variable requires multidimensional optimization. Optimization becomes increasingly difficult as the number of dimensions increases.
Static or dynamic	Dynamic optimization means that the output is a function of time, whereas static optimization means that the output is independent of time.
Discrete or continuous	Optimization can also be distinguished by discrete or continuous variables. Discrete variables have only have a finite number of possible values, whereas continuous variables have an infinite number of possible values. Discrete variable optimization is also known as combinatorial optimization, because the optimum solution consists of a combination of variables from the finite pool of all possible variables.
Constrained or unconstrained	These variables often have certain limits or constraints. Constrained optimization incorporates variable equalities and inequalities into the cost function. Unconstrained optimization allows the variables to take any value.
Random or minimum seeking	Some algorithms attempt to minimize cost by starting from an initial set of variable values. These are traditional optimization algorithms and are generally based on calculus methods moving from one variable set to another based on a certain sequence of steps. Random methods use probabilistic calculations to determine variable sets.

Constraints in optimization must be established before choosing an algorithm because most numerical optimization routines work best with unconstrained variables (HAUPT; HAUPT, 2004). A common approach to this problem is to convert a constrained variable into an unconstrained one. Constraints can be classified as equality or inequity constraints and linear or nonlinear constraints. A particular case, referred to as the box-constraint, must be highlighted. A box-constrained optimization can be written as (FACCHINEI; JÚDICE; SOARES, 1997)

$$\min_{x \in K} f_{\mathrm{obj}}(x), \tag{2.11}$$

where

$$K = \{x \in \mathbb{R}^n : l_{\mathrm{i}} \leq x_{\mathrm{i}} \leq u_{\mathrm{i}}, i = 1, \ldots, n\}, \tag{2.12}$$

where l_{i} and u_{i} are the lower and upper boundaries of the i^{th} variable x, respectively.

It is necessary to distinguish the optimization into three elements: (i) model, (ii) simulator, and (iii) optimizer. The model represents the physical problem using mathematical equations, which can be converted into a numerical model and then solved numerically using a finite element model software or Python code, for example. Finally, the optimizer or the optimization algorithm is the "search" method of the optimization process. Ideally, this process is capable of finding a solution that converges to the global optimum with little computational time, although this is usually very difficult.

For this work, the algorithm must be function-based, multiple variables, static, capable of working with both discrete and continuous variables or just discrete, and work with linear and box-type constraints. The need for discrete variables is related to the geometric parametrization of the numerical model, which is further discussed in Section 3.2. Linear and boxed constraints were used to maintain the design with the features that could be fabricated. The model used in this work is a so-called black-box. Thus, an analytical description of the derivative information is not available, e.g., the optimization algorithm must be adapted for black-box models. The algorithms investigated in this work are (i) the Differential Evolution (DE), (ii) Nelder-Mead (NM), and (iii) Surrogate Optimization (SO).

2.5.1 Differential Evolution Algorithm

DE falls into the heuristic category. Thus, it is a slower algorithm but better adapted to finding the global minimum when compared to mathematical programming (HAUPT; HAUPT, 2004). It uses an initial set of designs (or members) called a population, where new designs are formed at each iteration (denoted as generation) using current designs and certain random operations. The general algorithm follows a four steps program (ARORA, 2017): (i) generation of initial population, (ii) mutation with the difference of vectors to generate a so-called donor design vector, (iii) crossover/ recombination to generate a so-called trial design vector, and (iv) selection, e.g., acceptance or rejection of the trial design vector using the objective function.

Consider a design point or member represented by $\mathrm{X}_{\mathrm{i,G}} = \left\{\mathrm{x}^{1}_{\mathrm{i,G}}, \ldots, \mathrm{x}^{\mathrm{D}}_{\mathrm{i,G}}\right\}, \mathrm{i} = 1, 2, ...\mathrm{PN}$, where PN is the population number, $\mathrm{x}^{\mathrm{j}}_{\mathrm{i,G}}$ is the j^{th} parameter of the i^{th} member of generation G and D represents the parameter number of the member. The initialization of the problem is given by,

$$x^{j}_{i,0} = x^{j}_{\min} + \mathrm{rand}(0,1) \cdot \left(x^{j}_{\max} - x^{j}_{\min}\right), \tag{2.13}$$

where $\mathrm{x}^{\mathrm{j}}_{\mathrm{i,0}}$ will determine the initial parameters of all members in the population. $\mathrm{x}^{\mathrm{j}}_{\mathrm{min}}$ is the lower limit of the j^{th} parameter, $\mathrm{x}^{\mathrm{j}}_{\mathrm{max}}$ the upper limit of the j^{th} parameter, and $\mathrm{rand}(0,1)$ a function that generates a random number between 0 and 1.

After creating the population, it must create a mutant vector $\mathrm{V}_{\mathrm{i,G}}$ for each target vector (member) of the population,

$$V_{i,G} = X_{r^{i}_{1},G} + F \cdot \left(X_{r^{i}_{2},G} - X_{r^{i}_{3},G}\right) \tag{2.14}$$

where $\mathrm{r}^{\mathrm{i}}_{1}, \mathrm{r}^{\mathrm{i}}_{2}$, and $\mathrm{r}^{\mathrm{i}}_{3}$, are random natural values between 1 and PN, and F is a scale factor. With the target vector $\mathrm{X}_{\mathrm{i,G}}$ and its corresponding mutant vector. The recombination is performed by

$$u^{j}_{i,G} = \begin{cases} v^{j}_{i,G}, & \text{if } (\mathrm{rand}_{j}[0,1) \leq \mathrm{CR}) \\ x^{j}_{i,G}, & \text{otherwise} \end{cases} \tag{2.15}$$

where $\mathrm{u}^{\mathrm{j}}_{\mathrm{i,G}}$ is the j^{th} parameter of the descendant of $\mathrm{X}_{\mathrm{i,G}}$ and CR is a mutation factor that defines the probability from the descendant (trial vector) $\mathrm{U}_{\mathrm{i,G}}$ inherits the mutant vector parameter. Finally, the selection is performed by comparing the target vector with the trial vector from the objective function f_o.

2.5.2 Nelder-Mead

The Nelder-Mead algorithm minimizes the nonlinear functions of n parameters without using any derivative information. Thus, it is better adapted for fast convergence to the local minimum than a random algorithm. This method creates on each iteration a nondegenerate simplex[2], where one or more test points are computed along with their function values. The iteration terminates with a new (different) simplex such that the function values at its vertices satisfy some form of the condition compared to the previous simplex. Four coefficients must be specified for this method with standard values: (i) reflection $\rho_{\mathrm{NM}} = 1$, expansion $X_{\mathrm{NM}} = 2$, contraction $\lambda_{\mathrm{NM}} = \frac{1}{2}$, and shrinkage $\sigma_{\mathrm{NM}} = \frac{1}{2}$. Thus, the algorithm at the k^{th} iteration (k≥0) labels the vertices of a simplex with n+1 vertices as $x^{(\mathrm{k})}_{1}, ..., x^{(\mathrm{k})}_{\mathrm{n+1}}$, such that (LAGARIAS et al., 1998)

$$f^{(\mathrm{k})}_{1} \leq f^{(\mathrm{k})}_{2} \leq ... \leq f^{(\mathrm{k})}_{\mathrm{n+1}}, \tag{2.16}$$

where $f^{(k)}_{i}$ is the objective function value of the $x^{(k)}_{i}$ vertex. If the objective is to minimize the function, then $x^{(k)}_{1}$ is the best point and $x^{(k)}_{n+1}$ is the worst. The next step can either (i) generate a new vertex that replaces the worst performed by a reflect, expand, or contract step, or (ii) if shrink is performed, a set of n new vertex that forms the next simplex with the best point. All these steps are illustrated in Figure 2.33. One iteration of the algorithm performs the following steps:

1. Order simplex vertex;
2. Compute the **reflection** point:

   $$x_{\mathrm{r}} = \bar{x} + \rho_{\mathrm{NM}}(\bar{x} - f_{\mathrm{n+1}}), \tag{2.17}$$

   where $\bar{x}$ is the centroid of the n best points.

   - If $f_1 \leq f_{\mathrm{r}} \leq f_{\mathrm{n}}$, accept reflected point x_{r} and terminate the iteration.
3. If $f_{\mathrm{r}} \leq f_1$, calculate **expansion** point,

   $$x_{\mathrm{e}} = \bar{x} + X_{\mathrm{NM}}(x_{\mathrm{r}} - \bar{x}). \tag{2.18}$$

   - If $f_{\mathrm{e}} \leq f_{\mathrm{r}}$, accept expansion point x_e and terminate the iteration, otherwise accept x_{r} and terminate the iteration.
4. If $f_{\mathrm{r}} \geq f_{\mathrm{n}}$, calculate **contraction** point x_{c}.

   a) **Outside** contraction if $f_{\mathrm{n}} \leq f_{\mathrm{r}} < f_{\mathrm{n+1}}$,

   $$x_{\mathrm{c}} = \bar{x} + \lambda_{\mathrm{NM}}(x_{\mathrm{r}} - \bar{x}). \tag{2.19}$$

   - If $f_{\mathrm{c}} \leq f_{\mathrm{r}}$ accept x_{c} and terminate the iteration, otherwise perform shrink.

   b) **Inside** contraction if $f_{\mathrm{r}} \geq f_{\mathrm{n+1}}$,

   $$x_{\mathrm{cc}} = \bar{x} + \lambda_{\mathrm{NM}}(\bar{x} - x_{\mathrm{n+1}}). \tag{2.20}$$

   - If $f_{\mathrm{cc}} < f_{\mathrm{n+1}}$ accept x_{cc} and terminate the iteration, otherwise perform shrink.
5. Perform **shrink**, by calculating,

   $$v_{\mathrm{i}} = x_1 + \sigma_{\mathrm{NM}}(x_{\mathrm{i}} - x_1), \tag{2.21}$$

   where i = 2, ..., n+1, such that the (unordered) vertices of the next iteration are $x_1, v_2, ..., v_{\mathrm{n+1}}$.

---

[2] Geometric figure of N dimensions of nonzero volume that is a convex hull on N+1 vertices.

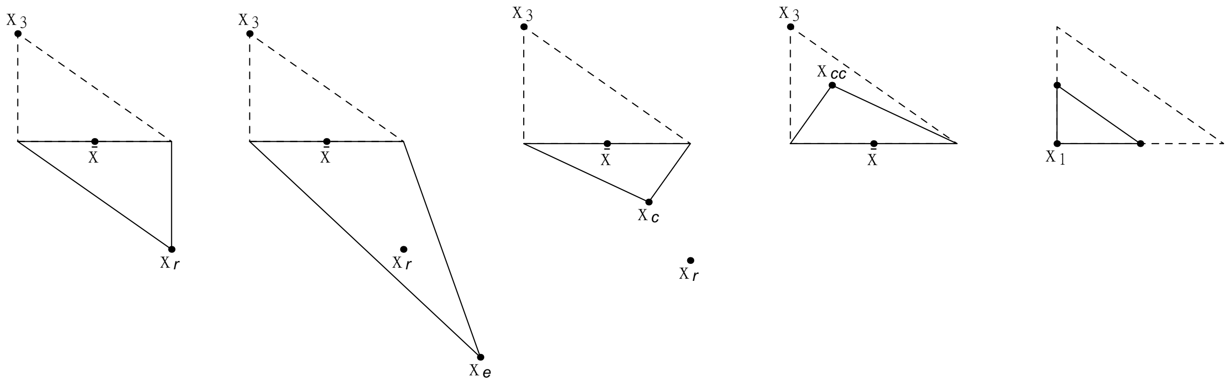

Figure 2.33 – Nelder-Mead simplices after reflection, expansion, outside contraction, inside contraction, and shrink, from left to right, respectively (Adapted from Lagarias et al. (1998)).

2.5.3 Surrogate Optimization Algorithm

In engineering, heavy computer simulations are often used to predict physical phenomena using methods such as the Finite Element Method (FEM). When described as black-box solvers, they do not have an analytical description or derivative information available. Furthermore, they can increase the computational cost of algorithms that calculate the objective function at each iteration, e.g., DE lose efficiency. Surrogate models have been developed to solve this type of optimization problem efficiently. Using the surrogate information, the costly objective function is only calculated at carefully selected points, thus finding near-optimal solutions more efficiently (MÜLLER, 2016). The *surrogateopt* (MATLAB, 2020) function from MATLAB can be separated into two phases as shown in Figure 2.34: The creation phase, where the surrogate curved is calculated, and the search phase, where the algorithm starts searching for the minimum.

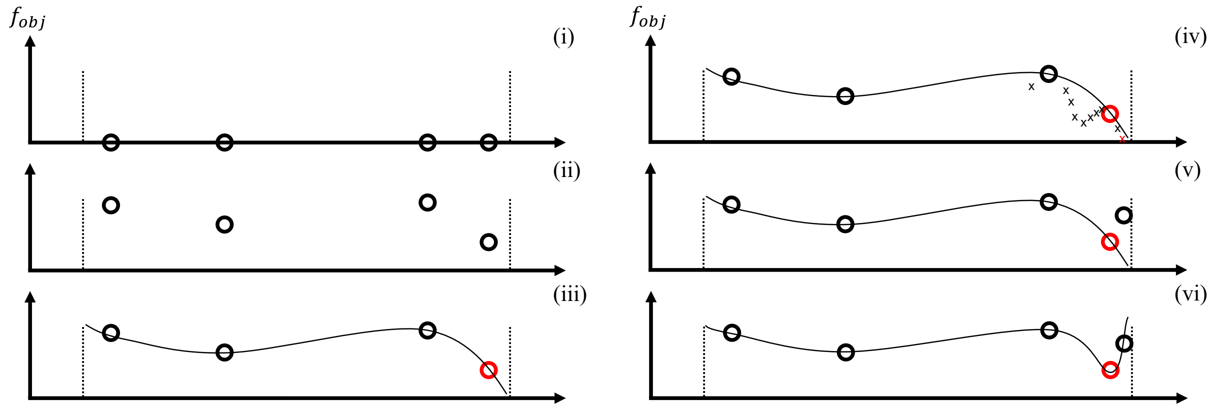

(a) Creation phase. (b) Search phase.

Figure 2.34 – Diagram of surrogate optimization (adapted from MATLAB (2020)).

The creation phase is composed of three steps: (i) quasi-random points are selected to aid in the construction of the surrogate, (ii) the objective function is evaluated for all selected points, and (iii) Radial Basis Functions (RBF) are used to interpolate the data and create a surrogate. After a surrogate function is constructed, the search phase begins, where another three steps are taken: (iv) sampling and evaluation of the merit function near the incumbent[3], (v) evaluation of the objective function for the best point, (vi) updating the surrogate function. The search continues to loop through these steps until convergence is achieved. The merit function used to determine where the following objective function will be evaluated defined as,

$$f_{\text{merit}}(x) = wS(x) + (1 - w)D(x), \tag{2.22}$$

---

[3] Point with the best value among all evaluated since the most recent reset.

for

$$S(x) = \frac{s(x) - s_{\text{min}}}{s_{\text{max}} - s_{\text{min}}}, \tag{2.23}$$

and

$$D(x) = \frac{d_{\text{max}} - d(x)}{d_{\text{max}} - d_{\text{min}}} \tag{2.24}$$

where w is a weight between 0 and 1, $S(x)$ is the scaled surrogate at point x, $s(x)$ is the surrogate value at point x, s_{min} is the minimum surrogate value among the sample points, s_{max} is the maximum surrogate value among all sample points, $D(x)$ is the scaled distance at point x, d_{max} is the maximum distance between any sample point to any evaluated point, d_{min} is the minimum distance between any sample point to any evaluated point. Weight w will defines the importance of the surrogate values, that is, if the weight is small, the attention will be given to points further from the evaluated point. During the search for the minimum, w cycles through 0.3, 0.5, 0.8, and 0.95. A different method for sampling points is set, depending on the weight value at each iteration. The points are selected via a quasi-random method at w equal to 0.3 and 0.5. At 0.8, the points are positioned along the axis of a randomly chosen orthogonal plane. This method is denoted OrthoMADS (MATLAB, 2020). At 0.95, almost the same procedure as OrthoMADS is used, but a non-rotated coordinate system is chosen instead. For all weights, the samples (for the merit function) are chosen within a scale that varies during the optimization. This scale length starts at 0.5 times the box-constraint size and doubles every three successful searches since the last scale change or is halved when N (dimension of problem) number of unsuccessful searches occurs. The minimum and maximum sizes of the scale are 10^{-5} times and 0.8 times the size of the box-constraint, respectively.

2.6 SYNTHESIS AND CONTRIBUTIONS

This review contains significant findings that could impact this project. They are summarized as:

- 20 Hz of bandwidth can be a challenge:

  Almost no devices in the lower frequency band (<200 Hz) had 20 Hz of bandwidth without implementing the broadband techniques presented in Section 2.3, except for the out-of-plane mode of the device of Yang, Chen, et al. (2014). Although the bandwidth was large, the NPD and F.o.M did not perform well because of the low power output of the device.

- Comparison of piezoelectric and electromagnetic transducers:

  Broadband techniques, such as multi-modal techniques, might be necessary. The goal of a maximum of 3.93 cm^3 can be divided into four or five to allow for different devices with shifted resonances. Thus, the requisite is significantly close to the “transition zone” mentioned by Marin (2013).

- NPD and F.o.M:

  These metrics are used in this work to compare the performance of different devices, but are not definitive measures. Devices are projected for different vibration amplitudes, natural frequencies, and vibration types, i.e., stochastic vibrations, sweeps, and others. These aspects were not considered by the metrics used here.

- Cantilever structure:

  Cantilever-type devices appear to be the most relevant and common approach when restricted to low frequencies and small volumes.

- Broadband techniques can be a give-and-take problem:

  Active frequency tuning consumes part (or all) of the energy generated by the harvester or usually requires the introduction of a structure that occupies a significant portion of the volume of the device (AYALA-GARCIA et al., 2010). Nonlinear techniques can limit the maximum power, as shown by Huicong Liu et al. (2012b,a). Multimodal devices composed of an array of cantilevers must divide the overall volume to fit devices with distinct resonances.

- No commercial device meets the requirements:

  All commercial devices found to be available during the period of this work occupy a large volume. Even with respectable performances, these devices fall under a different application because this work focuses on volumes smaller than 3.93 cm^3.

CHAPTER 3

METHODOLOGY

The objective of this work aims optimize the design of a PVEH that can output at least 160 µW over a frequency band of 20 Hz centered at 60 Hz. The PVEH has a maximum size of 7.7 mm x 25.5 ⌀ mm or 3.93 cm^3 as described by Table 1.1. To better compare the performances of different devices with the requirements of thes study, these values were converted into two performance metrics . The transformation of the objectives into NPD is written as

$$\mathrm{NPD}_{\mathrm{goal}} = \frac{2 * P_{\mathrm{req}}}{\frac{B}{B_{\mathrm{req}}} V_{\mathrm{req}}\ \ddot{x}_{\mathrm{opt}}^2}, \tag{3.1}$$

where $\mathrm{NPD}_{\mathrm{goal}}$ is the NPD a device must have to meet the requirements, B_{req} is the bandwidth required, P_{req} is the power required, V_{req} the volume required and $\ddot{x}_{\mathrm{opt}}$ is the optimum acceleration or, in other words, the energy that will be available to the harvester in the form of vibration. P_{req} is multiplied by two because the device should deliver P_{req} over B_{req}. This way, if the device's working frequency is assumed to be equal to its half-power bandwidth the actual power of the device should be 2 P_{req}. The $\frac{B}{B_{\mathrm{req}}}$ is a coefficient that determines the amount of space the device can occupy from the original V_{req} if a multimodal broadband approach is adopted. Thus, if a particular device has a half-power band of half the required band, there must be two devices with equal bandwidths to cover the requirement. Therefore, each device occupies half the available space. To get a performance metric that does not depend on the device's bandwidth, F.o.M. should be used, written as

$$\mathrm{F.o.M.}_{\mathrm{goal}} = \frac{2 * P_{\mathrm{req}}\ B_{\mathrm{req}}}{V_{\mathrm{req}}\ \ddot{x}_{\mathrm{opt}}}, \tag{3.2}$$

where $\mathrm{F.o.M.}_{\mathrm{goal}}$ is the F.o.M. a device must have to meet the requirements. To better understand the challenges and possibilities, Figure 3.1 shows the bandwidth of several devices from the literature with their corresponding natural frequency.

Analyzing the frequency range of 10 Hz to 100 Hz, it is evident that no devices have bandwidths above 7 Hz. If the PVEHs conceived in this study display a similar bandwidth or lower, a minimum of three different designs fitting within a 3.93 cm^3 volume will be needed. The objectives are described in terms of the NPD (for different bandwidths) and F.o.M. in Table 3.1. This works aims to address the requirements listed in Table 1.1. In addition, in order to meet these goals, an optimization procedure was used. This process follows the diagram in Figure 3.2.

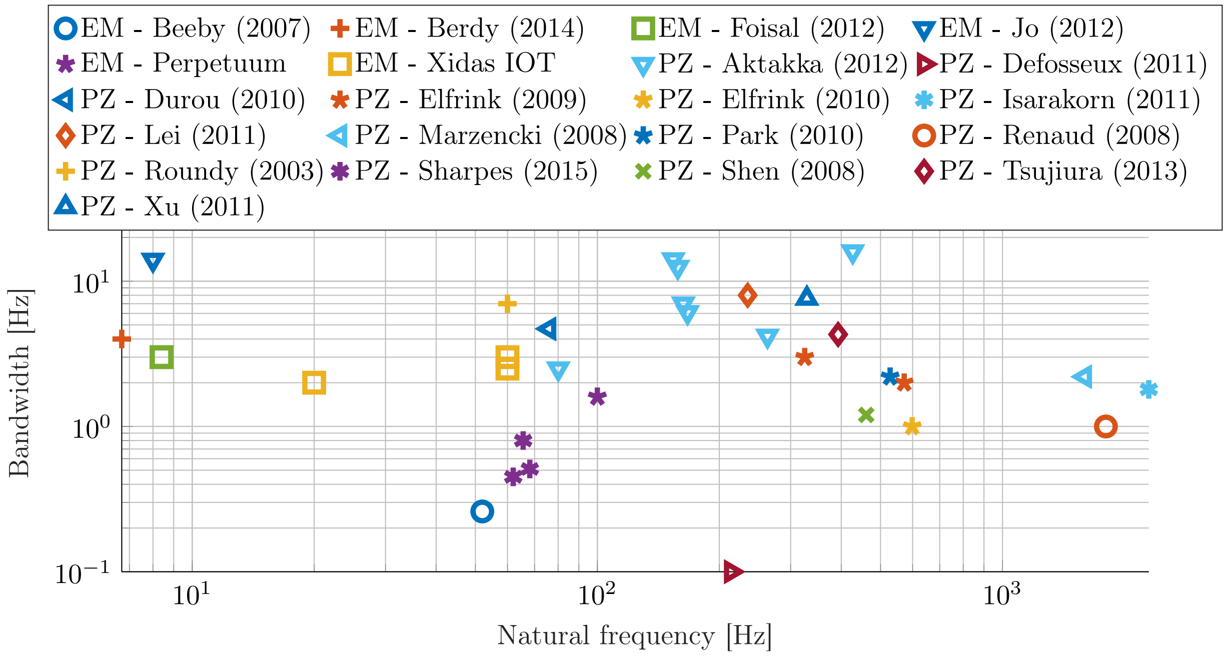

Figure 3.1 – Scatter graph of devices from the literature in terms of bandwidth as a function of natural frequency.

Table 3.1 – Project requirements regarding NPD and F.o.M. for various applied accelerations and band.

Metric	NPD [mW/(g^2 cm^3)]								F.o.M. [mW Hz/(g^2 cm^3)]
Band	1 Hz	2 Hz	3 Hz	4 Hz	5 Hz	6 Hz	7 Hz	8 Hz	-
1 g	1.63	0.81	0.54	0.41	0.33	0.27	0.23	0.20	1.63
2.25 m/s^2	30.92	15.46	10.31	7.73	6.18	5.15	4.42	3.86	31.86
1 m/s^2	156.52	78.26	52.17	39.13	31.30	26.36	22.36	19.56	156.52

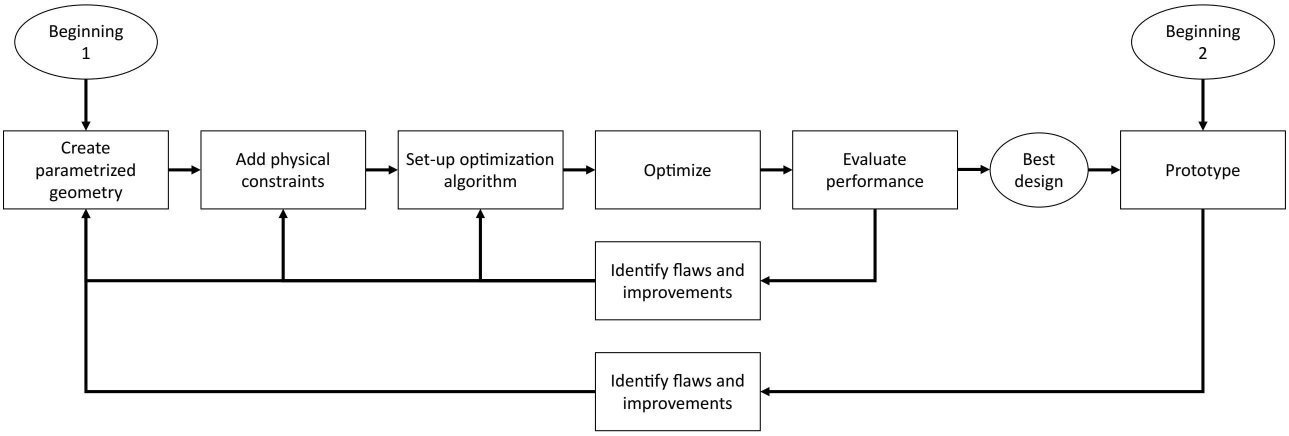

Figure 3.2 – Diagram of generalized optimization procedure for piezoelectric EH.

The optimization process can commence in two ways. Beginning one starts with a numerical model using information obtained from the literature. In contrast, Beginning two starts with a prototype that was not optimized to feed the initial numerical model. There are three main aspects to this optimization process: (i) numerical modeling of the device's physical behavior, (ii) implementation of an optimization algorithm, and (iii) fabrication and testing of the prototype. By the end of each optimization run, the entire process was analyzed with respect to the design output. If the final design does not meet any requirement, it is crucial to identify the part of the process that could improve the performance. After the fabrication and testing of any prototype, it was necessary to adjust the numerical model and determine if the fabrication process occurred as expected and if no electrical or mechanical parameters were changed.

3.1 NUMERICAL MODELING

The numerical modeling comprises building a parametric geometry and implementing physical constraints. Numerous types of geometries can be parameterized and subsequently optimized, each with a specific advantage. In what follows, four alternatives are presented: (i) cantilever, (ii) trampoline, (iii) flower (IANNACCI et al., 2015), and (iv) cantilever array. A top-view diagram of all these designs is shown in Figure 3.3.

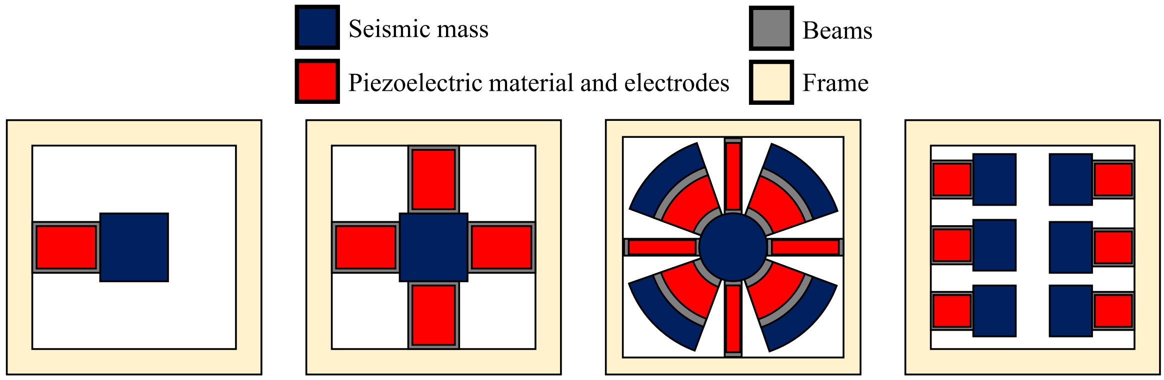

(a) Cantilever design. (b) Trampoline design. (c) Flower design. (d) Cantilever array.

Figure 3.3 – Top-view diagram of PVEH geometries.

The cantilever (Figure 3.3a) is one of the most commonly used designs for low-frequency energy harvesters (ROUNDY; LELAND, et al., 2005; PRIYA et al., 2019; TAKEI et al., 2016; WANG, L. et al., 2019; PARK et al., 2010; LIU, H. et al., 2012b,b; AKTAKKA; PETERSON; NAJAFI, 2012; HUANG et al., 2019), because it is easy to achieve low natural frequencies and relatively high average strain for a given frame acceleration. If the beam is built with a trapezoidal profile, it can supply more than twice the energy of a rectangular geometry (ROUNDY; LELAND, et al., 2005). The trampoline design (Figure 3.3b) is interesting in contrast to the cantilever that has a maximum strain at the base and is close to zero at the tip of the cantilever, whereas the trampoline has a maximum at both ends but with opposing signs. The flower design (Figure 3.3c) was based on the design of Iannacci et al. (2015) to create a multimodal structure that can cover large bandwidths. Finally, the Cantilever array design (Figure 3.3d) combines several cantilever designs. Although they have fundamentally the same design, a numerical model (and optimization) that simultaneously simulates all cantilevers can be more challenging due to the computational cost.

This study used COMSOL multiphysics (COMSOL MULTIPHYSICS® V. 5.6, n.d.) versions 5.4 and 5.6 as the simulator. A transition between the versions was made during the execution of these activities because of the significant features added to the latter version. In COMSOL multiphysics, it is possible to couple different physics to be solved directly, in contrast of solving each physics iteratively. Three different types of physics are used to model an energy harvester: (i) solid mechanics, (ii) electrostatic, and (iii) electrical circuit. Figure 3.4 exemplifies, in a generic form, how all EHs are simulated. One end of the beam of the model was fixed by connecting it to a frame that was subsequently fully constrained or by directly constraining the face in contact with the fixture. All materials in the simulation were subjected to a body force of $\rho \cdot \ddot{x}_\mathrm{b}$, where ρ is the density of the material and $\ddot{x}_\mathrm{b}$ is the acceleration of the fixture. During optimization, the resistive load R_l can also be written as 10^{α}_{Rl}. All the models have one or more seismic masses suspended by one or more beams. The beams were covered with piezoelectric materials and an electrode. All seismic masses were meshed with quadratic serendipity tetrahedral elements with high maximum element size, high element growth, and low narrow edge resolution. This was done to lower the computational cost of the model because deformation os the seismic mass is usually negligible. Similar meshing was applied to the frame (better represented in Figure 3.3) if the geometry was present in the model. The beam and piezoelectric material are the main components of the model. Thus, they were meshed with much smaller prismatic or hexahedral quadratic serendipity elements.

Four main damping sources act upon MEMS-scale cantilever structures: drag, squeeze-force, support losses, and structural damping (DUTOIT; WARDLE; KIM, 2005). Since the prototypes in this work were tested in free space (e.g., not close to a wall) under atmospheric conditions, the drag force is the

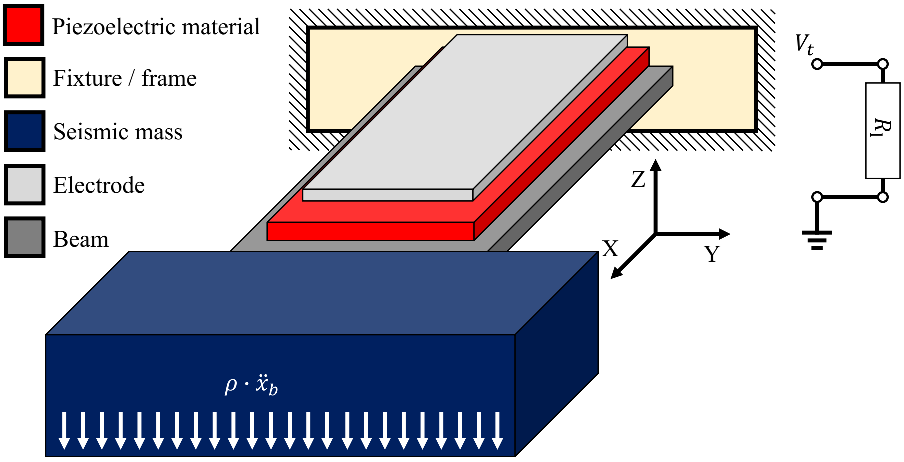

Figure 3.4 – Diagram of generic numerical model used in all optimizations.

dominant term. Therefore, a simplification is made, assuming the structural damping factor added to the numerical model can serve as an equivalent total damping factor. Thus, the following equations are applied to obtain the relationship between the viscous damping ratio ξ and the structural damping ratio η (COMSOL MULTIPHYSICS® V. 5.5, 2020),

$$Q \approx \frac{1}{2\xi} \tag{3.3}$$

and

$$\eta \approx 2\xi, \tag{3.4}$$

where Q is the quality factor. Both equations are valid only for $\xi \ll 1$, and Equation 3.4 is valid only at resonance (COMSOL MULTIPHYSICS® V. 5.5, 2020). Since Equation 3.4 is valid for the resonance, it is understood that the structural damping applied in COMSOL does not properly reflect the damping of the experiments but is a valid form of defining an equivalent damping model. Hence, the damping added to the numerical model was $1/Q$.

The two previous paragraphs comprise only solid mechanics physics applied to all materials in the model. On the other hand, electrostatic physics is applied only on piezoelectric films. Two constraints are considered in this physics: ground and terminal constraints. The face of the piezoelectric material in contact with the beam is the ground, which means that the face has a fixed value of 0 V. The face of the piezoelectric material in contact with the electrode on top of it is the terminal of the type of "circuit" imposing a total charge constraint associated with the current in the electrical circuit physics. This current couples the electrostatic domain with an electrical circuit via an "external I-terminal". This feature connects an arbitrary voltage-to-ground V_t measurement (in the electrode) as a voltage-to-ground assignment to a node in the electrical circuit. The resulting circuit current from the node is typically coupled back as a prescribed current source in the context of voltage measurement (COMSOL MULTIPHYSICS® V. 5.4, 2019). The total power is calculated using the COMSOL function "realdot(a, b)", which treats complex numbers a and b as if they were real-valued vectors of length two and returns their dot product. Thus, the power is obtained via the COMSOL equation $\frac{1}{2}\mathrm{realdot}(\mathrm{cir.R1_v}, \mathrm{cir.R1_i})$, where $\mathrm{cir.R1_v}$ and $\mathrm{cir.R1_i}$ are the voltage and current in the restive load R_l, respectively.

The simulation can be solved using two different methods: direct or modal analysis. A significant feature was added to COMSOL 5.6, regarding these solving methods. COMSOL 5.6 can solve the entire model with fully coupled physics using direct or modal analysis, whereas COMSOL 5.4 could not fully couple the electrical circuit physics when performing a modal analysis. Therefore, before the transition between versions, using modal analysis implied the need for another equation to calculate the power. This created a momentary need to uncouple the numerical model from the electrical circuit to calculate the resulting V_t. This is done by considering the system representation in Figure 3.5.

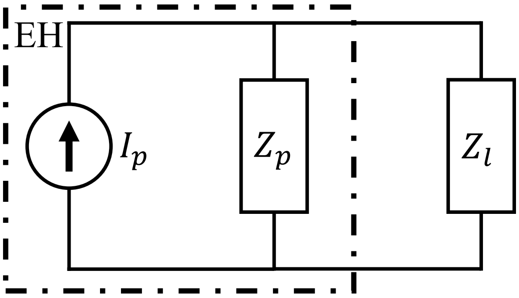

Figure 3.5 – Diagram of concentrated parameters of EH system connected to an impedance Z_l.

This diagram associated with the one in Figure 3.4, the load impedance can be reduced to a resistor $Z_\mathrm{l} = R_\mathrm{l}$, whereas Z_p is the capacitive impedance of the piezoelectric material,

$$Z_\mathrm{p} = \frac{1}{i\omega C_\mathrm{p}}, \tag{3.5}$$

where C_p is the capacitance of the piezoelectric material calculated using the numerical model. Finally, I_p is the current generated by the piezoelectric. Solving the circuit for the voltage across Z_l, it can be written

$$V_\mathrm{l} = \frac{V_\mathrm{p}\ Z_\mathrm{l}}{Z_\mathrm{l} + Z_\mathrm{p}}, \tag{3.6}$$

where V_p is the voltage at the terminal of the numerical model. The power is

$$P = \frac{V_\mathrm{rms}^2}{Z_\mathrm{l}} = \frac{V_\mathrm{l}^2}{2\ Z_\mathrm{l}}. \tag{3.7}$$

Combining Equations 3.5, 3.6, and 3.7, we get

$$P = \frac{\left(\frac{V_\mathrm{p} \cdot R_\mathrm{l}}{R_\mathrm{l} + \frac{1}{i\omega C_\mathrm{p}}}\right)^2}{2\ R_\mathrm{l}}. \tag{3.8}$$

Using Equation 3.8,the uncoupled power of the EH for a resistive load of value R_l can be calculated. This can only be used for a high R_l because the numerical model assumes an open circuit between the terminal and ground. If several independent terminals exist (the case with trampoline, flower, and cantilever array), V_p is calculated by

$$V_\mathrm{p} = \frac{|V_1| + |V_2| + \cdots + |V_\mathrm{n}|}{\sqrt{2}}, \tag{3.9}$$

where n denotes the total number of terminals in the model. This equation assumes loss-free rectification of each terminal separately to avoid energy loss due to the phase difference between each terminal.

3.1.1 MEMS Energy Harvester

Each numerical model has particularities, such as different materials and geometric parameters. The MEMS PVEH's beams and seismic masses presented here are made of Silicon, the piezoelectric material is made out of AlN and the electrode is aluminum. All those materials are used as fixed constraints from the MEMSCAP's PiezoMUMPs fabrication process, where the detailed steps are presented in Section 5.1. All three materials were initially modeled with the available material library from COMSOL. Aluminum is an isotropic material with a young modulus of 70 GPa and a density of 2700 kg/m^3. Silicon is an orthopedic material with the same properties as presented by Hopcroft, Nix, and Kenny (2010). AlN has $Y_{11} = 410$ GPa, piezoelectric coefficient $d_{31} = 1.9$ pC/N, relative permittivity $\epsilon_{33} = 10$, and density of 3300 kg/m^3. The main difference between the models is the parameterization and meshing of the beams. All designs shown in Figure 3.3 were built as MEMS devices. The first parameterized geometry presented here is the cantilever MEMS (Figure 3.6).

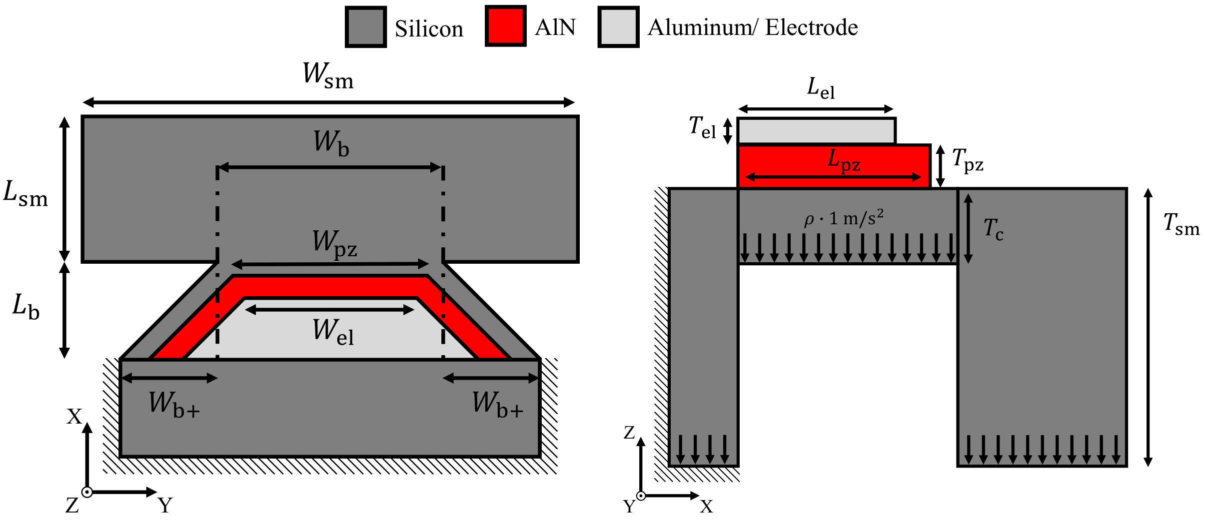

(a) Top view.

(b) Side view.

Figure 3.6 – Diagram of the geometrical parameters of the MEMS Energy Harvester numerical model.

Initially, this geometry was defined on the basis of 13 parameters: seismic mass width W_{sm}, beam width W_{b}, piezoelectric material width W_{pz}, electrode width E_{el}, increment to base width $W_{\mathrm{b+}}$, length of seismic mass L_{sm}, length of beam L_{b}, length of piezoelectric material L_{pz}, length of electrode L_{el}, the thickness of seismic mass T_{sm}, the thickness of beam T_{b}, the thickness of piezoelectric material T_{pz} and thickness of electrode T_{el}. The piezoelectric and electrode could have an independent parameter equivalent to $W_{\mathrm{b+}}$. However, to reduce parameters, their increment to base width is proportional to $W_{\mathrm{b+}}$ in the interest of keeping a steady distance from the border of one film to the other. The cantilever array design is equal to the cantilever, but all parameters are multiplied by the number of cantilevers. The trampoline design follows the same reasoning as if four cantilevers shared the same seismic mass. This way, has almost the same parameters as the cantilever, but the beam, piezoelectric, electrode length, width, and thickness are quadrupled, and $W_{\mathrm{b+}}$ is fixed at zero. Finally, because of its complexity, the flower design has a piezoelectric material and electrode covering the same area as the beam. The parameters of the model are shown in Figure 3.7.

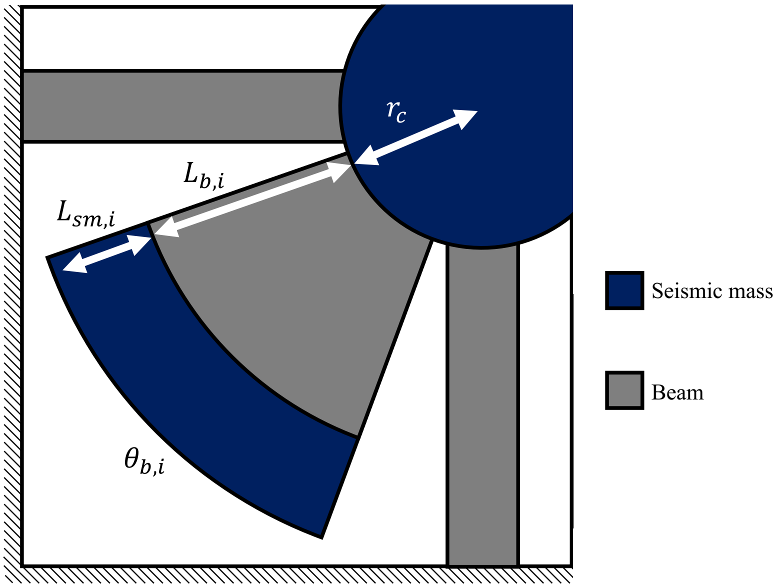

Figure 3.7 – Diagram of one section of the flower PVEH.

For better understanding, the diagram focuses on only one section of the structure. The total size of the device is equal to

$$L_{\text{total}} = 2 \max_{i \in n}(L_{\text{b,i}} + L_{\text{sm,i}}) + 2\, r_{\text{c}}, \tag{3.10}$$

where $L_{\text{b,i}}$ and $L_{\text{sm,i}}$ are the length of the i^{th} beam and seismic mass, n is the set of all four beams + seismic mass, r_{c} is the radius of the central seismic mass and $\theta_{\text{b,i}}$ is the angle of the i^{th} beam + seismic mass. All four MEMS designs share the same method of mesh built with the same type of elements. They use prismatic quadratic serendipity elements with a maximum-allowed size of $\min_{i \in n}(L_{\text{b,i}})/10$.

3.1.2 Micromachined Energy Harvester

As an alternative to MEMS technology, it is possible to build vibrational energy harvesters using off-the-shelf piezoelectric sheets. Three sources were analyzed: (i) PIEZO.COM, (ii) STEMINC, and (iii) Smart Materials. These three each have a corresponding parameterized numerical model. PIEZO.COM offers several possibilities for piezoelectric material. The beams from PIEZO.COM used in this work for numerical modeling only are the piezoelectric bimorphs using PZT-5H. This material is used for its higher piezoelectric effect and electromechanical coupling. The bimorphs comprise a PTZ-5H, a brass beam, and an electrode of a negligible thickness (according to the manufacturer). The material properties used here are shown in Table 3.2. PIEZO.COM materials were modeled and optimized because they offer bimorph sheets adequate for micromachining and good piezoelectric performance, as shown in the work of Roundy (2003). Nevertheless, the materials were not acquired for testing due to commercial difficulties.

Table 3.2 – Material properties of PIEZO.COM sheet.

Brass	Density	ρ kg/m^3	8300
	Young modulus	E GPa	100
PZT-5H	Density	ρ kg/m^3	7800
	Elastic constants	E_3 GPa E_1 GPa s_{55} TPa^{-1}	49 62 52.4
	Poisson's ratio	ν	0.31
	Piezoelectric coefficient	d_{33} pC/N d_{31} pC/N d_{15} pC/N	650 -320 1000
	Permittivity	e^{σ}_{r33} e^{σ}_{r11}	3800 -

Three matrices should be supplied in one of two ways to describe a iezoelectric material: the strain-charge or stress-charge form. The strain-charge is composed of the matrix of the piezoelectric coefficient in the strain-charge form $\boldsymbol{d}$, compliance matrix $\boldsymbol{s}^{\mathbf{E}}$, and the matrix of relative permittivity at constant stress $\boldsymbol{\varepsilon}_{\boldsymbol{r}}^{\boldsymbol{\sigma}}$. The stress-charge uses the matrix of piezoelectric coefficients in the stress-charge form $\boldsymbol{e}$, elasticity matrix $\boldsymbol{c}^{\mathbf{E}}$, and the matrix of relative permittivity at constant strain $\boldsymbol{\varepsilon}_{\mathbf{r}}^{\boldsymbol{\delta}}$. Usually, not all the properties of a single set of matrices are available. Therefore, the following equations can be used to get a matrix from the strain-charge form properties of the stress-charge form, and vice versa (COMSOL MULTIPHYSICS® V. 5.5, 2020):

$$\boldsymbol{c}^{\mathbf{E}} = \boldsymbol{s}^{\mathbf{E}^{-1}}, \tag{3.11}$$

$$\boldsymbol{e} = \boldsymbol{d}\, \boldsymbol{s}^{\mathbf{E}^{-1}}, \tag{3.12}$$

$$\boldsymbol{\varepsilon}^{\boldsymbol{\delta}} = \varepsilon_0\, \boldsymbol{\varepsilon}_{\mathbf{r}}^{\boldsymbol{\delta}} = \varepsilon_0\, \boldsymbol{\varepsilon}_{\boldsymbol{r}}^{\boldsymbol{\sigma}} - \boldsymbol{d}\, \boldsymbol{s}^{\mathbf{E}^{-1}}\, \boldsymbol{d}^{T}, \tag{3.13}$$

where $\boldsymbol{\varepsilon}^{\boldsymbol{\delta}}$ is the matrix of permittivity at a constant strain, ε_0 is the vacuum permittivity, the superscript ^{T} indicates the transposed matrix. The most common available parameters are $\boldsymbol{c}^{\mathbf{E}}$, $\boldsymbol{d}$, and $\boldsymbol{\varepsilon}_{\boldsymbol{r}}^{\boldsymbol{\sigma}}$, so it is easier to work in the strain-charge form and have the compliance matrix calculated by the elasticity properties. PZT-5H is a transversely isotropic material (OU; WU, 2003) with 4mm crystal symmetry (KHOLKIN; PERTSEV; GOLTSEV, 2008); thus, its compliance matrix, permittivity matrix, and piezoelectric coefficients can be represented as (DING; CHEN; ZHANG, 2006; MAITZLER et al., 1988)

$$\boldsymbol{s}^{\mathbf{E}} = \begin{bmatrix} \frac{1}{E_1} & -\frac{\nu_{12}}{E_1} & -\frac{\nu_{31}}{E_3} & 0 & 0 & 0 \\ -\frac{\nu_{12}}{E_1} & \frac{1}{E_1} & -\frac{\nu_{31}}{E_3} & 0 & 0 & 0 \\ -\frac{\nu_{13}}{E_1} & -\frac{\upsilon_{13}}{E_1} & \frac{1}{E_3} & 0 & 0 & 0 \\ 0 & 0 & 0 & \frac{1}{G_{13}} = s_{55} & 0 & 0 \\ 0 & 0 & 0 & 0 & \frac{1}{G_{13}} = s_{55} & 0 \\ 0 & 0 & 0 & 0 & 0 & \frac{1}{G_{12}} \end{bmatrix}, \tag{3.14}$$

$$\boldsymbol{d} = \begin{bmatrix} 0 & 0 & 0 & 0 & d_{15} & 0 \\ 0 & 0 & 0 & d_{15} & 0 & 0 \\ d_{31} & d_{31} & d_{33} & 0 & 0 & 0 \end{bmatrix}, \tag{3.15}$$

and

$$\boldsymbol{\varepsilon}_{\boldsymbol{r}}^{\boldsymbol{\sigma}} = \begin{bmatrix} \varepsilon_{11} & 0 & 0 \\ 0 & \varepsilon_{11} & 0 \\ 0 & 0 & \varepsilon_{33} \end{bmatrix}, \tag{3.16}$$

where

$$G_{12} = \frac{E_1}{2(1+\nu_{12})}. \tag{3.17}$$

The piezoelectric material properties are not fully described in Table 3.2 because some coefficients are missing. ε_{11}, ν_{12}, ν_{13}, and ν_{31} are not given; therefore, some simplifications must be made. ε_{11} is replaced by the same coefficient from the COMSOL library, and the following approximation is made $\nu_{12} = \nu_{13} = \nu_{31} = \nu$.

Figure 3.8 shows a schematic representation of the numerical model and some boundary conditions. The electrode in this model can be neglected; therefore, the terminal is selected as the piezoelectric region's exterior face, highlighted in blue. The upper and lower piezoelectric films are connected in parallel, e.g., the terminals are connected to the same node V_{t}. The purpose of seismic mass is to add mass to the system; thus, it could be made of any high-density material to decrease the active volume needed. This model used the identical element sizes as the MEMS models. However, the element type is hexahedral because it reduces the overall number of DoFs without losing accuracy, as shown in Appendix B. The MEMS devices use prismatic elements because it is easier to mesh the beam's face with triangular elements when the piezoelectric film is free to alter length and width over the beam.

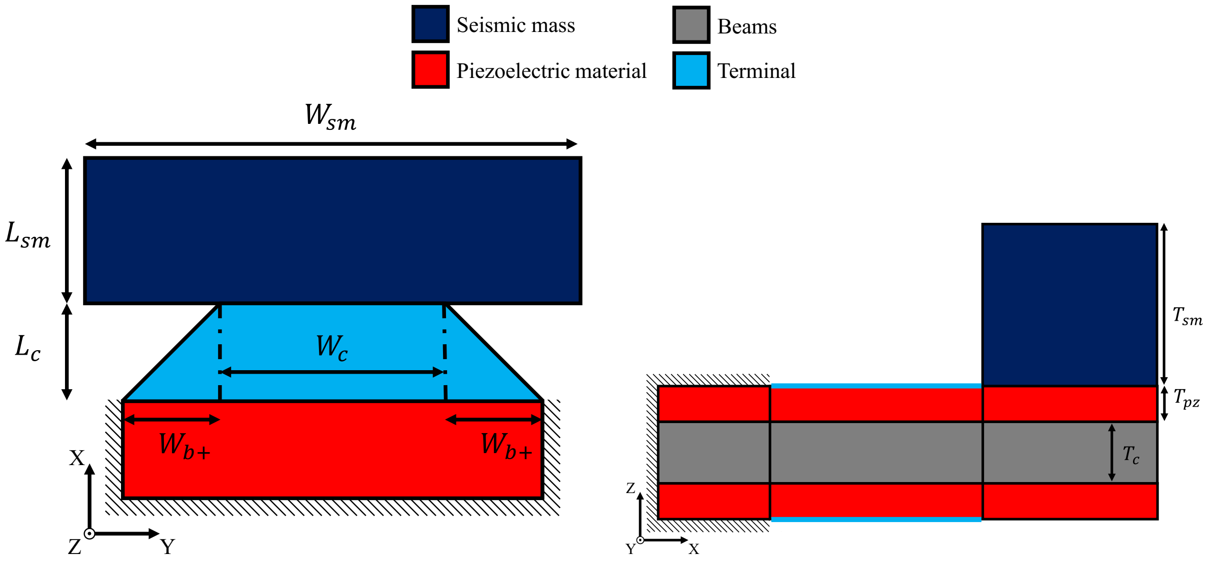

(a) Top view.

(b) Side view.

Figure 3.8 – Diagram of the geometrical parameters of the PIEZO.COM Energy Harvester numerical model.

The model that used STEMINC's films (with PZT-5H) uses the same geometries and Boundary Conditions (BCs) as in Figure 3.8. Table 3.3 shows the material properties supplied by the manufacturer. The beam's material and properties were not supplied; therefore, its properties are taken from the work of Rhimi (2013), which worked with the equivalent bi-morph beams. All other unavailable properties were assumed equal to PIEZO.COM's material, i.e., Poisson's ration and s_{55}.

Table 3.3 – Material properties of STEMINC's film.

Beam	Density	ρ kg/m^3	8900
	Young modulus	E GPa	11
PZT-5H	Density	ρ kg/m^3	7800
	Elastic constants	E_3 GPa E_1 GPa s_{55} TPa^{-1}	53 72 -
	Poisson's ratio	ν	-
	Piezoelectric coefficient	d_{33} pC/N d_{31} pC/N d_{15} pC/N	600 -270 -
	Permittivity	$\varepsilon^{\sigma}_{r33}$ $\varepsilon^{\sigma}_{r11}$	3500 -

The final material investigated here is the Macro Fiber Composite (MFC) films by Smart Materials. Figure 3.9 displays the composition of the MFC. It is a composite material made from rectangular ceramic rods aligned and fixed with an epoxy matrix sandwiched between electrodes, kapton, and acrylic (KHAZAEE; REZANIAKOLAIE; ROSENDAHL, 2020).

The numerical model is detailed in Figure 3.10, where the active area is composed of the same material layers as shown in Figure 3.9, and the passive area is composed of a single layer of kapton of the same thickness as the active area. Two MFC films are glued to a beam made from FR4 to form a bi-morph, and a seismic mass is positioned at the film's end. The material properties used in this model are shown in Table 3.4.

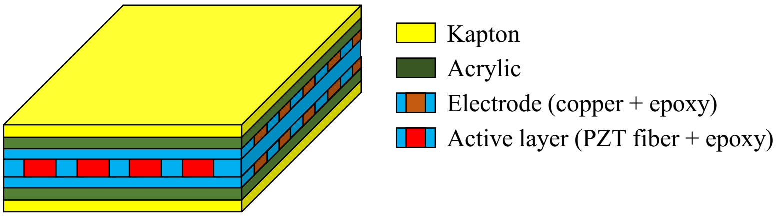

Figure 3.9 – Diagram of one section of the flower PVEH.

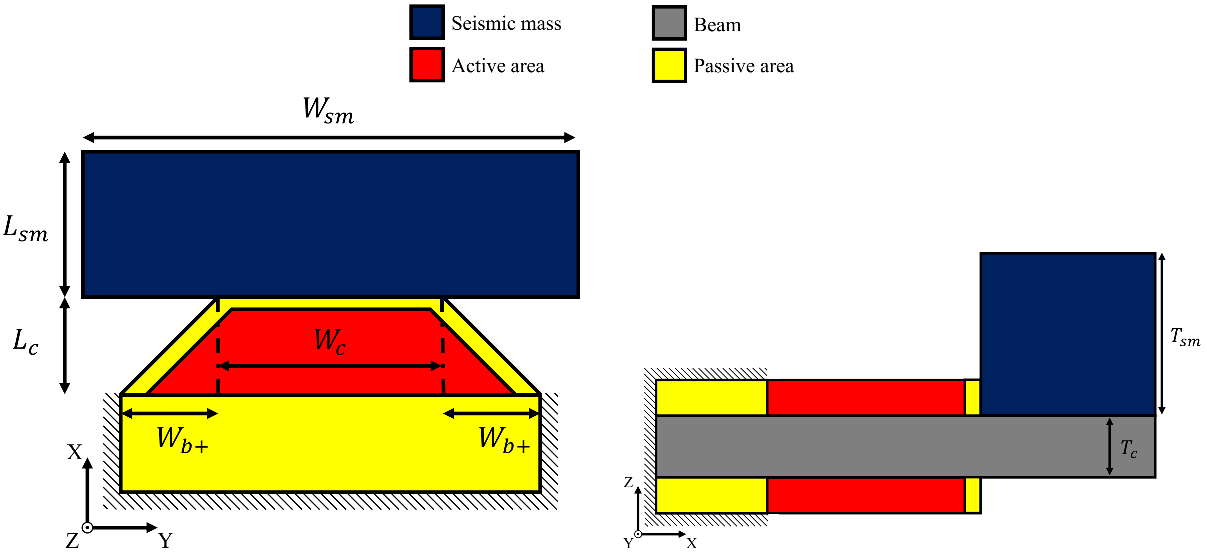

(a) Top view.

(b) Side view.

Figure 3.10 – Diagram of the geometrical parameters of the MFC Energy Harvester numerical model.

Table 3.4 – Material properties of MFC films (Obtained from Khazaee, Rezaniakolaie, and Rosendahl (2020))

Properties	PZT fiber	Epoxy	Copper	Acrylic	Kapton	FR4
Young's modulus (Gpa)	$E_1 = 53$ $E_2 = 61$	3.378	117.2	2.7	2.5	22
Shear modulus (Gpa)	$G_{12} = 12$ $G_{23} = 22.6$ $G_{13} = 22.6$	-	-	-	-	-
Poisson's ratio	$\nu_{12} = 0.384$ $\nu_{23} = 0.35$	0.27	0.31	0.35	0.34	0.15
Density (kg/cm^3)	7750	1400	8960	1185	1420	1900
Coupling charge (pC/N)	d_{31} = -167.28	-	-	-	-	-
Relative permitivity	1850	-	-	-	-	-

Two layers are composed of fibers fixed with an epoxy matrix, e.g., the active and electrode layers are modeled using an equivalent material with properties calculated using,

$$
\begin{aligned}
E_1 &= \mathscr{V}_f E_1^f + \left(1 - \mathscr{V}_f\right) E^m, \\
\frac{1}{E_2} &= \frac{\mathscr{V}_f}{E_2^f} + \frac{1 - \mathscr{V}_f}{E^m}, \\
v_{12} &= \mathscr{V}_f v_{12}^f + \left(1 - \mathscr{V}_f\right) v_{12}^m,
\end{aligned}
\tag{3.18}
$$

$$
\begin{aligned}
\frac{1}{G_{12}} &= \frac{\mathscr{V}_f}{G_{12}^f} + \frac{1-\mathscr{V}_f}{G^m}, \\
G_{13} &= \mathscr{V}_f G_{13}^f + (1-\mathscr{V}_f)\, G^m, \\
\frac{1}{G_{23}} &= \frac{\mathscr{V}_f}{G_{23}^f} + \frac{1-\mathscr{V}_f}{G^m},
\end{aligned}
\tag{3.19}
$$

where $\mathscr{V}_\mathrm{f}$ is the volume fraction of the fibers. Let us use superscripts ^{f} and ^{m} referring to the material properties of the fibers or matrix, respectively. Furthermore, the piezoelectric coefficients of the active layer can be calculated with,

$$
\begin{aligned}
d_{31} &= \frac{1}{E_1}\mathscr{V}_f d_{31}^f E_1^f, \\
d_{32} &= -d_{31}^f v_{12} + \mathscr{V}_f d_{31}^f E_1^f \left(1 + v_{12}^f\right), \\
\varepsilon_{33} &= \mathscr{V}_f \varepsilon_{33}^f.
\end{aligned}
\tag{3.20}
$$

Finally, the fiber's volume fraction of the active and electrode layers is shown in Table 3.5, in addition to the thickness of each layer.

Table 3.5 – Volume fraction, thickness and material of each layer of the MFC film.

Properties	Active layer	Electrode layer	Acrylic layer	Kapton layer
Fiber volume fraction	0.86	0.24	-	-
Layer thickness (µm)	177.8	17.76	12.7	25.4
Fiber material	PZT-5A	Copper	-	-
Matrix material	Epoxy	Epoxy	-	-

3.2 OPTIMIZATION SETUP

Three different algorithms are explored in this work and reviewed in Section 2.5: Differential Evolution (DE), Nelder-Mead (NM), and Surrogate Optimization (SO). DE is the "main optimization", e.g., the most used algorithm in this work and the first step of a two-step optimization procedure. DE is used to identify possible global minimums, and the other two (NM or SO) are used as a form of refined second-step optimization. This process can be arranged as in Figure 3.11. The first part of the optimization is performed with DE using a low-cost numerical model with a coarse mesh. In contrast, the second step performed by NM or SO uses a numerical model with heavy fine mesh. A mesh convergence analysis is presented in Appendix B shows that the mesh used in DE optimization has an approximate error of 0.6%. Depending on the total bandwidth and the application of the EHs, this error can be considered significant, so a second step is proposed and used on a case-by-case basis.

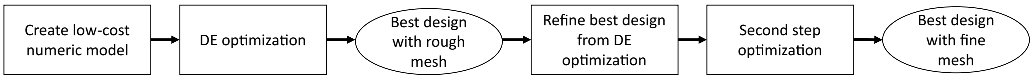

Figure 3.11 – Diagram of the two step optimization.

DE was chosen as the main optimization procedure since it has already been used for similar studies by our research group (MIRON; PAUL; CORDIOLI, 2022). Therefore, the parameters used here are the same as in previous works (GESING et al., 2018). The parameters are: Scale factor of 0.8, a crossover of 0.9, and an initial population of 10 N_{var}, where N_{var} is the number of parameters. The DE implemented in MATLAB (BUEHREN, 2014) is integrated with COMSOL following the diagram in Figure 3.12. The models presented in Section 3.1 are built here using the parameters from the initial trial vector. Their results are extracted to calculate the objective function that will rank each member at the selection stage. The following stages (mutation and crossover) will supply the next trial vector to feed the COMSOL models until the algorithm is stopped. The stopping criteria were 50 stall generations.

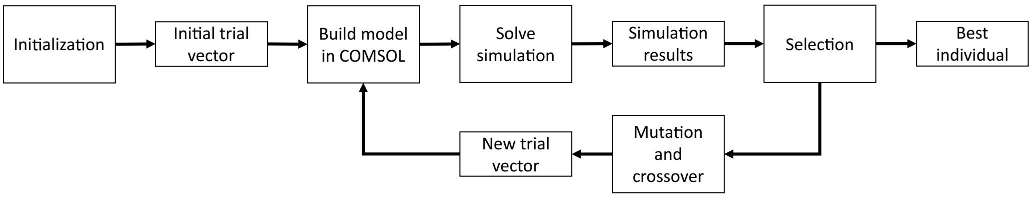

Figure 3.12 – DE optimization diagram.

NM and SO are implemented in MATLAB using the optimization functions "*fminserch*" and "*surrogateopt*", respectively. NM is a minimum-seeking algorithm that does not use derivative information; therefore, it is an attractive second-step optimization method. Nevertheless, contrary to DE's variables with discrete steps, NM allows only continuous variables, e.g., any parameter can assume any rational value within a given interval. Thus, it is necessary to introduce an adaptation to the procedure to avoid errors in the mesh construction due to extremely tiny features. The solution used in this case is to round the optimization variables. The smallest step possible is unitary; the smallest element needed would have 1 µm in size. *fminserch* is an unconstrained algorithm; therefore, another adjustment is necessary. Penalties are introduced to the objective function to avoid unfeasible designs. The penalized objective function can be considered as,

$$f_{\text{obj,pen}} = f_{\text{obj}} + \alpha \tag{3.21}$$

for

$$\alpha = \begin{cases} 0, & \text{if feasible} \\ 10^{20}, & \text{otherwise,} \end{cases} \tag{3.22}$$

where, $f_{\text{obj,pen}}$ is the penalized function, and f_{obj} is the original not penalized function (used in DE).

The *fminserch* algorithm allows changes to the stopping criteria but not to the search methods. Three parameters are set as stopping criteria: maximum iterations (*MaxInt*), termination tolerance on the function value (*TolFun*), and termination tolerance on x (*TolX*). NM finishes if the maximum number of iterations is reached or if both tolerances in the function value and x are met. For all NM optimizations it is used $MaxInt = 500$, $TolFunc = 10^{-4}$ and $TolX = 1$. Alternatively, *surrogateopt* can optimize both discrete and continuous variables, requiring no adaptation to the objective function (the same f_{obj} as DE can be used). The capability of optimizing continuous variables is especially interesting for the restive load and quality factor without a restriction imposed by the mesh.

Surrogateopt allows little changes in the search method or the surrogate creation. Other algorithms have been investigated, such as MATSUMOTO (MÜLLER, 2014) and MISO (MÜLLER, 2016). These algorithms can be more versatile in terms of surrogate creation. For example, MATSUMOTO can build the surrogate using different types of RBF, polynomial regression, Multivariate Adaptive Regression Spline, and mixed formulation of the previous methods. Although more versatile, MISO and MATSUMOTO do not allow linear inequality constraints, which are fundamental to impose restrictions such as maximum overall length, e.g., $L_{\text{c}} + L_{\sim\gg} \leq L_{\text{max}}$ where L_{max} is the maximum-allowed length of the device. The parameters used in *surrogateopt* are: the number of function evaluations before surrogate is updated is 1, the maximum number of objective functions evaluations is 200, maximum running time is two days, the minimum distance between trial points is 10^{-6}, and the minimum number of random sample points to crate at the start of a surrogate creation phase is $\max(20, 2\ N_{\text{var}})$.

3.3 PRELIMINARY MODEL VALIDATION

The first steps of model validation are performed using the experimental setup shown in Figure 3.13. A notebook [A] is connected to a Siemens LMS Scadas V8-E Data Acquisition (DAQ) system [B], where two input channels and one output channel are used. The first input channel is connected to a Polytec Laser Doppler Vibrometer (LDV) controller OFV-2500 with an OFV-534 sensor [C] that points to the prototype frame or fixture [D] to obtain the base acceleration. The prototype is then connected to a resistive load [E] in series with a B&K type 2692-C charge amplifier [F] connected to the second channel of the DAQ system. The output channel of the Scadas is connected to a power amplifier type 2735 from B&K [G] that feeds a B&K shaker type 4809 [D], where the prototype is attached.

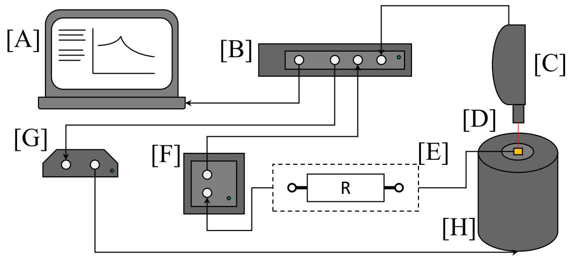

[A] – Notebook HP [B] – LMS Scadas [C] – Laser Doppler Vibrometer
[D] – Prototype [E] – Resistive Load [F] – Charge Amplifier
[G] – Power amplifier [D] – Shaker

Figure 3.13 – Diagram of experimental setup.

This work proposes two types of PVEH: the MEMS EH and the micromachined EH. Preliminary validation was performed on the MEMS EH model using a similar device of a different application (GESING et al., 2018). The same was done with the MM VEH models that were validated using the materials available in the laboratory before building an optimum design. Subsection 3.1.2 presents models using three different materials for the MM VEH. Of those, only the materials of STEMINC (Figure 3.14) and MFC (Figure 3.15) were bought for prototype building. The pictures included one real coin for size comparison. PIEZO.COM was modeled and optimized but not prototyped due to its price.

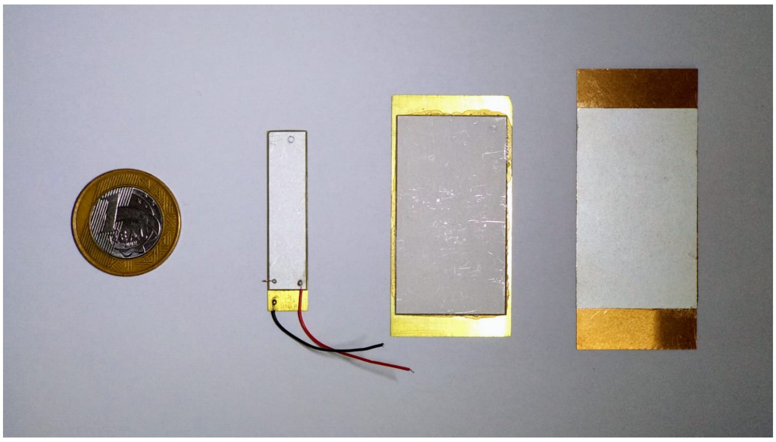

Figure 3.14 – Picture of the STEMINC films used for fabrication of micromachined piezoelectric Energy Harvester.

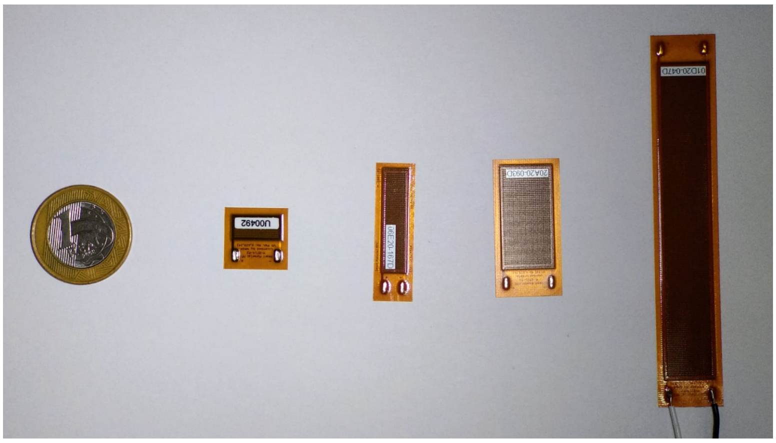

Figure 3.15 – Picture of the MFC films used for fabrication of micromachined piezoelectric Energy Harvester.

Two methods are used to fix the prototypes to the shaker, one for the MEMS devices and another for the micromachined. The MEMS devices are glued to aluminum blocks (Figure 3.16) for better transportation and can be easy fixed to the shaker. Here, the laser vibrometer (acceleration of the base reference point) is pointed to the frame of the MEMS. However, the micromachined devices are fixed to the shaker using a clamping structure as in Figure 3.17. Two materials were used as fixtures to clamp the bulk piezoelectric films, stainless steel, and 3D-printed ABS.

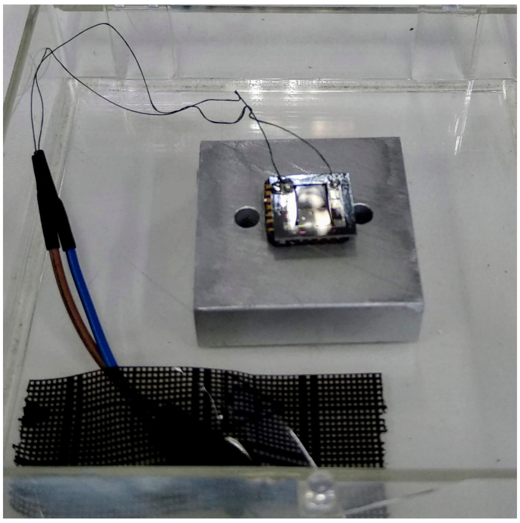

Figure 3.16 – Picture of the MEMS device bonded to an aluminum block.

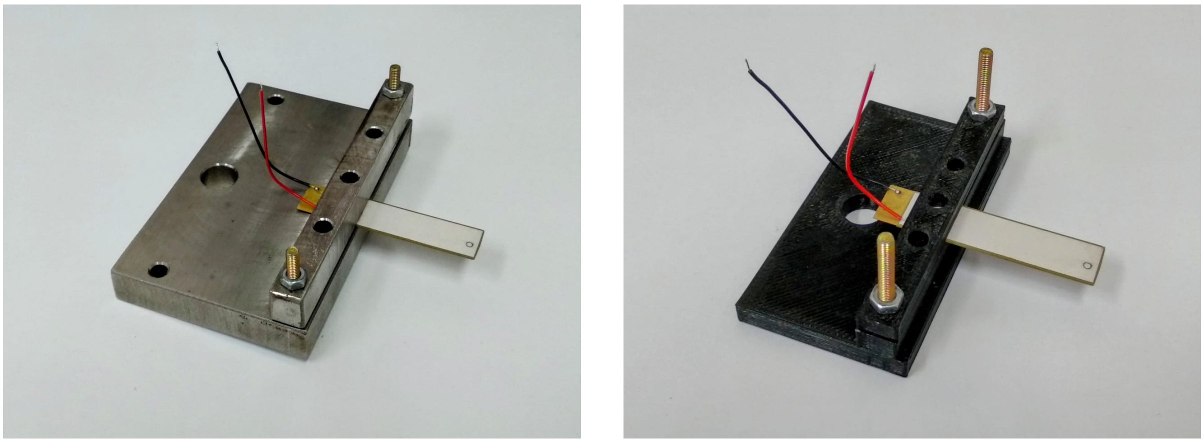

(a) Clamping base fabricated on stainless steel.

(b) Clamping base fabricated on ABS via 3D printing.

Figure 3.17 – Clamping fixtures used for fixing the Energy Harvesters cantilevers.

The clamping structure made from ABS was manufactured as an initial attempt to fix the EHs. However, this material is significantly flexible, rendering a fixture far from an ideal clamp condition. Because of that, the clamping of stainless steel was fabricated. Figure 3.18 shows the FRF response of a beam made from FR4 clamped at the same position by the ABS and steel clamps. It can be noted that the ABS introduces more flexibility to the system since the natural frequencies are lower than those observed for the steel clamp. Conversely, the steel clamp introduced some modes to the beam response that must be caused by the clamp's vibration modes, which are less attenuated than the ABS structure. Although the curves from the steel clamping are not free from fixture modes like the ABS, precisely pinpointing the natural frequency is more important to the validation process than having a clear curve. Therefore, steel clamping is used as the main fixture method to validate the numerical models.

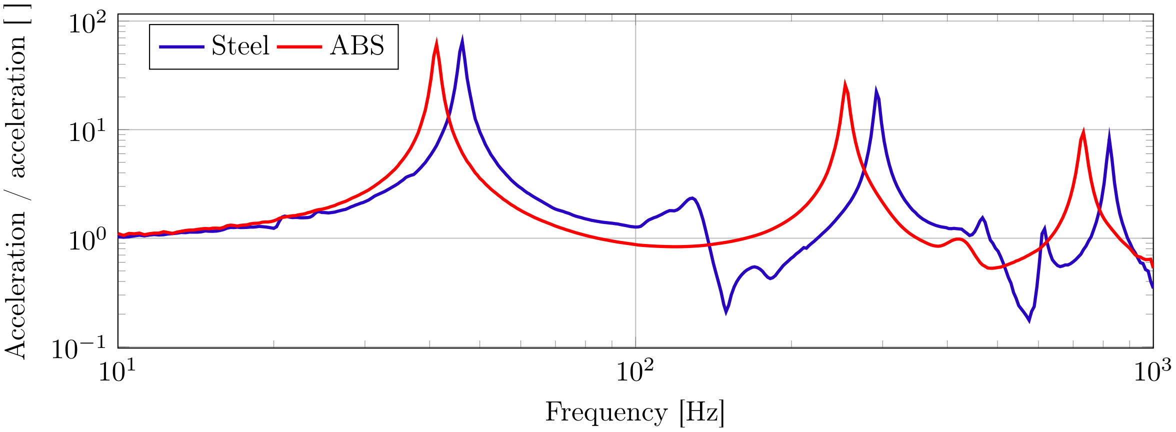

Figure 3.18 – Comparison of FRF of steel clamping compared to ABS clamping.

3.3.1 Initial validation of Micromachined VEHs

As discussed in the previous section, the MM VEH models can be prevalidated before running the optimization algorithms. With this aim, the SMBA bimorph (first material from left to right in Figure 3.14) was fixed to a shaker using a steel clamp, and its charge sensitivity was measured under three different scenarios. They are, with a seismic mass of 5.1 g positioned at the tip of the SMBA bimorph, a seismic mass of 10.2 g, and no seismic mass. Figure 3.19 shows the experimental data and the numerical model of the SMBA bimorph with different seismic masses after some material property adjustments.

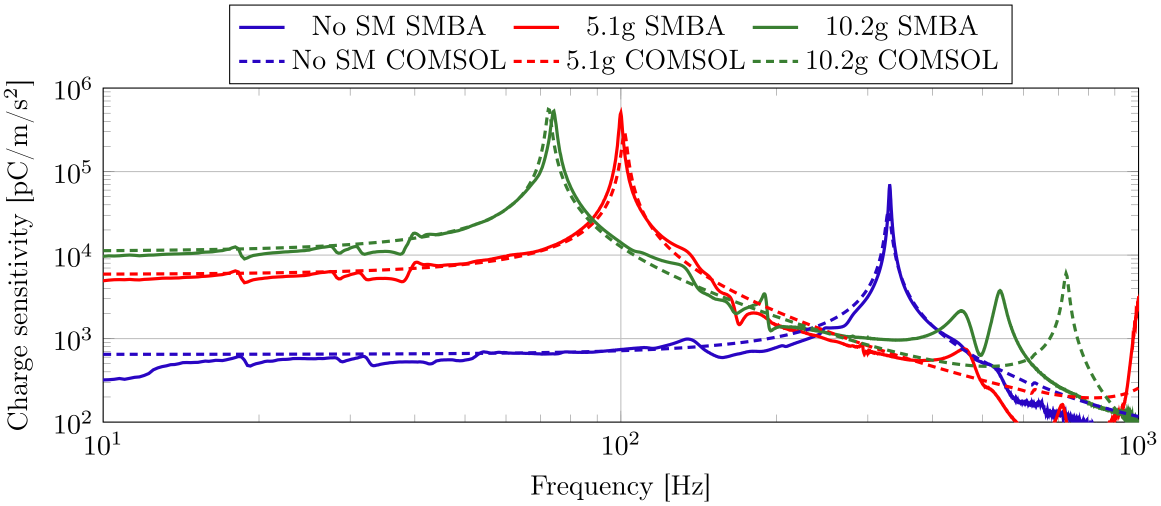

Figure 3.19 – Comparison of the experimental curves of the SMBA film compared with the numerical model in terms of charge sensitivity.

Adjustments to the materials are listed in Table 3.6. It is essential to highlight the significant drop in the coefficient d_{31} from -270 pC/N to -130 pC/N and the high density utilized in the beam material. Indeed, some material properties might not fit within the real material value; however, these properties fit well as an equivalent model.

Table 3.6 – Alterations in material properties of the SMBA bimorph.

Beam	Density	ρ kg/m^{3}	14000
PZT-5H	Elastic constants	E_1 GPa	85
	Piezoelectric coefficient	d_{31} pC/N	-130
	Damping coefficient	ξ	0.01

The MM VEH with MFC was built with two films glued to a central beam, as shown in Figure 3.10b. However, to validate the material properties, a unimorph beam was manufactured using FR4 and the larger MFC film, as shown in Figure 3.15. The experimental data and the numerical model are compared in Figure 3.20. The graph presents the use of the ABS fixture and the steel fixture. The same experiment was repeated for two days in a row, with the setup reassembled for each day. It shows how the fixture of steel presents better repeatability than ABS, which had a shift in natural frequency from day one to two. The COMSOL model associated with the sensitivity shown in Figure 3.20 already had the material properties adjusted. The adjusted material properties changed the piezoelectric coefficient of the active layer from -166 pC/N to -210 pC/N and added a damping of $\xi = 0.01$.

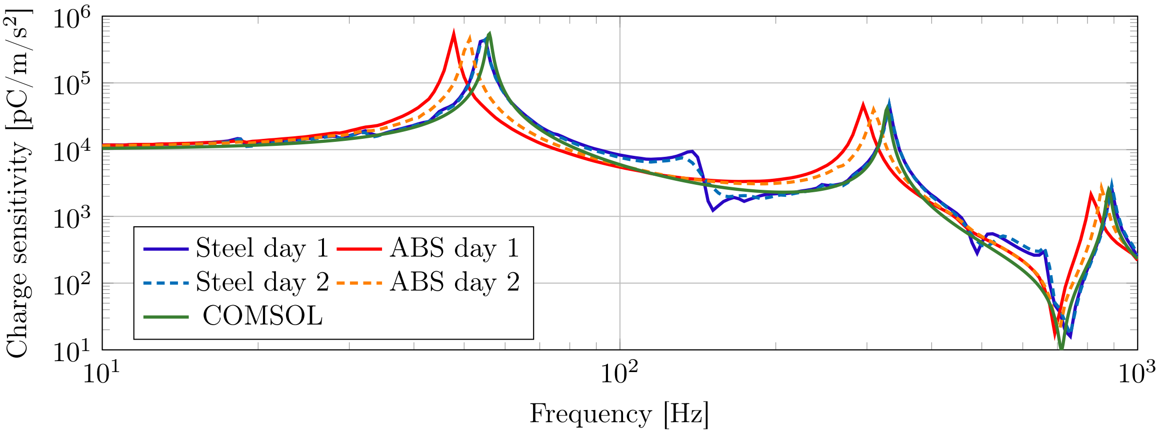

Figure 3.20 – Comparison of the experimental curves of the MFC film compared with the numerical model in terms of load sensitivity.

CHAPTER 4

OPTIMIZATION RESULTS

As mentioned in Section 3.2 the optimization process takes two steps: the rough mesh model using the Differential Evolution (DE) algorithm and finely meshed model using Nelder Mead (NM) or Surrogate Optimization (SO). This chapter presents the optimization results using all three algorithms focusing on the first step with DE.

4.1 PRELIMINARY OPTIMIZATIONS

The optimization process is initiated to perform a preliminary analysis of the possible designs and parameters that can be used during the procedure. In this study, the first and second batches of the procedures were performed. The first batch of preliminary optimization processes took the following objective function:

$$f_{\mathrm{obj}} = -\mathrm{P}(\mathrm{f}_1). \tag{4.1}$$

This objective function only considers the power at the frequency of interest (f_1 =60 Hz). The algorithm focuses on minimization, which is valid for all the optimization algorithms used in this study. It is why Equation 4.1 has a negative sign. This objective function was tested using different designs shown in Figure 4.1. The simple cantilever design (Figure 4.1a) and trampoline (Figure 4.1b) have a central seismic mass connected to a frame by four beams.

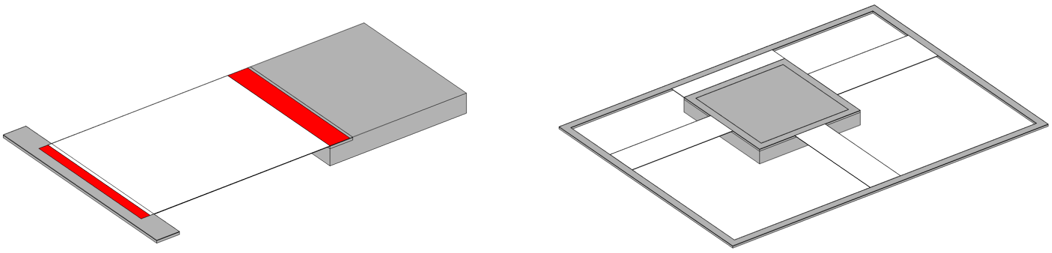

(a) Design with 1 cantilever with seismic mass at the end.

(b) "Trampoline" design.

Figure 4.1 – Optimums designs from first the batch of optimizations, where gray is the structure made from silicon, white is the electrode made from aluminum, and red is the piezoelectric material made from AlN.

These two models ran for 150 generations to analyze the convergence and progress up to this iteration. Figure 4.2 shows the objective function values during the optimization. The cantilever and trampoline models had 11 parameters for each optimization. The trampoline converged towards a local maximum and stayed there for more than 110 generations, while the cantilever maintained the best value for 40 generations.

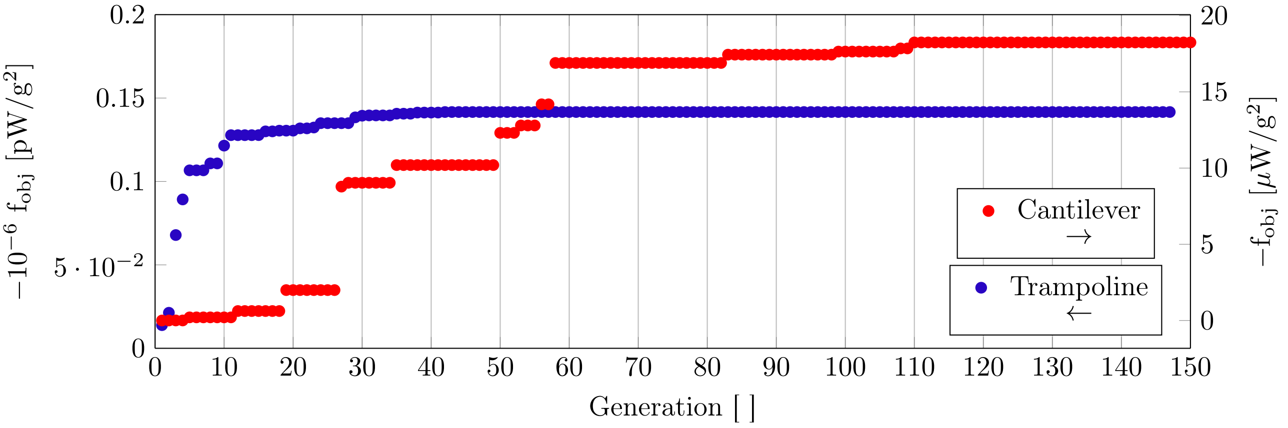

Figure 4.2 – History of objective function values during optimization of the cantilever and trampoline designs. The arrows in the legends indicate whether the corresponding curve is plotted on the left or right axis.

Figure 4.3 shows the normalized power for the optimized trampoline and cantilever models. The cantilever device centered the natural frequency at 60 Hz, whereas the first natural frequency of the trampoline was 610 Hz. The four cantilevers of the trampoline create excessive stiffness in the system for its natural frequency to reach lower values near the 60 Hz desired.

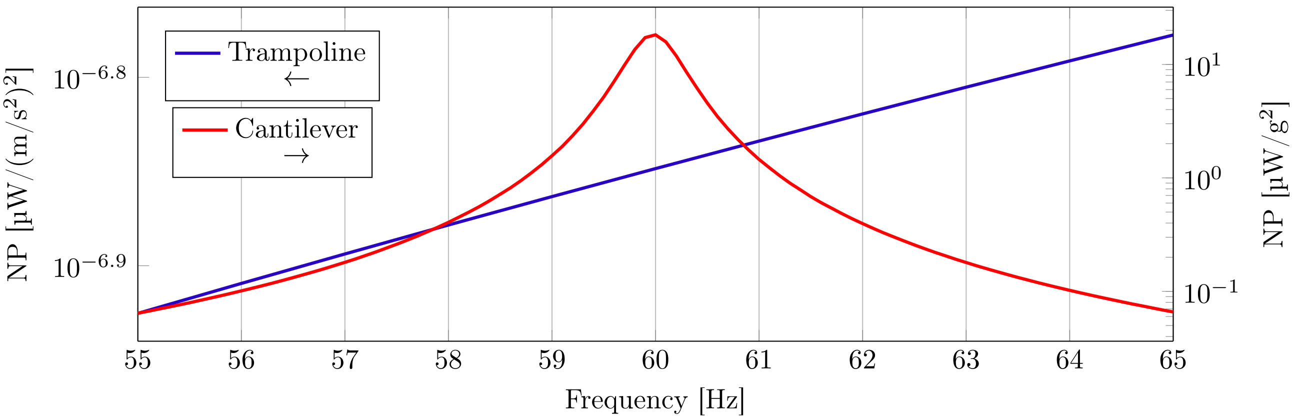

Figure 4.3 – Normalized power of the optimized numerical model trampoline and cantilever. The arrows in the legends indicate whether the corresponding curve is plotted on the left or right axis.

The initial quality factor chosen for the numerical optimization was 100 (Figure 4.4). This is a conservative first approach to optimization because MEMS piezoelectric energy harvesting approaches such values when packaged at atmospheric pressure (ELFRINK et al., 2010). A higher quality factor is expected from the prototype when compared to the numerical model, and consequently, it is expected to have higher power than predicted by the optimization. The normalized power of the cantilever design gave a maximum power of approximately 18 µW/g^2 and a total active volume of 8.47 mm^3, rendering a total NPD of 0.00015 mW/(cm^{3}g^2), which is considerably below the target. The maximum power increases to approximately 80 µW/g^2 using a more realistic 275 quality factor, which yields 0.00068 mW/(cm^{3}g^2) of NPD. The increase is significant, and the designs shown in Figure 4.5 will use this value.

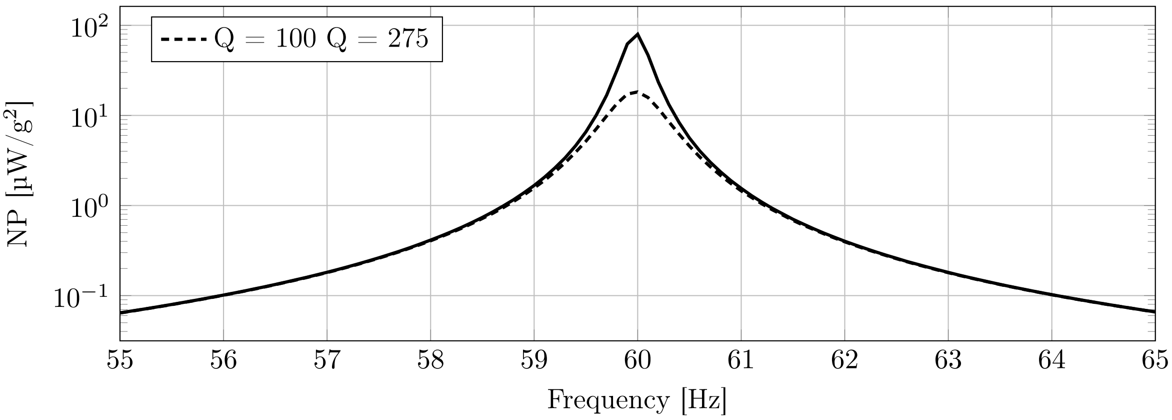

Figure 4.4 – Normalized power of optimized numerical model cantilever with different quality factors.

The possibility of using the cantilever array in the same model was investigated to implement a multimodal broadband technique during the optimization. The other designs used in these investigations are refered to as flower (Figure 4.5a) and are based on the work of Iannacci (2019) on a multimodal energy harvester. Moreover, the cantilever array (Figure 4.5b) design, in which six cantilever-style designs were modeled together. Because those designs are built so they can have several closes, but not equal, natural frequencies, the objective function is adapted to

$$f_{\text{obj}} = -\min(P(f_1 : f_2)). \tag{4.2}$$

In this manner, the algorithm attempts to maximize the minimum power inside the f_1 and f_2 frequency bands. For this purpose, an algorithm will be required to evenly distribute the vibration modes of the structure across the bandwidth. For this first multimodal optimization, f_1 was 55 Hz, and f_2 was 65 Hz.

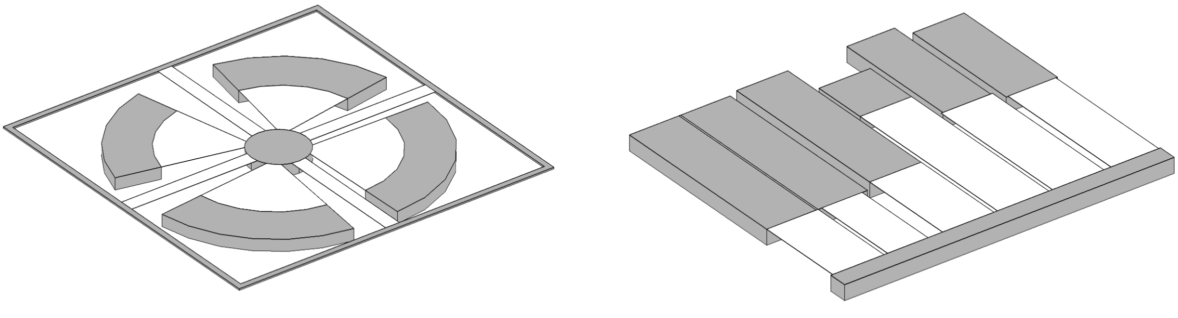

(a) "Flower" design based on (IANNACCI, 2019). (b) Cantilever array design made from 6 cantilevers side by side.

Figure 4.5 – Optimum designs from the first batch of optimizations, where gray is the structure made from silicon and white is the electrode made from aluminum.

The flower model has 14 parameters while the cantilever array has 26, and for that increased complexity, the flower and cantilever array ran for 200 generations. Figure 4.6 displays the values of the objective functions related to the generation. This step investigated the possibility of increasing the bandwidth of the harvester by combining these two structures.

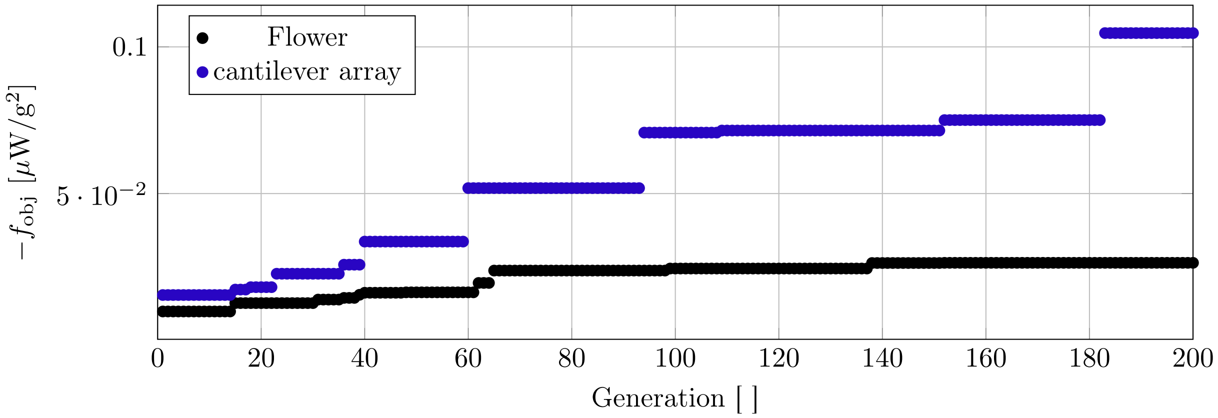

Figure 4.6 – History of objective function values during the optimization of flower design and cantilever array.

When comparing the flower with the cantilever array, we can see that the latter can increase the band of interest more easily. However, the additional parameters and complexity made the maximum NP of the cantilever better than that of the cantilever array, as shown in Figure 4.7. Alongside the reasoning from Section 3.1, this preliminary analysis exemplifies the reason for using cantilever-style designs that compose the rest of this work.

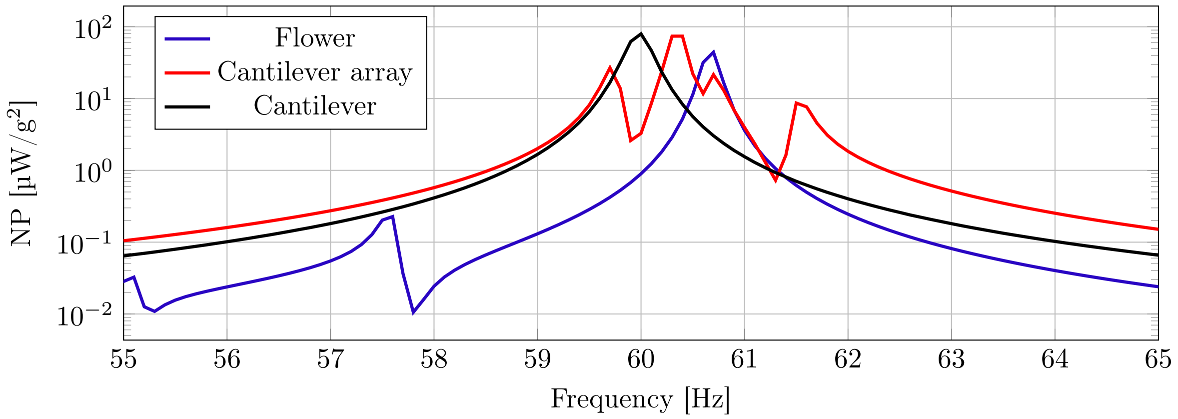

Figure 4.7 – Normalized power of optimized numerical model for flower, cantilever and cantilever array.

4.2 OPTIMIZING FOR MEMSCAP SPACE

After defining the cantilever model as the most promising design for the proposed application, manufacturing restrictions are now imposed more severely, and the target is well established. The overall device must fit into the allowed design space of the PiezoMUMPs process as detailed in Section 5.1. Therefore, a predefined area for the four cantilevers is specified as shown in Figure 4.8. The red areas represent the allowed optimization space for each of the four cantilevers. The blue area is the required TRENCH etching gap between cantilevers, and the white boxes are the areas left for wire-bonding the devices to the electrical measuring systems. The red areas have the following dimensions:

- Area A: 2.70 mm x 5.70 mm
- Area B: 2.75 mm x 5.65 mm
- Area C: 2.75 mm x 5.65 mm
- Area D: 2.25 mm x 6.50 mm

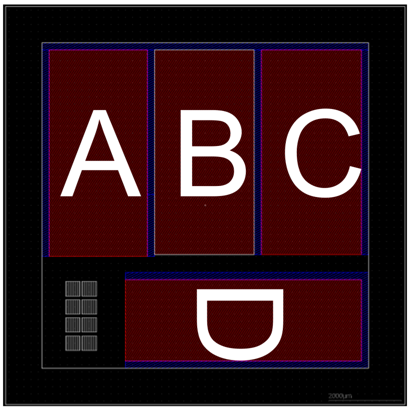

Figure 4.8 – Representation of how the space in the MEMSCAP die could be used highlighting the optimization space in red.

As defined in Table 1.1, the overall goal is to reach 160 µW with a 20 Hz bandwidth and a total size smaller than 7.7 mm x 25.5 ⌀ mm. This objective must be divided into smaller steps since the allowed design space of PiezoMUMPs is much smaller than the battery. The proposed new objective is a 20 µW with a 4 Hz bandwidth and a design space equal to the MEMSCAP die of 11.15 mm x 11.15 mm x 0.411 mm. With this objective, it is possible to build a device with several stacked MEMSCAP die-sized devices to achieve the desired goal. In this sense, it is proposed to develop five designs of the MEMSCAP die, each covering 4 Hz bandwidth, and then stack eight levels (of the same design) to reach the desired power and band.

This optimization stage was performed in two steps. The first step is the optimization of single cantilevers using areas B and D as restrictions and Equation 4.1 as the objective function. The result of this optimization was used as the initial geometry in the following step. The second step is the simultaneous optimization of all four cantilevers using the multimodal wideband method, with Equation 4.2 as the objective function and f_1 and f_2 equal to 58 and 62, respectively. Only areas B and D are used in step one because area B is identical (or close) to areas A and C. However, the same cannot be said for area D. Therefore, areas A and C can use the same initial geometry as area B or one with a lightly adjusted width, whereas area D needs its own initial geometry. Figure 4.9 shows the optimized design for areas B and D used as the initial geometry for step two.

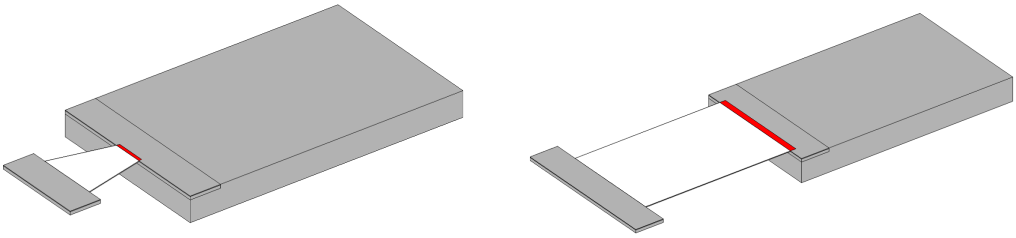
(a) Area B.

(b) Area D.

Figure 4.9 – Optimum designs from the first step of optimization for MEMSCAP space, where gray is the structure made from silicon, white is the electrode made from aluminum, and red is the piezoelectric material made from AlN.

Figure 4.10 shows the normalized power of the two designs and the objective. For the design to satisfy the objective, the NP should be entirely over the yellow box. Designs from areas B and D meet the requirements for approximately 0.58 Hz and 0.44 Hz bandwidth, respectively. Both devices were centered at 60 Hz as required.

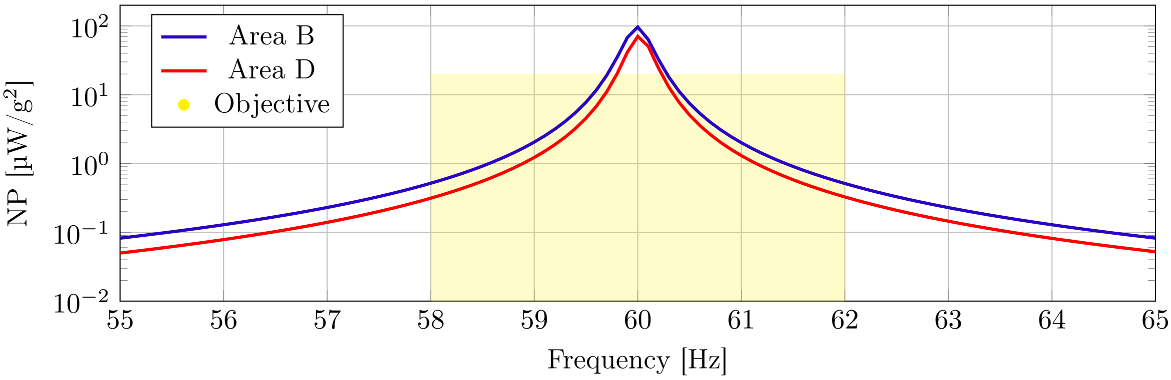

Figure 4.10 – Normalized power of optimized numerical model of area B e D.

The results of the second step are shown in Figure 4.11, where areas A to D are represented from left to right. Furthermore, the graph in Figure 4.12 is the sum of the rectified powers given by Equations 3.9 and 3.8. This design meets the power requirements for the frequency bands of 58.04 Hz to 58.76 Hz, 59.13 Hz to 59.58 Hz, and 59.95 Hz to 61.95 Hz. In other words, the device has approximately 4 Hz bandwidth with two small intervals of power deficiency between 58.76 Hz to 59.13 Hz and 59.58 Hz to 59.95 Hz. The total power deficiency is 0.74 Hz of 4 Hz of bandwidth.

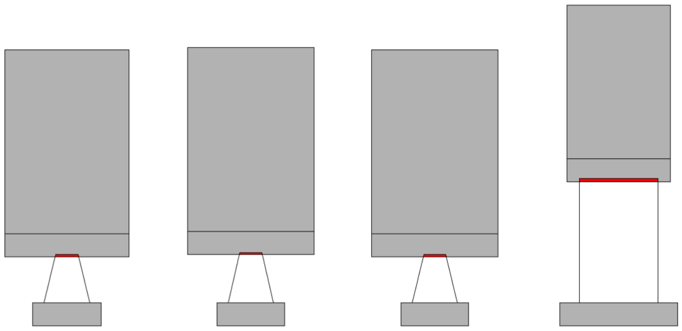

Figure 4.11 – Cantilever array final design, with areas A to D represented from left to right, where gray is the structure made from silicon, white is the electrode made from aluminum, and red is the piezoelectric material made from AlN.

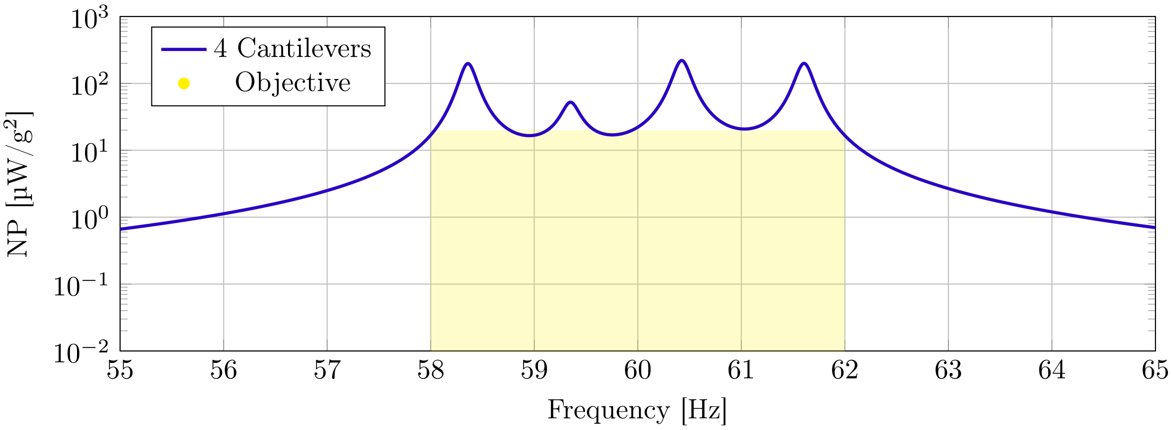

Figure 4.12 – Normalized power of the optimized cantilever array design, made to fit the MEMSCAP die.

The four natural frequencies were approximately 58.29 Hz, 59.33 Hz, 60.36 Hz, and 61.61 Hz. The vibration modes coupled to these natural frequencies are shown in Figure 4.13. The reason for the intervals of power deficiency is the device from area D, which has the first bending mode at 59.33 Hz but presents a lower power output than the other three devices. The only difference in the optimization between the four devices was the total allowed area. Area D had the smallest width but the largest length, suggesting an advantage for aspect ratios of larger widths and smaller lengths.

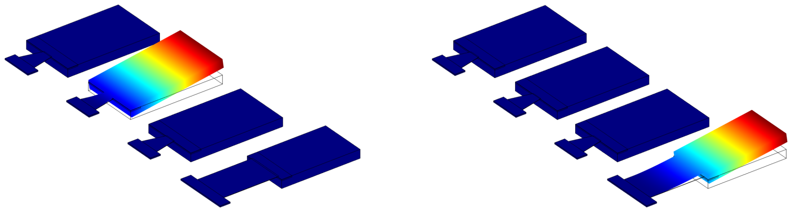

(a) First mode at 58.29 Hz. (b) Second mode at 59.33 Hz.

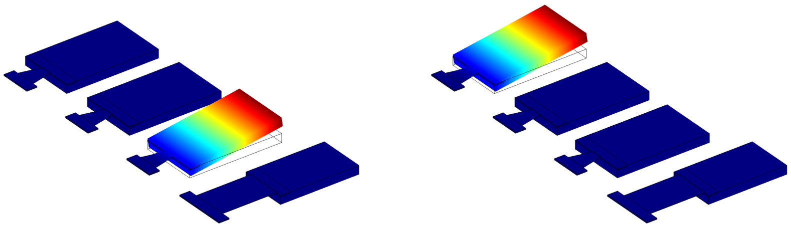

(c) Third mode at 60.36 Hz (d) Fourth mode at 61.61 Hz.

Figure 4.13 – Vibration modes of the four cantilever model.

All of these optimizations suffered from an objective function that was not properly restricted, although the requirements were almost met. The power of a piezoelectric energy harvester is directly proportional to the square of the induced stress in the piezoelectric material, as shown in Equation A.10 (Appendix A). Therefore, maximizing the power of a piezoelectric VEH without restricting, in any form, the induced stress in the piezoelectric material will most likely render it mechanically unfeasible designs. Figure 4.14 shows the stress field in the piezoelectric material of the cantilever from area C at its natural frequency

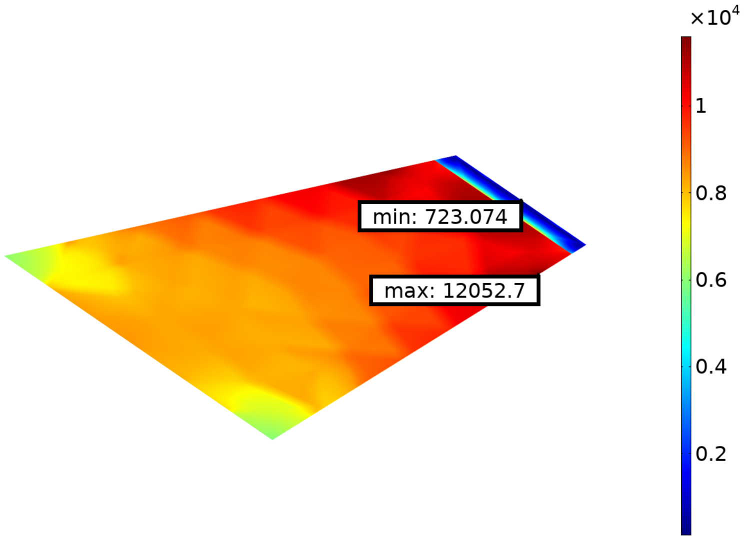

Figure 4.14 – Von-mises stress field in piezoelectric material of device from area C at 60.36 Hz in MPa.

of 60.36 Hz. Von-mises stress estimates possible device failure at 1 g of acceleration. This minimum and maximum values in this scenario are 723 MPa and 12 GPa, respectively. Considering the 300 MPa ultimate stress value for AlN (GANG ZONG et al., 2004) and the linear increase in the maximum stress, the device should be capable of withstanding up to only 0.025 g of acceleration.

4.3 OPTIMIZING IN TERMS OF NPD AND STRESS

The design and optimization process of Section 4.2 has some drawbacks in terms of design and optimization process, those are: (i) the power is directly proportional to the square of the stress in the piezoelectric, therefore there must be a mitigation component in the optimization function to prevent the stress from rising; (ii) it is essential important to establish an optimal acceleration point because the maximum stresses must be finely tuned to the intended accelerations imposed in the harvester and mechanical stoppers can be used to limit possible higher unwanted accelerations.; and (iii) the maximum width and length established in the optimization is critical to the final optimization result. All of those issues are addressed in this section.

Two different objective functions were proposed to address the stress problem. The first objective function addresses the stress as a penalty function,

$$f_{obj} = -P + \alpha_s \; 100 \; \frac{|\sigma_{\text{limit}} - \sigma_{\text{max,pz}}|}{\sigma_{\text{limit}}} + \alpha_f \; 100 \; \frac{|60 - f_{\text{n},1}|}{60}, \tag{4.3}$$

for

$$\alpha_s = \begin{cases} 0, & \text{if } \sigma_{\text{max,pz}} \leq \sigma_{\text{limit}} \\ 1, & \text{otherwise,} \end{cases} \tag{4.4}$$

and

$$\alpha_f = \begin{cases} 0, & \text{if } 55 \geq f_{\text{n},1} \leq 65 \\ 1, & \text{otherwise.} \end{cases} \tag{4.5}$$

Here, α_{s} is an auxiliary coefficient that indicating whether the maximum von-Mises stress in the piezoelectric film $\sigma_{\text{max,pz}}$ surpasses the maximum allowed stress σ_{limit}. The coefficient α_{f} indicates if the first natural frequency of the device $f_{\text{n},1}$ is within an acceptable bandwidth of 55 Hz to 65 Hz. Finally, the optimal acceleration point was maintained at 1g for being a typical magnitude used to measure these devices. The maximum width and length are established in Table 4.1, along with the other lower and upper boundaries of the following optimizations (box-constraints from optimizations that do not appear in the text are shown in Appendix C).

It is interesting to note that the quality factor is now used as a parameter of optimization because the high stresses are a vital aspect of the optimization process, and the damping of the structure can control the higher stresses that occur at the natural frequency. Most importantly, the quality factor can be a design parameter of the project since the damping of the structure can be altered by changing the internal pressure of the damping packaging (ELFRINK et al., 2010; MIRON; PAUL; CORDIOLI, 2022). The optimization started from the design of area B and finished in the device shown in Figure 4.15b using a modal analysis simulation running only at a frequency of 60 Hz.

Table 4.1 – Box-constraints for the optimization of MEMS A.

Parameter	Lower boundary	Upper boudary
W_{sm}	500 µm	2750 µm
W_{b}	500 µm	2750 µm
$W_{\mathrm{b+}}$	0 µm	500 µm
W_{pz}	500 µm	2750 µm
W_{el}	500 µm	500 µm
L_{sm}	2500 µm	4500 µm
L_{b}	500 µm	2000 µm
L_{pz}	500 µm	2000 µm
L_{el}	500 µm	2000 µm
Q	50	1000
α_{Rl}	5	8

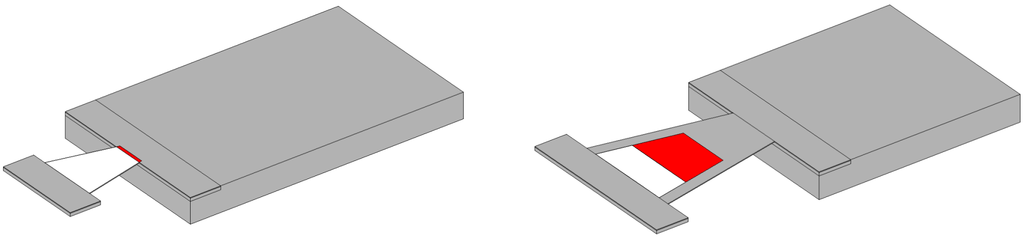

(a) Initial geometry.

(b) Final geometry.

Figure 4.15 – Initial and final geometries of the optimization of MEMS A.

The optimization ran for 124 generations, reaching its best value at generation 77, and remaining there for 47 generations. The graph starts at generation 16 because, before this generation, the best member was highly penalized, rendering $-f_{\mathrm{obj}}$ negative.

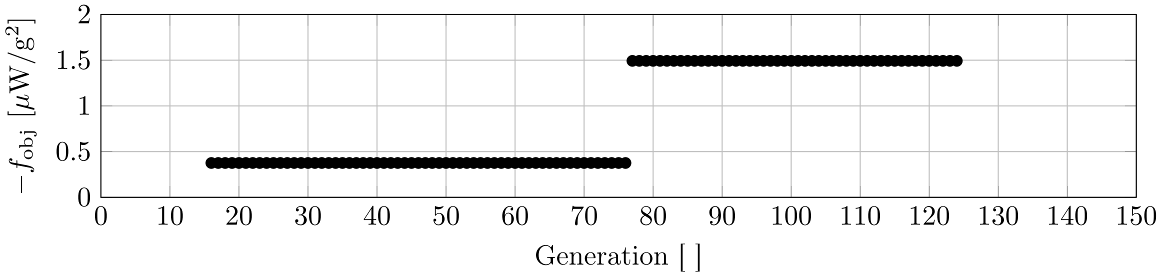

Figure 4.16 – History of objective function values during MEMS A design optimization.

The NP and $\sigma_{\mathrm{max,pz}}$ over the frequency range for this device are displayed in Figure 4.17. The following conclusions can be drawn from this simulation: (i) the first natural frequency is outside the allowed bandwidth even with the penalization introduced to the objective function; (ii) the stress levels for 60 Hz are within the allowed 300 MPa of von Mises Stress but are above around $f_{n,1}$; and (iii) allowing Q

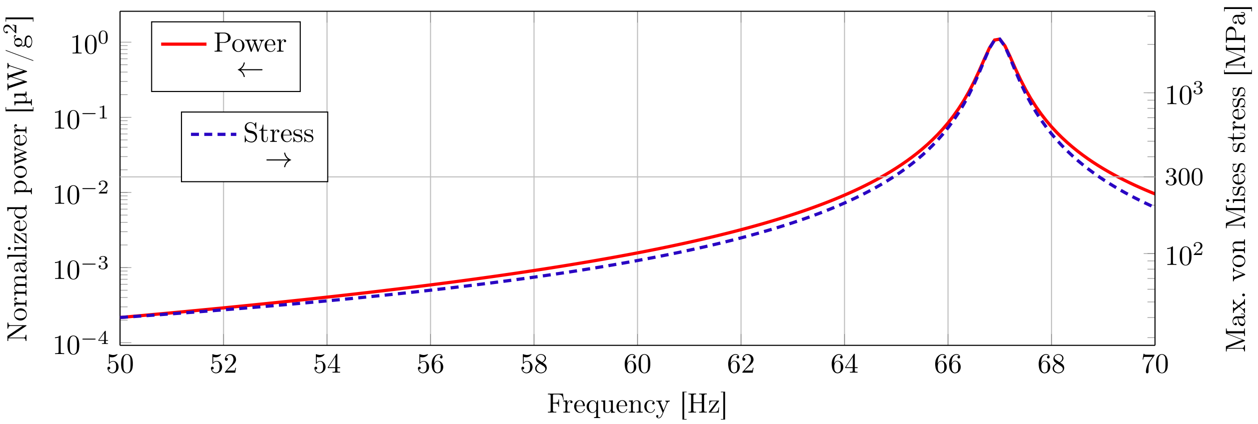

Figure 4.17 – Normalized power of the optimized numerical model design MEMS A. The arrows in the legends indicate whether the corresponding curve is plotted on the left or right axis.

as a parameter of optimization did not help the optimization reduce the stresses at the natural frequency. Overall, the high Q achieved by devices with AlN can create a challenge in designing a device capable of surviving 1 g of acceleration being exited at its resonance with a low natural frequency.

MEMSCAP was the most viable option for manufacturing MEMS prototypes during the period of this study. Therefore, changing the piezoelectric material was not viable. Two changes were made to address the problems with MEMS A optimization: (i) the stress limit σ_{limit} was changed from 300 MPa to 800 MPa; (ii) the objective function was altered to maximize the areal Normalized Power Density; and (iii) the penalization of the natural frequency was removed. These changes will (i) allow for higher stress values to avoid a shift in the natural frequency. In the future, these high-stress values can be mitigated by using a mechanical stopper. Change (ii) will allow smaller devices produce more energy over a given area, and (iii) will permit the simulations to be performed with a direct analysis saving computational cost (since only one frequency is calculated) and making the simulation more accurate. The adjusted objective function can be written as

$$f_{obj} = -\frac{P}{A_{\text{active}}} + \alpha_{\text{s}}\ 100\ \frac{|\sigma_{\text{limit}} - \sigma_{\text{max,pz}}|}{\sigma_{\text{limit}}} \tag{4.6}$$

for

$$\alpha_s = \begin{cases} 0, & \text{if } \sigma_{\text{max,pz}} \leq \sigma_{\text{limit}} \\ 1, & \text{otherwise.} \end{cases} \tag{4.7}$$

A_{active} is used instead of volume because the thickness is constant for the PiezoMUMPs process. Figure 4.18 shows that the optimization was performed over 600 generations, and the best value was reached at generation 430. The optimization started from the initial geometry shown in Figure 4.19a, and the output is shown in Figure 4.19b.

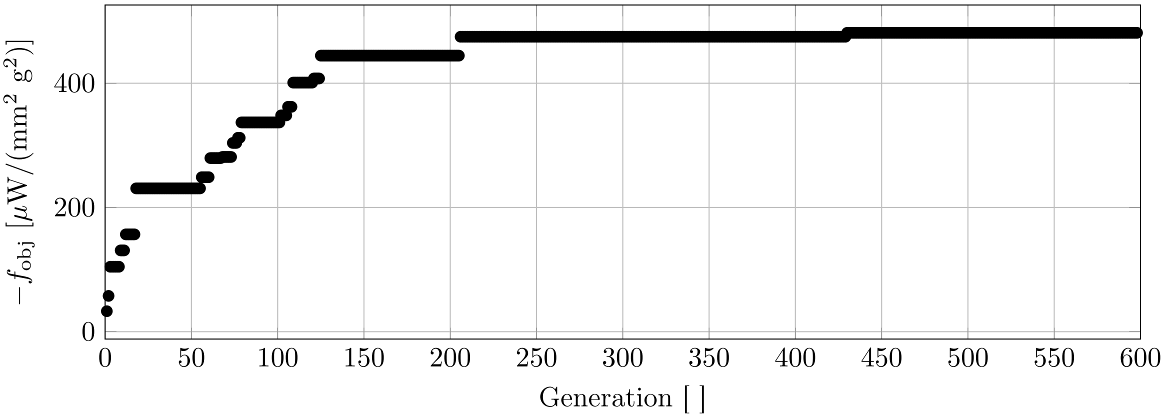

Figure 4.18 – History of objective function value during the optimization of MEMS B design.

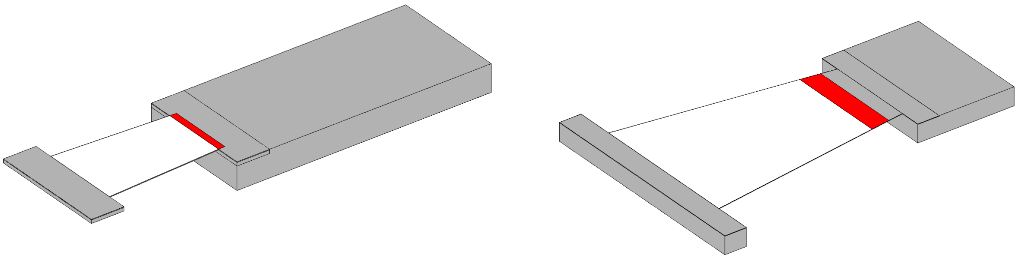

(a) Initial geometry. (b) Final geometry.

Figure 4.19 – Initial and final geometries of MEMS B optimization.

By increasing σ_{limit}, the natural frequency approached the desired 60 Hz but did not fully reach it, as shown in Figure 4.20. The device reached a maximum stress of 300 MPa at 59.47 Hz and 61.10 Hz frequencies. The power associated with these frequencies is 1.64 µW/g^2 and 1.70 µW/g^2, respectively. Therefore, the maximum power generated by this device under 1g of acceleration was 1.70 µW.

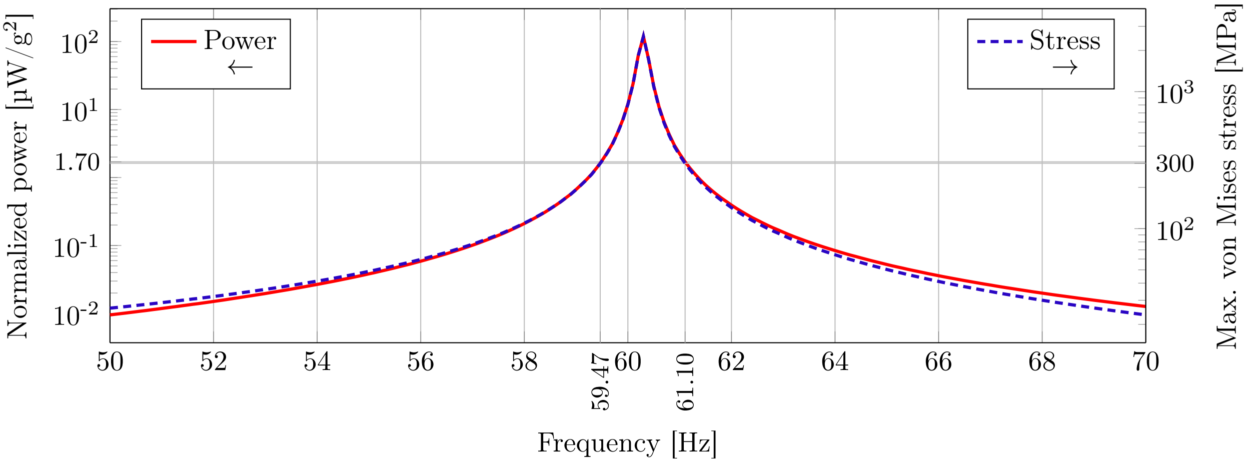

Figure 4.20 – Normalized power of the optimized numerical model design MEMS B. The arrows in the legends indicate whether the corresponding curve is plotted on the left or right axis.

The major limitation of the objective function is the maximum stress at resonance. Because of that, the objective function with the penalty function is replaced by

$$f_{\text{obj}} = -\frac{P}{A_{\text{active}}\ \sigma_{\text{max,pz}}}, \tag{4.8}$$

thus, the optimization will allow the resonance to be placed at 60 Hz, but the stress will be minimized simultaneously. Another solution could be to use a lower optimal acceleration; however, the power levels would also decrease since they are still relatively low compared to the goal. Thus, the acceleration level was kept constant. The objective function from Equation 4.8 should find the best compromise between power and mechanical stress, so that later on, the larger von Mises values can be restricted via a mechanical stopper. Thus, the objective was to achieve the highest power values with the smallest possible mechanical stress. As shown in Figure 4.21, the optimization ran for 219 optimizations and achieved its best value at generation 197, rendering only 22 stall generations before ceasing, the optimization was indeed stopped prematurely, and more time was required to reach an appropriate optimized design. The optimum design from this run is illustrated in Figure 4.22.

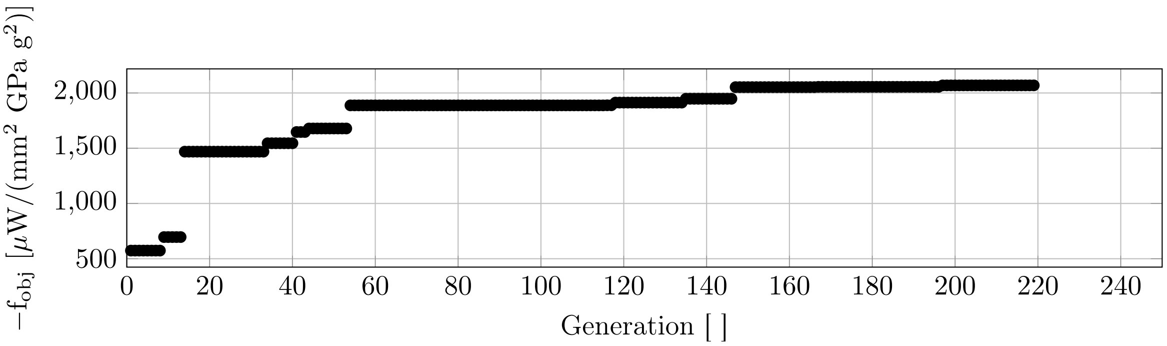

Figure 4.21 – History of objective function values during the optimization of MEMS C design.

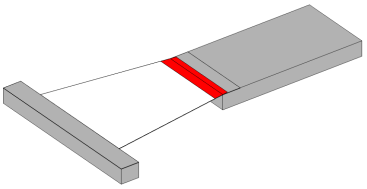

Figure 4.22 – Final optimized geometry of MEMS C.

The optimization did not proceed because the objective function was poorly formed. The best member from generations 167 to 196 (power and maximum stress represented in Figure 4.23a) had a higher maximum power per area than the best design from the last generation (power and maximum stress represented in Figure 4.23b). The device from the last generation reached a maximum stress of 300 MPa at

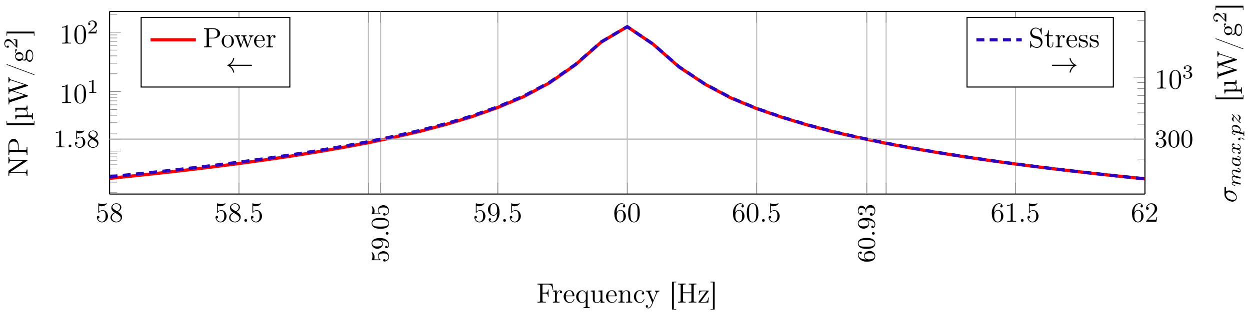

(a) Next to best member.

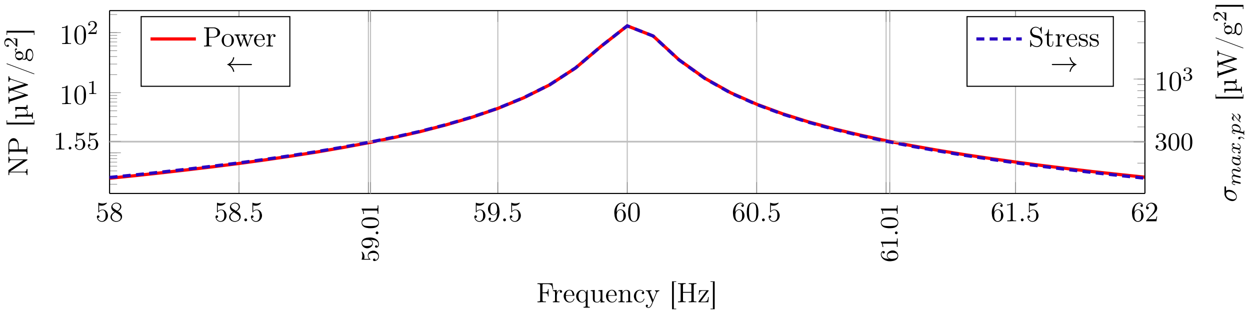

(b) Best member.

Figure 4.23 – Power and maximum von Mises stress in piezoelectric material for MEMS C design optimization. The arrows in the legends indicate whether the correspondent curve is plotted in the left or right ordinate axis.

frequencies of 59.01 Hz and 61.01 Hz. The power associated with these frequencies is 1.50 µW/g^2 and 1.55 µW/g^2, respectively. Therefore, the maximum power generated by this device under 1 g of acceleration was 1.55 µW. The previous best design (generations 167 to 196) reached maximum stress of 300 at 59.05 Hz and 60.96 Hz with an associated normalized power of 1.54 µW/g^2 and 1.58 µW/g^2, respectively, giving it a maximum power of 158 µW at 1 g of acceleration.

The next to best design, obtained from optimization of MEMS C, has an active area of 3 mm x 7.31 mm. In contrast, the best design is a 3 mm x 7.32 mm. In terms of the maximum power per active area, the next to best design has 7.20 µW/mm^2, and the best design 7.06 µW/mm^2. Thus, to prioritize power maximization at the feasible frequencies next to the resonance, the objective function is changed to

$$f_{obj} = -\frac{\min(P(f_1, f_2))}{A_{active}\ \max(\sigma_{max,pz}(f_1, f_2))}. \tag{4.9}$$

The “maximization of minimum” done by this equation was also executed in Equation 4.2. However, instead of several frequencies, it only used two, f_1 and $f_2$which were defined as 58 Hz and 62 Hz, respectively. It is crucial to choose two frequencies that provide an average that results in the desired natural frequency (which, in this case, is 60 Hz). The boundaries of the optimizations are listed in Table 4.2, the history is shown in Figure 4.24, and the best design is shown in Figure 4.25.

Table 4.2 – Boxed constraints for the optimization of MEMS D.

Parameter	Lower boundary	Upper boudary
W_{sm}	500 µm	4000 µm
W_c	500 µm	4000 µm
Y_0	0 µm	250 µm
W_{pz}	200 µm	4000 µm
W_{el}	200 µm	4000 µm
L_{sm}	1500 µm	4500 µm
L_c	1500 µm	5000 µm
L_{pz}	1500 µm	5000 µm
L_{el}	1500 µm	5000 µm
Q	50	500
α_{Rl}	5	8

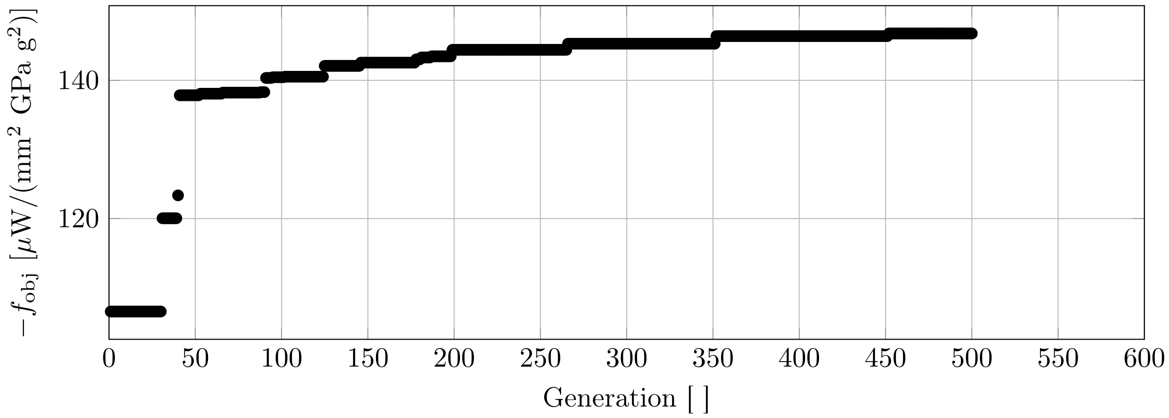

Figure 4.24 – History of objective function values during MEMS D design optimization.

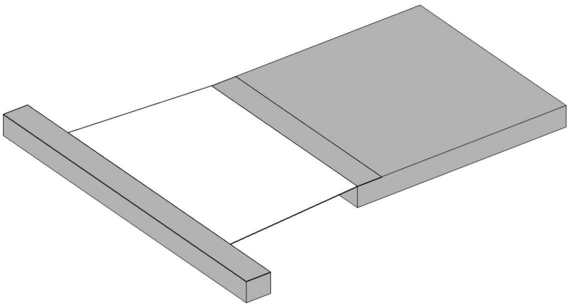

Figure 4.25 – Final optimized geometry of MEMS D.

Figure 4.26 shows the power and $\sigma_{\mathrm{max,pz}}$ of the optimized MEMS D. This model reached a maximum stress of 300 MPa at frequencies of 58.69 Hz and 61.27 Hz. The power associated with these frequencies is 2.19 µW/g^2 and 2.30 µW/g^2, respectively. Therefore, the maximum power generated by this device under 1 g of acceleration was 2.30 µW. For comparison purposes, the design described at the beginning of the chapter for area B of the MEMSCAP die reached the maximum stress at the frequencies of 55.49 Hz and 64.21 Hz with an associated power of 0.10 µW/g^2 and 0.12 µW/g^2, respectively. Considering the limitations imposed by the fabrication process and the low natural frequency required, this final design showed an improvement in the optimization methodology. However, this did not reach the desired power levels. Nevertheless, it is a feasible device that can be manufactured using MEMSAP's PiezoMUMPs process. It should enable model validation.

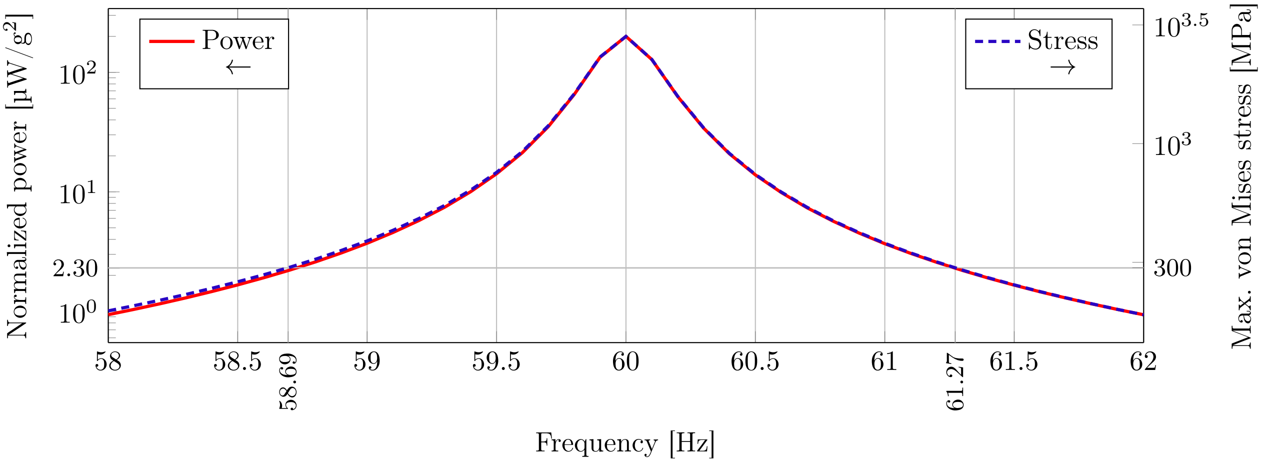

Figure 4.26 – Normalized power of optimized MEMS D numerical model design. The arrows in the legends indicate whether the corresponding curve is plotted on the left or right axis.

To better evaluate the capabilities of the MEMS design to achieve the targets defined in this work, a less restrictive fabrication process was defined so that some changes were made to the numerical model and optimization boundaries. Table 4.3 shows the new boundaries, where the most significant changes are related to the thickness of the cantilever and piezoelectric material. Another meaningful change was the alteration of the piezoelectric material from AlN to PZT-5H, which has a higher piezoelectric coefficient and electromechanical coupling. These alterations were concluded in an optimization where the objective function history is shown in Figure 4.27, and the final output is shown in Figure 4.28.

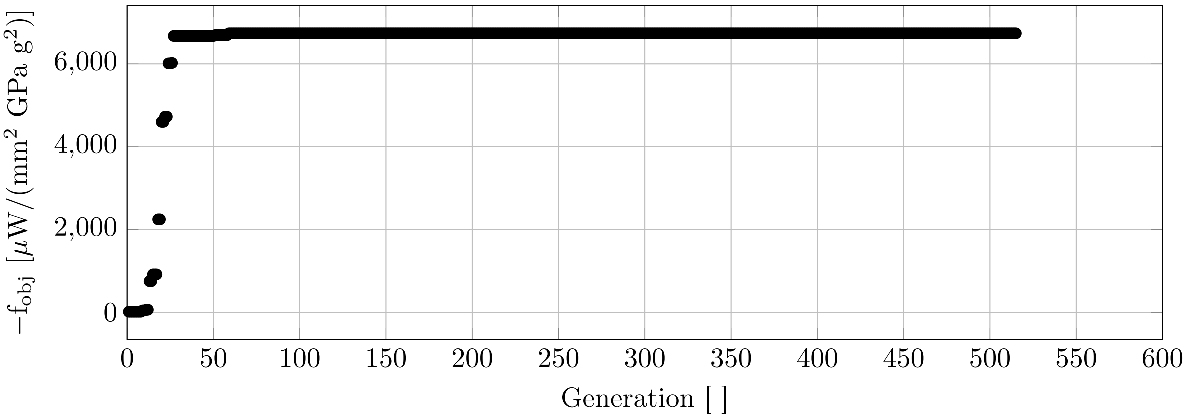

Figure 4.27 – History of objective function value during the optimization of MEMS-free design.

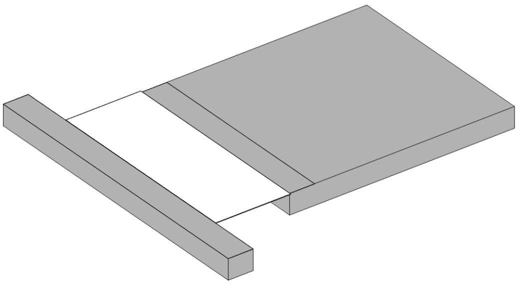

Figure 4.28 – Final MEMS free optimized geometry.

Table 4.3 – Boxed constraints of MEMS-free optimization.

Parameter	Lower boundary	Upper boudary
W_{sm}	500 µm	4000 µm
W_c	500 µm	4000 µm
Y_0	0 µm	2000 µm
W_{pz}	200 µm	4000 µm
W_{el}	200 µm	4000 µm
L_{sm}	1500 µm	4500 µm
L_c	1500 µm	4500 µm
L_{pz}	1500 µm	5000 µm
L_{el}	1500 µm	5000 µm
Q	50	500
α_{Rl}	5	8
t_v	5	200
t_{pz}	0.5	200

Figure 4.29 shows the power and $\sigma_{\text{max,pz}}$ of MEMS-free optimized. This model reached the maximum stress of 114.8 MPa of PZT (ANTON; ERTURK; INMAN, 2012) at 59.83 Hz and 60.15 Hz frequencies.

The power associated with these frequencies is 33.93 µW/g^2 and 34.09 µW/g^2, respectively. Therefore, the maximum power generated by this device under 1 g of acceleration was 34.09 µW. This device meets the requirements regarding a minimum of 20 µW between the frequencies of 58.67 Hz and 61.34 Hz, giving a total bandwidth of 2.67 Hz.

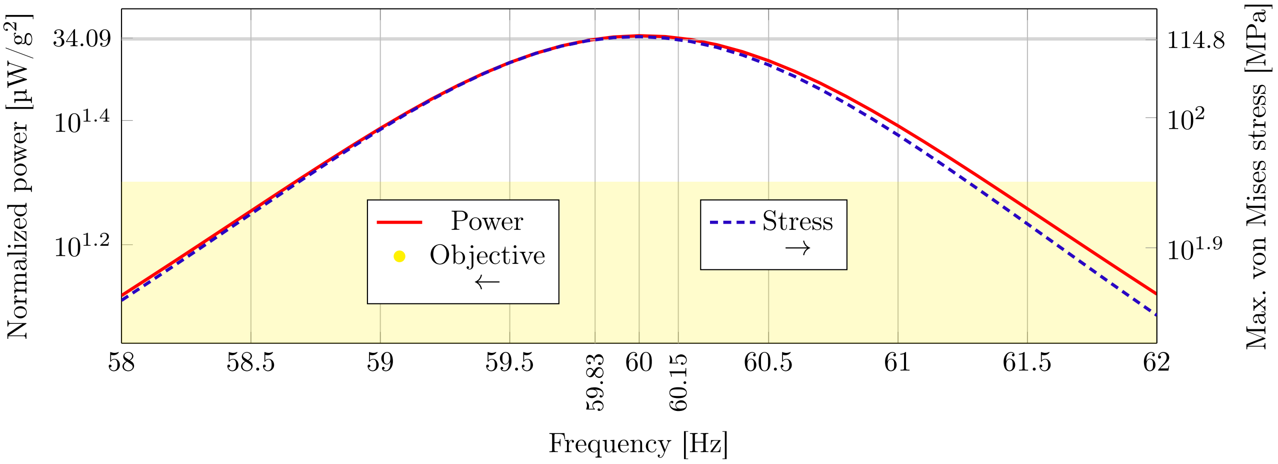

Figure 4.29 – Normalized power of optimized MEMS-free numerical model design. The arrows in the legends indicate whether the corresponding curve is plotted on the left or right axis.

Although the bandwidth did not match the required bandwidth, the active area occupied by the device was 4 mm x 6 mm or 24 mm^2, less than half the size of the MEMSCAP die area. In this way, two of these devices can be used with a minor shift in the natural frequency to cover the desired bandwidth while remaining within the desired area. Another alternative is the introduction of a nonlinear monostable broadband technique. That was analytically implemented and presented in Appendix E.

4.4 REFINED OPTIMIZATION

The optimization process using DE works for the problem proposed here; however one of its most significant disadvantages appears when using a costly objective function. If the numerical model solution is relatively computationally expensive, this algorithm may take too long to converge and might become a nonviable solution. Figure 4.30 shows the model of MEMS D with a rough prismatic element mesh (used in DE) with a maximum element size of $L_c/10$ covering the cantilever (21834 degrees of freedom) and a fine prismatic element mesh with a maximum size of $L_c/30$ (162531 degrees of freedom). These graphs show an approximate error of 0.5%. A more detailed convergence analysis of the mesh used during these optimizations is done in Appendix B.

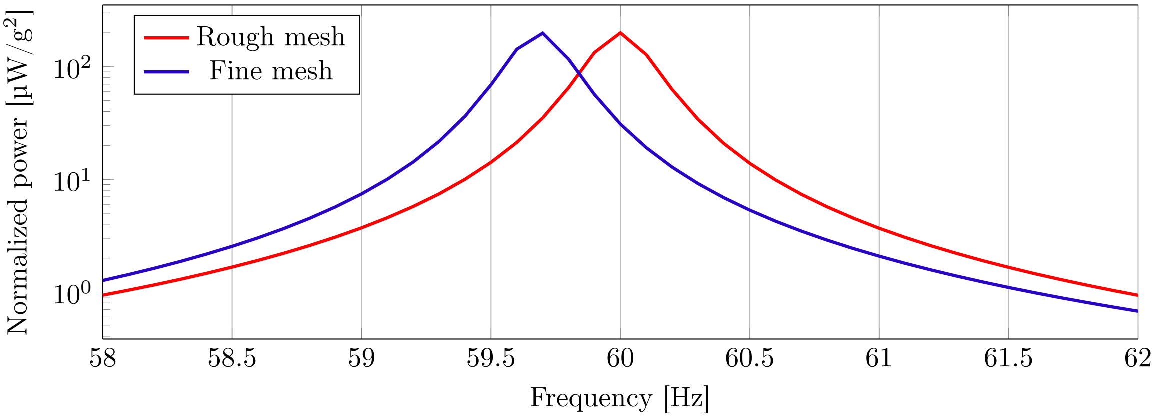

Figure 4.30 – Comparison of normalized power of optimized MEMS D numerical model design with rough and fine mesh.

Although the error is small, it is interesting to run an algorithm that can handle the heavier model to be used as the second step in optimization. First, the DE runs a rough mesh optimization, and then the second algorithm performs the final “local” optimization with a finer mesh. Because DE has already performed a global investigation of the domain, this algorithm does not need to be adapted to search for global minima, and only a local optimization should suffice. The results of the Nelder-Mead and Surrogate Optimization are shown in the following Subsections 4.4.1 and 4.4.2.

4.4.1 Nelder-Mead

The design chosen for the second-step optimization is the MEMS D using the procedure described in Section 3.2. The best-value history is shown in Figure 4.31. The algorithm converged quickly and ran for 101 iterations with 60 stall iterations. Figure 4.32 shows the progress of NM optimization. The most prominent feature identified here is the natural frequency. When a fine mesh was added to the model, the natural frequency was expected to decrease. The main goal of the second step is to reposition the resonance at 60 Hz; however, NM could not do that.

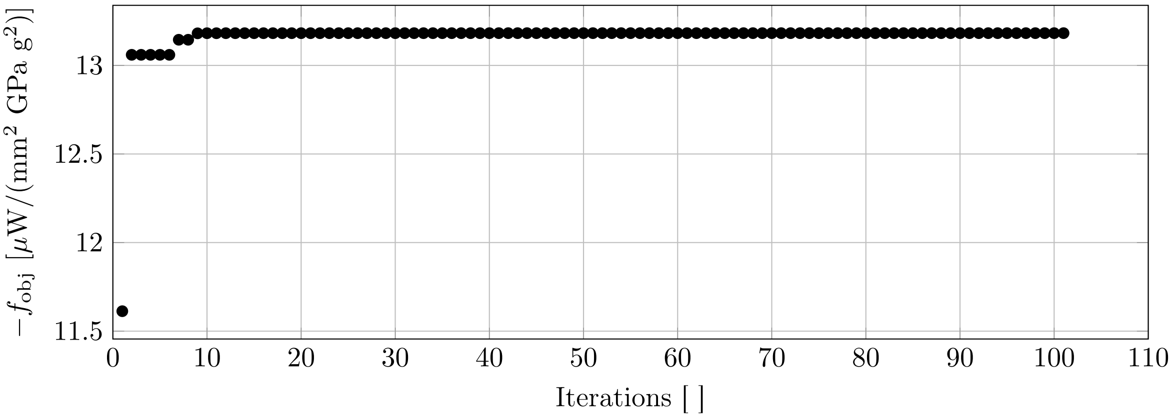

Figure 4.31 – Best value history of NM optimization.

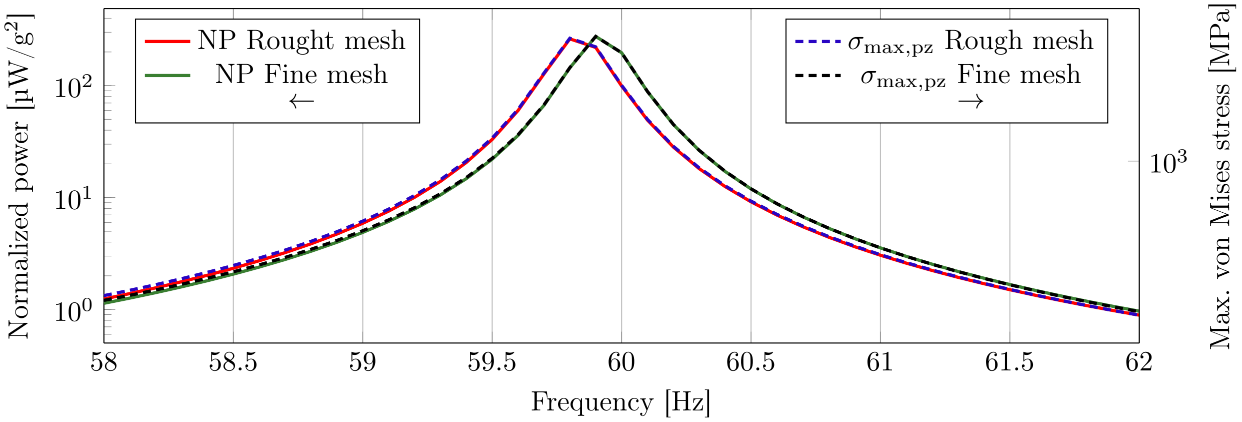

Figure 4.32 – Normalized power of optimized MEMS D numerical model design. The arrows in the legends indicate whether the corresponding curve is plotted on the left or right axis.

The algorithm did converged well, but the natural frequency was not at 60 Hz, and the only parameters that changed were $W_{\mathrm{b+}}$ from 200 µm to 210 µm and L_{el} from 2400 µm to 2403 µm. This raises the question of why NM did not center the natural frequency correctly. To understand the objective function’s behavior, a surface plot is displayed in Figure 4.33, where the X and Y axes are $W_{\mathrm{b+}}$ and L_{el}, respectively, whereas in the Z axes is the value of f_{obj}. Figure 4.34 shows the contour of the surface from Figure 4.33, which is also present in the X-Y plane of the Cartesian graph. The red and green dots indicate the best values from DE and NM, respectively. Appendix D presents more surface graphs of the objective function with two other varying parameters (while the others remain fixed). These graphs are

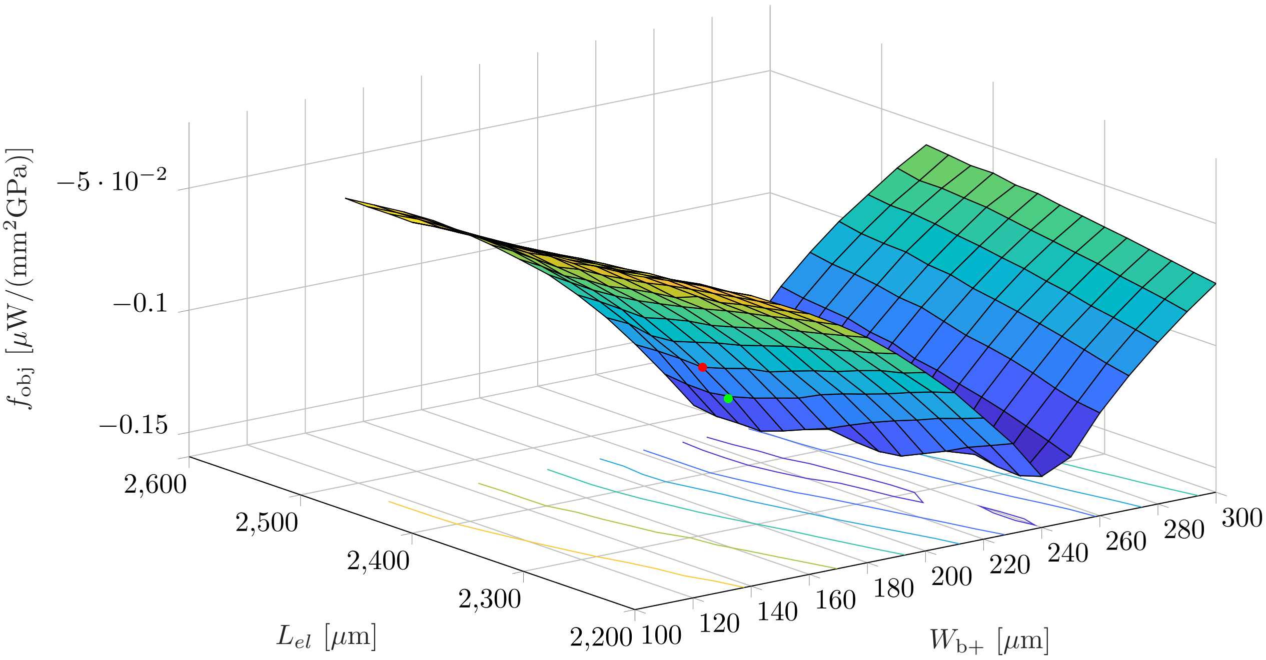

Figure 4.33 – Surface plot of objective function with varying parameters Y_0 and L_{el}.

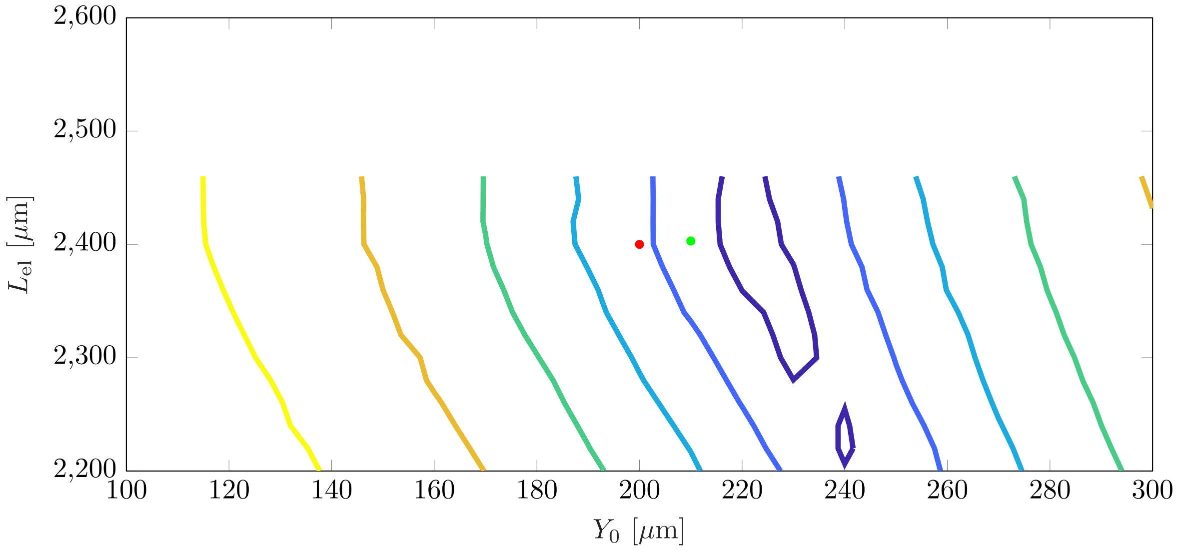

Figure 4.34 – Contour plot of objective function with varying parameters Y_0 and L_{el}.

not a good representation of the objective function, but serves the purpose of showing that the surfaces are well-behaved and should not be a problem to be locally optimized with simple algorithms such as NM.

It is clear from these images that the best value was not found because even when considering only $W_{\mathrm{b+}}$ and L_{el} (a 2D domain) NM did not reach the minimum value. No further investigation was performed to identify the problems with NM in this scenario. However, it is essential to note that NM is said to break down in large dimensions (LAGARIAS et al., 1998) (although only a few carefully made numerical results support these perceptions) and Torczon (1989) advises to be wary of the output of NM for dimensions larger than four.

4.4.2 Surrogate optimization

Surrogate optimization is an alternative to NM, where the main feature of this optimization process is finding minima with the least number of iterations possible. A new DE optimization was run with a slight numerical model change and an additional parameter. The silicon considered, so far, as an isotropic material is now modeled as orthotropic, and the additional parameter is θ, the angle of orientation of the device in the silicon wafer. The optimization was run for 450 generations with 18 stall iterations (Figure 4.35).

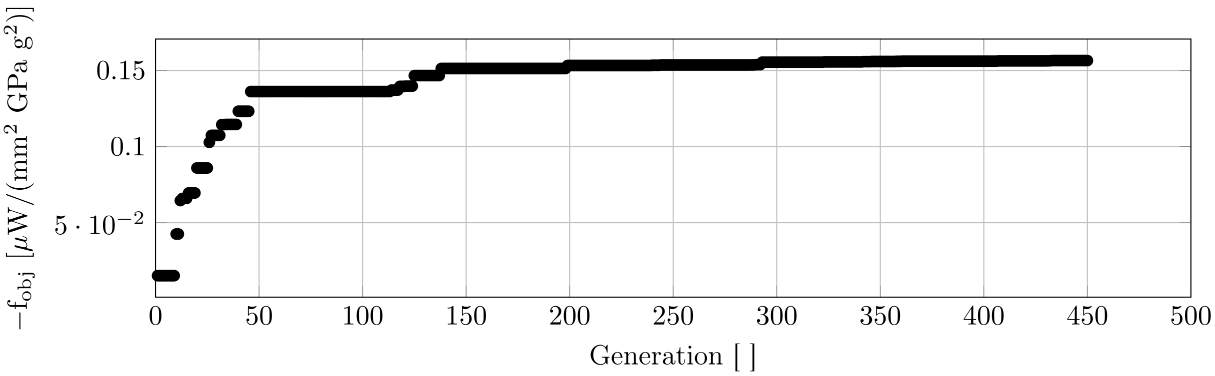

Figure 4.35 – Best value history of DE optimization as preparation for SO.

Figure 4.36 shows the power and $\sigma_{\mathrm{max,pz}}$ of the optimization with the mesh of DE and the finer mesh that is used in the SO. This model reached the maximum stress of 300 MPa at frequencies of 58.54 Hz and 61.43 Hz (with coarse mesh). The power associated with these frequencies is 1.98 µW/g^2 and 2.09 µW/g^2, respectively. However, with the fine mesh, the natural frequency shifts and the new maximum stress frequencies are 58.32 and 61.31, with associated NP of 1.81 µW/g^2 and 1.91 µW/g^2. A drop of 0.18 µW in maximum power from changing the mesh.

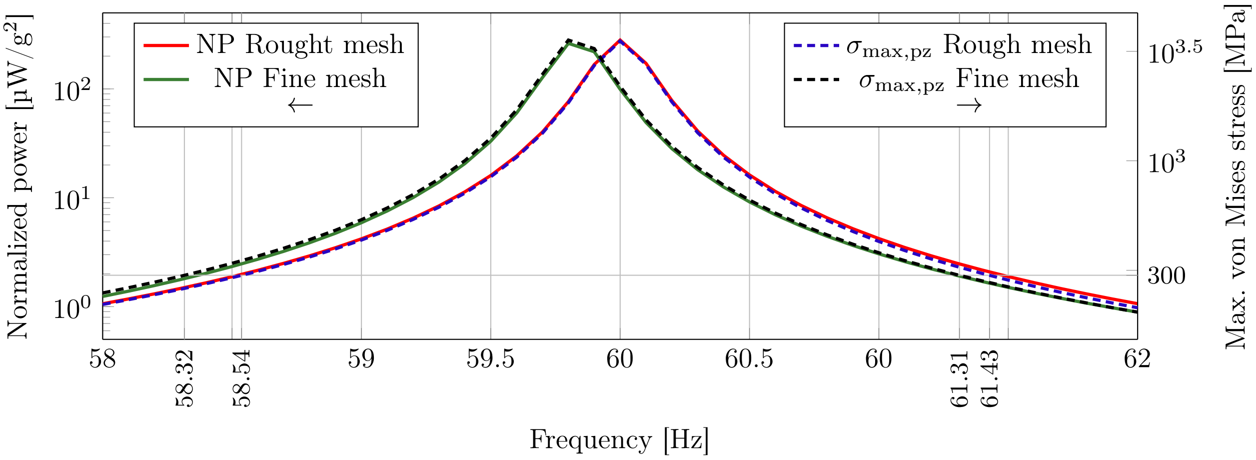

Figure 4.36 – Normalized power of the optimized numerical model used as the initial point for SO optimization with a rough and fine mesh. The arrows in the legends indicate whether the corresponding curve is plotted on the left or right ordinate axis.

The surrogate model was run with the previous design as a starting point. The history of this run is shown in Figure 4.37. With 96 function evaluations, the algorithm reached the best value and was kept there for 10 stall generations before resetting the surrogate. After the reset, the surrogate looked for other global minima, and since DE gave an excellent initial point, none of the other samples were close to the best value after the reset. Table 4.4 shows the changes in the model parameters between the DE best and surrogate best. The alterations were minor for all parameters. It is essential to note that this second step allowed for finer discretization of the parameters going from steps of 10 µm to 1 µm, whereas Q, α_{Rl} and θ were treated as continuous variables. Adding θ to the parameters did not have much influence because the best member used the unaltered device position in the silicon wafer (0°).

Figure 4.38 compares the refined mesh power and stress curves of DE optimization with the power and stress of the SO. Comparing these results to the curves in Figure 4.36, the surrogate optimization shows approximately the same behavior as the best design from the DE with a coarse mesh. This suggests that the second-step optimization is an excellent tool for a final, more precise approximation to the global maximum using a more trustworthy mesh.

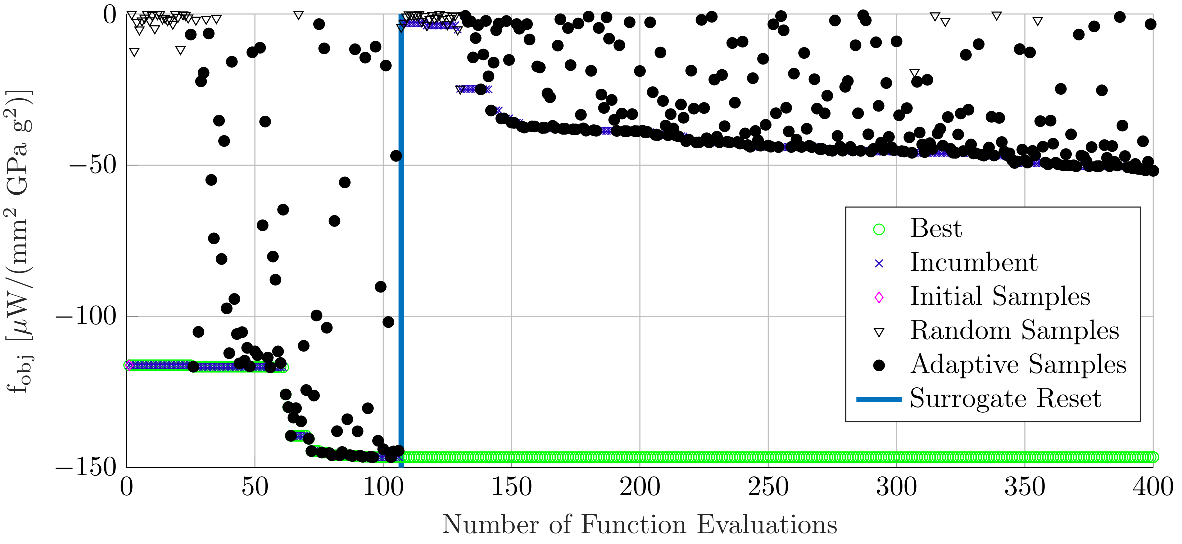

Figure 4.37 – Best value history of SO optimization.

Table 4.4 – Alterations of the best parameters from DE optimization to SO optimization.

Parameter	DE best	Surrogate best
W_{sm}	4000 µm	4000 µm
W_c	4000 µm	3998 µm
Y_0	200 µm	213 µm
W_{pz}	4000 µm	3998 µm
W_{el}	4000 µm	3861 µm
L_{sm}	4380 µm	4380 µm
L_c	2410 µm	2401 µm
L_{pz}	2460 µm	2701 µm
L_{el}	2400 µm	2399 µm
Q	500	499.9996
α_{Rl}	6.2	6.208
θ	0 °	0 °

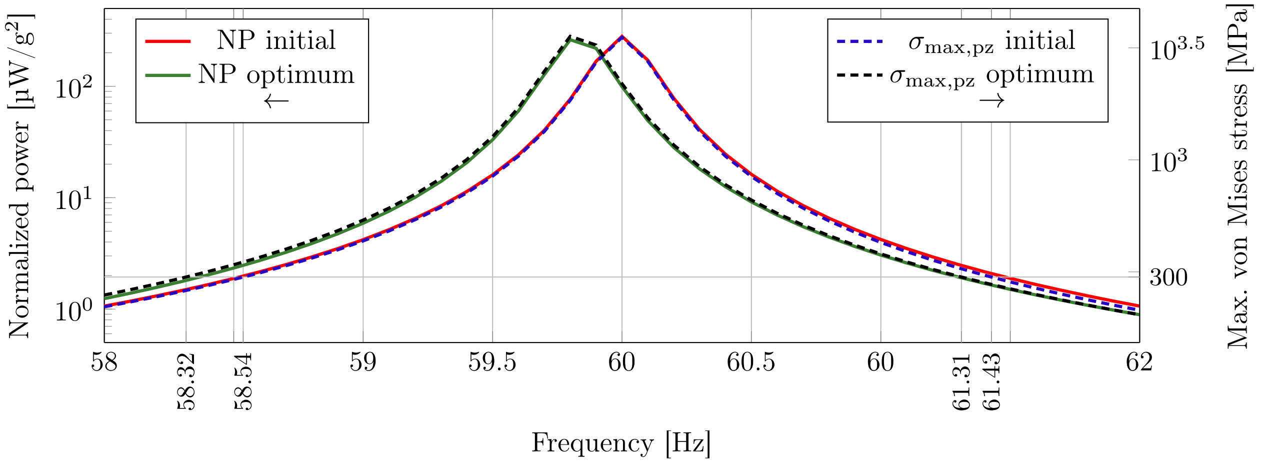

Figure 4.38 – Normalized power of optimized numerical model using SO. The arrows in the legends indicate whether the corresponding curve is plotted on the left or right axis.

4.5 OPTIMIZATION OF MICROMACHINED FILMS

An alternative to the MEMS models is presented in Subsection 3.1.2, using three different numerical models. The optimization process using these numerical models is presented here, beginning with PIEZO.COM bimorph sheets. The objective function in this run was slightly different from that one in Equation 4.9. In the previous chapter, due to fabrication restrictions, the NPD was calculated over the active area of the design, but for these runs, the active volume is considered for calculation of the NPD, written here as

$$f_{\mathrm{obj}} = -\frac{\min(P(f_1, f_2, f_3))}{(V_{active} + 2\max(V_{\mathrm{gap}}(f_1, f_2, f_3)))\,\max(\sigma_{\mathrm{max,pz}}(f_1, f_2, f_3))}. \tag{4.10}$$

The addition of V_{gap} is used to avoid devices with good NPD, but requires an extra volume to allow the seismic mass to move and the cantilever to bend. Another significant alteration was made. The optimum acceleration was altered from 1 g to 2.25 m/s^2, because Roundy (2003) uses this acceleration value in his experiments, and it is believed to be a better description of the amplitude of acceleration of machinery in the industry. It is relevant to consider that this value is not based on any collected data because this amplitude can vary depending on the type of machinery analyzed. The values of f_1, f_2, and f_3 were 58 Hz, 60 Hz, and 62 Hz, respectively. The history of the DE optimization is shown in Figure 4.39.

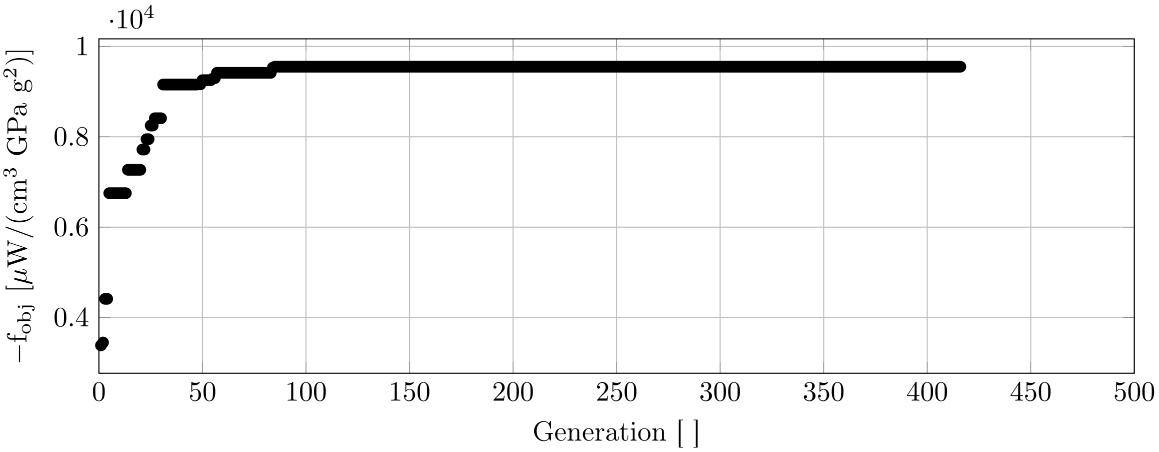

Figure 4.39 – Best value history of optimization of design PIEZO.COM A.

Optimizations with micromachined EHs must utilize considerably more space than MEMS. Because of that, the MEMS objective is not used here. The primary goal of 160 µW over 20 Hz is used as the objective. This design is denominated as MEMS PIEZO.COM A and is shown in Figure 4.40. The power of this design under an acceleration of 2.25 m/s^2 is shown in Figure 4.41, with the objective highlighted in yellow. The maximum $\sigma_{\mathrm{max,pz}}$ is approximately 19 MPa, well below the maximum of 114.8 MPa allowed for the PZT-5H. Therefore, the stress curve is not present in the graph. Since the stress levels are considerably low, there is still room for improvement in this design. This device presents an NP at the resonance of 8190

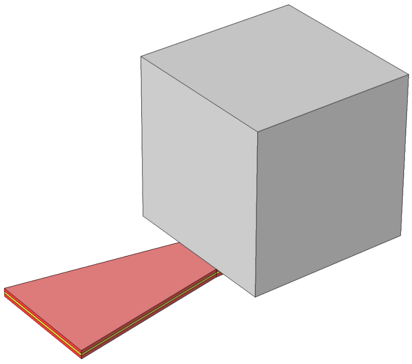

Figure 4.40 – Final optimized geometry of PIEZO.COM A design.

µW/g^2 and an active volume of 2.08 cm^3, therefore an NPD of 3.93 mW/(g^2cm^3). The device's bandwidth is 8.32 Hz giving an F.o.M. of 32.74 mW Hz/(g^2cm^3). It meets the criteria over 10.82 Hz; this way, two of those devices with a slight shift in natural frequency should meet the requirement, but the sum of those volumes renders a device of 4.16 cm^3, 0.23 cm^3 over the requirement.

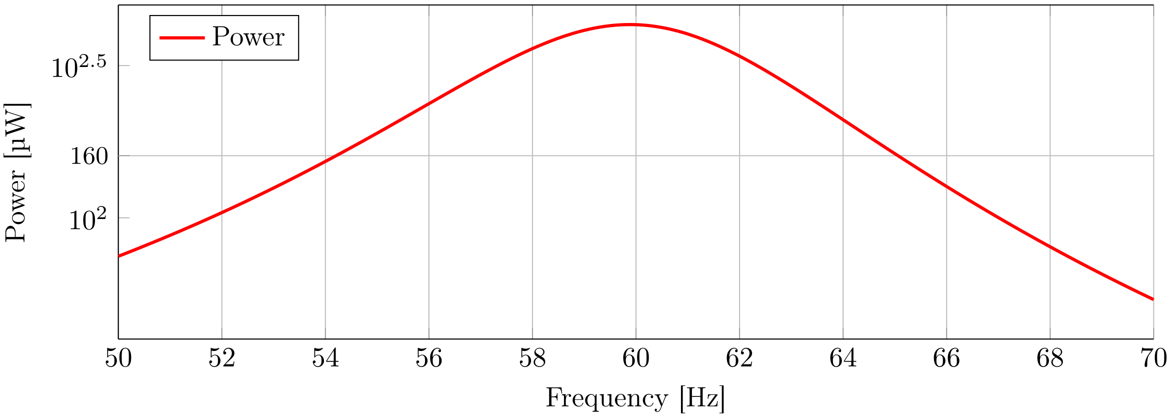

Figure 4.41 – Power at an acceleration of 2.25 m/s^2 for the optimized numerical model PIEZO.COM A design.

Since the stresses in the piezoelectric material are still low, another optimization is proposed with the same geometry as PIEZO.COM, with an objective function as

$$f_{obj} = -\frac{\min(P(f_1, f_2, f_3))}{(V_{\text{active}} + 2\max(V_{\text{gap}}(f_1, f_2, f_3)))} + 10^9\alpha_{\text{s}}, \tag{4.11}$$

which

$$\alpha_s = \begin{cases} 0, & \text{if } \sigma_{\text{max,pz}} \leq \sigma_{\text{limit}} \\ 1, & \text{otherwise.} \end{cases} \tag{4.12}$$

The σ_{limit} this time was 40 MPa to obtain a safety factor of approximately three from the ultimate tensile strength of PZT-5H. In this run, two sets of values, f_1, f_2, and f_3 were tested: (i) 58 Hz, 60, and 62 Hz and (ii) 59.5 Hz, 60 Hz, and 60.5 Hz, respectively. Figure 4.42a shows the best member for the optimization with 4 Hz of bandwidth (58 Hz to 62 Hz), and Figure 4.42b shows the best member for a bandwidth of 1 Hz (59.5 Hz to 60.5 Hz).

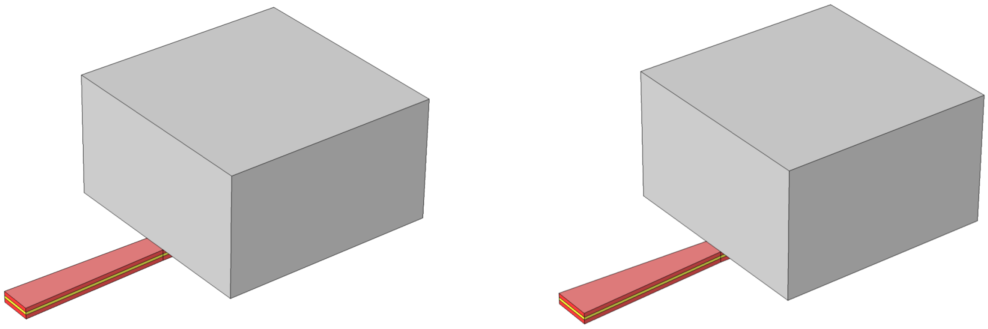

(a) 4 Hz. (b) 1 Hz.

Figure 4.42 – Best members from the optimization of design PIEZO.COM B altering frequency bandwidth of theobjective function.

The histories of those two runs are shown in Figure 4.43. The magnitude of the output values is affected by the chosen frequencies. With a band of 1 Hz, the minimum power will be higher than when using 4 Hz; this does not mean that the worst design is the latter.

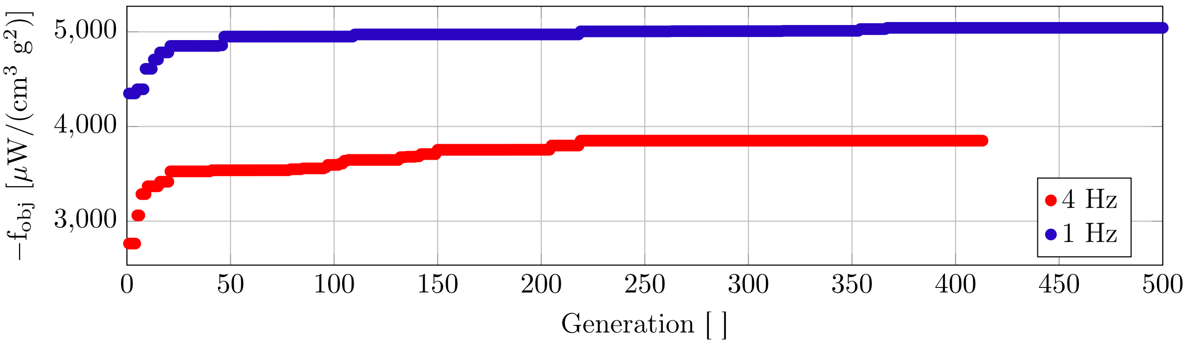

Figure 4.43 – Best value history of optimization of design PIEZO.COM B 4 Hz and PIEZO.COM B 1 Hz.

Figure 4.44 shows the power of the device at 2.25 m/s^2 of acceleration. As expected with 4 Hz, the optimization prioritized the band's widening while 1 Hz prioritized the power at resonance. In terms of the performance metrics, the optimization with 4 Hz finished with an NPD of 5.35 mW/(g^2 cm^3) and F.o.M. of 38.35 mW Hz/(g^2 cm^3), whereas the 1 Hz optimization rendered an NPD of 5.48 mW/(g^2 cm^3) and F.o.M. of 34.33 mW/(g^2 cm^3). In terms of meeting the requirements, the optimization of 4 Hz was 160 µW for 6.44 Hz and the 1 Hz optimization at 6.25 Hz. Both devices met the requirements of the F.o.M. Using three similar devices with slightly shifted natural frequencies both devices could cover approximately 19.32 Hz and 18.75 Hz with a total of 3.08 cm^3 and 3.32 cm^3 for the 4 Hz and 1 Hz designs, respectively. Although the band was still not within the expected volume, it was still below the maximum.

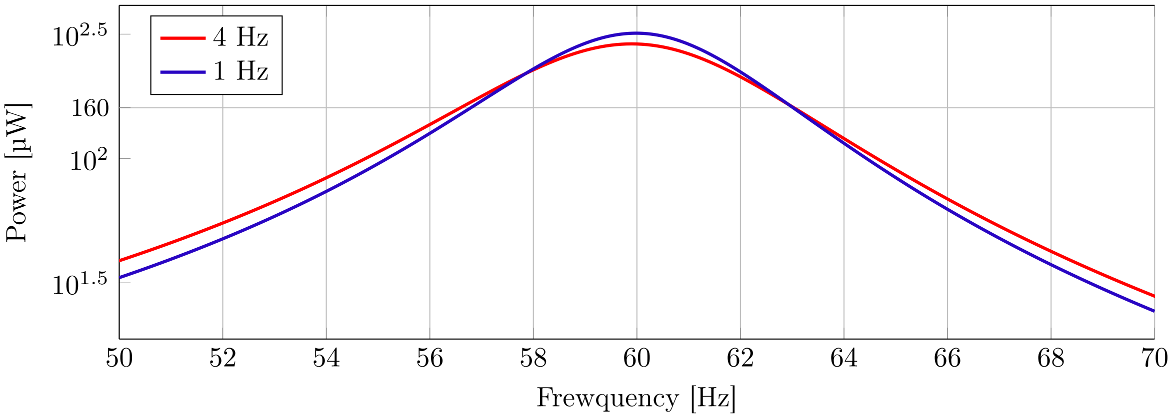

Figure 4.44 – Power at an acceleration of 2.25 m/s^2 of the optimized numerical model design PIEZO.COM B 4 Hz and 1 Hz.

The PIEZO.COM sheets appear to give good designs but owing to market prices during the execution of this work STEMINC sheets were used to fabricate the prototypes to validate the numerical models. Therefore, we run the same optimization as the previous one using a 1 Hz bandwidth but using the STEMINC numerical model. Figure 4.45 shows the best member, and Figure 4.46 shows the history of the best value for every generation.

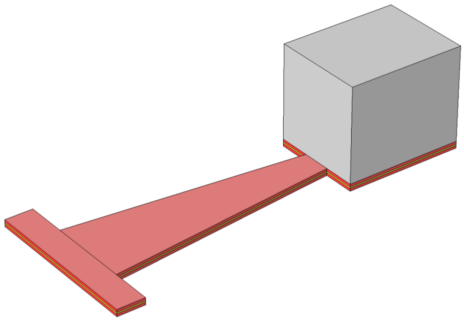

Figure 4.45 – Final optimized geometry of STEMINC A design.

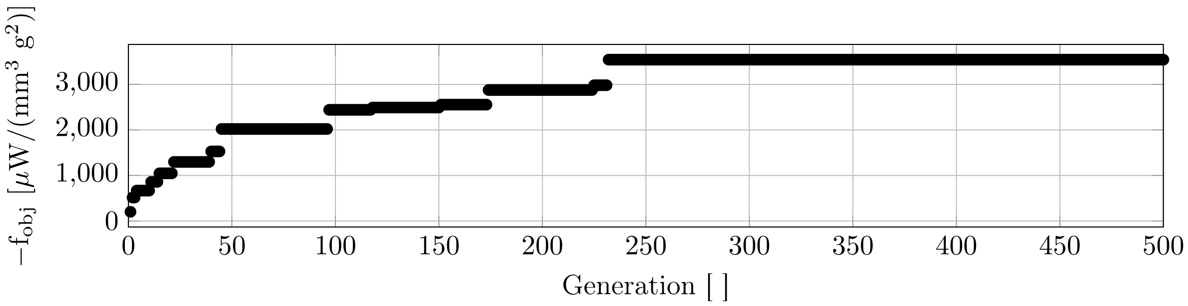

Figure 4.46 – Best value history of optimization of STEMINC A design.

Figure 4.47 displays the power at 2.25 m/s^2 and the von Mises maximum stress at the piezoelectric material. The same pattern as MEMS B occurred in this run; the natural frequency could not be placed at 60 Hz owing to the penalty in the objective function. Therefore, the objective function of Equation 4.10 is used for the subsequent optimization. In addition, to simplify the fabrication of the prototype, this optimization was performed with W_{b+} fixed at 0 µm. Thus, the cantilever cannot be trapezoidal, and the programming of the cutting is straightforward. Figure 4.48 shows the best member, whereas Figure 4.49 shows the history.

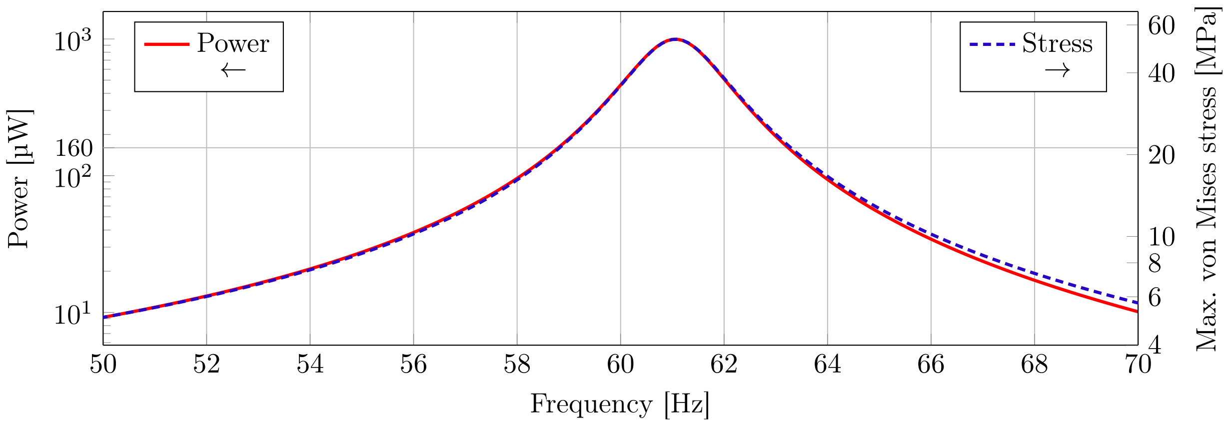

Figure 4.47 – The power at an acceleration of 2.25 m/s^2 of the optimized numerical model design STEMINC A. The arrows in the legends indicate whether the corresponding curve is plotted on the left or right axis.

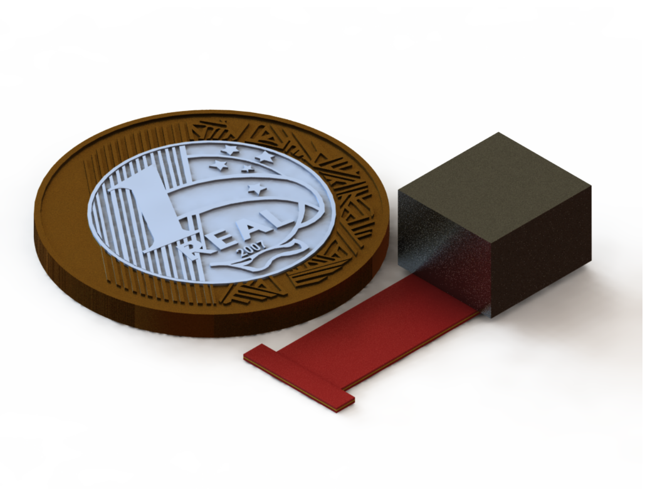

Figure 4.48 – Final optimized geometry of STEMINC B design.

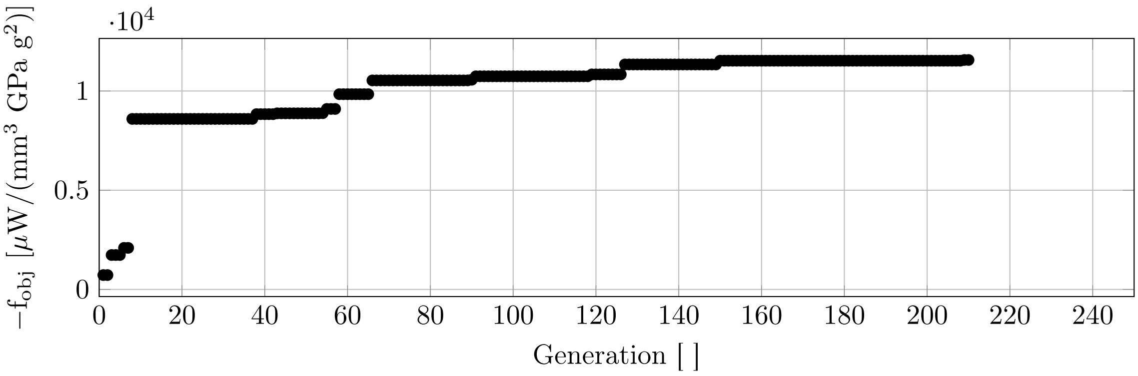

Figure 4.49 – Best value history of optimization of design STEMINC B.

In Figure 4.50, it is possible to see the power and stress curve which shows that the device meets the power requirement for 4.92 Hz. Approximately four similar devices with shifted natural frequencies are required to fulfill the requirements, rendering in a device of approximately 7.1 cm^3. A rectangular cantilever with small bandwidth can limit the possibility of a large bandwidth with a small stress field. This device has a $\sigma_{max,pz}$ of 101 MPa, which is below the maximum 114.8 MPa for PZT-5H but does not leave room for a good safety factor. The NPD of this device is one of the highest ones with 22.16 mW/(g^2 cm^3) but has a smaller F.o.M. of 30.35 mW Hz/(g^2 cm^3). A model based on this design is used for prototyping and experimental validation.

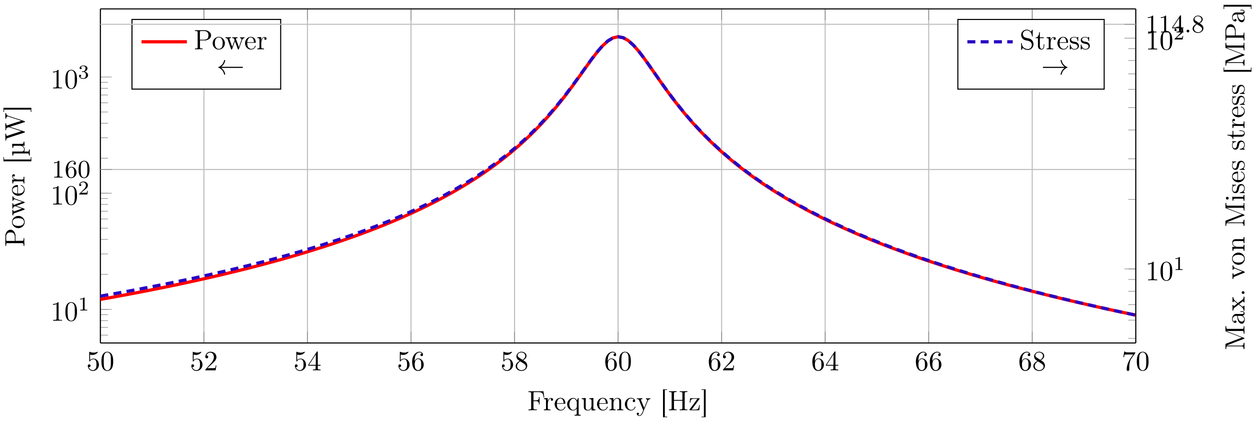

Figure 4.50 – Power at an acceleration of 2.25 $\mathrm{m/s}^2$ of the optimized numerical model design STEMINC B. The arrows in the legends indicate whether the corresponding curve is plotted on the left or right ordinate axis.

The large NPD predicted from STEMINC B is promising in terms of displaying the potential of the optimization methods and tools used in this study. Nevertheless, a much lower piezoelectric coefficient than that expected from PZT-5H was calculated during preliminary validation of the numerical model. Higher damping should be introduced to improve the bandwidth of the devices. A higher piezoelectric coefficient and electromechanical coupling are recommended to achieve this without losing efficiency. Equation A.5 clarifies how the introduction of higher piezoelectric values is linked to higher damping.

Using the MFC films as a bi-morph EH might facilitate higher electromechanical coupling, and therefore, a higher F.o.M. Best member image and optimization history is shown in Figure 4.51 and 4.52, respectively. Although the objective function is the same, this optimization does not use DE; it uses SO. The numerical model of the MFC films is quite heavy because it uses several layers of different materials, each with one quadratic element along the thickness. The SO can render better results in less time in such cases, where a computationally demanding objective function must be used. Therefore, the SO was exceptionally used as a the first-step optimization.

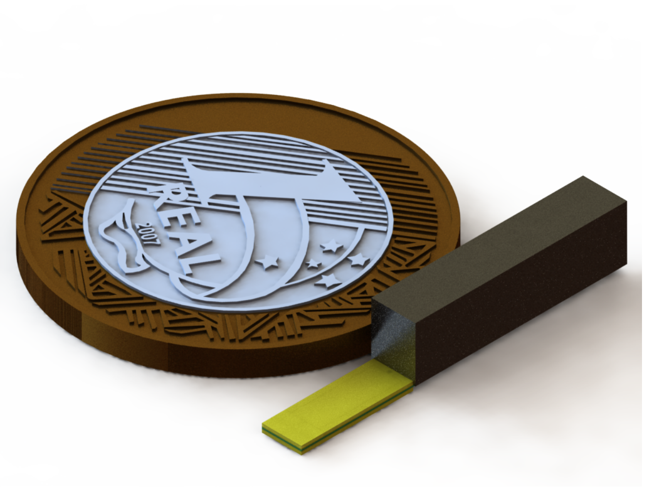

Figure 4.51 – Final optimized geometry of MFC design.

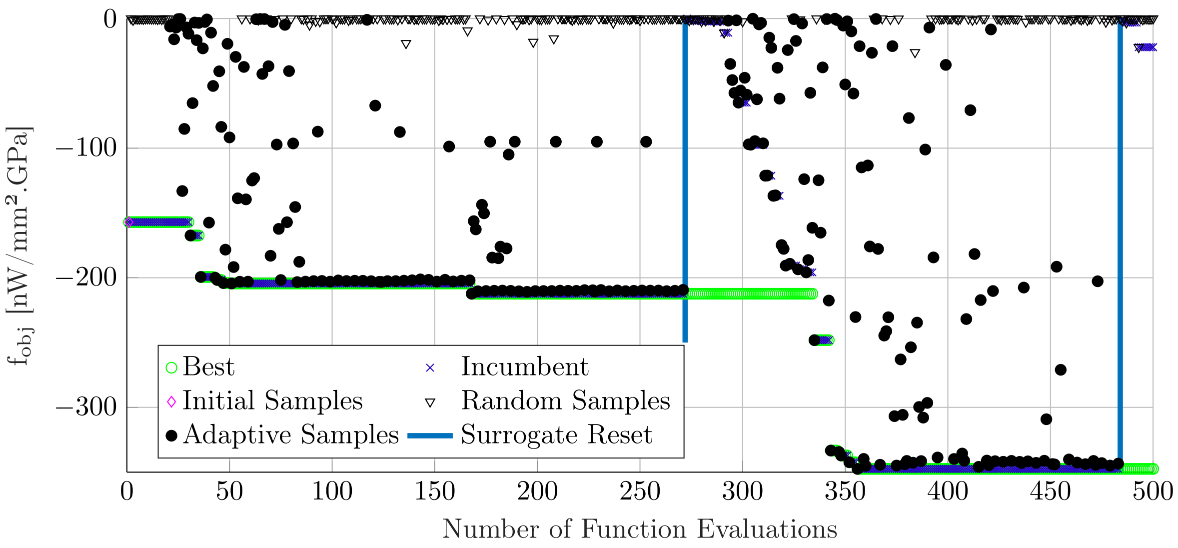

Figure 4.52 – SO history of the MFC A optimization.

Figure 4.53 shows the power and $\sigma_{\max,pz}$ curve of the MFC device. This device occupies a volume of 0.5416 cm^3, which is one of the lowest values for the micromachined devices. An NPD of 13.23 mW/(g^2 cm^3) and F.o.M. of 41.8 mW Hz/(g^2 cm^3), an acceptable value of NPD with the highest F.o.M. of this work. The device met the requirements of power over a band of 3.68 Hz. A device comprising of seven similar devices should sum to a total of 3.79 cm^3, slightly lower than the limit, and cover 25.76 Hz. This result should meet all the requirements imposed at the beginning of this study.

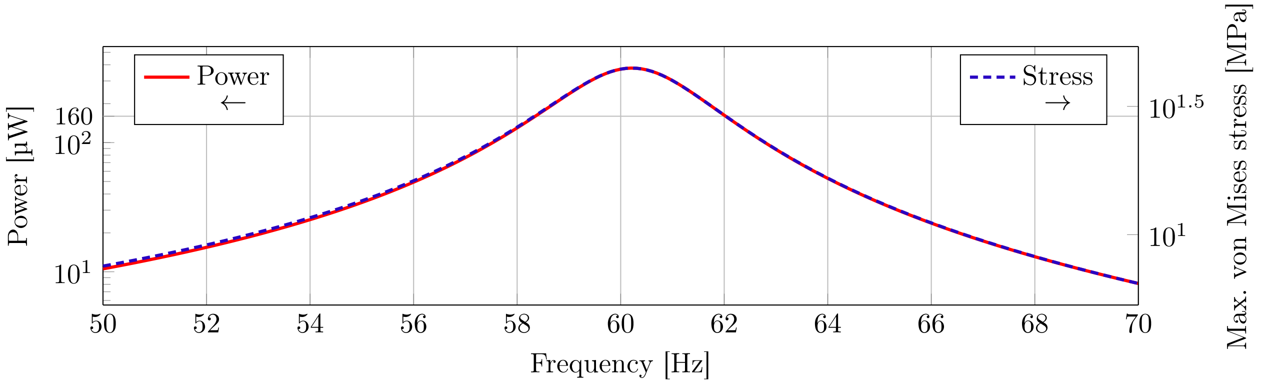

Figure 4.53 – Power at an acceleration of 2.25 m/s^2 of the optimized numerical model MFC A.

Owing to the promising F.o.M. of this device, a cantilever-array VEH was developed using this design as the base. Assuming that each cantilever covers a bandwidth of 3.6 Hz, the seismic mass widths associated with the following natural frequencies: 51.8 Hz, 55.4 Hz, 59 Hz, 62.6 Hz, 66.2, and 69.8 Hz are investigated. Figure 4.54 shows the relationship between these two variables. Based on this graph, interpolations were done performed to determine the associated W_{sm}. These are 2785 µm, 3130 µm, 3524 µm, 3961 µm, 4485 µm, and 5121 µm, in order of higher to the lower natural frequency. Summing the total volume occupied by the six devices with a 0.2 mm spacing between them, the total volume is 3.70 cm^2, 0.23 cm^2 below maximum. Finally, the power from the summation of all the devices is shown in Figure 4.55.

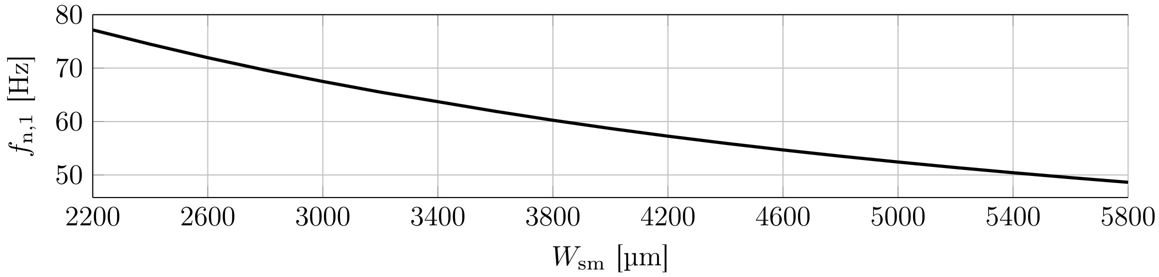

Figure 4.54 – Variation in the natural frequency of the device when altering the width of the seismic mass of design MFC A.

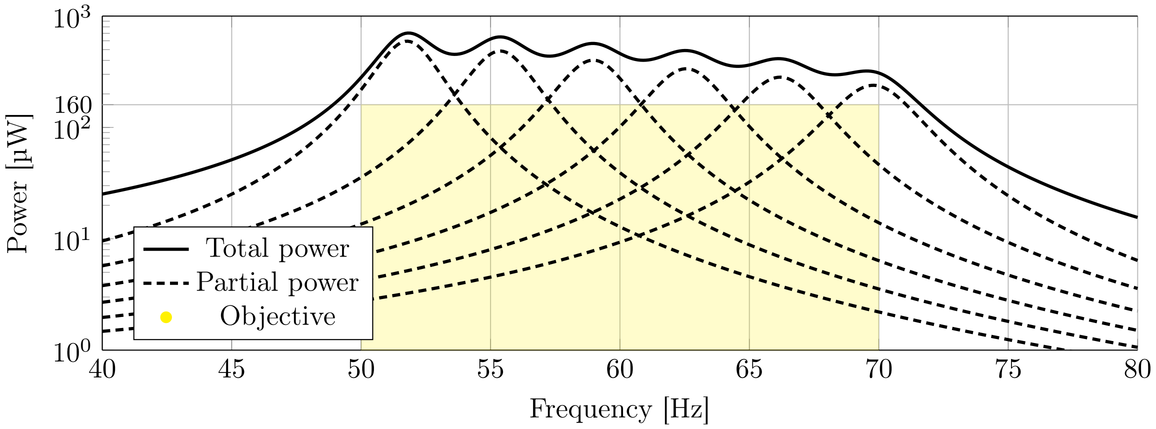

Figure 4.55 – Power at an acceleration of 2.25 $\mathrm{m/s}^2$ of the cantilever array based on design MFC A.

The total power was above the target area for all desired frequencies. Furthermore, the bandwidth with power over the 160 µW mark is from 48.92 Hz to 71.63 Hz (22.71 Hz of bandwidth), 2.71 Hz larger than the requirement. The maximum von Mises stress in the piezoelectric material occurred in the largest (lowest natural frequency) device at approximately 61 MPa, below the 114.8 MPa limit imposed by the tensile strength of the PZT.

CHAPTER 5

EXPERIMENTAL ANALYSIS

5.1 FABRICATION

The fabrication process known as PiezoMUMPs of the foundry MEMSCAP Inc. was chosen as the manufacturing method because of the lower cost of its multi-user process. Figure 5.1 shows the fabrication

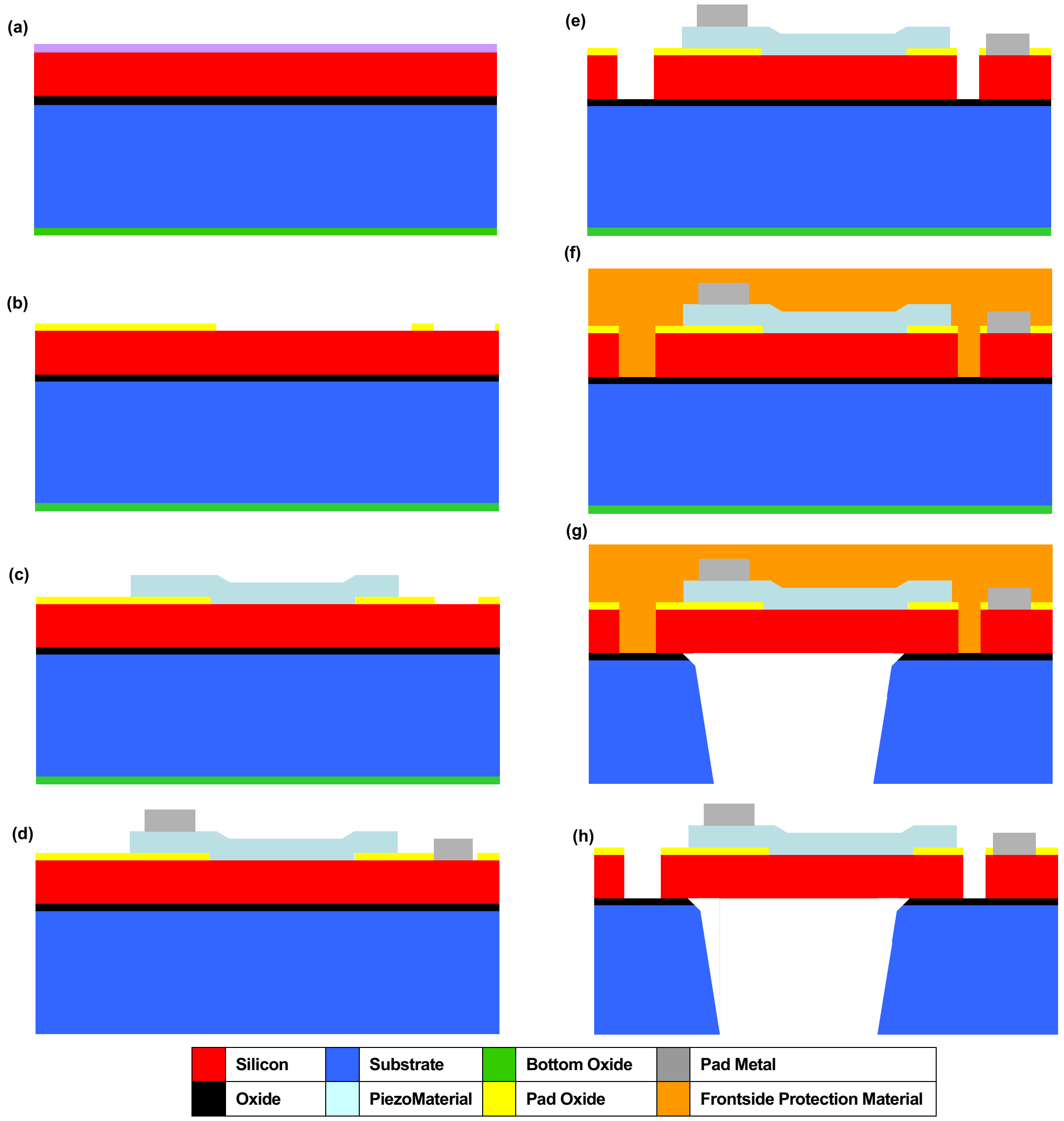

Figure 5.1 – Diagram of PiezoMUMPs fabrication process (Adapted from Cowen et al. (2014)).

process (COWEN et al., 2014). The sequence has eight steps from (a) to (h). The process begins with (a) the deposition of a phosphosilicate glass layer (PSG). The wafers are annealed at 1050°C for one hour in argon to drive the phosphorous dopant to the top surface of the silicon layer. The PSG layer is subsequently removed via wet chemical etching. Then, (b) a 2000 angstrom thermal oxide is grown and patterned by wet-etching, (c) the piezoelectric film AlN is deposited over the wafer by reactive sputtering and patterned via wet-etching, and (d) the wafer is coated with a patterned photoresist. A metal stack of 20 nm of chrome and 1000 nm of aluminum is deposited over the sub-sequentially dissolved photoresist to leave only the metal. (e) The oxide layer and the silicon are etched via Reactive Ion Etching (RIE) and Deep Reactive Ion Etching (DRIE), respectively. (f) A polyimide protective layer is added to the top of the wafer before backside etching. (g) RIE is used to etch the bottom side oxide layer, and DRIE removes the silicon substrate; later, a wet etch process is used to remove the oxide between the SOI wafer in the regions defined by the backside etch. Finally, (h) the front-side protection is removed by dry etching. Figure 5.2 shows a microscope photograph of the prototype.

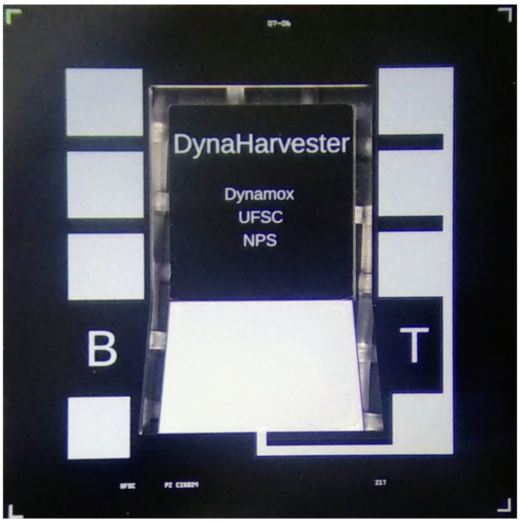

Figure 5.2 – Microscope photograph of the fabricated MEMS Energy Harvester.

The other prototype developed in this work was constructed using the STEMINC bimorphs. This fabrication process is a combination of hand assembly and micromachining techniques. The first step involved cutting the bimorph sheet to the desired geometry. It used an endless diamond wire saw (COSTA; SANTOS, et al., 2022; COSTA; WEINGAERTNER; XAVIER, 2022) with a costume-made fixture was used to hold the bimorph. Two steel seismic masses were machined using a tungsten mass to match the natural frequency of the prototype. The masses were positioned manually and bonded to the bimorph using cyanoacrylate. The resulting prototype is shown in Figure 5.3.

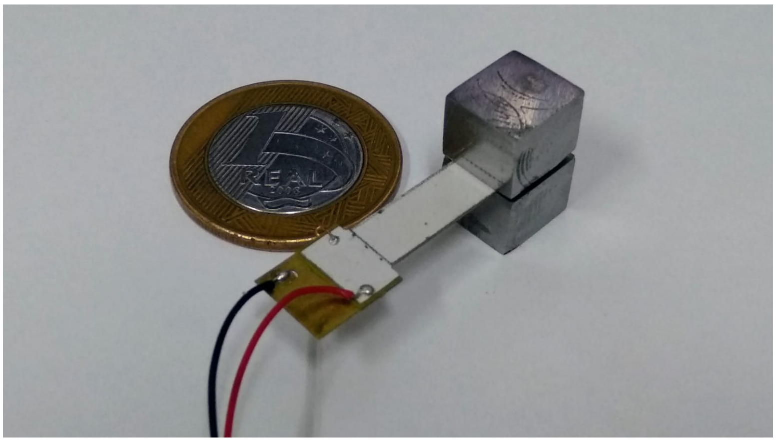

Figure 5.3 – Prototype fabricated from SMBA STEMINC films and two stainless steel seismic masses.

5.2 EXPERIMENT

Some Frequency Response Function (FRF) curves might display interference from the electrical grid and the laser vibrometer system at 60 Hz and ≈41 Hz, respectively. Figure 5.4 shows the autopower spectrum of the background noise of the LDV and the SMBA sheet. It is possible to see the component at ≈41 Hz and, therefore, it could be assumed that the sharp resonance at this frequency is not a mechanical mode of the structure but is, indeed, an interference signal from the LDV.

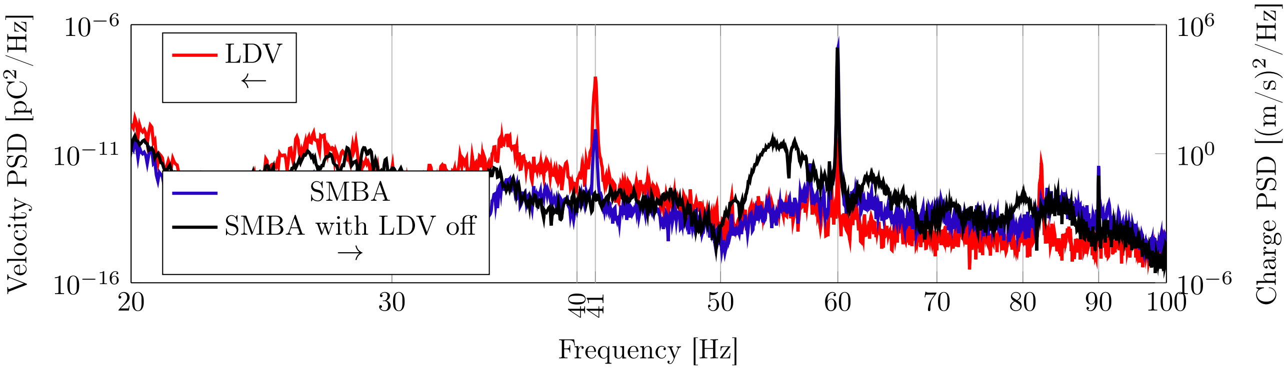

Figure 5.4 – Power Spectral Density of background noise of the LDV. The arrows in the legends indicate whether the corresponding curve is plotted on the left or right axis.

5.2.1 MEMS VEH

In Figure 5.5, the charge sensitivity of the MEMS numerical model is compared to two of the tested MEMS prototypes EH A and B. The difference between the maximum sensitivity of the model and that of the prototypes was owing to the damping considered in the numerical model. As previously described, the damping of the model was given as an optimization parameter because it was possible to control it to a certain extent. However, the tested MEMS prototypes were not encapsulated with a well-defined internal pressure; thus, the sensors were tested at atmospheric pressure without encapsulation. ξ is calculated from the charge sensitivity curves of the prototypes using the Rational Fraction Polynomial method (ACUÑA, 2007), so the equivalent structural damping fits with the total damping from the experiments.

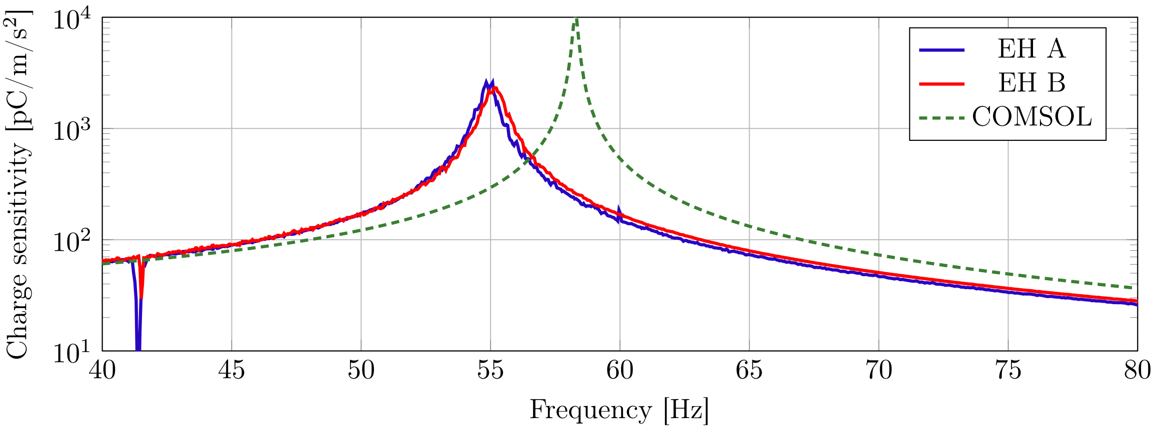

Figure 5.5 – Comparison, in terms of charge sensitivity, of the experimental curves of the EH prototypes A and B with the numerical model of COMSOL with no change in damping.

The difference in the natural frequencies of the prototype and the model was adjusted to correct the differences between the nominal design dimensions and the manufactured ones. Notably, the PiezoMUMPs manufacturing process presents an undercutting of up to 50 μm (COWEN et al., 2014). With these geometric adjustments plus the damping correction, the black curve shown in the graph in Figure 5.6 is obtained.

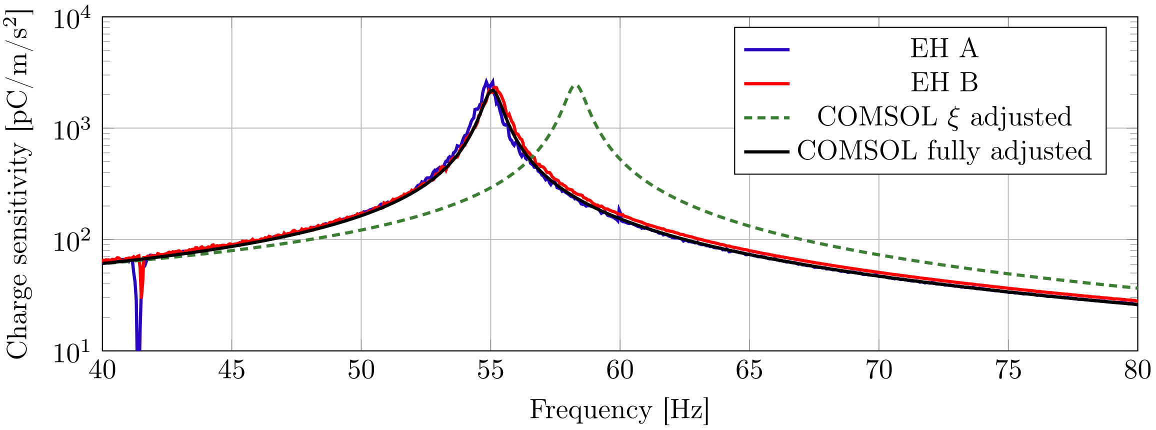

Figure 5.6 – Comparison, in terms of load sensitivity, of the experimental curves of the EH A and B prototypes with the numerical model of COMSOL with damping adjustment only and another with geometric adjustments.

Although the validation of numerical models using a charge amplifier has some advantages, such as eliminating the influence of cables on the acquisition board, this validation may not accurately represent the circuit used to calculate the power extracted from the EH. Almost the same experimental setup as in Figure 3.13 was maintained to calculate the power, except for the charge amplifier, which is replaced by a resistive circuit mounted on a breadboard. This setup, from where the data presented in Figure 5.7 was extracted, shows the maximum power (at the natural frequency) obtained by the prototype as a function of the load resistance variation. The experimental power curve was calculated using the relationship $P = V^2/R$.

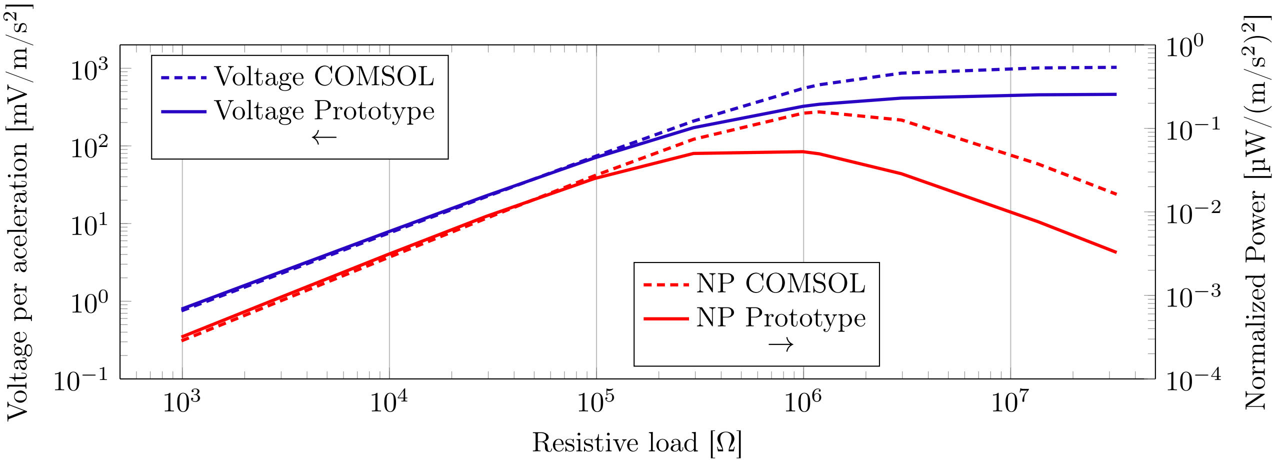

Figure 5.7 – Comparison regarding voltage, power, and the resistive load of experimental curves of prototype EH A with numerical model measured without a charge amplifier. The arrows in the legends indicate whether the corresponding curve is plotted on the left or right axis.

After ≈100 kΩ, there was an increase in the error between the experimental NP-R_l curve and the numerical model. It occurs due to the limitations of the DAQ system, which has input channels with an impedance of 1 MΩ. Thus, when the resistance is close to the impedance of the channels in the DAQ circuit. The coupling with the prototype becomes stronger, which influences the behavior of the EH. If the original experimental setup with the charge amplifier is adopted instead, it is possible to use the relationship $P = R_l \omega^2 Q^2$ (ZHANG; WU; SESSLER, 2015) to convert the charge signal to power. Thus, the error at higher impedance is reduced, as shown in Figure 5.8.

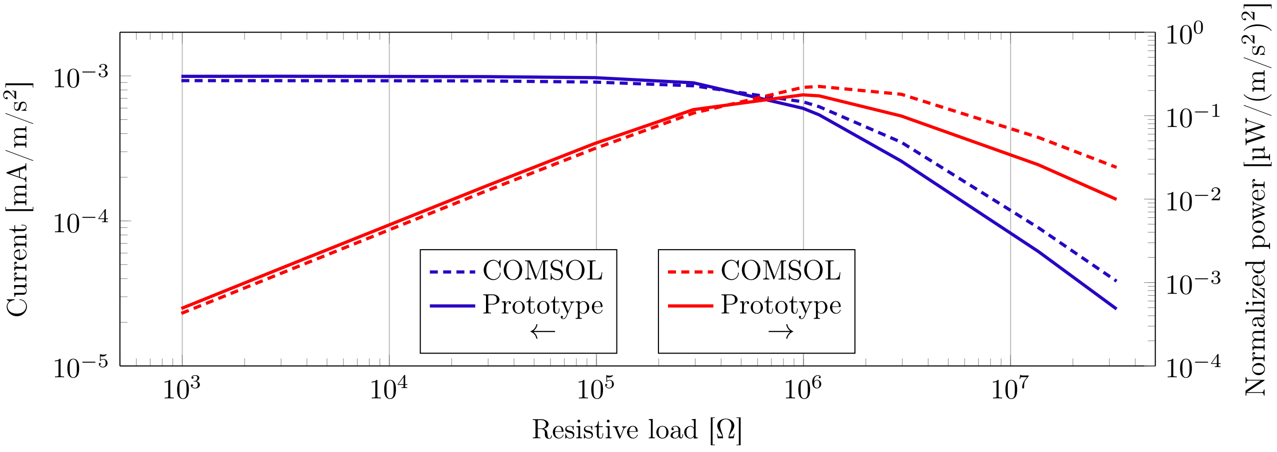

Figure 5.8 – Comparison in terms of current, power, and resistive load of experimental curves of prototype EH A with a numerical model measured using a charge amplifier. The arrows in the legends indicate whether the corresponding curve is plotted on the left or right axis.

Despite the limitations of the experiments, it is possible to see that the experimental data and COMSOL model represent well the format of a characteristic power-R_l graph of an energy harvester, with a close match in the optimum resistive load value of 1 MΩ and 1.2 MΩ for the experimental and numerical models, respectively. Figure 5.9 shows the normalized power at resonance on the left axis, viscous damping ξ on the right axis, and the acceleration of the prototype based on the abscissa axis. For accelerations greater than 0.01 m/s^2, the prototype presents a considerable drop in efficiency, where the power produced drops and the damping ξ increases. This power drop is expected from a device when it starts to show non-itineraries due to a significant increase in the acceleration of the base (MACHADO et al., 2020). Therefore, an optimal acceleration of 0.006 m/s^2 and a limit of 0.01 m/s^2 for an optimized state operation are considered for this design.

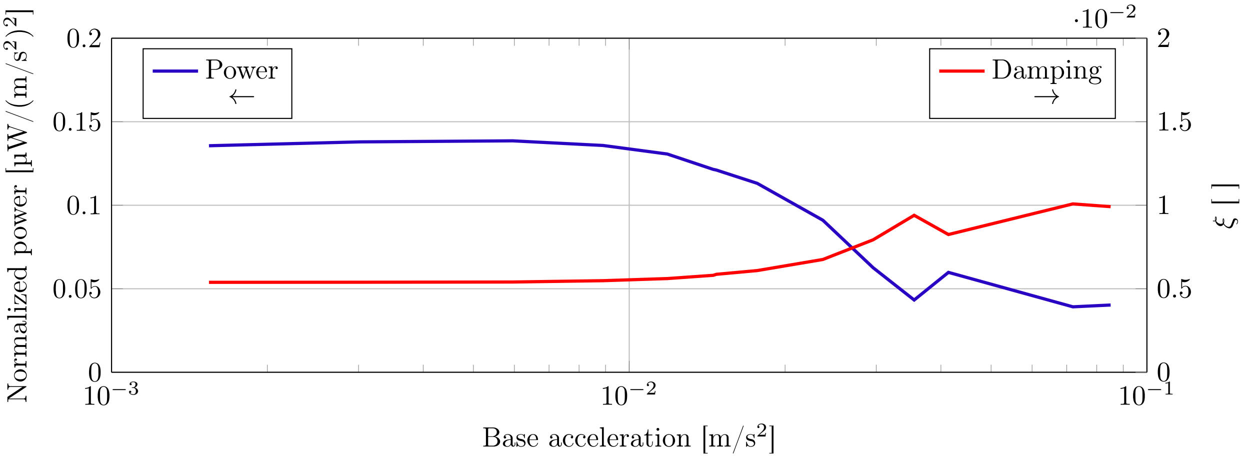

Figure 5.9 – Comparison in terms of power, damping and acceleration of experimental curves of prototype EH A. The arrows in the legends indicate whether the corresponding curve is plotted on the left or right axis.

The power-frequency graph at the optimum load of 1.2 MΩ is shown in Figure 5.10. The numerical data is in accordance with the numerical model. The maximum normalized power obtained by the prototype was 177 nW/m/s^2, while that of the model was 224 nW/m/s^2. This results in an NPD of 1.3 mW/cm^3/g^2 for the prototype and 1.6 mW/cm^3/g^2 for the model, respectively. Due to the damping adjustment, both have approximately the same 0.7 Hz half-power band. Therefore, giving an F.o.M. of 0.9 mW Hz/cm^3/g^2 and 1.1 mW Hz/cm^3/g^2 for the prototype and model, respectively.

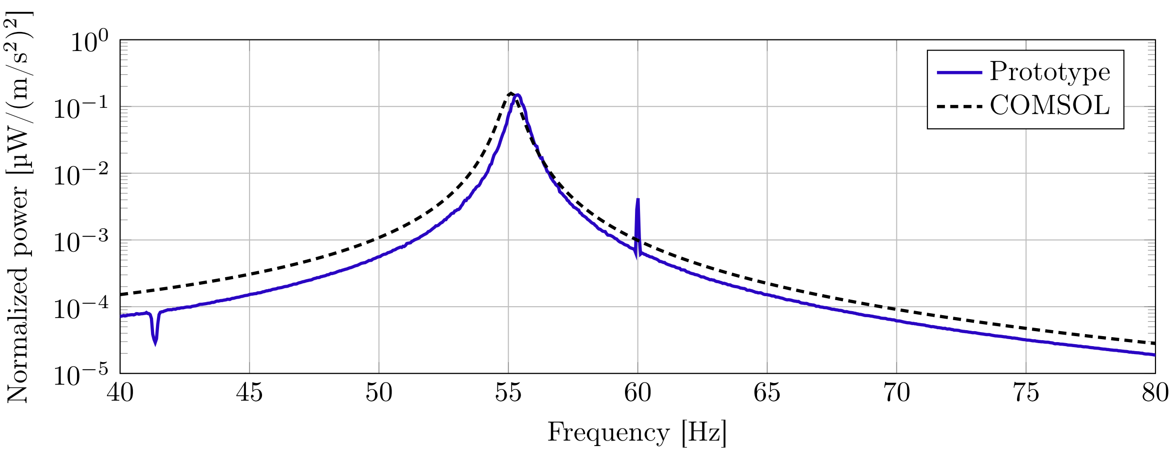

Figure 5.10 – Comparison, in terms of normalized power, of the experimental curves of the EH A prototype with the COMSOL numerical model.

5.2.2 Micromachined VEH

The MEMS prototype was chronologically executed before the STEMINC prototype; therefore, only the setup with a charge amplifier was used. Figure 5.11 shows the FRF of the acceleration of the seismic mass per acceleration of the base. There were some difficulties with the micromachining processes, where the length and width of the cantilever suffered some changes from the nominal value. By adding the fabricated geometric values to the numerical model, the natural frequency shifted from the original 60 Hz to approximately 57.5 Hz, whereas the experimental data indicated a natural frequency of 56.5 Hz. An error of approximately 2% in the prediction. These errors may be due to several factors, such as damage to the device during fabrication or misalignment of the seismic masses during assembly.

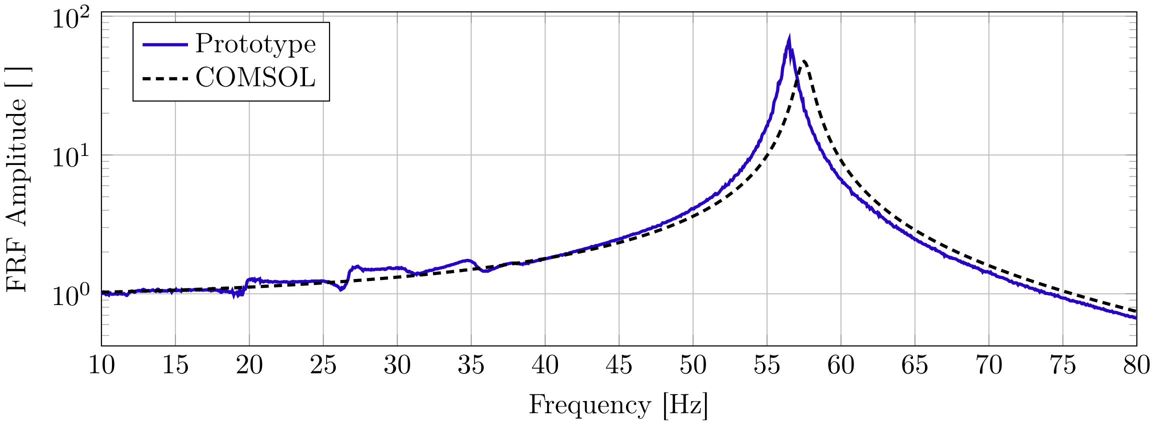

Figure 5.11 – Comparison of the experimental FRF of acceleration of SM per acceleration of the base of the SMBA prototype compared with the numerical model.

The experiment in Figure 5.11 used a steel clamp. However, a cork sheet was positioned between the steel clamp and the EH. This sheet created a fixture that did not damage the wires between the clamps. Because of this non-ideal fixture, the fixed end of the numerical model was changed to a spring foundation of an isotropic stiffness of 53 MN/m, to match the experimental data. The charge sensitivity-frequency graph of the prototype and numerical model is shown in Figure 5.12. With the equivalent spring foundation to match the stiffness of the system with the cork sheet, the natural frequency of the numerical model matches well with the experiment. However, the amplitude of the numerical model is significantly lower than that of the experimental data. This may indicates that the original $d_{31} = -130$ pC/N may be too low. The coefficient was altered to -150 pC/N for correction.

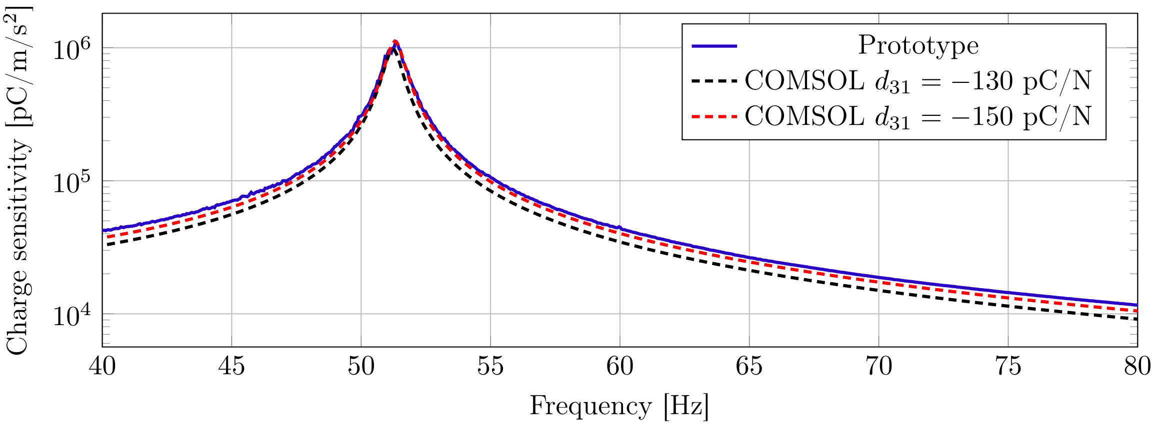

Figure 5.12 – In terms of charge sensitivity, the experimental curves of the SMBA prototype were compared with those of the numerical model.

Figure 5.13 shows ξ calculated via half-power band vs. resistive load for the experimental data and COMSOL model with different input mechanical damping. It is important to note that the simplification of Equation 3.4 is still being used. The figure shows that the COMSOL damping model predicts a much smaller change in total system damping. It may be due to the high coupling coefficient of PZT since the AlN of the MEMS device did not have such an accentuated effect, as shown by the dashed black and red curves. In other words, the numerical model cannot correctly predict the changes in total damping as a function of resistive load for high electromechanical coupling devices. Geometric and material nonlinearity may play a role in this behavior.

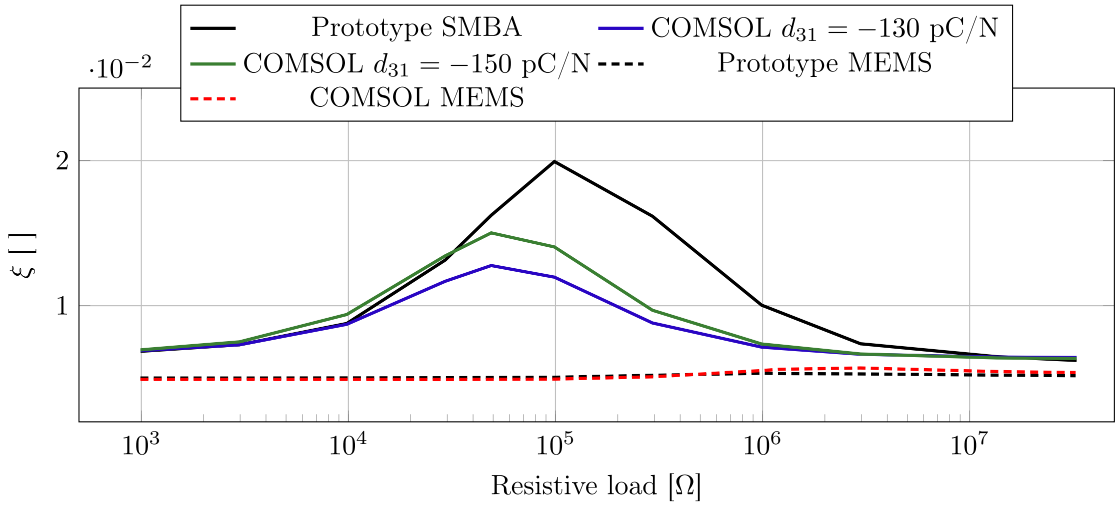

Figure 5.13 – Comparison of the experimental curves of the SMBA prototype with the mathematical model and the MEMS prototype and model in terms of damping ratio and resistive load.

Figure 5.14 is another example of how the damping modeled in COMSOL does not behave well when the electromechanical coupling increases. The graph shows an increase in the natural frequency as the resistive load increases, which is much lower in the COMSOL model (using $d_{31} = -130$ pC/N). The model can get closer to the data using $d_{31} = -150$ pC/N. Nevertheless, a graph of the current and power as a function of the resistive load is shown in Figure 5.15, demonstrates that the numerical model can still predict, with reasonable accuracy, the variation in power and current output as a function of the load of the device. However, as observed with the MEMS prototypes, the models lose accuracy when using higher loads. In this case, the numerical model underestimated the power and charge outputs. The experimental power does not reduce after its optimum value at approximately 30 kΩ; in fact, the power increases again, creating two optimal loads. It indicates that the electromechanical coupling is higher than predicted because the high coupling of the devices may present two optimal resistive loads (LEFEUVRE et al., 2007). The prototype's optimum global load was approximately 30 kΩ and that of the numerical model was at 50 kΩ.

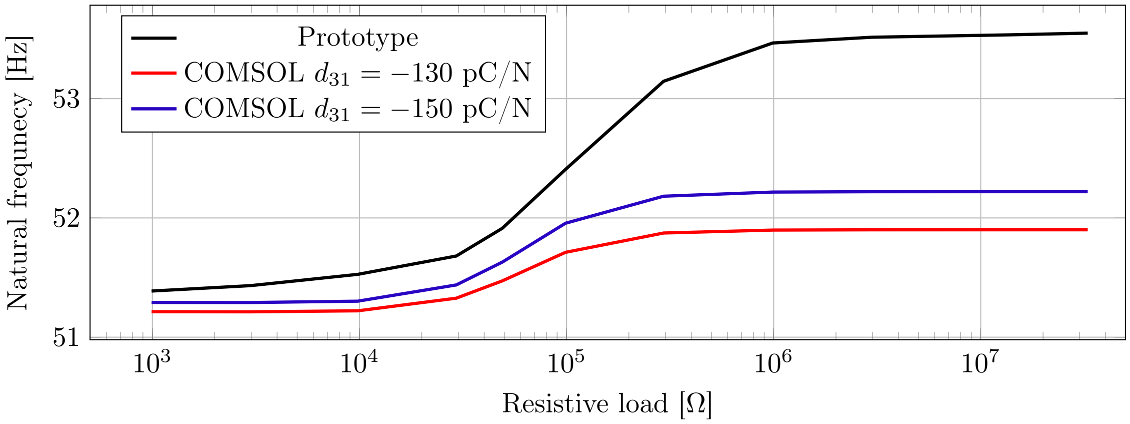

Figure 5.14 – Comparison of the experimental curves of the SMBA prototype with those of the numerical model in terms of natural frequency and resistive load.

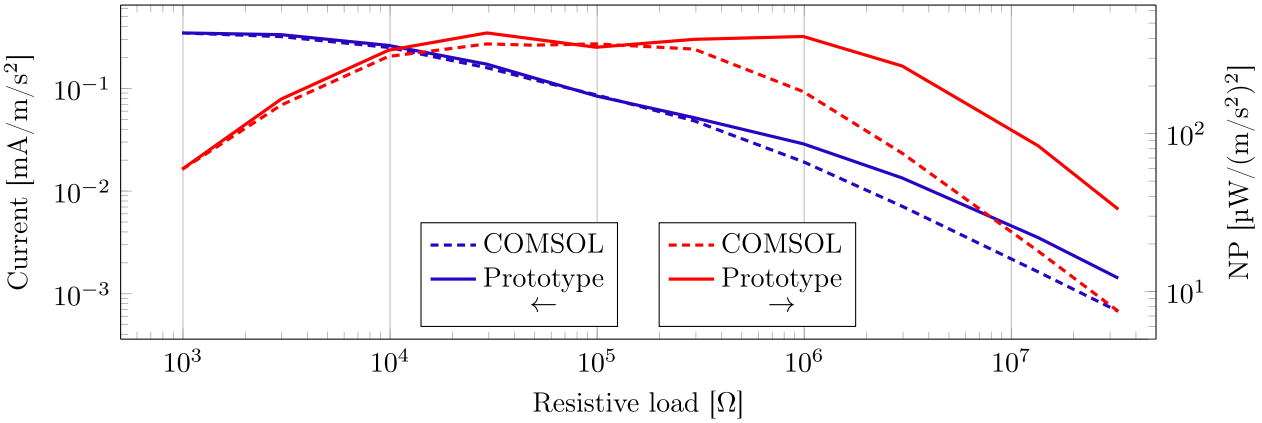

Figure 5.15 – Comparison in terms of current, power and resistive load of the experimental curves of the SMBA prototype compared with the numerical model. The arrows in the legends indicate whether the corresponding curve is plotted on the left or right axis.

The power-frequency graph of the prototype compared with the numerical model for an optimum load of approximately 30 kΩ, is shown in Figure 5.16. The prototype had an active volume of 4.5 cm^3 but could be as low as 1.8 cm^3 if a tungsten mass was used. The normalized power output of the device is 433 μW/m/s^2, rendering an NPD of approximately 9.2 mW/cm^3/g^2, but it could be as high as 23.4 mW/cm^3/g^2 with a tungsten mass of similar weight. The device's bandwidth is 1.45 Hz rendering an F.o.M. of 13.4 mW/cm^3/g^2 for the steel seismic mass and 34.0 mW/cm^3/g^2 if the tungsten mass is used.

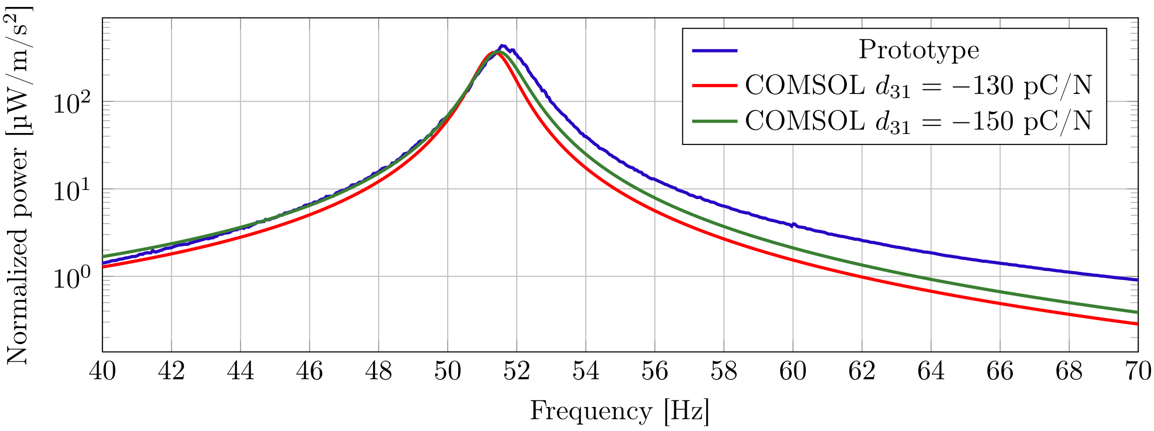

Figure 5.16 – Comparison, of the normalized power of the experimental curves of the SMBA prototype with the numerical model.

5.2.3 Comparison

There are two fabricated and tested prototypes described in this work, the MEMS and the Micromachined devices. In addition, the assumption of another prototype with the same performance as the MM prototype was proposed. However, in this case, the device used a volume that would be achieved if a tungsten mass was used. It was denoted as Micromachined W (MMW) device. Table 5.1 shows the performance metrics of all three prototypes. The micromachined devices performed significantly better than the MEMS devices for both NPD and F.o.M. Multiple factors may play a role in why MM is much better than MEMS at fulfilling the requirements of this study. I.e., thicker piezoelectric films, beam materials with lower stiffness than Si, higher electromechanical coupling, and easier-to-fabricate devices with denser seismic masses, generally lower stresses, and others. Indeed, MEMS devices seem to be better suited only when the volume is much smaller, approximately hundreds of mm^3 or less. The devices proposed here are also compared to others in the literature in terms of NPD (Figure 5.17) and F.o.M. (Figure 5.18), where MMW is among the best NPD and F.o.M. of the devices below 100 Hz.

Table 5.1 – Performance metrics for the prototypes developed in this work, as well as the performance metrics for the MM device assuming tungsten mass.

Prototype	MEMS	Micromachined	Micromachined W
Resonance [Hz]	54	50	50
NP	177 nW/(m/s^2)^2	433 µW/(m/s^2)^2	433 µW/(m/s^2)^2
Volume	13.4 mm^3	4.5 cm^3	1.8 cm^3
Bandwidth [Hz]	0.7	1.45	1.45
NPD [mW/cm^3/g^2]	1.3	9.2	23.4
F.o.M. [mW Hz/cm^3/g^2]	0.9	13.4	33.0

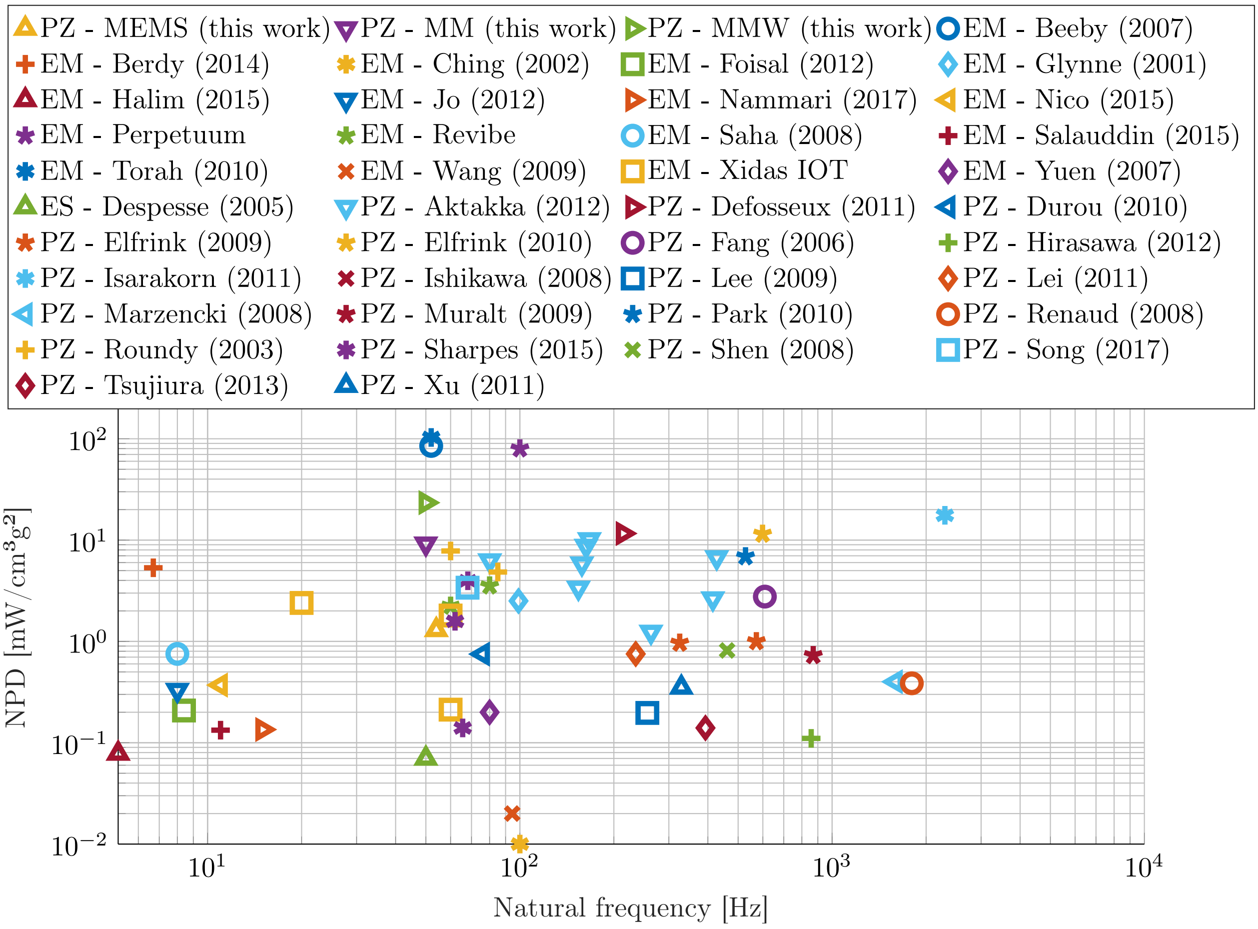

Figure 5.17 – Scatter graph of devices from literature in terms of NPD as a function of natural frequency.

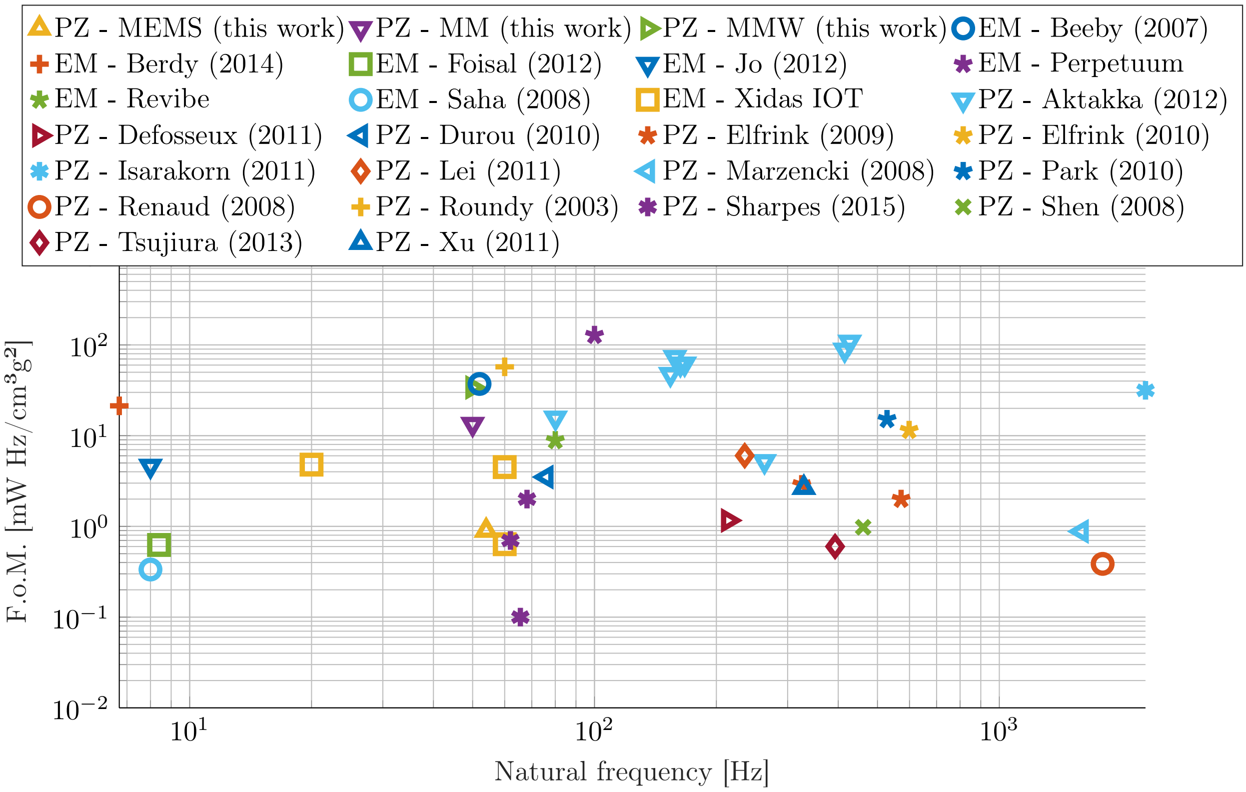

Figure 5.18 – Scatter graph of devices from literature in terms of F.o.M. as a function of natural frequency.

CHAPTER 6

FINAL REMARKS

This work performed a complete design, optimization, prototyping, and validation process twice, using two different fabrication techniques as the basis for design and optimization. Each approach imposes distinct types of restrictions. In other words, MEMS fabrication has restricting limitations regarding the thickness of every layer in the design, as well as being restricted to silicon as the beam material and AlN as the piezoelectric material. Neither was suitable for the proposed project outlines because of its large stiffness and low piezoelectric coefficients. MM fabrication is restricted to the available off-the-shelf piezoelectric sheets; although they usually perform well, there is a considerable restriction regarding the thickness of the layers. The methodology has been proven to work because it allows the development of two devices with competitive metrics, given its limitations.

The numerical model was proven to be accurate for devices with lower electromechanical coupling but presented some deviations when the coupling increased. Therefore, the MEMS numerical model could mimic the actual device's behavior well for low accelerations where the system remained linear, whereas the MM model could not describe the behavior of the device for varying load resistances, which is vital for impedance matching. Nevertheless, the design process of the MM device developed a prototype with performance metrics close to those predicted by the optimization. This indicates that the optimization process leads to devices with outstanding performance despite the limitations of the numerical model.

The piezoelectric MEMS energy harvester design investigated here achieved an NPD of 1.3 mW/cm^3/g^2 and F.o.M. of 0.9 mW Hz/cm^3/g^2. Comparing the device obtained here in terms of NPD with others in the literature, the device can be considered to have good performance, significantly far from the worst documented values, and away from the best. in terms of the F.o.M., the device was placed near the worst performers. The main factor that makes the proposed device a nonviable solution is the optimal acceleration value. That is, industrial machinery monitoring sensors are exposed to vibration amplitudes much greater than the 0.01 m/s^2 threshold of this device. Thus, it is crucial to establish the EH operating point in terms of supplied power, dimensions, operating frequency, and dynamic range. It is believed that some changes to the manufacturing limitations and the optimization method should be able to generate EHs with more appropriate performance for the application. For example, replacing the piezoelectric material with PZT or PMN-32PT should allow the device to generate significantly more more energy at the same volume. The use of bimorphic beam should also provide significant design advances.

In contrast to MEMS, the MM device performed well in terms of NPD and F.o.M. However, it is significantly lower when using steel seismic masses instead of denser materials such as tungsten. Using a tungsten seismic mass of a similar weight to the two steel masses would lower the active volume to less than half and increase the NPD and F.o.M. to where the MMW meets the requirements in terms of NPD and F.o.M. Nevertheless, broadband techniques, such as multimodal cantilever arrays or nonlinear monostable techniques, are still required to achieve the desired bandwidth. It is essential to acknowledge the MFCs films, where the prevalidated optimized model displayed an F.o.M. of 41.8 mW Hz/cm^3/g^2, and an array of similar devices were shown to meet all the requirements proposed in this work.

In the eyes of the author, this work highlights the need to correctly specifying the objective function; the maximum stress and optimal acceleration are the main features to be observed when optimizing PVEH in terms of NPD. Since the power is directly proportional to the square of the stress in the piezoelectric material, mechanical failure and dynamic range will always be significant restrictions to the optimization. Objective functions, where the stress is imposed as a penalty function, seem well-defined when the excitation allows the natural frequency to be placed at the desired position without exceeding the stress limits. However, when working with devices with low damping or large excitation, an objective function in the form of NPD/σ_{max} allows the algorithm to decrease the stresses as much as possible. Thus, the designer can implement mitigation techniques to reduce the possibility of failure by adding a damping or mechanical stopper after the optimization algorithm is complete.

REFERENCES

ACUÑA, Cristian Gutiérrez. **Rational Fraction Polynomial Method**. [S.l.]: MATLAB Central File Exchange, 2007. Available from: <https://www.mathworks.com/matlabcentral/fileexchange/3805-rational-fraction-polynomial-method>. Cited 1 time on page 113.

AKTAKKA, Ethem Erkan; PETERSON, Rebecca L; NAJAFI, Khalil. **Integration of Bulk Piezoelectric Materials into Microsystems**. 2012. PhD thesis – The University of Michigan. Cited 8 times on pages 13, 36, 46–48, 52, 69.

ALTENA, G et al. Design improvements for an electret-based MEMS vibrational electrostatic energy harvester. **Journal of Physics: Conference Series**, v. 476, p. 012078, 2013. ISSN 1742-6588. DOI: 10.1088/1742-6596/476/1/012078. Available from: <https://iopscience.iop.org/article/10.1088/1742-6596/476/1/012078>. Cited 1 time on pages 44, 45.

ANTON, S. R.; ERTURK, A.; INMAN, D. J. Bending strength of piezoelectric ceramics and single crystals for multifunctional load-bearing applications. **IEEE Transactions on Ultrasonics, Ferroelectrics and Frequency Control**, v. 59, n. 6, p. 1085–1092, 2012. ISSN 0885-3010. DOI: 10.1109/TUFFC.2012.2299. Available from: <http://ieeexplore.ieee.org/document/6217557/>. Cited 1 time on page 97.

ARORA, Jasbir Singh. Introduction to Design Optimization. In: INTRODUCTION to Optimum Design. [S.l.]: Elsevier, 2017. P. 3–18. DOI: 10.1016/B978-0-12-800806-5.00001-9. Available from: <https://linkinghub.elsevier.com/retrieve/pii/B9780128008065000019>. Cited 3 times on pages 59–61.

AYALA-GARCIA, I N et al. A tunable kinetic energy harvester with dynamic over range protection. **Smart Materials and Structures**, v. 19, n. 11, p. 115005, 2010. ISSN 0964-1726. DOI: 10.1088/0964-1726/19/11/115005. Available from: <https://iopscience.iop.org/article/10.1088/0964-1726/19/11/115005>. Cited 3 times on pages 42, 54, 64.

BATRA, Ashok K.; ALOMARI, Almuatasim. **Power Harvesting via Smart Materials**. [S.l.]: SPIE, 2017. ISBN 9781510608504. DOI: 10.1117/3.2268643. Available from: <https://spiedigitallibrary.org/ebooks/PM/Power-Harvesting-via-Smart-Materials/eISBN-9781510608504/10.1117/3.2268643>. Cited 3 times on pages 42, 44, 49.

BECKERT, Wieland; KREHER, Wolfgang S. Modelling piezoelectric modules with interdigitated electrode structures. **Computational Materials Science**, v. 26, p. 36–45, 2003. ISSN 09270256. DOI: 10.1016/S0927-0256(02)00390-7. Available from: <https://linkinghub.elsevier.com/retrieve/pii/S0927025602003907>. Cited 1 time on page 51.

BEEBY, S P et al. A micro electromagnetic generator for vibration energy harvesting. **Journal of Micromechanics and Microengineering**, v. 17, n. 7, p. 1257–1265, 2007. ISSN 0960-1317. DOI: 10.1088/0960-1317/17/7/007. Cited 3 times on pages 42, 54.

BEHRISCH, Rainer. Introduction and overview. In: [s.l.: s.n.], 1981. P. 1–8. DOI: 10.1007/3540105212_6. Available from: <http://link.springer.com/10.1007/3540105212_6>. Cited 1 time on page 52.

BILGEN, Onur; WANG, Ya; INMAN, Daniel J. Electromechanical comparison of cantilevered beams with multifunctional piezoceramic devices. **Mechanical Systems and Signal Processing**, v. 27, p. 763–777, 2012. ISSN 08883270. DOI: 10.1016/j.ymssp.2011.09.002. Available from: <https://linkinghub.elsevier.com/retrieve/pii/S0888327011003700>. Cited 1 time on page 51.

BOWEN, C. R. et al. Optimisation of interdigitated electrodes for piezoelectric actuators and active fibre composites. **Journal of Electroceramics**, v. 16, n. 4, p. 263–269, 2006. ISSN 1385-3449. DOI: `10.1007/s10832-006-9862-8`. Available from: <`http://link.springer.com/10.1007/s10832-006-9862-8`>. Cited 1 time on page 51.

BRIAND, Danick et al. **Micro energy harvesting**. [S.l.]: Wiley-VCH, 2015. Cited 3 times on pages 13, 39, 52.

BUEHREN, Markus. **Differential Evolution**. [S.l.]: MATLAB Central File Exchange, 2014. Available from: <`https://www.mathworks.com/matlabcentral/fileexchange/18593-differential-evolution`>. Cited 3 times on pages 14, 36, 77.

CEPNIK, Clemens; LAUSECKER, Roland; WALLRABE, Ulrike. Review on Electrodynamic Energy Harvesters—A Classification Approach. **Micromachines**, v. 4, n. 2, p. 168–196, 2013. ISSN 2072-666X. DOI: `10.3390/mi4020168`. Available from: <`http://www.mdpi.com/2072-666X/4/2/168`>. Cited 1 time on page 43.

CHING, Neil N H et al. A laser-micromachined multi-modal resonating power transducer for wireless sensing systems. **Sensors and Actuators A: Physical**, v. 97-98, p. 685–690, 2002. ISSN 0924-4247. DOI: `https://doi.org/10.1016/S0924-4247(02)00033-X`. Available from: <`http://www.sciencedirect.com/science/article/pii/S092442470200033X`>. Cited 1 time on page 43.

COMSOL MULTIPHYSICS®. **Understanding, and changing, the element order - Knowledge Base**. COMSOL AB, Stockholm, Sweden: [s.n.], 2021. Available from: <`https://www.comsol.nl/support/knowledgebase/1270`>. Cited 0 time on page 135.

COMSOL MULTIPHYSICS® V. 5.4. **AC / DC Module User ' s Guide**. COMSOL AB, Stockholm, Sweden: [s.n.], 2019. Cited 1 time on page 70.

COMSOL MULTIPHYSICS® V. 5.5. **Structural Mechanics Module User's Giude**. COMSOL AB, Stockholm, Sweden: [s.n.], 2020. Cited 3 times on pages 70, 73.

COMSOL MULTIPHYSICS® V. 5.6. **www.comsol.com**. COMSOL AB, Stockholm, Sweden: [s.n.]. Cited 3 times on pages 13, 36, 69.

COSTA, Erick Cardoso; SANTOS, Caroline Piesanti dos, et al. Study on surface integrity and ductile cutting of PV polycrystalline silicon and wear mechanisms of electroplated diamond wire. **The International Journal of Advanced Manufacturing Technology**, v. 122, n. 3-4, p. 1539–1553, 2022. ISSN 0268-3768. DOI: `10.1007/s00170-022-09990-8`. Available from: <`https://link.springer.com/10.1007/s00170-022-09990-8`>. Cited 2 times on pages 14, 112.

COSTA, Erick Cardoso; WEINGAERTNER, Walter Lindolfo; XAVIER, Fabio Antonio. Influence of single diamond wire sawing of photovoltaic monocrystalline silicon on the feed force, surface roughness and micro-crack depth. **Materials Science in Semiconductor Processing**, v. 143, p. 106525, 2022. ISSN 13698001. DOI: `10.1016/j.mssp.2022.106525`. Available from: <`https://linkinghub.elsevier.com/retrieve/pii/S1369800122000737`>. Cited 2 times on pages 14, 112.

COSTANZO, Luigi; VITELLI, Massimo. Tuning Techniques for Piezoelectric and Electromagnetic Vibration Energy Harvesters. **Energies**, v. 13, n. 3, p. 527, 2020. ISSN 1996-1073. DOI: `10.3390/en13030527`. Available from: <`https://www.mdpi.com/1996-1073/13/3/527`>. Cited 1 time on page 52.

COWEN, Allen et al. **PiezoMUMPs™ Design Handbook**. [S.l.], 2014. Cited 3 times on pages 14, 111–113.

DESPESSE, Ghislain et al. Fabrication and characterization of high damping electrostatic micro devices for vibration energy scavenging. **Proc. Design, Test, Integration and Packaging of MEMS and MOEMS**, June, p. 386–390, 2005. Available from: <`https://hal.archives-ouvertes.fr/hal-00748983/`>. Cited 1 time on page 44.

DHADWAL, Harbans S; RASTEGAR, Jahangir. **Energy Harvesting for Low-Power Autonomous Devices and Systems**. [S.l.]: SPIE, 2017. ISBN 9781510604919. DOI: `10.1117/3.2256429`. Available from: <`https://spiedigitallibrary.org/ebooks/TT/Energy-Harvesting-for-Low-Power-Autonomous-Devices-and-Systems/eISBN-9781510604919/10.1117/3.2256429`>. Cited 5 times on pages 13, 39, 40.

DING, Haojiang; CHEN, Weiqiu; ZHANG, L. Basic Equations of Anisotropic Elasticity. In: ELASTICITY of Transversely Isotropic Materials. Berlin/Heidelberg: Springer Netherlands, 2006. P. 1–27. ISBN 978-1-4020-4034-4. DOI: `10.1007/1-4020-4034-2_1`. Available from: <`https://doi.org/10.1007/1-4020-4034-2_1`>. Cited 1 time on page 74.

DUROU, Hugo et al. Micromachined bulk PZT piezoelectric vibration harvester to improve effectiveness over low amplitude and low frequency frequency vibrations. **Proceedings of PowerMEMS**, p. 27–30, 2010. Available from: <`http://cap.ee.ic.ac.uk/$%5Csim$pdm97/powermems/2010/oral-pdfs/027_Durou_138.pdf`>. Cited 3 times on pages 47, 48.

DUTOIT, NOËL E.; WARDLE, BRIAN L.; KIM, SANG-GOOK. DESIGN CONSIDERATIONS FOR MEMS-SCALE PIEZOELECTRIC MECHANICAL VIBRATION ENERGY HARVESTERS. **Integrated Ferroelectrics**, v. 71, n. 1, p. 121–160, 2005. ISSN 1058-4587. DOI: `10.1080/10584580590964574`. Available from: <`https://www.tandfonline.com/doi/full/10.1080/10584580590964574`>. Cited 3 times on pages 51, 69, 133.

DYNAMOX®. **Datasheet DynaLogger AS**. Florianópolis, Brasil, 2021. P. 1. Available from: <`https://dynamox.net/img/Datasheet-DynaLogger-AS-PT.pdf`>. Cited 1 time on page 35.

ELFRINK, R et al. Vacuum-packaged piezoelectric vibration energy harvesters: damping contributions and autonomy for a wireless sensor system. **Journal of Micromechanics and Microengineering**, v. 20, n. 10, p. 104001, 2010. ISSN 0960-1317. DOI: `10.1088/0960-1317/20/10/104001`. Available from: <`https://iopscience.iop.org/article/10.1088/0960-1317/20/10/104001`>. Cited 3 times on pages 46, 47, 84, 90.

FACCHINEI, Francisco; JÚDICE, Joaquim; SOARES, João. Generating box-constrained optimization problems. **ACM Transactions on Mathematical Software**, v. 23, n. 3, p. 443–447, 1997. ISSN 0098-3500. DOI: `10.1145/275323.275331`. Available from: <`https://dl.acm.org/doi/10.1145/275323.275331`>. Cited 1 time on page 61.

GAMMAITONI, Luca. There's plenty of energy at the bottom (micro and nano scale nonlinear noise harvesting). **Contemporary Physics**, v. 53, n. 2, p. 119–135, 2012. ISSN 0010-7514. DOI: `10.1080/00107514.2011.647793`. Available from: <`http://www.tandfonline.com/doi/abs/10.1080/00107514.2011.647793`>. Cited 3 times on pages 13, 36.

GANG ZONG, Deng et al. Tensile strength of aluminium nitride films. **Philosophical Magazine**, v. 84, n. 31, p. 3353–3373, 2004. ISSN 1478-6435. DOI: `10.1080/14786430412331283604`. Available from: <`http://www.tandfonline.com/doi/abs/10.1080/14786430412331283604`>. Cited 1 time on page 90.

GESING, A. L. et al. On the design of a MEMS piezoelectric accelerometer coupled to the middle ear as an implantable sensor for hearing devices. **Scientific Reports**, v. 8, n. 1, p. 3920, 2018. ISSN 2045-2322. DOI: `10.1038/s41598-018-22219-7`. Available from: <`http://www.nature.com/articles/s41598-018-22219-7`>. Cited 2 times on pages 77, 79.

GU, Lei. Low-frequency piezoelectric energy harvesting prototype suitable for the MEMS implementation. **Microelectronics Journal**, v. 42, n. 2, p. 277–282, 2011. ISSN 00262692. DOI: `10.1016/j.mejo.2010.10.007`. Available from: <`https://linkinghub.elsevier.com/retrieve/pii/S0026269210002351`>. Cited 1 time on page 55.

HARNE, R L; WANG, K W. A review of the recent research on vibration energy harvesting via bistable systems. **Smart Materials and StructuresMaterial**, p. 12, 2013. DOI: `10.1088/0964-1726/22/2/023001`. Cited 1 time on page 56.

HAUPT, Randy L.; HAUPT, Sue Ellen. **Practical Genetic Algorithms Second Edition GLOSSARY**. [S.l.: s.n.], 2004. P. 243–250. ISBN 0471455652. arXiv: `arXiv:1011.1669v3`. Cited 3 times on pages 60, 61.

HOPCROFT, Matthew A.; NIX, William D.; KENNY, Thomas W. What is the Young's Modulus of Silicon? **Journal of Microelectromechanical Systems**, v. 19, n. 2, p. 229–238, 2010. ISSN 1057-7157. DOI: `10.1109/JMEMS.2009.2039697`. Available from: <`http://ieeexplore.ieee.org/document/5430873/`>. Cited 1 time on page 71.

HUAN XUE; YUANTAI HU; QING-MING WANG. Broadband piezoelectric energy harvesting devices using multiple bimorphs with different operating frequencies. **IEEE Transactions on Ultrasonics, Ferroelectrics and Frequency Control**, v. 55, n. 9, p. 2104–2108, 2008. ISSN 0885-3010. DOI: `10.1109/TUFFC.903`. Available from: <`http://ieeexplore.ieee.org/document/4626940/`>. Cited 1 time on pages 54, 55.

HUANG, Manjuan et al. A Low-Frequency MEMS Piezoelectric Energy Harvesting System Based on Frequency Up-Conversion Mechanism. **Micromachines 2019, Vol. 10, Page 639**, Multidisciplinary Digital Publishing Institute, v. 10, n. 10, p. 639, 2019. DOI: `10.3390/MI10100639`. Available from: <`https://www.mdpi.com/540260`>. Cited 2 times on pages 55, 69.

IANNACCI, Jacopo. Microsystem based Energy Harvesting (EH-MEMS): Powering pervasivity of the Internet of Things (IoT) – A review with focus on mechanical vibrations. **Journal of King Saud University - Science**, v. 31, n. 1, p. 66–74, 2019. ISSN 10183647. DOI: `10.1016/j.jksus.2017.05.019`. Available from: <`https://linkinghub.elsevier.com/retrieve/pii/S1018364717303579`>. Cited 1 time on page 85.

IANNACCI, Jacopo et al. A novel MEMS-based piezoelectric multi-modal vibration energy harvester concept to power autonomous remote sensing nodes for Internet of Things (IoT) applications. In: 2015 IEEE SENSORS. [S.l.]: IEEE, 2015. P. 1–4. ISBN 978-1-4799-8203-5. DOI: `10.1109/ICSENS.2015.7370550`. Available from: <`http://ieeexplore.ieee.org/document/7370550/`>. Cited 2 times on page 69.

KHALIGH, A.; PENG ZENG; CONG ZHENG. Kinetic Energy Harvesting Using Piezoelectric and Electromagnetic Technologies—State of the Art. **IEEE Transactions on Industrial Electronics**, v. 57, n. 3, p. 850–860, 2010. ISSN 0278-0046. DOI: `10.1109/TIE.2009.2024652`. Available from: <`http://ieeexplore.ieee.org/document/5071287/`>. Cited 2 times on pages 13, 36.

KHAZAEE, Majid; REZANIAKOLAIE, Alireza; ROSENDAHL, Lasse. A broadband macro-fiber-composite piezoelectric energy harvester for higher energy conversion from practical wideband vibrations. **Nano Energy**, v. 76, p. 104978, 2020. ISSN 22112855. DOI: `10.1016/j.nanoen.2020.104978`. Available from: <`https://linkinghub.elsevier.com/retrieve/pii/S2211285520305553`>. Cited 1 time on pages 75, 76.

KHOLKIN, Andrei; PERTSEV, N.; GOLTSEV, Alexander. Piezoelectricity and Crystal Symmetry. In: PIEZOELECTRIC and Acoustic Materials for Transducer Applications. [S.l.: s.n.], 2008. chap. 2, p. 17–38. ISBN 978-0-387-76538-9. DOI: `10.1007/978-0-387-76540-2_2`. Cited 1 time on page 74.

KIM, Seon-Bae et al. Comparison of MEMS PZT Cantilevers Based on d_{31} and d_{33} Modes for Vibration Energy Harvesting. **Journal of Microelectromechanical Systems**, v. 22, n. 1, p. 26–33, 2013. ISSN 1057-7157. DOI: `10.1109/JMEMS.2012.2213069`. Available from: <`http://ieeexplore.ieee.org/document/6293833/`>. Cited 1 time on page 51.

LAGARIAS, Jeffrey C. et al. Convergence Properties of the Nelder–Mead Simplex Method in Low Dimensions. **SIAM Journal on Optimization**, v. 9, n. 1, p. 112–147, 1998. ISSN 1052-6234. DOI: `10.1137/S1052623496303470`. Available from: <`http://epubs.siam.org/doi/10.1137/S1052623496303470`>. Cited 2 times on pages 62, 63, 100.

LEFEUVRE, Elie et al. Buck-boost converter for sensorless power optimization of piezoelectric energy harvester. **IEEE Transactions on Power Electronics**, v. 22, n. 5, p. 2018–2025, 2007. ISSN 08858993. DOI: `10.1109/TPEL.2007.904230`. Available from: <`http://ieeexplore.ieee.org/document/4300887/`>. Cited 1 time on page 117.

LI, Huidong; TIAN, Chuan; DENG, Z. Daniel. Energy harvesting from low frequency applications using piezoelectric materials. **Applied Physics Reviews**, v. 1, n. 4, p. 041301, 2014. ISSN 1931-9401. DOI: `10.1063/1.4900845`. Available from: <`http://aip.scitation.org/doi/10.1063/1.4900845`>. Cited 1 time on page 51.

LIU, Huicong et al. A new S-shaped MEMS PZT cantilever for energy harvesting from low frequency vibrations below 30 Hz. **Microsystem Technologies**, v. 18, n. 4, p. 497–506, 2012. ISSN 0946-7076. DOI: `10.1007/s00542-012-1424-1`. Available from: <`http://link.springer.com/10.1007/s00542-012-1424-1`>. Cited 4 times on pages 57, 64, 134, 150.

________. Investigation of a MEMS piezoelectric energy harvester system with a frequency-widened-bandwidth mechanism introduced by mechanical stoppers. **Smart Materials and Structures**, v. 21, n. 3, 2012. ISSN 0964-1726. DOI: 10.1088/0964-1726/21/3/035005. Cited 8 times on pages 57, 64, 69, 149, 150.

LIU, Jing-Quan et al. A MEMS-based piezoelectric power generator array for vibration energy harvesting. **Microelectronics Journal**, v. 39, n. 5, p. 802–806, 2008. ISSN 00262692. DOI: 10.1016/j.mejo.2007.12.017. Available from: <https://linkinghub.elsevier.com/retrieve/pii/S0026269207003965>. Cited 1 time on pages 54, 55.

MACHADO, Sebastián P et al. A piezoelectric beam model with geometric, material and damping nonlinearities for energy harvesting. **Smart Materials and Structures**, v. 29, n. 9, p. 095009, 2020. ISSN 0964-1726. DOI: 10.1088/1361-665X/ab9ddb. Available from: <https://iopscience.iop.org/article/10.1088/1361-665X/ab9ddb>. Cited 1 time on page 115.

MAITZLER, A. H. et al. IEEE Standard on Piezoelectricity. **ANSI/IEEE Std 176-1987**, 1988. DOI: 10.1109/IEEESTD.1988.79638. Cited 2 times on pages 50, 74.

MARIN, Anthony. **Mechanical Energy Harvesting for Powering Distributed Sensors and Recharging Storage Systems**. 2013. PhD thesis – Virginia Polytechnic Institute. Cited 4 times on pages 40, 41, 64.

MATLAB. **Surrogateopt copyright 2018-2020**. Natick, Massachusetts: The MathWorks, Inc., 2020. Available from: <https://www.mathworks.com/help/gads/surrogate-optimization-algorithm.html>. Cited 2 times on pages 63, 64.

MIRON, Guilherme; PAUL, Stephan; CORDIOLI, Julio. On the design and packaging of piezoelectric accelerometers for hearing devices. In: XII CONGRESSO IBEROAMERICANO DE ACÚSTICA. Florianópolis, Brasil: [s.n.], 2022. P. 9. Cited 4 times on pages 14, 77, 90.

MITCHESON, P D et al. Performance limits of the three MEMS inertial energy generator transduction. September, 2007. DOI: 10.1088/0960-1317/17/9/S01. Cited 1 time on page 45.

MÜLLER, Juliane. MATSuMoTo: The MATLAB Surrogate Model Toolbox For Computationally Expensive Black-Box Global Optimization Problems, 2014. arXiv: 1404.4261. Available from: <http://arxiv.org/abs/1404.4261>. Cited 1 time on page 78.

________. MISO: mixed-integer surrogate optimization framework. **Optimization and Engineering**, v. 17, n. 1, p. 177–203, 2016. ISSN 1389-4420. DOI: 10.1007/s11081-015-9281-2. Available from: <http://link.springer.com/10.1007/s11081-015-9281-2>. Cited 2 times on pages 63, 78.

OU, Z.C.; WU, Xijia. On the crack-tip stress singularity of interfacial cracks in transversely isotropic piezoelectric bimaterials. **International Journal of Solids and Structures**, v. 40, n. 26, p. 7499–7511, 2003. ISSN 00207683. DOI: 10.1016/j.ijsolstr.2003.08.021. Available from: <https://linkinghub.elsevier.com/retrieve/pii/S0020768303004797>. Cited 1 time on page 74.

PARK, Jung-Hyun et al. Analysis of Stress Distribution in Piezoelectric MEMS Energy Harvester Using Shaped Cantilever Structure. **Ferroelectrics**, v. 409, n. 1, p. 55–61, 2010. ISSN 0015-0193. DOI: 10.1080/00150193.2010.487125. Available from: <http://www.tandfonline.com/doi/abs/10.1080/00150193.2010.487125>. Cited 1 time on page 69.

PERPETUUM LTD. **Vibration Energy Harvesters Technical Datasheet**. Southampton, UK, 2013. Cited 1 time on pages 42, 43.

PRIME FARADAY PARTNERSHIP. **An Introduction to MEMS**. Ed. by Prime Faraday Partnership. Loughborough: Loughborough University, 2002. ISBN 1-84402-020-7. Cited 1 time on page 39.

PRIYA, Shashank et al. A Review on Piezoelectric Energy Harvesting: Materials, Methods, and Circuits. **Energy Harvesting and Systems**, v. 4, n. 1, p. 3–39, 2019. ISSN 2329-8774. DOI: 10.1515/ehs-2016-0028. Available from: <https://www.degruyter.com/document/doi/10.1515/ehs-2016-0028/html>. Cited 4 times on pages 40, 69.

RAMLAN, R. et al. Potential benefits of a non-linear stiffness in an energy harvesting device. **Nonlinear Dynamics**, v. 59, n. 4, p. 545–558, 2010. ISSN 0924-090X. DOI: `10.1007/s11071-009-9561-5`. Available from: <`http://link.springer.com/10.1007/s11071-009-9561-5`>. Cited 2 times on pages 45, 56.

RANDALL, Robert B. Introduction and Background. In: VIBRATION-BASED Condition Monitoring. Chichester, UK: John Wiley & Sons, Ltd, 2010. P. 1–23. DOI: `10.1002/9780470977668.ch1`. Available from: <`https://onlinelibrary.wiley.com/doi/10.1002/9780470977668.ch1`>. Cited 5 times on pages 13, 35.

REVIBE ENERGY. Model Q Datasheet, 2021. Cited 1 time on page 57.

RHIMI, Mohamed. Power Management and Damage Assessment Techniques for Self-Powered Sensing Based on Piezoelectric, 2013. Available from: <`https://d.lib.msu.edu/etd/2188/datastream/OBJ/download/Power_management_and_damage_assessment_techniques_for_self-powered_sensing_based_on_piezoelectric_transduction.pdf`>. Cited 1 time on page 75.

ROUNDY, S; WRIGHT, P K. A piezoelectric vibration based generator for wireless electronics. **Smart Materials and Structures**, v. 13, n. 5, p. 1131–1142, 2004. ISSN 0964-1726. DOI: `10.1088/0964-1726/13/5/018`. Available from: <`https://iopscience.iop.org/article/10.1088/0964-1726/13/5/018`>. Cited 2 times on pages 13, 39, 41.

ROUNDY, S.; LELAND, E.S., et al. Improving Power Output for Vibration-Based Energy Scavengers. **IEEE Pervasive Computing**, v. 4, n. 1, p. 28–36, 2005. ISSN 1536-1268. DOI: `10.1109/MPRV.2005.14`. Available from: <`http://ieeexplore.ieee.org/document/1401840/`>. Cited 4 times on pages 13, 39, 41, 69.

ROUNDY, Shad. **Energy Scavenging for Wireless Sensor Nodes with a Focus on Vibration to Electricity Conversion**. 2003. PhD thesis – The university of california, Berkeley. Cited 5 times on pages 47, 73, 103.

ROUNDY, Shad; ZHANG, Yang. Toward self-tuning adaptive vibration-based microgenerators. In________. **Smart Structures, Devices, and Systems II, Proceedings of SPIE**. [S.l.: s.n.], 2005. P. 373. DOI: `10.1117/12.581887`. Available from: <`http://proceedings.spiedigitallibrary.org/proceeding.aspx?doi=10.1117/12.581887`>. Cited 3 times on pages 52, 54.

SELVAN, Krishna Veni; MOHAMED ALI, Mohamed Sultan. Micro-scale energy harvesting devices: Review of methodological performances in the last decade. **Renewable and Sustainable Energy Reviews**, v. 54, p. 1035–1047, 2016. ISSN 13640321. DOI: `10.1016/j.rser.2015.10.046`. Available from: <`https://linkinghub.elsevier.com/retrieve/pii/S1364032115011259`>. Cited 2 times on pages 13, 36.

SHARPES, Nathan; ABDELKEFI, Abdessattar; PRIYA, Shashank. Two-dimensional concentrated-stress low-frequency piezoelectric vibration energy harvesters. **Applied Physics Letters**, v. 107, n. 9, p. 093901, 2015. ISSN 0003-6951. DOI: `10.1063/1.4929844`. Available from: <`http://aip.scitation.org/doi/10.1063/1.4929844`>. Cited 1 time on page 46.

SIROHI, Jayant; CHOPRA, Inderjit. Fundamental Understanding of Piezoelectric Strain Sensors. **Journal of Intelligent Material Systems and Structures**, v. 11, n. 4, p. 246–257, 2000. ISSN 1045-389X. DOI: `10.1106/8BFB-GC8P-XQ47-YCQ0`. Available from: <`http://journals.sagepub.com/doi/10.1106/8BFB-GC8P-XQ47-YCQ0`>. Cited 1 time on page 50.

SODANO, Henry A; LLOYD, Justin; INMAN, Daniel J. An experimental comparison between several active composite actuators for power generation. **Smart Materials and Structures**, v. 15, n. 5, p. 1211–1216, 2006. ISSN 0964-1726. DOI: `10.1088/0964-1726/15/5/007`. Available from: <`https://iopscience.iop.org/article/10.1088/0964-1726/15/5/007`>. Cited 1 time on page 51.

SONG, Hyun-Cheol et al. Ultra-Low Resonant Piezoelectric MEMS Energy Harvester With High Power Density. **Journal of Microelectromechanical Systems**, v. 26, n. 6, p. 1226–1234, 2017. ISSN 1057-7157. DOI: `10.1109/JMEMS.2017.2728821`. Available from: <`http://ieeexplore.ieee.org/document/8006212/`>. Cited 4 times on pages 14, 45–47.

STANTON, Samuel C.; MCGEHEE, Clark C.; MANN, Brian P. Reversible hysteresis for broadband magnetopiezoelastic energy harvesting. **Applied Physics Letters**, v. 95, n. 17, p. 174103, 2009. ISSN 0003-6951. DOI: `10.1063/1.3253710`. Available from: <`http://aip.scitation.org/doi/10.1063/1.3253710`>. Cited 1 time on page 56.

TAKEI, Ryohei et al. Design of piezoelectric MEMS cantilever for low-frequency vibration energy harvester. **Japanese Journal of Applied Physics**, v. 55, 6S1, 06gp14, 2016. ISSN 0021-4922. DOI: `10.7567/JJAP.55.06GP14`. Available from: <`https://iopscience.iop.org/article/10.7567/JJAP.55.06GP14`>. Cited 1 time on page 69.

TANG, Lihua; YANG, Yaowen; SOH, Chee Kiong. Toward Broadband Vibration-based Energy Harvesting. **Journal of Intelligent Material Systems and Structures**, v. 21, n. 18, p. 1867–1897, 2010. ISSN 1045-389X. DOI: `10.1177/1045389X10390249`. Available from: <`http://journals.sagepub.com/doi/10.1177/1045389X10390249`>. Cited 2 times on pages 52, 53.

TIAN, Wenchao et al. A Review of MEMS Scale Piezoelectric Energy Harvester. **Applied Sciences**, v. 8, n. 4, p. 645, 2018. ISSN 2076-3417. DOI: `10.3390/app8040645`. Available from: <`http://www.mdpi.com/2076-3417/8/4/645`>. Cited 1 time on page 45.

TORAH, Russel et al. Energy aware wireless microsystem powered by vibration energy harvesting. **PowerMEMS**, n. 01, 2007. Cited 1 time on page 42.

TORCZON, Virginia Joanne. **Multidirectional search: A direct search algorithm for parallel machines**. 1989. PhD thesis – Rice University. Available from: <`https://hdl.handle.net/1911/16304`>. Cited 1 time on page 100.

TSUJIURA, Yuichi et al. Lead-Free Piezoelectric MEMS Energy Harvesters of (K,Na)NbO 3 Thin Films on Stainless Steel Cantilevers. **Japanese Journal of Applied Physics**, v. 52, 9S1, 09kd13, 2013. ISSN 0021-4922. DOI: `10.7567/JJAP.52.09KD13`. Available from: <`https://iopscience.iop.org/article/10.7567/JJAP.52.09KD13`>. Cited 2 times on pages 45, 56.

UCHINO, K. The Development of Piezoelectric Materials and the New Perspective. In: ADVANCED Piezoelectric Materials. [S.l.]: Elsevier, 2017. P. 1–92. DOI: `10.1016/B978-0-08-102135-4.00001-1`. Available from: <`https://linkinghub.elsevier.com/retrieve/pii/B9780081021354000011`>. Cited 1 time on page 52.

VIEZO. **Powerail**. [S.l.: s.n.], 2022. Available from: <`https://www.linkedin.com/posts/viezo_its-all-about-the-details-activity-6881893985770622976-O8fl?utm_source=share&utm_medium=member_desktop`>. Cited 0 time on page 58.

WANG, Lu et al. High accuracy comsol simulation method of bimorph cantilever for piezoelectric vibration energy harvesting. **AIP Advances**, v. 9, n. 9, p. 095067, 2019. ISSN 2158-3226. DOI: `10.1063/1.5119328`. Available from: <`http://aip.scitation.org/doi/10.1063/1.5119328`>. Cited 1 time on page 69.

WANG, Peihong et al. A micro electromagnetic low level vibration energy harvester based on MEMS technology. **Microsystem Technologies**, v. 15, n. 6, p. 941–951, 2009. ISSN 0946-7076. DOI: `10.1007/s00542-009-0827-0`. Available from: <`http://link.springer.com/10.1007/s00542-009-0827-0`>. Cited 1 time on page 44.

XIDAS IOT. **VEG Datasheet**. [S.l.]. Available from: <`https://xidasiot.com/power/veg#`>. Cited 1 time on page 57.

XU, R.; KIM, S. G. FIGURES OF MERITS OF PIEZOELECTRIC MATERIALS IN ENERGY HARVESTERS. In: POWERMEMS. [S.l.: s.n.], 2012. Cited 1 time on page 52.

XU, Ruize. **The Design of Low-frequenci, Low-g Piezoelectric Micro Energy Harvesters**. 2012. S. 122. PhD thesis – Massachusetts Institute of Technology. Cited 1 time on page 40.

YANG, Jin; CHEN, Jun, et al. Broadband Vibrational Energy Harvesting Based on a Triboelectric Nanogenerator. **Advanced Energy Materials**, v. 4, n. 6, p. 1301322, 2014. ISSN 16146832. DOI:

10.1002/aenm.201301322. Available from: <https://onlinelibrary.wiley.com/doi/10.1002/aenm.201301322>. Cited 4 times on pages 39, 49, 50, 64.

YANG, Zhengbao; TAN, Yimin; ZU, Jean. A multi-impact frequency up-converted magnetostrictive transducer for harvesting energy from finger tapping. **International Journal of Mechanical Sciences**, v. 126, p. 235–241, 2017. ISSN 00207403. DOI: 10.1016/j.ijmecsci.2017.03.032. Available from: <https://linkinghub.elsevier.com/retrieve/pii/S0020740316307718>. Cited 3 times on pages 39, 49, 55.

YUEN, Steve et al. An AA-Sized Vibration-Based Microgenerator for Wireless Sensors. **IEEE Pervasive Computing**, v. 6, n. 1, p. 64–72, 2007. ISSN 1536-1268. DOI: 10.1109/MPRV.2007.4. Available from: <http://ieeexplore.ieee.org/document/4101144/>. Cited 1 time on page 43.

ZHANG, Xiaoqing; WU, Liming; SESSLER, Gerhard M. Energy harvesting from vibration with cross-linked polypropylene piezoelectrets. **AIP Advances**, v. 5, n. 7, p. 077185, 2015. ISSN 2158-3226. DOI: 10.1063/1.4928039. Available from: <http://aip.scitation.org/doi/10.1063/1.4928039>. Cited 1 time on page 114.

ZHOU, Shengxi et al. Broadband tristable energy harvester: Modeling and experiment verification. **Applied Energy**, v. 133, p. 33–39, 2014. ISSN 03062619. DOI: 10.1016/j.apenergy.2014.07.077. Available from: <https://linkinghub.elsevier.com/retrieve/pii/S0306261914007600>. Cited 2 times on pages 56, 57.

ZOU, Hong-Xiang et al. Mechanical modulations for enhancing energy harvesting: Principles, methods and applications. **Applied Energy**, v. 255, p. 113871, 2019. ISSN 03062619. DOI: 10.1016/j.apenergy.2019.113871. Available from: <https://linkinghub.elsevier.com/retrieve/pii/S0306261919315582>. Cited 2 times on pages 13, 36.

Appendix

APPENDIX A

Piezoelectric Energy Harvester Equation

To write the power equation of an energy harvester, let us begin with an equilibrium analysis, where the governing equations can be written in terms of (DUTOIT; WARDLE; KIM, 2005),

$$\ddot{x} + 2\zeta_{\mathrm{m}}\omega_{\mathrm{n}}\dot{x} + \omega_{\mathrm{n}}^2 x - \omega_{\mathrm{n}}^2 d_{33} V_{\mathrm{t}} = -\ddot{x}_{\mathrm{b}}, \tag{A.1}$$

and

$$R_{\mathrm{eq}} C_{\mathrm{p}} \dot{V}_{\mathrm{t}} + V_{\mathrm{t}} + m_{\mathrm{eq}} R_{\mathrm{eq}} d_{33} \omega_{\mathrm{n}}^2 \dot{x} = 0, \tag{A.2}$$

where R_{eq} is the parallel resistance of the load and piezoelectric leakage resistance, and m_{eq} is the equivalent mass of the one DoF system. Assuming harmonic base excitation and making some simplifications, the voltage per acceleration can be written as

$$\left|\frac{v}{\ddot{x}_{\mathrm{b}}}\right| = \frac{m_{\mathrm{eq}} R_{\mathrm{eq}} d_{33} \omega_{\mathrm{n}} \Omega}{\sqrt{\left[1 - \left(1 + 2\xi_{\mathrm{m}} r\right)\Omega^2\right]^2 + \left[\left(1 + k_{\mathrm{e}}^2\right) r\Omega + 2\xi_{\mathrm{m}}\Omega - r\Omega^3\right]^2}}, \tag{A.3}$$

where $\Omega = \omega/\omega_{\mathrm{n}}$, $r = \omega_{\mathrm{n}} R_{\mathrm{eq}} C_{\mathrm{p}}$, and $k_{\mathrm{e}}^2 = \frac{k_{33}^2}{1-k_{33}^2} = \frac{d_{33}^2}{s_{33}^E \varepsilon_{33}^\sigma}$. Using the relation $P = V^2/R$ it is possible to write the power at the restive load connected to the EH,

$$\left|\frac{P_{\mathrm{out}}}{\left(\ddot{x}_{\mathrm{b}}\right)^2}\right| = \frac{m_{\mathrm{eq}} 1/\omega_{\mathrm{n}} r k_{\mathrm{e}}^2 R_{\mathrm{eq}}/R_{\mathrm{l}} \Omega^2}{\left[1 - \left(1 + 2\xi_{\mathrm{m}} r\right)\Omega^2\right]^2 + \left[\left(1 + k_{\mathrm{e}}^2\right) r\Omega + 2\xi_{\mathrm{m}}\Omega - r\Omega^3\right]^2}. \tag{A.4}$$

Interestingly, by isolating V_{t} from Equation A.2 and using Equation A.1, it is possible to derive an equation that highlights the effects of the piezoelectric coefficient on the movement equation,

$$\ddot{x} + 2\left(\xi_{\mathrm{m}} + \frac{m_{\mathrm{eq}} R_{\mathrm{eq}} d_{33}^2 \omega_{\mathrm{n}}^3}{2}\right)\omega_{\mathrm{n}}\dot{x} + \omega_{\mathrm{n}}^2 x = -\left(\ddot{x}_{\mathrm{b}} + \omega_{\mathrm{n}}^2 d_{33} R_{\mathrm{eq}} C_{\mathrm{p}} \dot{V}_{\mathrm{t}}\right). \tag{A.5}$$

In this form the equation highlights,

$$\left(\xi_{\mathrm{m}} + \frac{m_{\mathrm{eq}} R_{\mathrm{eq}} d_{33}^2 \omega_{\mathrm{n}}^3}{2}\right), \tag{A.6}$$

as a form of equivalent damping ratio, where a higher d_{33} increases the damping of the movement of the mass.

Huicong Liu et al. (2012a) took a similar approach but highlighted the stress in the piezoelectric film in the equilibrium equation, where the Equations A.1 and A.2, would take the form,

$$m_{\mathrm{eq}}\ddot{x} + b_{\mathrm{m}}\dot{x} + k_{\mathrm{sp}}x + \frac{z_1 c_{11} d_{31}}{t_{\mathrm{pz}}} V_{\mathrm{t}} = -m\ddot{x}_{\mathrm{b}}, \tag{A.7}$$

and

$$\frac{z_2 d_{31} t_{\mathrm{pz}}}{\varepsilon}\dot{x} - \frac{1}{R_{\mathrm{l}} C_{\mathrm{p}}} V_{\mathrm{t}} = \dot{V}_{\mathrm{t}}, \tag{A.8}$$

where b_{m} is the mechanical damping coefficient of the one DoF system, k_{sp} is the equivalent spring constant of the one DoF system, z_1 is the ratio of vertical force to stress in the piezoelectric layer, z_2 is the ratio of stress in the piezoelectric layer to vertical displacement of the seismic mass. This way, assuming harmonic perturbation, the voltage per acceleration takes the form,

$$\frac{v}{\ddot{x}_{\mathrm{b}}} = \frac{-j\omega \frac{z_2 d_{31} t_{\mathrm{pz}}}{\varepsilon}}{\left[\frac{1}{R_{\mathrm{l}} C_{\mathrm{p}}}\omega_{\mathrm{n}}^2 - \left(\frac{1}{R_{\mathrm{l}} C_{\mathrm{p}}} + 2\varsigma\omega_{\mathrm{n}}\right)\omega^2\right] + j\omega\left[\omega_{\mathrm{n}}^2\left(1 + k_{31}^2\right) + \frac{2\xi\omega_{\mathrm{n}}}{R_{\mathrm{l}} C_{\mathrm{p}}} - \omega^2\right]}. \tag{A.9}$$

Assuming that ω matches the natural frequency, the power equation can be written in the form,

$$\frac{P}{\ddot{x}_{\mathrm{b}}^2} = \frac{1}{2}\frac{\frac{1}{\omega_{\mathrm{n}}^2} R_{\mathrm{l}} C_{\mathrm{p}}^2 \left(\frac{z_2 d_{31} t_{\mathrm{pz}}}{\varepsilon}\right)^2}{\left(R_{\mathrm{l}} C_{\mathrm{p}} \omega_{\mathrm{n}}\right)^2 \left(4\xi^2 + k_{31}^4\right) + R_{\mathrm{l}} C_{\mathrm{p}} 4\xi\omega_{\mathrm{n}} k_{31}^2 + 4\xi^2}. \tag{A.10}$$

APPENDIX B

MESH ANALYSIS OF COMSOL MODELS

The element type nomenclature used in this work follows the illustration presented in Figure B.1. This illustrates the node placement and the shape of several second-order elements. The black, white, and gray nodes are all present in the Lagrangian elements, whereas the gray nodes are removed from the Serendipity.

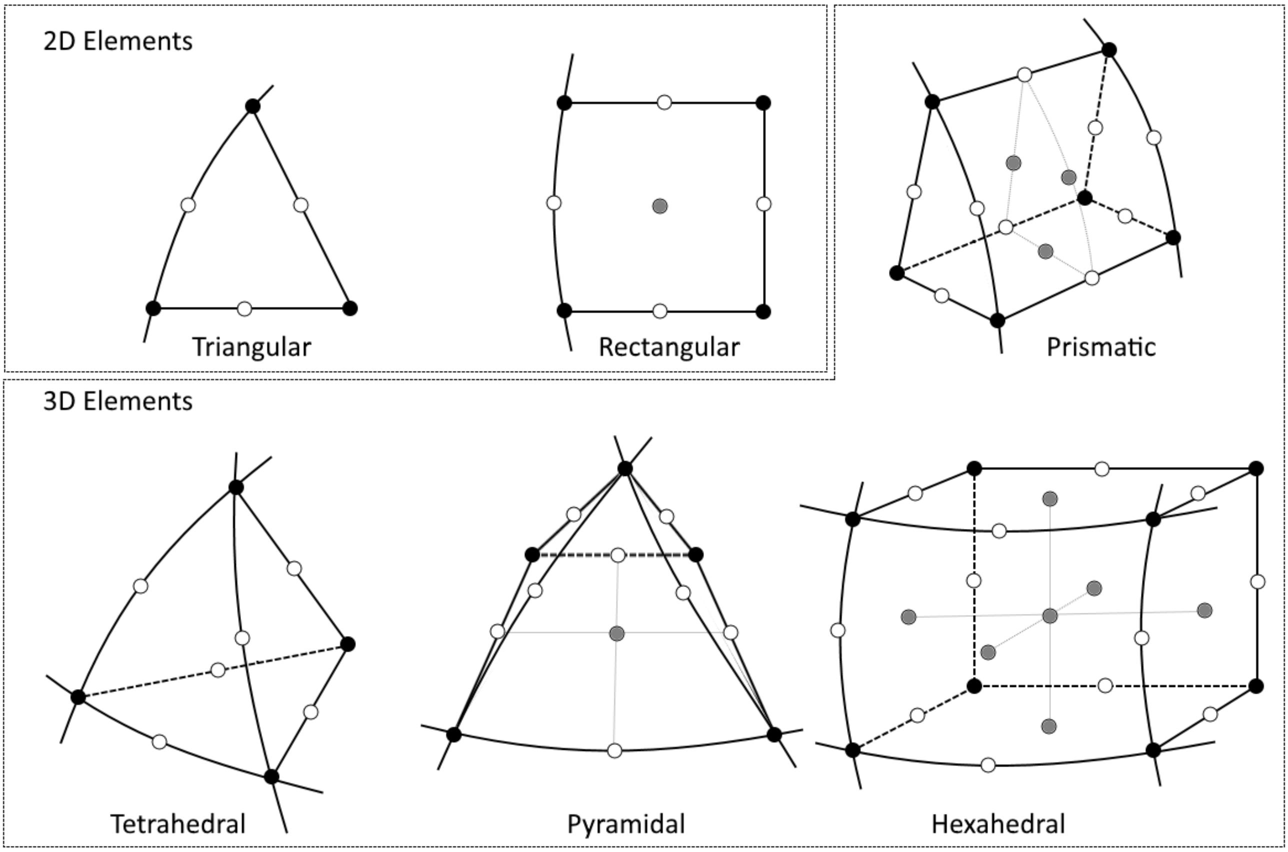

Figure B.1 – Visualization of node placement in second-order elements (Obtained from COMSOL Multiphysics® (2021)).

The meshes in Figure B.2 were used to identify whether the models used during the optimization of the MEMS cantilever were acceptable. The mesh with the maximum element size $L_c/10$ was used during the DE optimizations, and the mesh used in the second step optimization (NM or SO) was the mesh with $L_c/30$ element size. The original mesh (used in DE) had second-order serendipity prismatic elements.

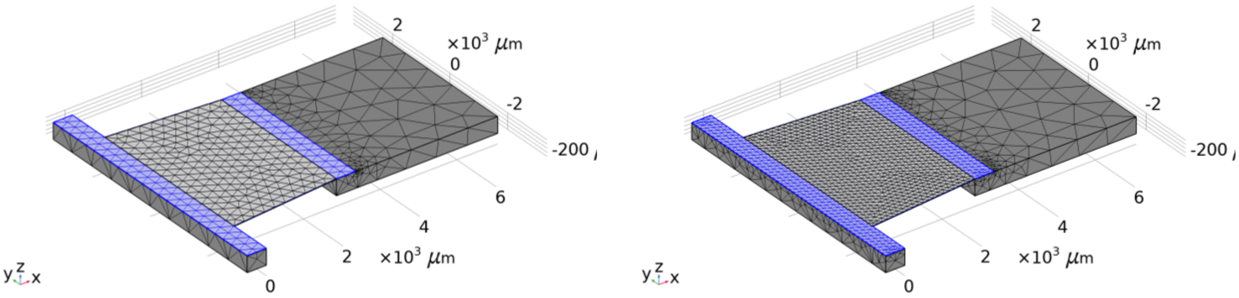

(a) $L_c/10$ prismatic element.

(b) $L_c/20$ prismatic element.

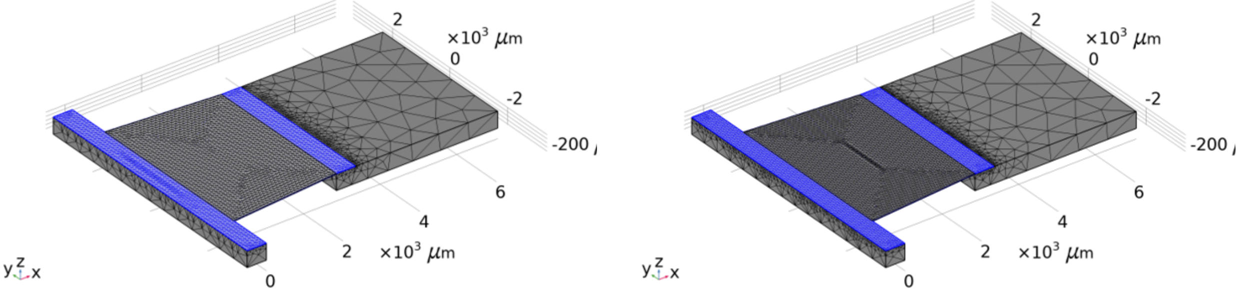

(c) $L_c/30$ prismatic element.

(d) $L_c/40$ prismatic element.

Figure B.2 – Different meshes used in the mesh analysis.

The critical features that must be validated to analyze the convergence are the natural frequency, power amplitude, and von Mises stress amplitude. Figure B.3 shows the effects of introducing five elements on the thickness of the piezoelectric material or three elements on the thickness of the cantilever. However, no significant changes were observed.

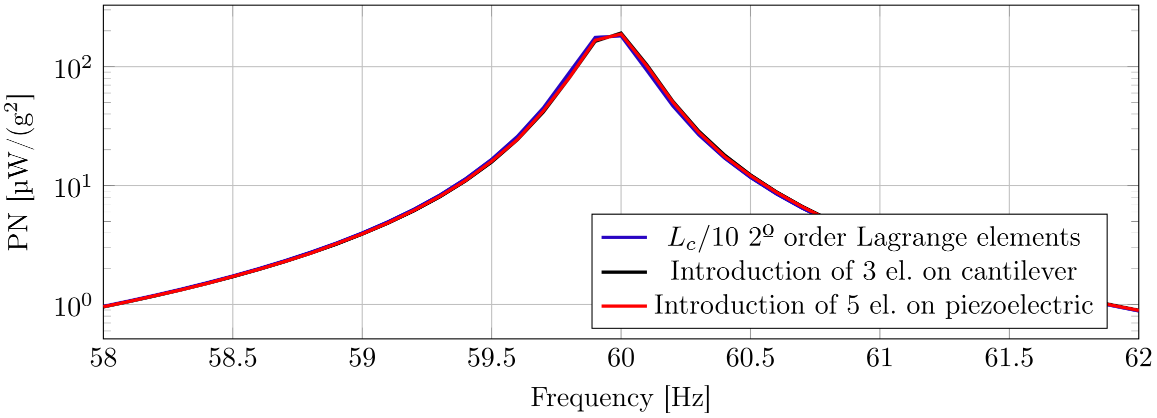

Figure B.3 – Power per frequency comparison between different element discretizations along the thickness of the piezoelectric and the beam.

Figure B.4 shows the change in power as a function of frequency with a change in the maximum element size over the cantilever. The corresponding number of degrees of freedom for each model is 20595 for $L_c/10$ serendipity, 26499 for $L_c/10$ Lagrange, 93453 for $L_c/20$ Lagrange, 207447 for $L_c/30$ Lagrange, and 359793 for $L_c/40$ Lagrange. The error in the natural frequency between the original mesh and the $L_c/40$ Lagrange mesh power was approximately 0.6%. However, the amplitude did not change significantly.

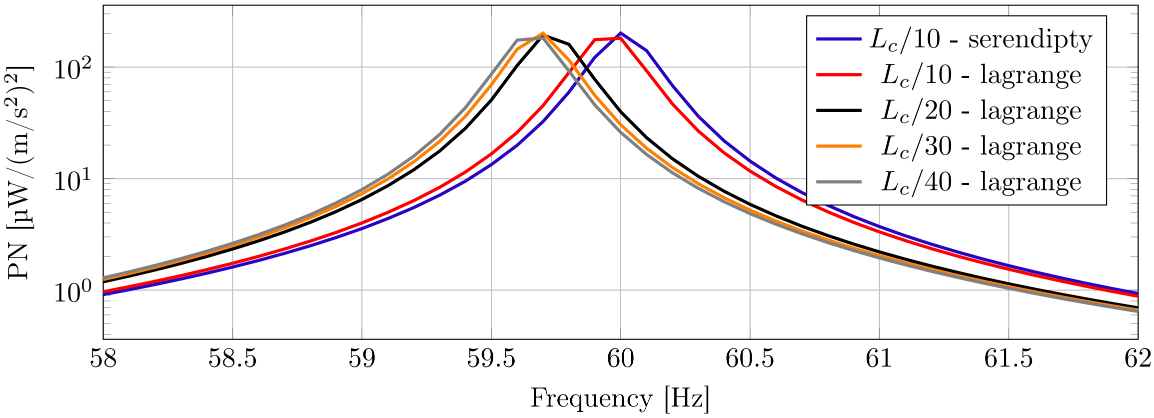

Figure B.4 – Power per frequency comparison between different element discretizations along the length and width of the beam.

So far, the elements used in this analysis are all second-order prismatic; Figure B.5 shows different order Lagrange elements. The correspondent number of degrees of freedom of each model is: 26499 for $L_c/10$ quadratic, 77550 for $L_c/10$ cubic, 173427 for $L_c/10$ quartic, 359793 for $L_c/40$ quadratic. There is a discrepancy between the fourth-order elements and the third-order elements, but the fourth-order elements seem to converge with $L_c/40$ second-order element mesh. This suggests that the third-order elements are artificially reducing the stiffness of the model. The fourth-order elements appear to validate the results of the $L_c/40$ second-order mesh.

Figure B.6 shows the von Mises stress field on the piezoelectric material along with the maximum and minimum values. The error in terms of the von Mises stress magnitude between the original mesh and the $L_c/40$ 2º order Lagrange mesh is approximately 1.9%. The stress does not monotonically converge to a value, primarily because of the simulation's frequency discretization of 0.1 Hz. Overall, the error was still low. In addition, the same pattern was observed in the stress field for higher-order elements in Figure B.7.

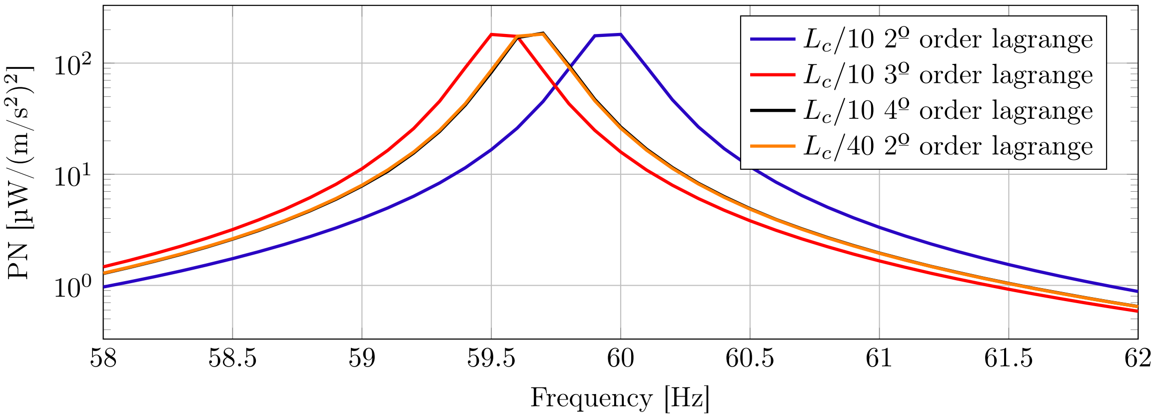

Figure B.5 – Power per frequency comparison of different element order.

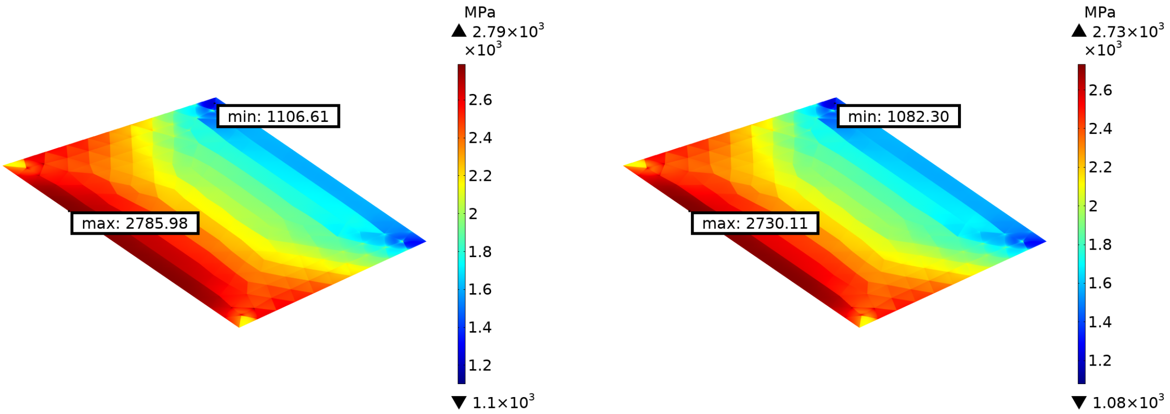

(a) $L_c/10$ 2º order serendipity.

(b) $L_c/10$ 2º order Lagrange.

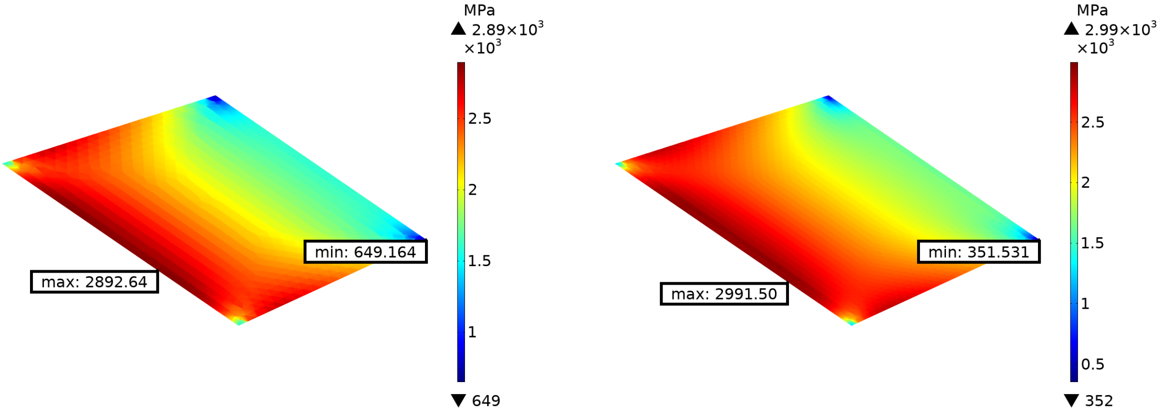

(c) $L_c/20$ 2º order Lagrange

(d) $L_c/30$ 2º order Lagrange

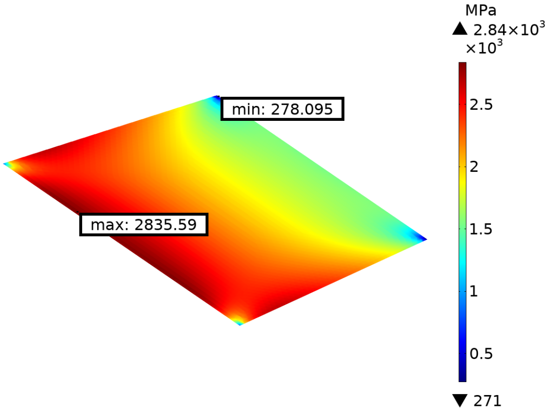

(e) $L_c/40$ 2º order Lagrange

Figure B.6 – Von Mises Stress field on frequency with maximum power output.

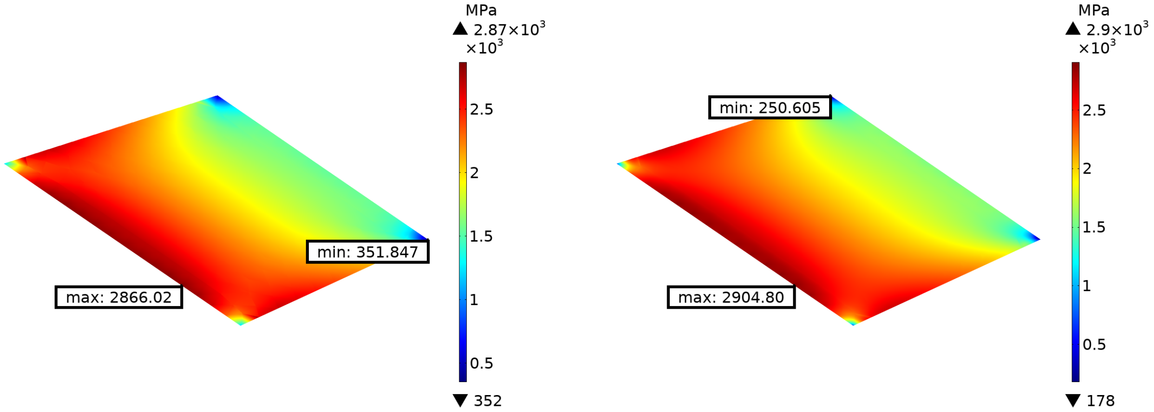

(a) $L_c/10$ 3º order Lagrange

(b) $L_c/10$ 4º order Lagrange

Figure B.7 – Von Mises Stress field on frequency with maximum power output for different order element.

APPENDIX C

OPTIMIZATIONS BOUNDARIES

This appendix presents the optimization box-constraints for all optimizations in this work, which were not presented in the text. Specifically, the devices presented in Section 4.1 (Tables C.1 to C.4), Section 4.2 (Tables C.5 and C.6), and Section 4.5 (Tables C.7 to C.9).

Table C.1 – Box-constraints of cantilever in preliminary optimization.

Parameter		Lower boundary	Upper boundary
W_{sm}	[µm]	500	3000
W_c	[µm]	500	3000
W_{pz}	[µm]	500	3000
W_{el}	[µm]	500	3000
L_{sm}	[µm]	500	3000
L_c	[µm]	500	5000
L_{pz}	[µm]	500	5000
L_{el}	[µm]	500	5000
D_{pz}	[µm]	-300	1500
D_{el}	[µm]	-300	1500
R_{load}	[Ω]	10^2	10^6

Table C.2 – Box-constraints of trampoline in preliminary optimization.

Parameter		Lower boundary	Upper boundary
W_{sm}	[µm]	500	3000
$W_{b,i}$ $(i = 1, ..., 4)$	[µm]	500	3000
L_{sm}	[µm]	500	3000
$L_{b,i}$ $(i = 1, ..., 4)$	[µm]	500	3000
R_l	[Ω]	10^2	10^6

Table C.3 – Box-constraints of flower in preliminary optimization.

Parameter		Lower boundary	Upper boundary
r_c	[µm]	200	1000
$\theta_{b,i}\ (i = 1, ..., 4)$	[°]	15	90
$L_{b,i}\ (i = 1, ..., 4)$	[µm]	400	3000
$L_{sm,i}\ (i = 1, ..., 4)$	[µm]	500	3000
R_{load}	[Ω]	10^2	10^6

Table C.4 – Box-constraints of cantilever array in preliminary optimization.

Parameter		Lower boundary	Upper boundary
$W_{sm,i}\ (i = 1, ..., 6)$	[µm]	400	1400
$L_{sm,i}\ (i = 1, ..., 6)$	[µm]	1500	5000
$W_{b,i}\ (i = 1, ..., 6)$	[µm]	400	1400
$L_{c,i}\ (i = 1, ..., 6)$	[µm]	1500	5000
R_{load}	[Ω]	10^4	10^7

Table C.5 – Box-constraints of area B MEMS optimization.

Parameter		Lower boundary	Upper boundary
W_{sm}	[µm]	500	2750
W_b	[µm]	500	2750
W_{b+}	[µm]	0	500
W_{pz}	[µm]	500	2750
W_{el}	[µm]	500	2750
L_{sm}	[µm]	2500	4500
L_b	[µm]	500	2000
L_{pz}	[µm]	500	2000
L_{el}	[µm]	500	2000
R_l	[Ω]	10^4	10^8

Table C.6 – Box-constraints of area D MEMS optimization.

Parameter		Lower boundary	Upper boundary
W_{sm}	[µm]	500	2250
W_b	[µm]	500	2250
W_{b+}	[µm]	0	500
W_{pz}	[µm]	500	2250
W_{el}	[µm]	500	2250
L_{sm}	[µm]	2500	5000
L_b	[µm]	1000	3000
L_{pz}	[µm]	1000	3000
L_{el}	[µm]	1000	3000
R_l	[Ω]	10^4	10^8

Table C.7 – Box-constraints of all PIEZO.COM devices optimizations.

Parameter		Lower boundary	Upper boundary
L_{sm}	[µm]	4000	10000
W_{sm}	[µm]	4000	10000
T_{sm}	[µm]	4000	10000
L_b	[µm]	4000	10000
W_b	[µm]	1000	8000
W_{b+}	[µm]	0	5000
R_l	[Ω]	10^3	10^7

Table C.8 – Box-constraints of all STEMINC devices optimizations.

Parameter		Lower boundary	Upper boundary
L_{sm}	[µm]	2000	24500
W_{sm}	[µm]	2000	10000
T_{sm}	[µm]	2000	7000
L_b	[µm]	1000	23500
W_b	[µm]	1000	10000
W_{b+}	[µm]	0	5000
R_l	[Ω]	10^3	10^8

Table C.9 – Box-constraints of MFC device optimization.

Parameter		Lower boundary	Upper boundary
L_{sm}	[µm]	2000	24500
W_{sm}	[µm]	2000	10000
T_{sm}	[µm]	2000	7000
L_b	[µm]	1000	23500
W_b	[µm]	1000	10000
T_c	[µm]	100	1000
R_l	[Ω]	10^3	10^8

APPENDIX D

OPTIMIZATION DOMAIN INVESTIGATION

To further understand how the objective function presented in Equation 4.9 behaves, surface plots were generated using the MEMS D, simultaneously varying a pair of parameters. Hence, the Figures D.1 to D.10 are presented below.

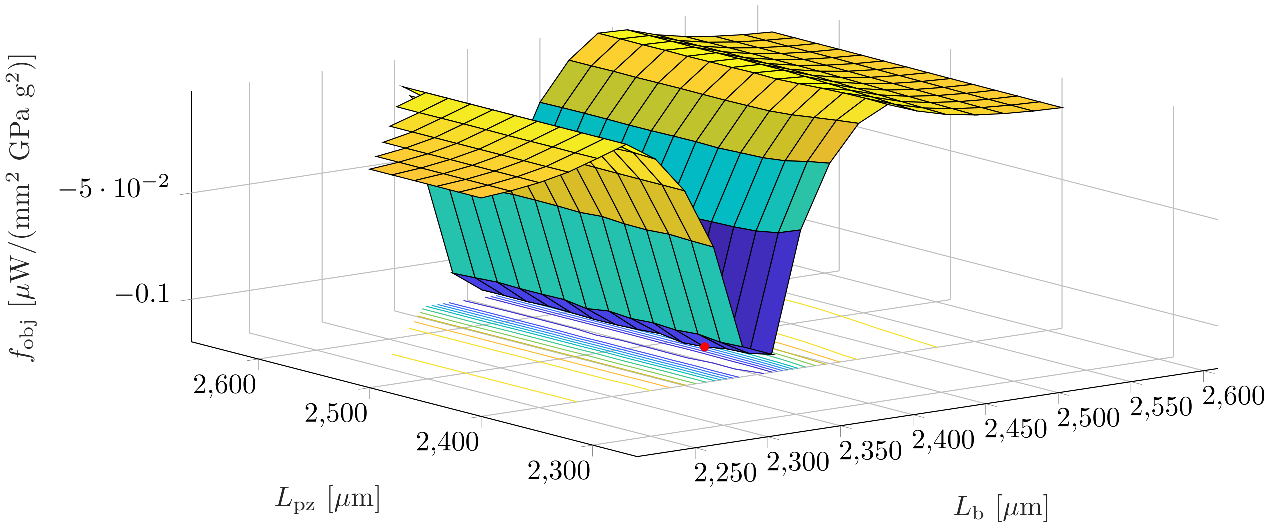

Figure D.1 – Surface plot of objective function with varying parameters L_{b} and L_{pz}.

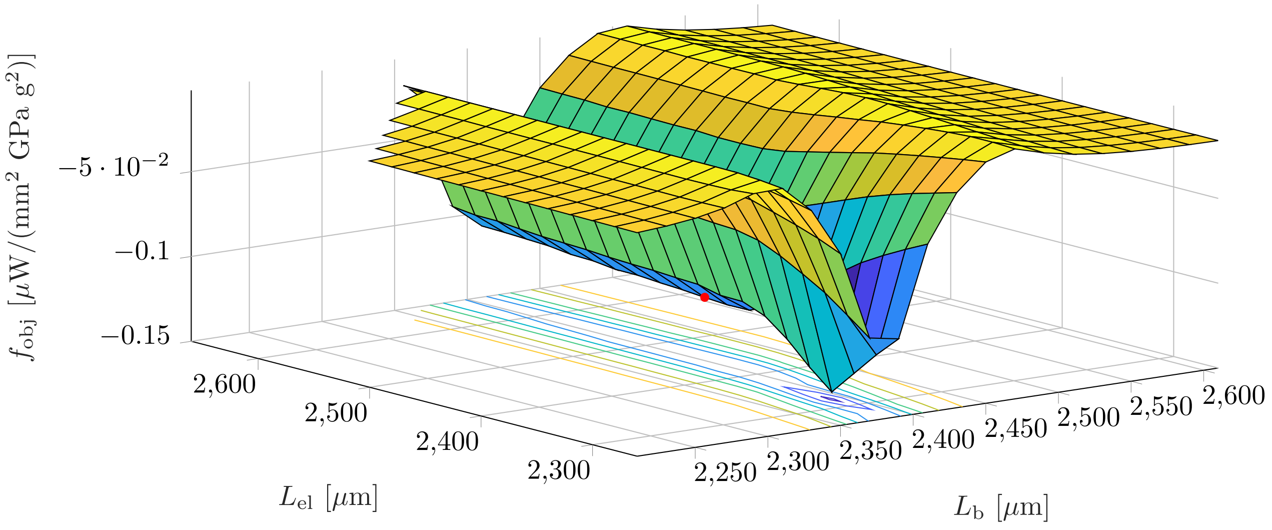

Figure D.2 – Surface plot of objective function with varying parameters L_{b} and L_{el}.

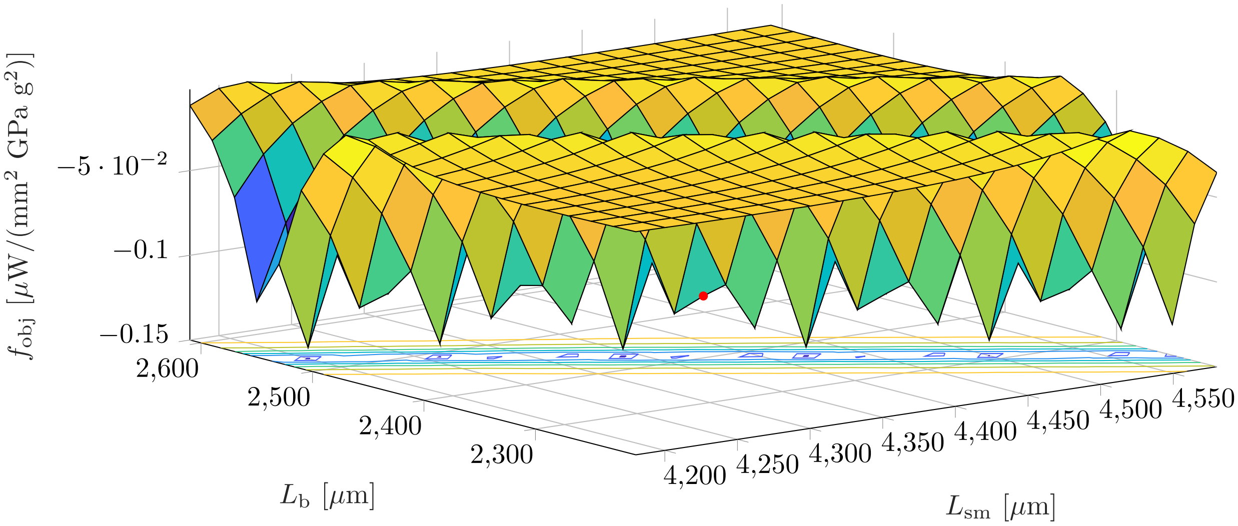

Figure D.3 – Surface plot of objective function with varying parameters L_{sm} and L_{b}.

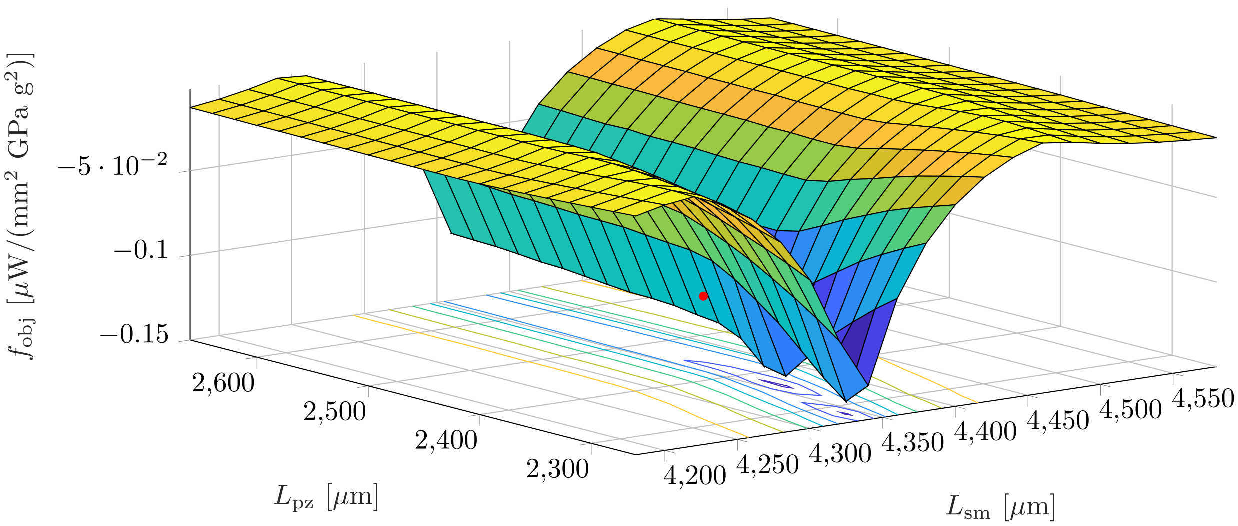

Figure D.4 – Surface plot of objective function with varying parameters L_{sm} and L_{pz}.

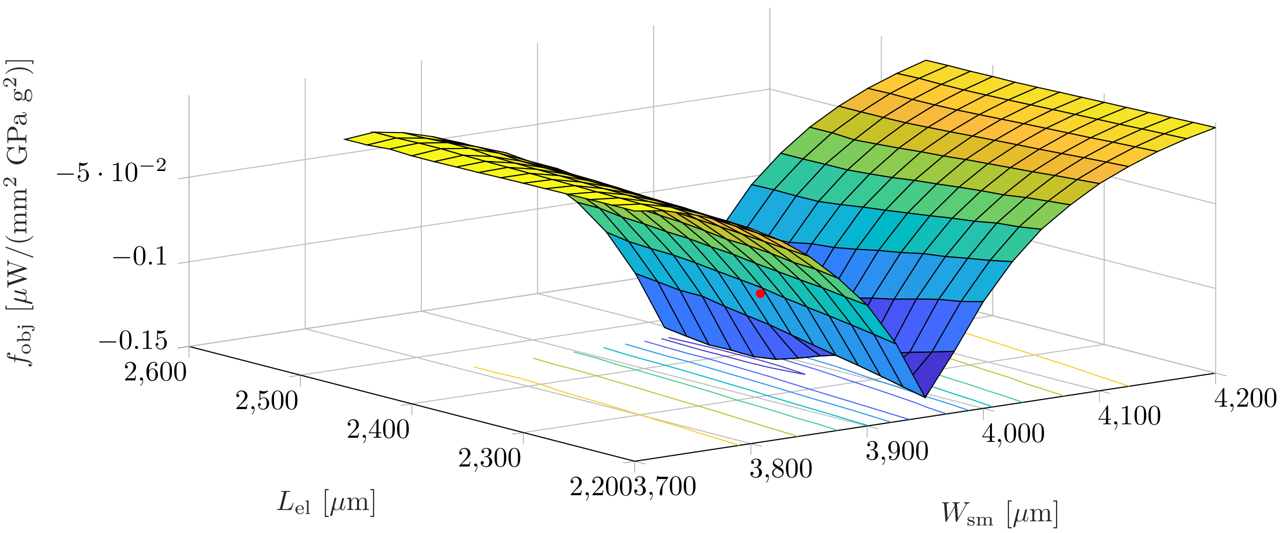

Figure D.5 – Surface plot of objective function with varying parameters W_{sm} and L_{el}.

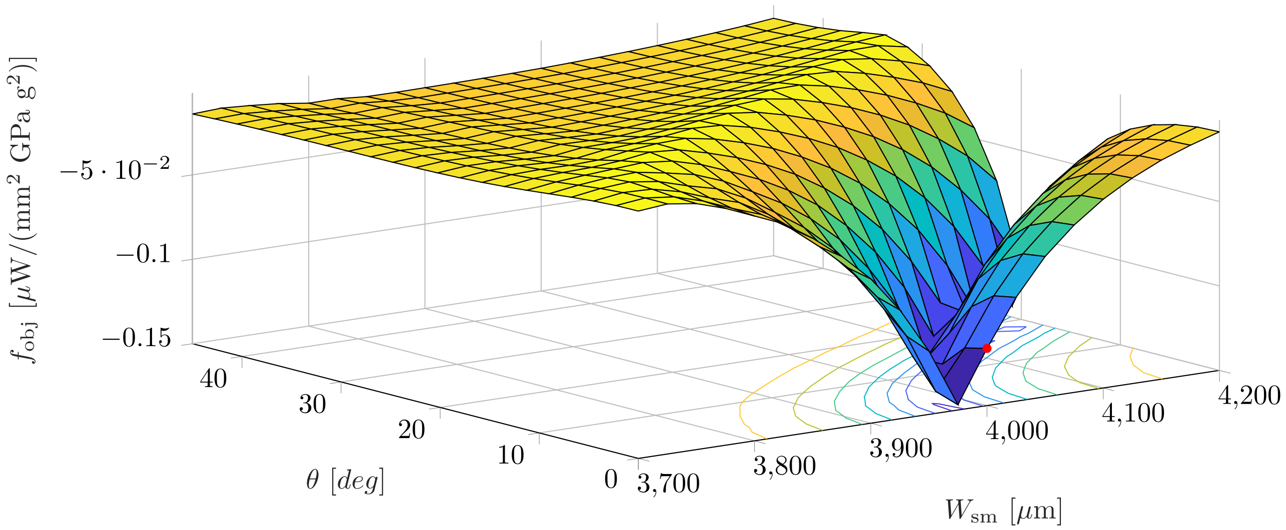

Figure D.6 – Surface plot of objective function with varying parameters W_{sm} and θ.

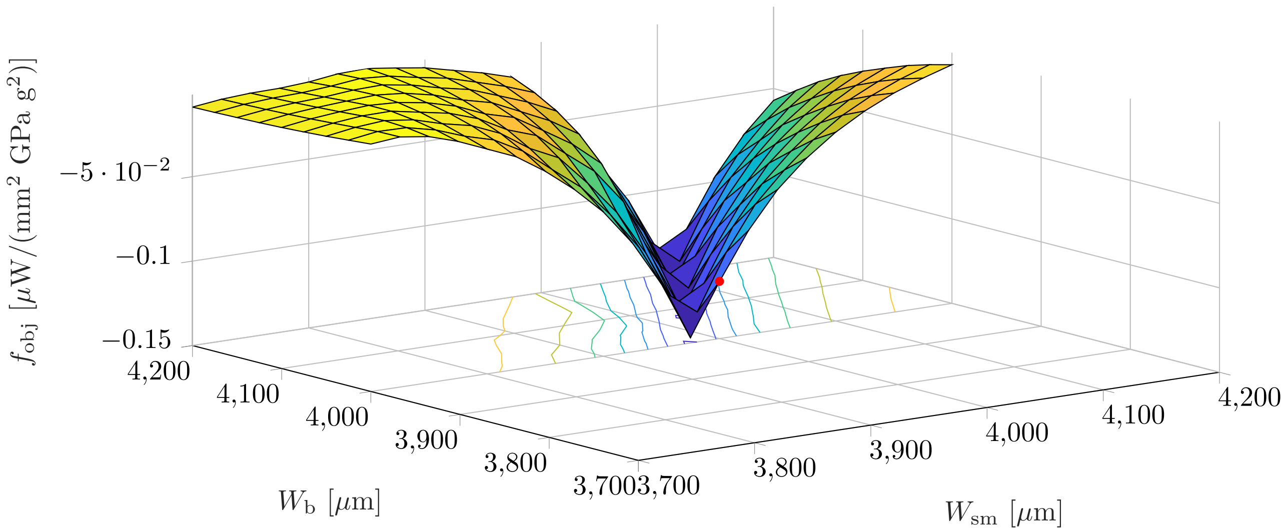

Figure D.7 – Surface plot of objective function with varying parameters W_{sm} and W_{b}.

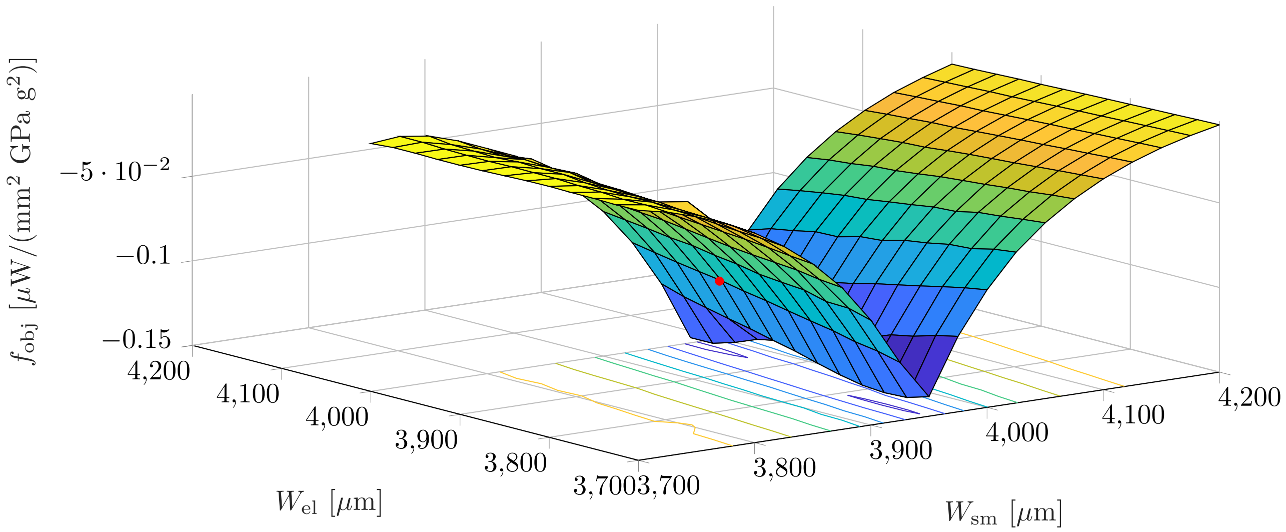

Figure D.8 – Surface plot of objective function with varying parameters W_{sm} and W_{el}.

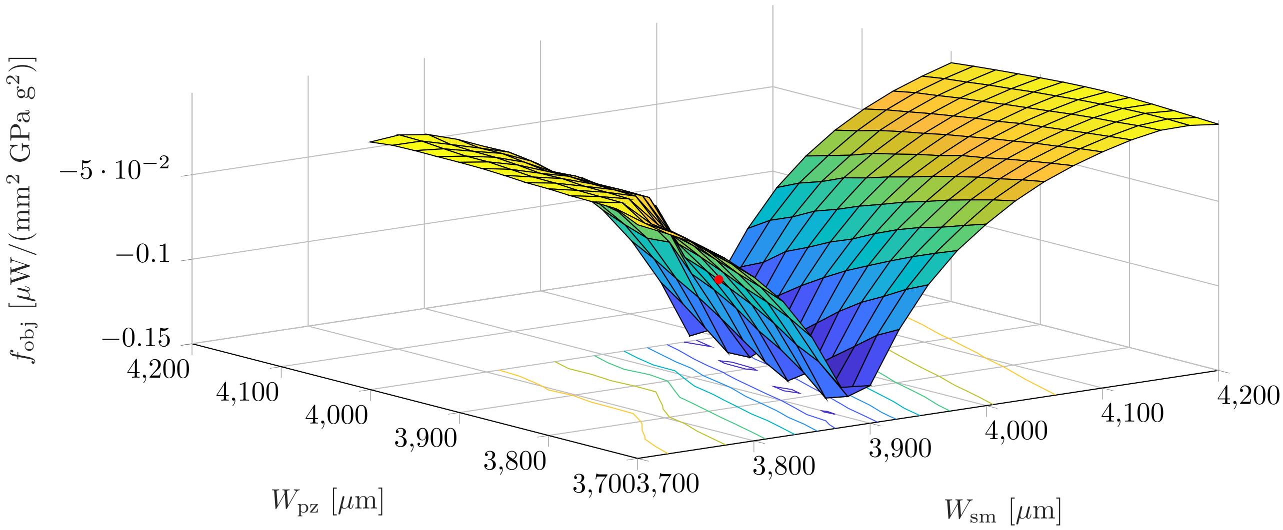

Figure D.9 – Surface plot of objective function with varying parameters W_{sm} and W_{pz}.

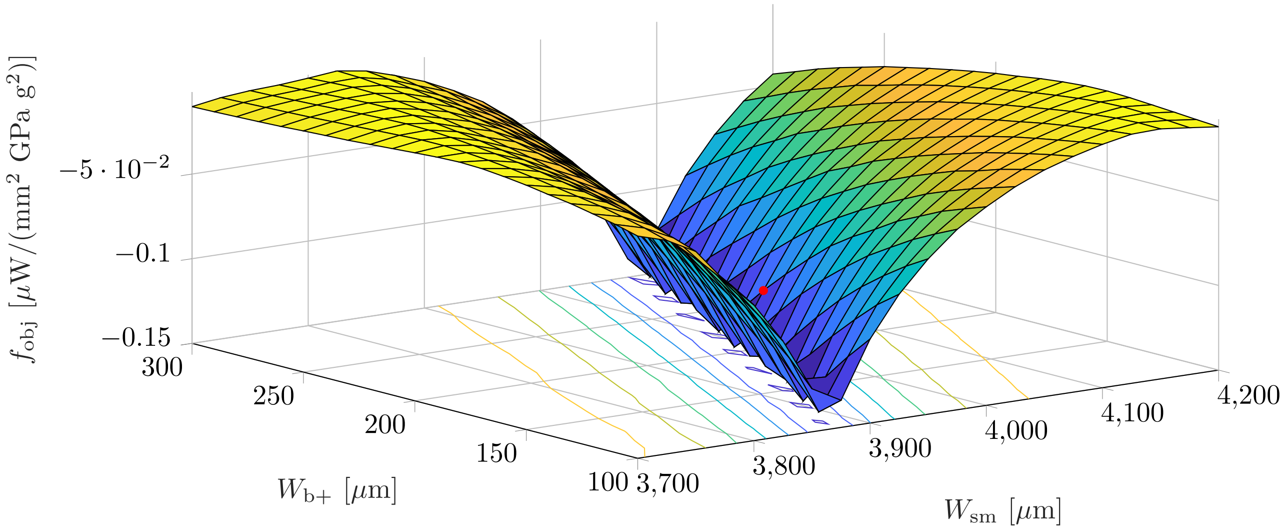

Figure D.10 – Surface plot of objective function with varying parameters W_{sm} and $W_{\mathrm{b+}}$.

APPENDIX E

MONOSTABLE BROADBAND TECHNIQUE

Huicong Liu et al. (2012b) developed a monostable nonlinear device cantilever type, whose nonlinearity is introduced via a mechanical stopper. Thus, when in contact with the stopper, the seismic mass introduces hardening to the system that consequently "pulls the natural frequency up," creating a broadband effect. Figure E.1 illustrates the effect on the relative motion of the PVEH's seismic mass. It can be highlighted the existence of the "stable cure," e.g., the curve that represents the displacement amplitude of the PVEH only when an up-frequency sweep excitation sweeps the device.

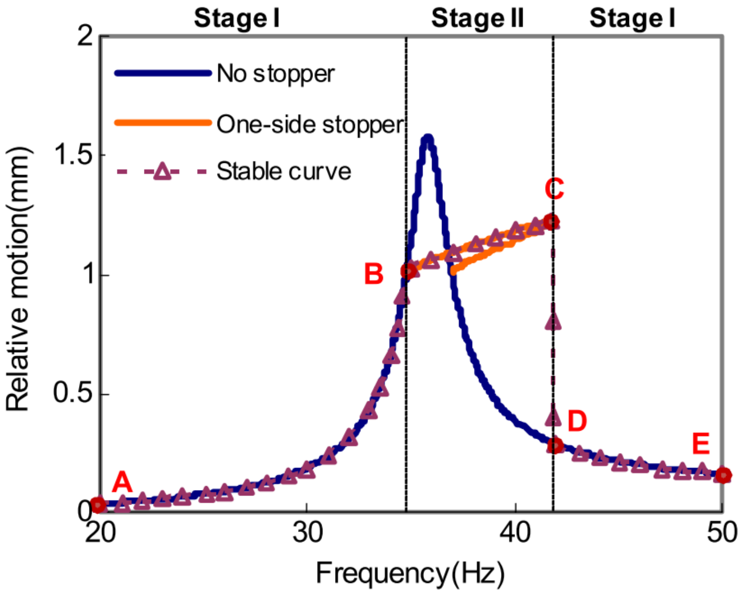

Figure E.1 – Illustration of the effect of a mechanical stopper non-linear system (Obtained from Huicong Liu et al. (2012b)).

Together with this device, Huicong Liu et al. (2012b) developed a 1-degree-of-freedom analytical model for a seismic mass subject to an upper and lower mechanical stopper at the d_1 and $-d_2$ positions, respectively. The displacement amplitude x for this problem is governed by the following transcendent equation:

$$\pi^2\Omega^4 = X_1^2 + X_2^2 \tag{E.1}$$

Where

$$\begin{aligned} X_1 = &-2\xi_0 x\Omega\pi - \Omega_1\xi_1 x\Omega\left(\pi - 2\varphi_1 - \sin 2\varphi_1\right) \\ &- \Omega_2\xi_2 x\Omega\left(\pi - 2\varphi_2 - \sin 2\varphi_2\right), \end{aligned} \tag{E.2}$$

and

$$\begin{aligned} X_2 =& \pi x\left(1-\Omega^2\right)-\frac{1}{2}\Omega_1^2 x\left(2\varphi_1-\sin 2\varphi_1-\pi\right) \\ &+\frac{1}{2}\Omega_2^2 x\left(2\varphi_2-\sin 2\varphi_2-\pi\right)+2\Omega_1^2\Delta_1\cos\varphi_1+2\Omega_2^2\Delta_2\cos\varphi_2, \end{aligned} \tag{E.3}$$

where $\varphi_1 = \text{sen}^{-1}(\Delta_1/x)$ and $\varphi_2 = \text{sen}^{-1}(\Delta_2/x)$ are the phase angle at which the seismic mass meets the upper and lower mechanical stoppers, respectively. Also, $\Delta_\mathrm{i} = d_\mathrm{i}/x_\mathrm{b}$, $\Omega_\mathrm{i}^2 = \omega_\mathrm{i}/\omega_\mathrm{n}$, $\omega_\mathrm{i}^2 = k_\mathrm{i}/m_\mathrm{eq}$, $2\xi_\mathrm{i}\omega_\mathrm{i} = b_\mathrm{i}/m_\mathrm{eq}$ where the subscript i identifies whether the property belongs to the mass-spring-damper system (0), the upper mechanical stopper (1) or the lower mechanical stopper (2), where k_i is the stiffness, and b_i is the viscous damping constant.

Figure E.2 presents the validation of the analytical model of Huicong Liu et al. (2012b,a), where "S" and "E" represent the simulation results (which make use of the Equation E.1) and the experimental results, respectively. P1, P2 and P3 represent different height levels between the seismic mass and the stopper, being 1.7 mm, 1.2 mm, and 0.7 mm, respectively. From this result, we can verify that the lower the height of the stopper, the lower the maximum power, but the more significant is the bandwidth increase. Therefore, it is necessary to correctly set the height of the stopper to optimize the ratio between maximum power and bandwidth.

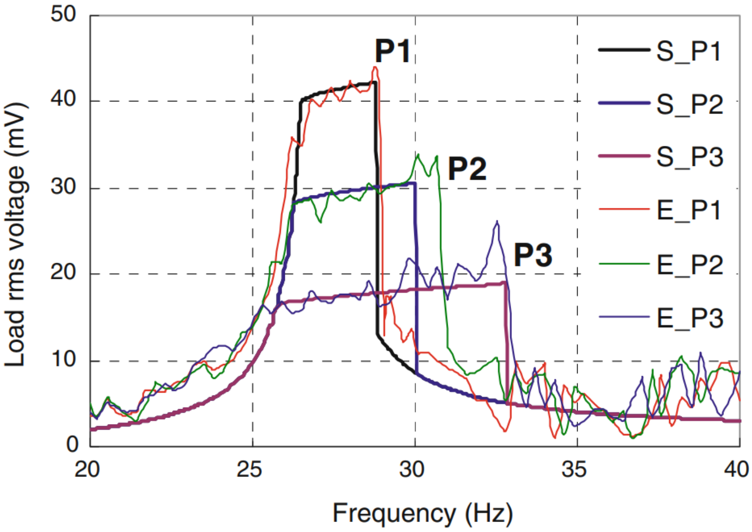

Figure E.2 – Experimental result from Liu's et al. monostable device (obtained from (LIU, H. et al., 2012a)).

This mathematical model was implemented to predict the increase in bandwidth that MEMS devices could operate working with a mechanical stopper. Figure E.3 and E.4 show the normalized power curves of MEMS D and MEMS-free using a mechanical stopper with a spacing of 1.4 mm and 0.67 mm, respectively. The 1 DoF mathematical model representation of the COMSOL model was obtained by curve-fitting the seismic mass displacement. Variables such as mechanical stopper damping and natural frequency were assumed to be equal to those used by Huicong Liu et al. (2012b). The total bandwidth obtained by the mathematical model of MEMS D was 4.1 Hz (defined by the difference of the frequencies where the maximum von Mises stress was reached in the piezoelectric material), where the original bandwidth was 2.6 Hz (defined the same way). For MEMS free, the bandwidth was increased from 3.2 Hz to 7.1 Hz; in this case, the bandwidth was defined using the half power band. Therefore, the increase in the band occurs at the cost of maximum power. If the band is defined by the 10 µW mark, the increase was from 4.9 Hz to 5.5 Hz. Using a fixed power value (or stress like with MEMS D) can better reflect the band widened by the mechanical stopper.

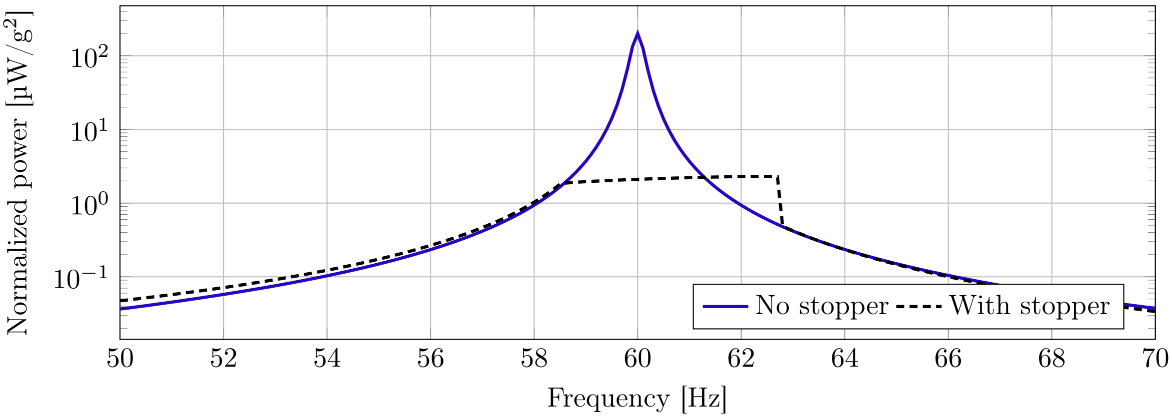

Figure E.3 – Comparison of normalized power of COMSOL model MEMS D without stopper and mathematical model of monostable broadband technique with movement limited by mechanical stopper.

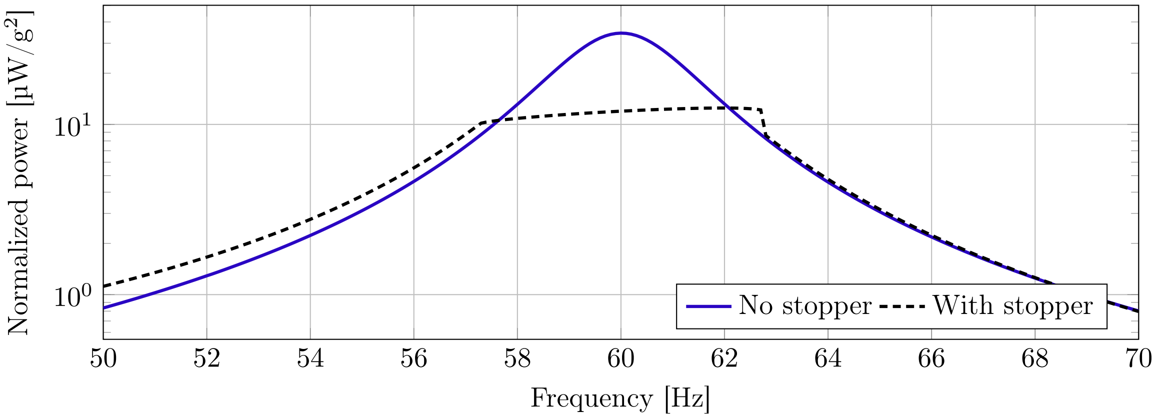

Figure E.4 – Comparison of normalized power of COMSOL model MEMS free without stopper and mathematical model of monostable broadband technique with movement limited by mechanical stopper.